

Doctoral thesis

Doctoral theses at NTNU, 2022:130

Wahyu Wijanarko

# Ionic Liquids as Additives in Low Viscosity Lubricants – A Surface Adsorption and Tribofilm Study

**NTNU**  
Norwegian University of Science and Technology  
Thesis for the Degree of  
Philosophiae Doctor  
Faculty of Engineering  
Department of Mechanical and Industrial  
Engineering



Norwegian University of  
Science and Technology



Wahyu Wijanarko

# **Ionic Liquids as Additives in Low Viscosity Lubricants – A Surface Adsorption and Tribofilm Study**

Thesis for the Degree of Philosophiae Doctor

Trondheim, May 2022

Norwegian University of Science and Technology  
Faculty of Engineering  
Department of Mechanical and Industrial Engineering



Norwegian University of  
Science and Technology

**NTNU**

Norwegian University of Science and Technology

Thesis for the Degree of Philosophiae Doctor

Faculty of Engineering

Department of Mechanical and Industrial Engineering

© Wahyu Wijanarko

ISBN 978-82-326-5366-9 (printed ver.)

ISBN 978-82-326-5264-8 (electronic ver.)

ISSN 1503-8181 (printed ver.)

ISSN 2703-8084 (online ver.)

Doctoral theses at NTNU, 2022:130

Printed by NTNU Grafisk senter



# Preface

This doctoral thesis is submitted to the Norwegian University of Science and Technology for partial fulfilment of degree of philosophiae doctor.

This research has been performed at the Department of Mechanical and Industrial Engineering, Norwegian University of Science and Technology under the supervision of Professor Nuria Espallargas (NTNU) and co-supervisor Dr. Hamid Khanmohammadi (NTNU) and Dr. Fahmi Mubarak (Sepuluh Nopember Institute of Technology (ITS), Surabaya, Indonesia) during the period of August 2017 to February 2022.

The scholarship awarded to Wahyu Wijanarko has been financed by Indonesia Endowment Fund for Education (LPDP). This PhD thesis is part of the M-era.Net project “GreenCOAT” funded by Research Council of Norway. The research work has also received economical support from the Norwegian Micro- and Nano-fabrication facility, NorFab.

The thesis consists of two parts. Part I (Chapter 1 to 10) includes introduction, literature review, and a summary of the work published in peer-reviewed journals. Part II contains three peer-reviewed journal papers published in scientific journals.

*This page is intentionally left blank*

# Acknowledgments

First of all, I would like to thank my supervisor Professor Nuria Espallargas for giving me the opportunity to do this Ph.D. here at NTNU Norway. I also would like to thank my co-supervisor Dr. Fahmi Mubarak, for the information about this Ph.D. position. It was a rainy season in Indonesia back in 2016 when he called and informed me that Professor Nuria Espallargas had a Ph.D. vacancy in tribology that I could apply to. Without both of them, I would not be here.

Doing a Ph.D. is one hell of a journey; this is why I would like to express my sincere gratitude to my supervisor Professor Nuria Espallargas for the amazing support, patience, and guidance over the last four and half years. Her encouragement and constructive criticism developed my competencies for fulfilling my Ph.D. and forged me to become a better researcher. I also would like to express my sincere gratitude to my co-supervisor and fellow office mate Hamid Khanmohammadi for his support, suggestions, discussions, hospitality, and chats from the premier league to the world cup.

I acknowledge the financial support from Indonesia Endowment Fund for Education (LPDP), MERA.NET GreenCOAT project (Project Number 4153 funded by Research Council of Norway). I also acknowledge the economic support for part of my research work from the Norwegian Micro- and Nanofabrication Facility, NorFab. I also acknowledge, the economic support of the Department of Mechanical and Industrial Engineering (NTNU) for supporting my stay in Trondheim.

I would like to thank all the staff at the Mechanical and Industrial Engineering Department, NTNU especially Aud Bodil Olsen, Natalia Trotsenko, Øyvind Andersen, and Børge Holen for their support with administration, IT, and workshop. I also would like to thank SINTEF Corrosion lab, NTNU Nanolab staff, especially Nils-Inge Nilsen, Ann-Karin Kvernbråten, Amin Hossein Zavieh, and Ken Roger Ervik for their assistance in the lab. I thank all my friends and colleagues in the Tribology Research Group, especially Emil Valaker, Szymon Bernat, Amin Hossein Zavieh, Cristian Torres Rodriguez, Gaute Stenerud, Carlos R. Pascual Guzman, and Aidan von Bonin, for their presence, company and help during my Ph.D. time.

My sincere thanks also go to my parents Widji Soekamto and Eko Wirahayu, for believing and investing in me. Both of them always worked hard so I could have an amazing childhood and excellent education. I would also thank my sister Dinar Puspitarini Wijayanti for all the support and kindness.

Last but not least, I express my deepest gratitude to the love of my life, Indri Desiati, for her incredible love, unconditional support, and remarkable patience. My deepest gratitude also goes to my children Dzaky Ahmad Ghaisan, Muhammad Nabil Al Mu'afa, and Syifa Nadhifah Azzhara for their laughs, happiness, patience, and company during this period.

*This page is intentionally left blank*

# Abstract

The trend in lubrication nowadays is towards low viscosity lubricants. Low viscosity lubricants flow more easily, increasing the lubricant volume circulation thus improving the cooling performance and cleaning ability of the lubricants. In addition, low viscosity lubricants reduce the viscous drag thus lowering the frictional energy losses and increasing the efficiency of components. Moreover, low viscosity lubricants are the best candidates for lubricating electric vehicles (EVs) due to the presence of more torque transfer components (transmission) than in internal combustion engine vehicles. Therefore, the application of low viscosity lubricants will increase the performance and extend the lifetime of EVs. While low viscosity lubricants offer many advantages, there are also challenges that go with them. Firstly, there will be more pair contact at the beginning of the operation. Secondly, the low viscosity of the lubricant will result in a higher friction at the boundary and mixed lubrication regimes. Lastly, the low viscosity the lubricant will result in longer running-in times at the boundary and mixed lubrication regimes. To overcome these challenges, one of the proposed strategies is developing multifunctional additives which simultaneously will work as anti-wear and friction reduction at the same time. To tackle these issues, this Ph.D. thesis investigates the potential use of ionic liquids (ILs) as additives in low viscosity lubricants.

Firstly, preliminary studies of six ILs with different anion, cation, and alkyl chain length as additives were performed. The selected ILs were 1,3-dimethylimidazolium dimethylphosphate (IM), (2-hydroxyethyl) trimethylammonium dimethylphosphate (AM), tributylmethylphosphonium dimethylphosphate (PP), 1-butyl-1-methylpyrrolidinium tris(pentafluoroethyl) trifluorophosphate (BMP), trihexyltetradecylphosphonium bis(2,4,4-trimethylpentyl)phosphinate (PB), and trihexyltetradecylphosphonium decanoate (PC). The ILs were mixed individually in low viscosity lubricants (polar and non-polar), i.e., four water-glycol mixtures (as polar base lubricant) and two polyalphaolefins (as non-polar base lubricant). The water-glycol base lubricants were water-monoethylene glycol (WMEG), water-diethylene glycol (WDEG), water-monopropylene glycol (WMPG), and water-dipropylene glycol (WDPG). The polyalphaolefin base lubricants were polyalphaolefin 2 cSt and 8 cSt. All lubricants combinations were analyzed in terms of mixture stability and solubility and tribological performances of the ionic liquids as lubricant additives. The results showed that long alkyl chain ILs, PB and PC, resulted in high turbidity numbers and poor stability. The tribological performances of short alkyl chain ILs, IM, AM, PP, and BMP, showed no improvement in wear protection. In the case of friction, only WDPG-ILs and PAO8-IL combinations brought lower friction evolution than the corresponding base lubricant.

Secondly, the effect of the additives' concentration was investigated in terms of tribological performances (friction and wear). Five different concentrations of ILs were studied 0.25, 0.5, 1, 2, and 4 wt.%. The results obtained from preliminary studies led to the selection of short alkyl chain ILs (IM, AM, PP, and BMP) and WDPG and PAO8 as the base lubricants. For simplicity, WDPG and PAO8 will be called only WG and PAO, respectively. A comprehensive analysis of the influence of ILs and their concentration on friction and wear were conducted using a Two-way ANOVA. The results showed that an increase in the ILs' concentration raised both the coefficient of friction (COF) and specific wear rate (SWR) for WG lubricants however, it reduced COF and SWR for PAO lubricants depending on the IL type and concentration. From this study, PP and BMP were selected for further studies with the concentration of 1 wt.%.

Thirdly, the adsorption behavior of the selected ILs, PP and BMP, were investigated in both polar (WG) and non-polar (PAO) media. The adsorption behavior of the ILs was compared with a well-known organic friction modifier additive, i.e., carboxylic acid (dodecanoic acid, C12). The adsorption studies were performed using a quartz crystal microbalance with dissipation (QCM-D). The adsorption behaviors of the additives were investigated on two surfaces, namely iron and stainless steel surfaces by using iron (Fe)-coated sensor and stainless steel (SS)-coated sensor. The results showed that PP and BMP formed thicker multi-layer structures in non-polar media compared to polar media. In the case of C12, the results showed that C12 formed a thicker, more viscous, and more rigid adsorbed layer in polar media than in non-polar media. For WG lubricants, there was no significant difference in the adsorption behavior of the additives between Fe and SS coated sensors. However, for PAO lubricants, only PP and BMP showed higher adsorption kinetics and initially adsorbed layer on the SS surface than the Fe surface, whereas C12 showed no significant differences in the adsorption behaviour.

Lastly, the tribological performances of PP and BMP as additives in polar (WG) and non-polar (PAO) base lubricants were investigated on two types of steel, namely AISI 52100 bearing steel and AISI 316L stainless steel. The tribological performances of ILs were compared with C12. Intensive surface analyses using several advanced techniques were performed, such as scanning electron microscopy equipped with focused ion beam (FIB-SEM), scanning-transmission electron microscopy equipped with X-ray energy dispersive spectroscopy (STEM-EDS), and X-ray photoelectron spectroscopy (XPS). The results from adsorption studies by QCM-D were used to correlate the adsorption behavior with the tribological performance. In the case of the polar lubricants, the tribological performance of ILs was controlled by the presence of thick tribofilms which lowered the wear yet increasing the friction for AISI 52100 steel. On the other hand, thick tribofilms could not be formed due to the tribocorrosion process taking place on AISI 316L steel, thus the tribological performance of the ILs was controlled by

the tribocorrosion process. In the case of non-polar lubricants, the tribological performance of the ILs was controlled by the presence of thick tribofilms which increased both wear and friction for AISI 52100 steel. In the case of AISI 316L, the tribological performance of the ILs was controlled by both tribofilm durability and the properties of the adsorbed layer.

*This page is intentionally left blank*



# Table of Contents

Cover	i
Preface	iii
Acknowledgments	v
Abstract	vii
Table of Contents	xi
List of Figures	xv
List of Tables	xix
<b>1. Introduction and overview</b>	<b>1</b>
1.1. Background	1
1.2. Motivation	2
1.3. Objectives	3
1.4. Scope	4
1.5. Structure of the thesis	5
1.6. List of papers	7
<b>2. Literature review and state of the art</b>	<b>9</b>
2.1. Tribology and lubrication	9
2.2. Lubricants	12
2.3. Lubricant additives for boundary lubrication conditions	15
2.3.1. Friction modifiers	15
2.3.2. Antiwear additives	18
2.4. Ionic liquids	21
2.4.1. ILs as neat lubricants	21
2.4.2. ILs as lubricant additives	24
2.5. Viscoelastic layers in a bulk liquid: Continuum mechanics approach	26
<b>3. Experimental</b>	<b>31</b>
3.1. Materials and preparation	31
3.1.1. Lubricants	31
3.1.2. Steel specimens	33

3.2. Testing, statistical analysis and characterization.....	34
3.2.1. Density, conductivity, pH, and OCP .....	34
3.2.2. Dynamic viscosity .....	34
3.2.3. Lubricant stability study .....	34
3.2.4. Adsorption study.....	35
3.2.5. Tribological tests .....	37
3.2.6. Wear analysis.....	40
3.2.7. Statistical analysis.....	42
3.2.7.1. Two-way ANOVA analysis .....	42
3.2.7.2. Post-Hoc test.....	45
3.2.8. Surface topography and cross-section analysis .....	46
3.2.9. Tribo- and oxide film analysis.....	48
3.2.9.1. Scanning-transmission electron microscopy equipped with an x-ray energy dispersive spectroscopy (STEM/EDS).....	48
3.2.9.2. X-ray photoelectron spectroscopy (XPS).....	52
<b>4. Preliminary studies of ionic liquids as lubricant additives in water-glycol and polyalphaolefin base lubricants .....</b>	<b>57</b>
4.1. Mixture solubility and stability study.....	57
4.1.1. Mixture solubility and stability of ionic liquids in water-glycol .....	57
4.1.2. Mixture solubility and stability of ionic liquids in PAO .....	58
4.2. Tribological behavior study.....	59
4.2.1. Tribological performance of ionic liquids in water-glycol.....	59
4.2.2. Tribological performance of ionic liquids in PAO .....	60
4.3. Conclusion.....	62
<b>5. Influence of ionic liquid concentration on the tribological performance.....</b>	<b>63</b>
5.1. Study of ionic liquid concentration on the tribological performance in WG.....	63
5.1.1. The Two-way ANOVA analysis for the friction of WG lubricants .....	64
5.1.2. The Two-way ANOVA analysis for the wear of WG lubricants .....	67
5.2. Study of ionic liquid concentration on the tribological performance in PAO.....	69
5.2.1. The Two-way ANOVA analysis for the friction of PAO lubricants .....	70
5.2.2. The Two-way ANOVA analysis for the wear of PAO lubricants .....	72
5.3. Summary.....	75
5.4. Conclusion.....	76

<b>6. Adsorption study of ionic liquids additives in polar and non-polar media on iron and stainless steel coated sensors using Quartz Crystal Microbalance technique.....</b>	<b>77</b>
6.1. Adsorption study of ionic liquids additives in polar media (WG).....	78
6.2. Adsorption study of ionic liquids additives in non-polar media (PAO).....	81
6.3. Summary.....	86
6.4. Conclusion.....	87
<b>7. A tribological study of ionic liquids as boundary additives in a polar base lubricant .....</b>	<b>89</b>
7.1. Friction and wear performance in water-glycol.....	89
7.2. The effect of additives and surface chemistry on tribofilm formation .....	93
7.3. The effect of adsorbed layer and tribofilm on friction.....	98
7.4. The effect of adsorbed layer and tribofilm on wear.....	101
7.5. Summary.....	103
7.6. Conclusion.....	105
<b>8. A tribological study of ionic liquids as boundary additives in a non-polar base lubricant .....</b>	<b>107</b>
8.1. Friction and wear performance in PAO .....	107
8.2. The effect of additives and surface chemistry on tribofilm formation .....	111
8.3. The effect of adsorbed layer and tribofilm on friction.....	116
8.4. The effect of adsorbed layer and tribofilm on wear.....	119
8.5. Summary.....	121
8.6. Conclusion.....	121
<b>9. Conclusions and future work.....</b>	<b>123</b>
9.1. Conclusions.....	123
9.2. Future work.....	125
<b>10. References.....</b>	<b>127</b>

*This page is intentionally left blank*

# List of Figures

<b>Figure 2-1.</b>	Stribeck curve illustrating the different lubrication regimes.....	10
<b>Figure 2-2.</b>	Two mechanisms for the fatty acids' adsorption onto the metal surface .....	16
<b>Figure 2-3.</b>	The formation of normal micelle and reverse micelle as function of polarity of the medium.....	17
<b>Figure 2-4.</b>	Three organomolybdenum FMs and the R is alkyl group.....	18
<b>Figure 2-5.</b>	The structure of zinc dithiophosphate and the R group dictates whether it is an alky- or aryl-dithiophosphate .....	20
<b>Figure 2-6.</b>	Typical ionic liquid cations and anions molecular structures.....	23
<b>Figure 2-7.</b>	Chemical structure of trihexyltetradecylphosphonium bis(2-ethylhexyl) phosphate...	25
<b>Figure 2-8.</b>	Quartz crystal covered by a viscoelastic adsorbed layer .....	27
<b>Figure 3-1.</b>	Dynamic viscosity measurement procedure .....	34
<b>Figure 3-2.</b>	The principle of turbidity measurement .....	35
<b>Figure 3-3.</b>	Measurement of frequency shift and dissipation shift at multiple harmonics.....	36
<b>Figure 3-4.</b>	Schematic illustration of the viscoelastic model and formulae used in modelling .....	37
<b>Figure 3-5.</b>	Illustration of tribological test setup.....	38
<b>Figure 3-6.</b>	Illustration top surface of the sample and specific wear rate calculation.....	41
<b>Figure 3-7.</b>	Illustration of wear cross-section profile .....	41
<b>Figure 3-8.</b>	The F distribution showing the P-value.....	44
<b>Figure 3-9.</b>	The t distribution showing the P-value.....	45
<b>Figure 3-10.</b>	A working principle of SEM .....	47
<b>Figure 3-11.</b>	Imaging is performed by SEM, while milling and deposition are carried out by FIB (A). The high-energy ion beam collides with the surface atoms and causes the atoms to be ejected from the surface (B). Protective layer deposition using either electron or ion beam (C) .....	47
<b>Figure 3-12.</b>	Images were taken during first layer deposition (A), second layer deposition (B), and regular and cleaning cross-section processes (C). Example of the cross-section image taken using TLD detector (D).....	49
<b>Figure 3-13.</b>	A working principle of STEM.....	49
<b>Figure 3-14.</b>	The principle of EDS .....	50

<b>Figure 3-15.</b> Images were taken during thin lamella preparation: lamella U-cut (A), lamella mounting and thinning (B), and electron transparent lamella after thinning (C). Example of the cross-section TEM bright-field image (D), EDS elemental mapping of the cross-section (E), and EDS chemical point analysis of the tribofilm (F) .....	51
<b>Figure 3-16.</b> A schematic diagram of an XPS system using a monochromatized X-ray source.....	52
<b>Figure 3-17.</b> Survey scan of stainless steel and correspond regional scan for Fe 2p .....	53
<b>Figure 4-1.</b> The turbidity measurement of ILs in WMEG, WDEG, WMPG, and WDPG base lubricants.....	58
<b>Figure 4-2.</b> The turbidity measurement of ILs in PAO2 and PAO8 base lubricants.....	59
<b>Figure 4-3.</b> Friction evolution of AISI 316L stainless steel tested with different ILs in WMEG, WDEG, WMPG, and WDPG base lubricants.....	60
<b>Figure 4-4.</b> The specific wear rate (SWR) of AISI 316L stainless steel tested with different ILs in WMEG, WDEG, WMPG, and WDPG base lubricants .....	61
<b>Figure 4-5.</b> Friction evolution of AISI 316L stainless steel tested with different ILs in PAO2 and PAO8 base lubricants.....	62
<b>Figure 4-6.</b> The specific wear rate (SWR) of AISI 316L stainless steel tested with different ILs in PAO2 and PAO8 base lubricants .....	62
<b>Figure 5-1.</b> The friction of AISI 316L stainless steel influenced by WG lubricants and IL concentrations variables.....	65
<b>Figure 5-2.</b> The Two-way ANOVA result of friction for the interaction between lubricant and concentration.....	66
<b>Figure 5-3.</b> The wear of AISI 316L stainless steel influenced by WG lubricants and IL concentration variables .....	67
<b>Figure 5-4.</b> The Two-way ANOVA result of wear for the interaction between lubricant and concentration.....	68
<b>Figure 5-5.</b> The friction of AISI 316L stainless steel influenced by PAO lubricants and IL concentrations variables.....	71
<b>Figure 5-6.</b> The Two-way ANOVA result of friction for the interaction between lubricant and concentration.....	72
<b>Figure 5-7.</b> The wear of AISI 316L stainless steel influenced by PAO lubricants and IL concentrations variables.....	73

<b>Figure 5-8.</b> The Two-way ANOVA result of wear for the interaction between lubricant and concentration .....	74
<b>Figure 5-9.</b> Summary of all ANOVA results .....	75
<b>Figure 6-1.</b> The frequency and dissipation evolution during QCM testing using Fe and SS coated sensors for additivated WG lubricants at room temperature .....	78
<b>Figure 6-2.</b> Pourbaix diagram of iron and chromium at 25 °C. The studied lubricants are located in the diagram based on their measured OCP and pH from Table 6-1 .....	79
<b>Figure 6-3.</b> Viscoelastic properties of adsorbed layer on Fe and SS coated sensor derived from modelling .....	80
<b>Figure 6-4.</b> The frequency and dissipation evolution during QCM-D testing using Fe and SS coated sensors for additivated PAO lubricants at room temperature .....	82
<b>Figure 6-5.</b> The numerical simulation of the frequency shift (A) and the dissipation shift responses (B) as a function of the shear elasticity modulus and the shear viscosity coefficient of the thin viscoelastic layer for PAO-C12. A contour plot is taken from (A) and (B), showing the different regions of $\Delta f$ and $\Delta D$ value (C).....	83
<b>Figure 7-1.</b> Friction evolution and wear rates of AISI 52100 steel and AISI 316L stainless steel lubricated by WG with and without additives .....	90
<b>Figure 7-2.</b> SEM images of the wear tracks of AISI 52100 steel and AISI 316L stainless steel disks tested in WG with and without additives.....	91
<b>Figure 7-3.</b> FIB cross-section images of the wear tracks of AISI 52100 steel and AISI 316L stainless steel disks tested in WG with and without additives .....	92
<b>Figure 7-4.</b> STEM cross-section images and EDS elemental mapping of the wear tracks on AISI 52100 steel tested in WG with and without additives .....	94
<b>Figure 7-5.</b> STEM cross-section images and EDS elemental mapping of the wear tracks on AISI 316L stainless steel tested in WG with and without additives .....	95
<b>Figure 7-6.</b> XPS spectra inside the tribofilm of the AISI 52100 steel and AISI 316L stainless steel lubricated by WG-PP and WG-BMP.....	97
<b>Figure 7-7.</b> The top view, cross-section, and STEM image with elemental mapping of AISI 52100 steel worn surface lubricated by WG-BMP tested for 100 m and 300 m.....	99
<b>Figure 7-8.</b> Wear cross-section profile and the calculated wear area of AISI 52100 steel and AISI 316L stainless steel lubricated by WG with and without additives.....	101

<b>Figure 7-9.</b> The calculated wear area of AISI 52100 steel lubricated by WG-BMP tested for 100 m and 300 m.....	102
<b>Figure 7-10.</b> The summary of the tribological study of ionic liquids and carboxylic acid as boundary additives in water-glycol for a non-passive and hard metal (AISI 52100 steel).....	104
<b>Figure 7-11.</b> The summary of the tribological study of ionic liquids and carboxylic acid as boundary additives in water-glycol for a passive and soft metal (AISI 316L stainless steel) ...	104
<b>Figure 8-1.</b> Friction evolution and wear rates of AISI 52100 steel and AISI 316L stainless steel lubricated by PAO with and without additives .....	108
<b>Figure 8-2.</b> SEM images of the wear tracks of AISI 52100 steel and AISI 316L stainless steel disks tested in PAO with and without additives.....	109
<b>Figure 8-3.</b> FIB cross-section images of the wear tracks of AISI 52100 steel and AISI 316L stainless steel disks tested in PAO with and without additives .....	110
<b>Figure 8-4.</b> STEM cross-section images and EDS elemental mapping of the wear tracks on AISI 52100 steel tested in PAO with and without additives .....	112
<b>Figure 8-5.</b> STEM cross-section images and EDS elemental mapping of the wear tracks on AISI 316L stainless steel tested in PAO with and without additives .....	113
<b>Figure 8-6.</b> XPS spectra inside the tribofilm of the AISI 52100 steel and AISI 316L stainless steel lubricated by PAO-PP and PAO-BMP .....	115
<b>Figure 8-7.</b> The top view, cross-section, and STEM image with elemental mapping of AISI 52100 steel worn surface lubricated by PAO-BMP tested for 100 m and 300 m.....	117
<b>Figure 8-8.</b> Wear cross-section profile and the calculated wear area of AISI 52100 steel and AISI 316L stainless steel lubricated by PAO with and without additives.....	118
<b>Figure 8-9.</b> The calculated wear area of AISI 52100 steel lubricated by PAO-C12 and PAO-BMP tested for 100 m .....	119
<b>Figure 8-10.</b> Schematic illustration of the wear mechanism of hard versus soft substrate lubricated by PAO-C12 and PAO-IL.....	120



# List of Tables

<b>Table 2-1.</b> Physical properties of commercial low viscosity PAOs.....	13
<b>Table 2-2.</b> Physical properties of commercial glycol-based lubricants .....	13
<b>Table 2-3.</b> Antiwear additives.....	19
<b>Table 3-1.</b> Chemical formula, density, and chemical structure of all base lubricants .....	32
<b>Table 3-2.</b> Chemical formula, density, and chemical structure of all additives.....	32
<b>Table 3-3.</b> Chemical composition, microstructure, and hardness of AISI 52100 steel and AISI 316L stainless steel .....	33
<b>Table 3-4.</b> Tribological test parameters .....	38
<b>Table 3-5.</b> Lambda value calculation.....	40
<b>Table 3-6.</b> Example of a Two-way ANOVA matrix.....	43
<b>Table 3-7.</b> Two-way ANOVA matrix with all the mean values calculation .....	43
<b>Table 3-8.</b> Detailed curve-fitting modeling parameters used for XPS evaluation and quantification .....	54
<b>Table 5-1.</b> The COF for all WG lubricants and concentrations .....	64
<b>Table 5-2.</b> The SWR for all WG lubricants and concentrations .....	64
<b>Table 5-3.</b> Overall ANOVA results of friction for all WG lubricants and concentrations .....	65
<b>Table 5-4.</b> Mean comparisons (LSD test) of friction between WG-IL lubricants .....	66
<b>Table 5-5.</b> Mean comparisons (LSD test) of friction between WG-IL concentrations .....	66
<b>Table 5-6.</b> Overall ANOVA results of wear for all WG lubricants and concentrations .....	67
<b>Table 5-7.</b> Mean comparisons (LSD test) of wear between WG-IL lubricants .....	68
<b>Table 5-8.</b> Mean comparisons (LSD test) of wear between WG-IL concentrations .....	68
<b>Table 5-9.</b> The COF for all PAO lubricants and concentrations.....	70
<b>Table 5-10.</b> The SWR for all PAO lubricants and concentrations.....	70
<b>Table 5-11.</b> Overall ANOVA results of friction for all PAO lubricants and concentrations.....	71
<b>Table 5-12.</b> Mean comparisons (LSD test) of friction between PAO-IL lubricants.....	72
<b>Table 5-13.</b> Mean comparisons (LSD test) of friction between PAO-IL concentrations .....	72
<b>Table 5-14.</b> Overall ANOVA results of wear for all PAO lubricants and concentrations.....	73

<b>Table 5-15.</b> Mean comparisons (LSD test) of wear between PAO-IL lubricants .....	74
<b>Table 5-16.</b> Mean comparisons (LSD test) of wear between PAO-IL concentrations.....	74
<b>Table 6-1.</b> Physical and electrical properties of all lubricants .....	77
<b>Table 6-2.</b> Summary of the adsorbed layer properties on both Fe and SS coated sensors for WG lubricants.....	86
<b>Table 6-3.</b> Summary of the adsorbed layer properties on both Fe and SS coated sensors for PAO lubricants.....	86
<b>Table 7-1.</b> EDS chemical composition analysis of the tribofilms tested in WG with and without additives (at.%) .....	96
<b>Table 7-2.</b> Wear track chemical composition after XPS analysis for Fe spectra tested in WG-PP and WG-BMP .....	96
<b>Table 8-1.</b> EDS chemical composition analysis of the tribofilms tested in PAO with and without additives (at.%) .....	114

# Chapter 1

## Introduction and overview

### 1.1. Background

The production of electric vehicles (EVs) has grown in recent years due to the need for greener technologies that can reduce CO<sub>2</sub> emissions. EVs are powered either by battery electric vehicles (BEVs), plug-in hybrid electric vehicles (PHEVs), or hybrid electric vehicles (HEVs). In 1997, only two electric vehicle models were available, compared to 98 models introduced to the market in 2019 and predicted to nearly triple by 2025 [1,2]. Electric vehicles are considered a feasible solution to reduce CO<sub>2</sub> emissions (global warming) and air pollutants (NO<sub>x</sub>, carbon monoxide, unburnt hydrocarbons, and soot particles) which are characteristic of exhaust gases produced by internal combustion engine vehicles (ICEVs). According to the European Environment Agency data, changing from ICEVs to BEVs reduces the CO<sub>2</sub> emissions by 140 gCO<sub>2</sub>/km (from 210 to 70 gCO<sub>2</sub>/km) [3]. In addition, EVs use 77% of the total electric energy from the grid to move the vehicle, and the remaining 23% accounts for the energy losses, compared to ICEVs, which use about 21% of total fuel energy to move the vehicle and 79% for the energy losses [4]. It is known that EVs are about 3.7 times more efficient than ICEVs. Despite that, they can further be improved by reducing the energy losses produced by friction which account for 4% of all energy losses (1% due to motor friction and 3% loss in power transmission).

Similar to ICEVs, EV components need lubricants; however, to operate effectively, they require other characteristics due to the different tribological conditions. To develop lubricants for EVs, three essential aspects need to be considered, i.e., corrosion towards copper components or wirings, compatibility with polymers and resins, and improvement of their electrical and thermal properties. Moreover, lubricants in EVs will be exposed to higher speeds than those in ICEVs, shifting the high load-bearing function found in ICEVs towards torque transferring function in EVs [5]. Because of this, the development of new lubricants suitable for EVs should move towards low viscosity lubricants. Moreover, low viscosity lubricants are preferable due to better cooling performance and higher temperature stability [6]. However, the development of low viscosity lubricants will face new challenges. Firstly, there will be more tribological pair contact at the beginning of operation (start-up, time 0 seconds) due to the lower viscosity. This lower viscosity lubricant will result in a higher

initial coefficient of friction (COF) at the start-up condition. According to the Hamrock-Dowson formula for EHL contacts, lower viscosity will lead to thinner lubricant film thickness and lower  $\lambda$  value. The  $\lambda$  value is a parameter that relates the local film variation as a function of roughness, in which the lower the  $\lambda$  value implies a thinner lubricant film thickness. As the system speed increases, the film thickness will increase and at some point, the lubrication regime will change from boundary lubrication (very thin lubricant film thickness) to mixed lubrication regime and then to hydrodynamic lubrication regime (thick lubricant film thickness). Due to the lower initial  $\lambda$  value, the boundary and mixed lubrication regime will be longer, leading to longer running-in distance with higher friction. To overcome these challenges, several strategies for lubricant formulation have been proposed, i.e., new antiwear and friction reduction additives such as ionic liquids, nanotechnology-based antiwear and friction reduction additives such as MoS<sub>2</sub> and WS<sub>2</sub> and other types of nanoparticles, and low friction coatings such as DLC coatings [7–10].

This Ph.D. thesis focuses on ionic liquids as a potential new multifunctional solution (friction reduction and antiwear properties) in environmentally friendly low viscosity base lubricants (water-glycol and short-chain polyalphaolefin) to overcome the challenges in the development of functional low viscosity lubricants for EVs and other applications where low viscosity lubricants can represent a step forward sustainability.

## **1.2. Motivation**

Ionic liquids (ILs) are organic salts consisting of positive ions (cations) and negative ions (anions) that are liquid at low temperature (< 100 °C). ILs are very attractive substances due to their physical and chemical properties that can be altered by changing the cation or anion parts to meet specific requirements in different applications. ILs are considered “green” substances due to their low volatility, which is not emit hazardous volatile compounds to the environment [11–13]. In addition, ILs are considered excellent lubricants due to their extreme polarity, making them highly surface-active with a tendency to adsorb on metallic surfaces easily [14]. To replace traditional lubricants with more environmentally friendly alternatives, the cost of the new lubricants should also be considered. In the case of ILs, their price is higher than mineral base lubricants or synthetic base lubricants; moreover, they are produced in small quantities; therefore, the use of ILs as neat lubricants is limited to applications where money is not an issue, such as aerospace lubrication, or where only small amounts are required, such as micro-electromechanical systems [14]. Therefore, this Ph.D. thesis focuses on ILs as a lubricant additive and not as neat lubricants.

ILs as lubricant additives have been studied since 2003. P. Iglesias et al. studied 1 wt.% of n-dodecylammonium chloride and compared it with two liquid crystals (4,4'-dibutylazobenzene, cholesteryl linoleate) as additives in a high viscosity mineral oil beyond their oil solubility limit [15]. In 2012, Qu et al. reported phosphonium-based ILs to be soluble in non-polar hydrocarbon oils. Since then, the number of oil miscible ILs being synthesized and tested has significantly increased [16]. Most of these ILs have long alkyl chains since they improve the solubility in non-polar lubricants; however, this strategy is not suitable for polar lubricants [17,18]. Moreover, the toxicity increases with the alkyl chain length [19]. In this Ph.D., two groups of ILs (short alkyl chain length and long alkyl chain length) and two types of base lubricants (polar and non-polar) have been selected to study the effect of the chemical structure on solubility and tribological behavior.

In addition, the lubricating mechanisms of ILs as lubricant additives are still unclear, which is probably due to a large number of IL combinations available, each one with its properties. This is expected due to the large variety of chemistries and structures; however, a systematic approach in which a mechanism can be predicted based on the chemical structure or other characteristics is not found in the literature. There are two mechanisms typically reported in the literature. Firstly, the positively charged metal surface attracts the ILs' anion to form a mono- or multi- adsorbed layer on the surface, eventually reducing friction. Secondly, the ILs' cation or/and anion reacts with the metal surface to form a protective layer (tribofilm) on the metal surface, eventually increasing wear resistance and reducing friction [20]. Therefore, it is necessary to investigate the lubricating mechanism of selected ILs by studying and correlating the adsorption processes and tribofilm formation with their chemical structure and the base oil-IL mixture properties (e.g., mixture stability, pH, electrical conductivity).

### **1.3. Objectives**

This Ph.D. thesis's main purpose is to obtain a deep understanding of the role of ILs as friction reduction and antiwear additives in low viscosity lubricants for their potential use in EV applications and other applications where low viscosity lubricants can represent a step forward sustainability. In this Ph.D. thesis, the work has been focused on performing a comprehensive study of the tribological behavior and surface adsorption mechanisms of different ILs as additives in two types of base lubricants (polar and non-polar) and using two different surface chemistries (austenitic stainless steel and bearing steel). Through this research, several objectives are to be reached:

- To study the effect of the chemical structures on the ILs' solubility in polar and non-polar base lubricants.

- To evaluate the effect of the ILs' chemical structures on their tribological performance when used as additives in polar and non-polar lubricants.
- To identify the role of the base lubricant's polarity in the performance of ILs as additives.
- To study the effect of the lubricant's pH and electrical conductivity on their tribological performance.
- To study the tribofilm formation and properties (thickness, chemical composition, and chemical structure) on the surface of stainless and bearing steels.
- To study the adsorption mechanisms of ILs as additives in both polar and non-polar lubricants on stainless and bearing steel surfaces.
- To assess the correlation between the lubricant's polarity, pH, electrical conductivity, tribofilm formation, subsurface microstructure, and additive's adsorption on their frictional and antiwear performance.

## 1.4. Scope

To obtain a deep knowledge of the ILs' role as a lubricant additives, it is important to understand the lubricating mechanisms of ILs and their influence on friction and wear on metal surfaces. Therefore, a comprehensive study of the tribological behavior and surface adsorption mechanisms of ILs as additives must be performed on different surface chemistries and base lubricant polarities. To reveal the effect of the ILs' structure, six ILs with different anion, cation, and alkyl length were selected: 1,3-dimethylimidazolium dimethylphosphate (IM), (2-hydroxyethyl) trimethylammonium dimethylphosphate (AM), tributylmethylphosphonium dimethylphosphate (PP), 1-butyl-1-methylpyrrolidinium tris(pentafluoroethyl) trifluorophosphate (BMP), trihexyltetradecylphosphonium bis(2,4,4-trimethylpentyl)phosphinate (PB), and trihexyltetradecylphosphonium decanoate (PC). Two types of low viscosity base lubricants (polar and non-polar) were used to study the effect of the lubricants' polarity, pH, and electrical conductivity on their tribological performance. The base lubricants were four water-glycol mixtures and two polyalphaolefins (PAO's). To investigate the effect of the mechanical properties and chemistry of the metal surfaces, two different disk materials were used for the tribological tests, i.e., AISI 316L stainless steel and AISI 52100 bearing steel. The solubility and stability of the ILs in both the polar and non-polar lubricants were examined using a turbidity meter. The friction tests were performed using an alumina ball on a pin-on-disc sliding tribometer followed by an Infinite Focus Microscope (IFM) examination to measure the wear rate. Advanced surface characterization techniques were used to study the surface and subsurface microstructure transformation, crack formation, surface

chemistry, and tribofilm formation. These advanced characterization techniques include Scanning Electron Microscope equipped with Focused Ion Beam (SEM-FIB), X-ray Photoelectron Spectroscopy (XPS), and Scanning Transmission Electron Microscope equipped with Energy Dispersive X-ray (STEM-EDS).

For the surface adsorption studies, Quartz Crystal Microbalance with dissipation mode (QCM-D) was used to study the adsorption kinetics of the ILs, bonding strength between the IL layer and the sensor surface, and also the viscoelastic properties of the adsorbed ILs. Similar to the tribological tests, two types of solvents (water-glycol and PAO) and two coated quartz sensors (stainless steel SS304 and iron) were used during the QCM testing. Dodecanoic acid (C12) was selected as the reference additive for all studies.

## **1.5. Structure of the thesis**

This thesis consists of nine chapters. An outline and summary of each chapter are presented here:

### ***Chapter 1 Introduction and overview***

This chapter provides a background to the field of interest of this research work, i.e., ILs as additives in low viscosity lubricants. This chapter also includes the motivation, objectives, and scope of the thesis.

### ***Chapter 2 Literature review and state of the art***

This chapter provides a detailed literature review explaining tribology and lubrication, which also covers the tribofilm formation. Further, a thorough review of low viscosity lubricants is explored, and the challenges of using them are described. Lastly, the role of friction modifiers and antiwear additives is explained, and ILs that could have both functions simultaneously are presented.

### ***Chapter 3 Experimental***

This chapter is dedicated to explaining the test apparatuses and characterization methods. This chapter also includes the types of lubricants, ILs, and materials used during the research work. It starts with lubricants preparation, followed by testing procedures and characterization methods.

### ***Chapter 4 Preliminary studies of ionic liquids as lubricant additives in water-glycol and polyalphaolefin base lubricants***

This chapter focuses on polar and non-polar base lubricant selection. For polar base lubricants, six different water-glycol media were prepared and examined based on their pH. Base lubricants having a pH value below 6.5 were disregarded. In the case of non-polar base lubricants, polyalphaolefin

2 cSt and 8 cSt were selected. The remaining base lubricants were additivated with ILs and tested for their mixture solubility and stability, friction, and wear performance. In the end, one polar base lubricant, one non-polar base lubricant, and four ILs were selected based on their mixture stability and solubility and tribological performance for further study.

#### ***Chapter 5 Influence of ionic liquid concentration on the tribological performance***

In this chapter, the selected base lubricants and ILs from the previous chapter were further studied. The ILs concentration was varied and individually mixed with each base lubricant. The selected concentrations were 0.25, 0.5, 1, 2, and 4 wt.%. Two-way ANOVA was used to analyze the friction and wear data to determine the influence of concentration and IL type on the tribological performance. In the end, one concentration and two ILs were selected based on their tribological performance for further study.

#### ***Chapter 6 Adsorption study of ionic liquids additives in polar and non-polar media on iron and stainless steel coated sensors using Quartz Crystal Microbalance technique***

To fully understand the lubricating mechanism of ILs, a study of the adsorption mechanisms was conducted using Quartz Crystal Microbalance with Dissipation (QCM-D). The adsorption mechanism of ILs has been compared with a dodecanoic acid additive. Based on the frequency and dissipation shift, the adsorbed layer can be quantified for its thickness, shear viscosity, and shear elasticity modulus. The adsorption studies were performed using two surfaces, i.e., iron and stainless steel coated sensors as they were used in the tribological study.

#### ***Chapter 7 A tribological study of ionic liquids as boundary additives in a polar base lubricant***

In this chapter, the performance of ILs as lubricant additives in water-glycol is explained in detail and compared with dodecanoic acid. The first part of the chapter discusses the tribological performance of ILs tested on AISI 52100 steel and AISI 316L stainless steel. In the second part of the chapter, the surface and subsurface of the worn area are analyzed in detail using SEM-FIB, XPS, and STEM-EDS. In addition, the QCM-D result from chapter 6 was used to further analyze the influence of the adsorbed layer properties on the tribological performance.

#### ***Chapter 8 A tribological study of ionic liquids as boundary additives in a non-polar base lubricant***

In this chapter, the tribological performance of ILs as lubricant additives in polyalphaolefin is examined thoroughly and compared with dodecanoic acid. Similar to the previous chapter, the tribological performance of ILs was tested on AISI 52100 steel and AISI 316L stainless steel. SEM-FIB, XPS, and STEM-EDS are used to analyze the worn surface and tribofilm formation. The adsorption study by QCM-D from chapter 6 was used to investigate the influence of the adsorbed layer on the tribological performance.



## ***Chapter 9 Conclusions and future work***

This chapter concludes all the work performed during this Ph.D. thesis. Based on the results obtained, future work is proposed as a continuation of this research.

## ***Chapter 10 Reference***

This chapter consists of all the references used in this Ph.D. thesis.

## **1.6. List of papers**

During this Ph.D. thesis, three peer-reviewed journal papers were produced and published. The lists of the journal papers are:

### **Paper I**

W. Wijanarko, H. Khanmohammadi, and N. Espallargas

*Ionic liquids as boundary additives in water-based and PAO lubricants*

Friction 2021

### **Paper II**

W. Wijanarko, H. Khanmohammadi, and N. Espallargas

*Ionic Liquid Additives in Water-Based Lubricants for Bearing Steel – Effect of Electrical Conductivity and pH on Surface Chemistry, Friction and Wear*

Frontiers in Mechanical Engineering 2022, Vol. 7

### **Paper III**

W. Wijanarko, H. Khanmohammadi, and N. Espallargas

*Effect of steel hardness and composition on the boundary lubricating behavior of low viscosity PAO formulated with dodecanoic acid and ionic liquid additives*

Langmuir 2022, Vol. 38, 2777–2792

For all papers, the author and co-author's contribution in the papers are following:

- **Wahyu Wijanarko** has prepared all the contents including tests and analysis of data as well as the full text of all papers.
- **Hamid Khanmohammadi** has contributed with intellectual discussions of results and conclusions, editing, and advice on all papers.
- **Nuria Espallargas** has contributed with experimental work supervision and discussion, intellectual discussions of results and conclusions, editing, and advice on all papers.

*This page is intentionally left blank*

# Chapter 2

## Literature review and state of the art

### 2.1. Tribology and lubrication

Tribology is the science and engineering to study the interaction between surfaces that move relative to each other. The term “tribology” was first introduced by Peter Jost in his report in 1966, in which the cost of tribology to the United Kingdom’s economy was highlighted [21]. Despite the fact that the term *tribology* has been only used since 1966, humanity has faced tribological problems and has used tribology as a solution to many challenges since thousands of years ago. For example, in 2400 BC, Egyptians used water, vegetable oil, and mud as lubricants to facilitate the transport of large stone statues [22]. In addition, basic tribological concepts like friction have been a topic of study since Leonardo da Vinci (1452-1519), and it is still far from being fully understood. Tribology is an interdisciplinary subject studied by multi-academic fields, including physics, chemistry, biology, mathematics, materials science, and engineering. Although many studies have already existed in this field over the years, there are still many aspects of tribology to explore today and in the future. This is due to the fact that tribology is fully dependent on the system conditions, i.e., contact materials, speed, temperature, environment, etc.

In tribology, three aspects are at play, i.e., friction, wear, and lubrication [23]. Low friction means low energy loss due to heat, while low wear means a long lifetime of the components. Lubrication is achieved by applying lubricants to reduce friction between the surfaces and prevent the surfaces from suffering wear. In general, there are two main types of lubrication, i.e., dry (solid) and wet lubrication [24]. In dry lubrication, solid materials are used to reduce friction due to low surface energy or easy shear plane. In the case of wet lubrication, lubricating liquids or greases are applied to create a thin lubricant film layer that separates two mating surfaces.

In wet lubrication, the correlation between lubricant film thickness and the combined roughness of the two mating surfaces defines the lubrication condition, and this is generally referred to as lambda ( $\lambda$ ) ratio ( $\lambda = h/\sigma$ , where  $h$  = lubricant film thickness and  $\sigma$  = combined surface roughness) [22]. If the lubricant film thickness is much larger than the surface roughness (generally  $\lambda > 3$ ), there will be no surface contact, and this condition is called hydrodynamic lubrication. In this condition, the lubricant

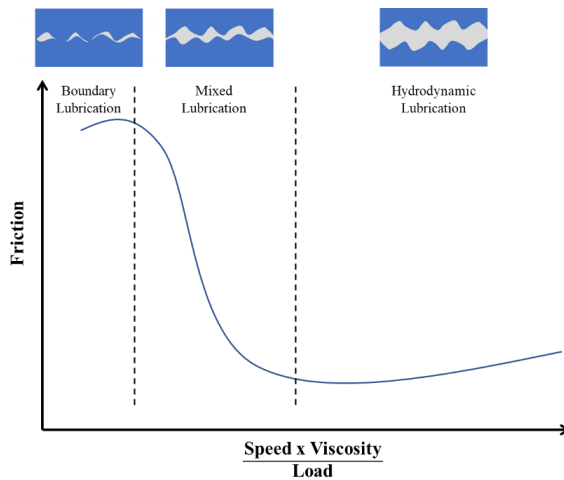


**Figure 2-1.** Stribeck curve illustrating the different lubrication regimes.

fully supports the applied load, and the lubricant's viscosity will influence the friction, and as a result, the friction is very low. As the lubricant film thickness decreases, it may not sufficiently support the hydrodynamic pressure. At some points, there will be solid (asperity) contact between the surfaces. The applied load will be supported with both the contact asperities and the lubricant film, resulting in the increase of friction. This condition is termed as mixed lubrication. In this condition, the average lubricant film thickness is still larger than the combined surface roughness, and the  $\lambda$  ratio is  $1 < \lambda < 3$ . As the lubricant film thickness further decreases and becomes equal or less than the combined surface roughness, the  $\lambda$  ratio is  $< 1$ , and this condition is known as boundary lubrication. In boundary lubrication, the applied load is mainly supported by the asperity contacts of the mating surfaces, which collide during the rubbing action and undergo elastic and/or plastic deformation, resulting in high friction.

The so-called Stribeck curve is a fundamental well-known concept in lubrication. This curve proves that the lubricant film thickness is proportional with the relative sliding speed of surfaces ( $v$ ) and the viscosity of the lubricant ( $\eta$ ), and inversely proportional with the normal load ( $F_n$ ). The relation of these parameters and friction can be plotted as shown in **Figure 2-1** [25]. Early in the 20<sup>th</sup> century, Richard Stribeck along with Mayo Hersey pioneered this concept while working within the railway industry however, the results of their research were in line with previous researchers publishing similar results. This curve is very useful since it allows identifying different lubricating regimes in a tribosystem depending on the operating conditions.

In the hydrodynamic lubrication regime, as shown in **Figure 2-1**, the friction increases at a higher relative speed because the lubricant's shear force increases, which is related to its viscosity.

For components working mostly in the hydrodynamic lubrication regime, the recent industrial trend is using lower viscosity lubricants, leading to lower friction, thus increasing the efficiency. In addition, the new electrification trends in the automotive industry (and probably others) will force the development of lower viscosity lubricants simply because the needs for their components will be moved from a load-bearing function to a torque transfer function. Tribosystems are exposed to start/stop periods, shock loads, direction changes, and slow to intermediate speeds, where the system goes into boundary lubrication conditions. Thus, even though a lubricant is meant to work at the hydrodynamic regime (load-bearing) or as a torque transfer, it still faces all regimes during operation. Thus, the challenges low viscosity lubricants will face in each lubrication regime can be summarized as follows:

a. Starting periods and boundary lubrication regime

The lubricant film thickness is proportional to the lubricant's viscosity so that a lower viscosity lubricant will have lower initial film thickness than a high viscosity lubricant. Hence the initial  $\lambda$  value of a low viscosity lubricant will be lower than the one of a high viscosity lubricant ( $\lambda_{low \eta} < \lambda_{high \eta}$ ). The lubricant regime transition value for boundary lubrication regime to mixed lubricant regime is  $\lambda = 1$ . Thus, a higher increment of  $\lambda$  would be required for a low viscosity lubricant to reach a value of 1, which implies a higher speed increment. At the same acceleration, a low viscosity lubricant in boundary lubrication will take longer to reach the mixed or hydrodynamic lubrication regime than a high viscosity lubricant.

b. Mixed lubrication regime

A  $\lambda$  increment of 2 is needed in the mixed lubrication regime to reach the hydrodynamic lubrication. Again, a higher speed increment is required for a low viscosity lubricant to reach the hydrodynamic lubrication regime compared to a high viscosity lubricant. At the mixed lubrication regime, the friction will decrease as the speed increases. A low viscosity lubricant will lead to slower friction reduction compared to a high viscosity lubricant. In addition, the pressure-viscosity effect plays a significant role in this lubrication regime, in which the viscosity increases under high load. Low viscosity lubricants tend to increase their viscosity less than high viscosity lubricants under pressure, resulting in slower friction reduction. As a result, a low viscosity lubricant will experience higher friction for a longer time.

c. Hydrodynamic lubrication regime

As the speed increases further to reach the hydrodynamic lubrication regime, a low viscosity lubricant has an advantage over a high viscosity lubricant due to the lower friction value expected due to its lower fluid shear. In addition, the pressure-viscosity effect of low viscosity lubricant gives lower viscosity increment, leading to lower friction due to the fluid shear.

## 2.2. Lubricants

Depending on the application and use, current lubricating oils' formulations consists of about 70-99% base lubricant and 30-1% lubricant additives. Base lubricants can come from biological or non-biological sources. In the case of biological sources, these can comprise animal fat (hard or soft fats) to vegetables (based on palm, rapeseed, soybean, corn, castor). In the case of the non-biological sources, they comprise mostly mineral or synthetic oils derived from the distillation of crude oil. In general, animal oils, vegetable oils, and mineral oils are non-polar. On the other hand, due to a wide variety of synthesis processes, synthetic oils can be non-polar (e.g., polyalphaolefin - PAO) or polar (e.g., glycols). Polar synthetic oils can be mixed with water, leading to new lubricants, e.g., hydraulic fluids that typically contain a 1:1 mixture of water and a polar synthetic oil. Water-based lubricants can be used where fire safety is an issue. In water-based lubricants, the main purpose of mixing water with synthetic oils is to increase the viscosity of water and decrease the freezing/pour point so they can be used at low temperatures. Moreover, some synthetic oils like glycols are biodegradable, so mixing with water can result in environmentally acceptable lubricants.

Lubricant additives are chemical compounds added to base lubricants to increase the lubricant's performance for specific applications. Additives radically change the properties of lubricants. Additives are a mixture of many different chemicals covering several functional categories such as friction modifiers, antiwear and/or extreme-pressure additives, antioxidants, dispersants, viscosity modifiers, anti-corrosion, anti-foaming, pourpoint depressants, etc [26,27]. Every function of a lubricant additive is fulfilled by single chemicals carefully designed to avoid competition with each other. Lubricant additives can be classified into three main function areas: surface protective additives, performance additives, and lubricant protective additives [28]. Surface protective additives are friction modifiers, antiwear additives, extreme pressure additives, corrosion inhibitors, detergents, and dispersant additives. Performance additives are pour-point depressants and viscosity index improvers, and lubricant protective additives are antioxidants and antifoam additives. Each additive, or group of additives, serves a purpose in one or more lubrication regimes (i.e., boundary, mixed, and hydrodynamic). In boundary or mixed lubrication regimes, extreme pressure, antiwear, and friction modifier additives are most important, especially in their role with tribofilm formation to protect the surface from high friction and excessive wear.

Generally, lubricants could be classified into low viscosity and high viscosity lubricants. Nowadays, the trend is moving towards using low viscosity lubricants as one of the routes to increase fuel efficiency. The change towards low viscosity lubricants will face several challenges that need to be solved. Low viscosity lubricants result in low load-bearing capacity of the lubricant, which will

**Table 2-1.** Physical properties of commercial low viscosity PAOs [29]

Parameter*	PAO 2	PAO 4	PAO 6	PAO 8	PAO 10
KV at 100 °C, cSt	1.80	3.84	5.98	7.74	9.87
KV at 40 °C, cSt	5.54	16.68	30.89	46.30	64.50
KV at -40 °C, cSt	306	2390	7830	18,200	34,600
Viscosity index	—	124	143	136	137
Pour point, °C	-63	-72	-64	-57	-53
Flash point, °C	165	213	235	258	270
Parameter*	PAO 2	PAO 4	PAO 6	PAO 8	PAO 10

\*KV is kinematic viscosity

**Table 2-2.** Physical properties of commercial glycol-based lubricants [30–33]

Parameter*	Monoethylene Glycol	Diethylene Glycol	Monopropylene Glycol	Dipropylene Glycol
DV at 60 °C, cP	—	—	8.42	10.9
DV at 40 °C, cP	10.35	13.44	—	—
DV at 25 °C, cP	—	—	48.6	75.0
DV at 20 °C, cP	19.83	35.7	—	—
Pour point, °C	—	—	< -57	-39
Freezing point, °C	-11.2	-6.5	Supercools	Supercools
Flash point, °C	111	138	104	124

\*DV is dynamic viscosity

increase the wear and friction of the components, especially at the boundary or mixed lubrication regime. To overcome these problems, low viscosity lubricants need to be carefully designed. The selection of high-quality base lubricants and additives to improve their tribological performance is therefore necessary. According to Rudnick, PAOs up to PAO 10 are considered to be low viscosity lubricants [29]. The low viscosity PAOs are synthetically produced either from 1-decene or 1-dodecane precursors. The physical properties of commercially low viscosity PAOs are shown in **Table 2-1**. In the case of polar lubricants, commercially available low viscosity glycol-based lubricants are monoethylene glycol, diethylene glycol, monopropylene glycol, and dipropylene glycol. The physical properties of these commercial glycol-based lubricants are presented in **Table 2-2**. These synthetic base lubricants have several advantages over mineral base lubricants, such as better oxidation properties, higher thermal stability, higher viscosity index, and better low-temperature properties. These advantages will keep the viscosity of synthetic lubricants stable over a wide range of temperatures.

As mentioned earlier, it is obvious that low viscosity lubricants have disadvantages during the starting and stopping periods where the lubricant undergoes boundary and mixed lubrication regimes. In these conditions, the lubricant film is not thick enough to separate the mating surfaces thus, allowing contact between the surface asperities. Because ideal smooth surfaces are difficult to achieve during preparation, a surface consists of many asperities. As two solid surfaces are in contact, the real contact

area is much smaller than the nominal contact area. For dry contacts, the real contact area is proportional to the normal load and inversely proportional to the material's hardness. For wet or oil lubricated contacts, the real contact area also depends on the lubricant properties in addition to the normal load and the hardness of the material [25]. During the rubbing action, these surface asperities collide with each other. The surface asperities are deformed elastically and/or plastically or are removed due to high shear stresses. The collision produces stresses that create friction and changes the surface topography that subsequently creates wear. The friction produces heat, raising the local temperature at the contact asperities [34]. In addition, a nascent highly reactive surface is created after asperities' removal. In the presence of a lubricant, and with the assistance of localized high temperature due to the mechanical action, there will be chemical or/and physical interactions between lubricant molecules and the nascent surface (tribochemical reactions). As a result, tribofilms can be formed on the surface [35].

The tribofilm formed on the surface possesses a microstructure and properties different from the lubricant and the rubbing solid materials. Tribofilms have been intensively studied in terms of their formation mechanisms, chemical composition, and mechanical properties. Despite many years of research, the tribofilm formation and its properties are still not well understood. This is due to the fact that tribofilm formation is a unique phenomenon that depends on the lubricant composition, (mechanical) contact conditions, environment, and the rubbing materials' composition [35–37]. The presence of tribofilms plays an essential role in reducing friction and protecting the surface from more severe wear. In general, decent tribofilms cannot be achieved only using a base lubricant alone; however, additives are necessary to be added into lubricants to facilitate tribofilm formation.

The tribofilm formation is affected not only by the lubricant composition and contact conditions but also the chemical composition and microstructure of the rubbing materials (for example, different tribofilms are expected in steel, stainless steel, cast iron, or copper). The interaction between the lubricant additives and the rubbing material composition and microstructure in the boundary lubrication regime has received little attention in the field of tribology, which tends to focus more on additives rather than on the complete system. The effectiveness of the tribofilm to improve the tribological performance depends on its composition and structure. As the tribofilm is composed of compounds originally coming from the chemical reaction between lubricant additives and the rubbing materials, it is obvious that the chemical composition and microstructure of the rubbing materials play an important role in the tribofilm formation and its properties. Specific alloying elements or microstructural features will have a tendency to react with specific additives to form effective tribofilms. This gap has been thoroughly studied in this Ph.D. thesis for low viscosity lubricants.



## 2.3. Lubricant additives for boundary lubrication conditions

### 2.3.1. Friction modifiers

The main purpose of friction modifier additives (FMs) is to reduce the friction on the contacting surfaces at the boundary and mixed lubrication regimes. The basic principle of the boundary lubrication condition implies that materials with low shear strength and high hardness are needed in order to obtain low friction. Materials with such combination of properties are difficult to produce. However, low friction can be obtained if a low shear strength layer is deposited on a hard substrate. These low shear strength layers can be obtained either by adsorption films or chemical reaction films.

Adsorption films form monomolecular or multimolecular layers that separate the contacting surfaces, providing a low shear strength interface between two mating surfaces. These monomolecular or multimolecular layers are formed by the adsorption of chemical substances (lubricant additives) on the worn surface. Organic compounds with amphiphilic structures (a polar head and a non-polar hydrocarbon tail) are commonly used for this purpose. They are commonly known as organic friction modifiers (OFMs). One example of OFMs is fatty acids which have been used for over a century. The structure of a fatty acid consists of a polar head (carboxyl group  $-\text{COOH}$ ) and a non-polar tail (alkyl chain  $\text{R-CH}_2\text{-CH}_3$ ). The polar head allows the molecules to attach to the tribosurface, while the non-polar hydrocarbon tail stretches out to the lubricant to repel other molecules, providing a low shear strength interface. The effectiveness of OFMs to reduce friction depends on the type of adsorption, molecular structure, and concentration.

Tribosurfaces are typically covered with oxides and organic contamination. During the rubbing action in boundary lubricating conditions, these oxides, surface contamination, and some surface materials are removed, leaving a positively charged nascent surface exposed to the lubricant. This positively charged nascent surface is highly reactive towards oxygen and organic molecules, in this case, the polar head of OFMs. Depending on the reactivity of the nascent surface, the adsorption of lubricant additives onto the surface can take place through either physical or chemical adsorption. Physical adsorption occurs through weak Van der Waals forces between the polar head of OFMs and the metal surface, which is a temperature-dependent reversible mechanism. Since most metals (e.g., iron) are reactive, OFMs like fatty acids will chemically adsorb on them forming metal carboxylates under monodentate forms (one oxygen atom binds to the metal surface leaving the  $\text{C=O}$  bond free) or bidentate (two oxygen carboxylate atoms bind to the metal surface in a symmetric way) [38]. The schematic of these two adsorption mechanisms is shown in **Figure 2-2**. These mechanisms have a significant impact in practical applications due to their effectiveness in reducing friction.

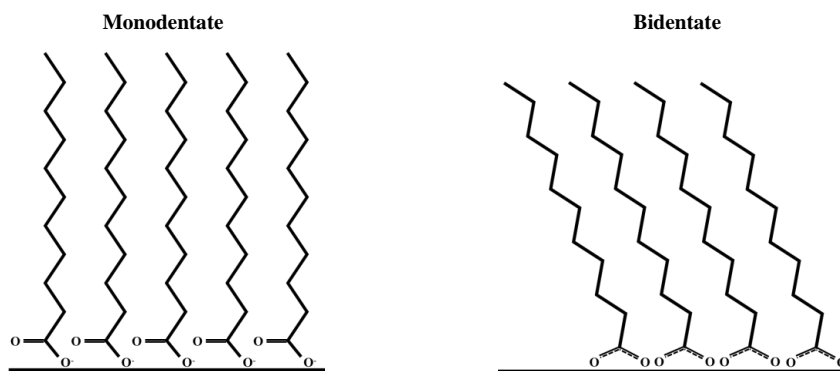


**Figure 2-2.** Two mechanisms for the fatty acids' adsorption onto the metal surface. Figure adapted from [38].

The molecular structure of the adsorbate has a strong influence on friction reduction effectiveness. For example, fatty acid molecules can have linear or branch alkyl chains. It was found that the ability of fatty acids to form close-packed adsorbate structures on the metal surface influences lubrication effectiveness [39]. Close-packed adsorbate structures can only be obtained if the molecular shape is linear, i.e., more bonding between  $\text{CH}_2$  groups of adjacent fatty acids happens compared to branched molecular shapes. As a result, durable films are formed, ensuring their resistance against shear forces producing low shear strength interfaces resulting in low friction [25]. Another molecular feature that influences the lubrication effectiveness of fatty acids is the alkyl chain length. For linear fatty acids, it was found that a minimum alkyl chain length of  $n = 9$  is required to obtain effective lubrication [25]. This can be explained by the weak Van der Waal forces between the alkyl chains. A minimum number of adjacent  $-\text{CH}_2-$  groups are required to obtain a strong bonding.

The shear stress generated during the rubbing action can remove the adsorbate layer from the contacting surfaces. In this case, the ability of FMs to replenish the contact region of a tribopair is an important property. This is mainly controlled by the concentration of the FMs in the base lubricant and the chain length. A minimum concentration is needed to ensure the balance between adsorption and removal rate by the shear stress. It was found that there is a transition concentration where the decrease in friction decelerates with increasing concentration. And also, the transition concentration shifts towards lower values with increasing the chain length [40]. Another interesting feature of fatty acids is micelle formation which is highly influenced by the base lubricant and concentration. Micelles are aggregates of fatty acid molecules dispersed in a liquid forming a colloidal suspension. They are formed when the concentration exceeds the critical micelle concentration (CMC). Depending on the polarity of the media, micelles can form normal micelles in polar media (with the hydrophilic head in contact with the surrounding media) or reverse micelles in non-polar media (with the hydrophobic phase in contact with the surrounding media), as shown in **Figure 2-3** [28].

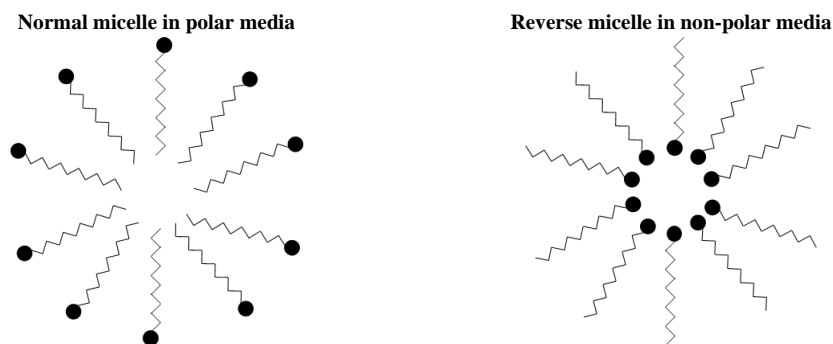
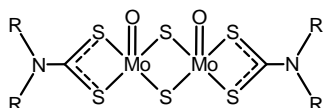


**Figure 2-3.** The formation of normal micelle and reverse micelle as function of polarity of the medium. Figure adapted from [28].

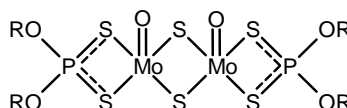
Critical micelle concentration is shifted towards lower concentrations in aqueous media with increasing the chain length [41]. Micelles can have a greater effect on friction than FMs alone. In a study of a water-glycol lubricant containing different concentrations and chain lengths of fatty acids, the lowest friction was found for the fatty acid concentrations above CMC regardless of the alkyl chain length [42].

FMs working with the chemisorption mechanism are typically oil-soluble organomolybdenum compounds. Three families of organomolybdenum friction modifiers are molybdenum dialkyldithiophosphate (MoDTP), molybdenum dialkyldithiocarbamate (MoDTC), and molybdate ester [43]. The chemical structure of three organomolybdenum FMs is shown in **Figure 2-4**. MoDTP is a sulfur- and phosphorus-containing compound, MoDTC is a sulfur-containing and phosphorus-free compound, and molybdate ester is a sulfur- and phosphorus-free compound. Organomolybdenum compounds react with the sliding surface during the rubbing action, forming a layer-lattice structure of molybdenum disulfide ( $\text{MoS}_2$ ) on the rubbing asperities. The low shear strength between the layers of the  $\text{MoS}_2$  structure results in friction reduction. MoDTP and MoDTC already contain sulfur in their composition, which provides the source of sulfur to form  $\text{MoS}_2$ . However, molybdate ester needs other sources of sulfur to be effective as a friction modifier. The other sources could be other additives such as antiwear additives, extreme pressure additives, or detergents [44]. An important feature of  $\text{MoS}_2$  formation is that it only forms at severe contact stresses when the contact between the asperities of two surfaces takes place. Therefore, they are very effective in reducing friction in boundary or mixed lubrication regimes [45,46].  $\text{MoS}_2$  acts as a sacrificial film. Therefore, if the supply of organomolybdenum is stopped, loss of  $\text{MoS}_2$  or oxidation to  $\text{MoO}_3$  will occur, resulting in increased friction [44]. Another example of the chemisorption mechanism is the formation of amorphous films on the rubbing surfaces. Due to the fact that additives forming amorphous films also can act as antiwear additives, this will be discussed in detail in the next section.

**Molybdenum dialkyldithiocarbamate**



**Molybdenum dialkyldithiophosphate**



**Organomolybdates**

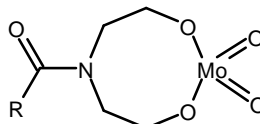
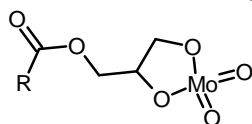


**Figure 2-4.** Three organomolybdenum FMs and the R is alkyl group. Figure adapted from [43].

### 2.3.2. Antiwear additives

In the boundary lubrication regime, surface contamination and oxides will be removed during the rubbing action leaving a nascent highly active surface. This highly active surface has a higher affinity towards chemicals in the lubricant, especially from lubricant additives. The adsorbed layer formed on the surface during the first action is a prerequisite for subsequent chemical reactions. Depending on some lubricant characteristics (chemical composition, conductivity, pH, etc.) and some surface material characteristics (microstructure, chemical composition), the chemical reaction product can be beneficial or detrimental in terms of wear. A protective layer on the surface is an example of beneficial reaction products, while a corrosion or degradation layer is an example of a detrimental reaction product.

Antiwear additives (AWs) facilitate the formation of protective films on the tribosurfaces preventing excessive wear, especially in the boundary or mixed lubrication regions. Sulfur and phosphorus are the main chemical elements usually used in AWs [28]. During the rubbing action, the frictional heat between surface asperities provides energy for the chemical reaction between the sulfur or phosphorus from the AWs and the tribosurface to form a protective tribofilm. This tribofilm may consist of metal sulfides, metal phosphates, or organometallic compounds [28].

Similar to FMs, the general structure of AWs consists of a polar functional head group and a non-polar hydrocarbon tail. The non-polar hydrocarbon chain length will define the solubility in the lubricant. Longer chains have better solubility in non-polar lubricant media, while shorter chains have better solubility in polar lubricant media. The polar head group contains the main elements (sulfur or phosphorus), which adsorbs on the tribosurface (forming an adsorbed film) and subsequently reacts (tribochemical reaction) to form a protective tribofilm with the assistance of the frictional heat. Three parameters influence the effectiveness of AWs during the adsorption process, i.e., the adsorption

**Table 2-3.** Antiwear additives [48]

Metal	Phosphorus	Sulfur	Examples
✓	✓	✓	Metal dialkyldithiophosphate
✓	✓	o	Metal dialkylphosphates
✓	o	✓	Metal dithiocarbamates
o	✓	✓	Thiophosphates, thiophosphonates
o	✓	o	Phosphates, phosphonates, amine phosphates
o	o	✓	Organosulphides, S-containing heterocyclics, ashless dithiocarbamates
o	o	o	Organoboron compounds, N-based heterocyclic compounds

kinetics, the rigidity of the adsorbed film, and the bonding strength with the surface [47]. The ability of AWs to adsorb on the tribosurface depends on their polarity (the higher the polarity, the higher the adsorption kinetics). During the rubbing action, the removal of the adsorbed film will take place, and higher adsorption kinetics are desirable to provide continuous additive supply to the surface.

The adsorbed film reacts with the surface to form a tribofilm. The mechanism of tribofilm formation to protect the substrate can be explained by sacrificial wear protection. The tribofilm provides a low shear strength layer that is easily removed by the mechanical action, not only protecting the substrate but also giving low friction. Due to this sacrificial mechanism, the tribofilm formation rate has to be greater than the tribofilm removal rate. To be effective, the tribofilm formed on the worn surface should have a greater thickness than the roughness of the surface. The durability of the tribofilm to withstand the shear force also plays a significant role in which a durable tribofilm leads to a lower wear rate. The durability of the tribofilm is determined by the chemical composition and the structure of the tribofilm.

Antiwear additives can be classified into three groups, i.e., organo-metallic compounds, phosphorus-containing and/or sulfur-containing compounds, and phosphorus-free and sulfur-free compounds. Typical antiwear additives are shown in **Table 2-3** [48]. Metal dialkyldithiophosphate (MDDP) compounds have been extensively used as lubricant additives due to not only their antiwear properties but also due to other properties, for example, friction modifying, anti-oxidant, and anti-corrosion. Metals that have been used in MDDP are zinc [49], molybdenum [50], titanium [51], copper [52], and gadolinium [53]. Among all MDDPs, Zinc dialkyldithiophosphate (ZDDP) is the most commonly used.

Indeed, ZDDP was first introduced in lubricants as an anti-oxidant in 1941. The antiwear properties of ZDDP remained unknown for the next 14 years. In 1955, it was found on cam and follower systems that ZDDP-containing lubricants generated less wear than those without it [49]. Since then, ZDDP has been extensively used and studied for its antiwear behavior, nature, and the properties of the tribofilms that forms on tribosurfaces. The tribofilm formation consists of three process steps: (1) adsorption of ZDDP on the worn surface, (2) decomposition of ZDDP at the asperity contacts

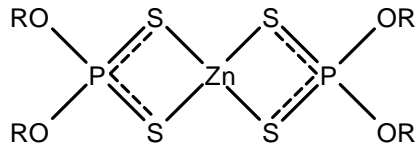


**Figure 2-5.** The structure of zinc dithiophosphate and the R group dictates whether it is an alky- or aryl-dithiophosphate. Figure adapted from [54].

activated by frictional heat, and (3) tribochemical reaction between the ZDDP decomposition products and the worn surface.

The ZDDP chemical structure consists of a polar organometallic head (one zinc atom bonded to two dithiophosphate esters) and an alkyl tail. The antiwear effectiveness of ZDDP depends on the structure of the alkyl group, with the order of secondary alkyl, primary alkyl, and aryl [49]. The chemical structure of ZDDP is shown in **Figure 2-5**. The polar head adsorbs to the metal surface via the sulfur atom of the P=S bond [55]. Due to the rubbing process, a tribofilm forms on the worn surface with thicknesses in the range of 50 to 200 nm. The tribofilm has a pad-like structure with deep valleys in between. The tribofilm consists mainly of amorphous zinc/iron phosphates with a thin outer layer of zinc polyphosphate (~ 10 nm thick) [49]. The tribofilm acts as a barrier providing wear protection. It was also suggested that the sulfur reacts with abrasive iron oxide wear particles transforming into less abrasive iron sulfide [56]. Two important features making ZDDP such an effective antiwear additive are (1) the fast tribochemical reaction to form a protective tribofilm and (2) the low content of iron in the tribofilm implying minimum tribocorrosion of the substrate during the film removal and rebuilding.

Besides the excellent antiwear properties, ZDDP also has other functionalities such as antioxidant and corrosion inhibition making ZDDP a widely used lubricant additive over the past 80 years. However, ZDDP has detrimental effects for the environment due to the volatility of Zn, P, and S, which leads to the formation of sulfated ashes, phosphorus oxide, and sulfur oxide [48]. In addition, ZDDP is an aquatotoxic compound, and this can be a problem in applications like forestry and marine [57]. To reduce gas emissions coming from ICEVs, several governments have decreased the limits on ash-forming compounds (i.e., phosphorus, sulfur) in the lubricant additives since ashes block the catalytic exhaust converters in cars impeding their emission-reducing function. This influences the use of ZDDP, which may require complete replacement by other additives in the future [58]. This has also influenced the reputation of phosphorus and sulfur in lubricant additives when, in most cases, they are not directly responsible for gas emissions whereas, their full combustion might be the main issue. Additives containing P and S might not be that harmful in applications outside ICEs. However, the need to find new and environmentally friendly antiwear additives becomes crucial.

## 2.4. Ionic liquids

Ionic liquids (ILs) are low melting point ( $< 100\text{ }^{\circ}\text{C}$ ) organic salts consisting of cations and anions. Some ILs have a melting point below room temperature and are called room temperature ILs (RT-ILs). Due to the delocalized charges of the cation or the anion and the asymmetry of the molecules, ILs have poor lattice coordinated structures, preventing them from forming solid crystals. Hence, IL compounds are liquid at a temperature below  $100\text{ }^{\circ}\text{C}$  or even at room temperature [14,59]. Due to the number of cation and anion precursors for ILs, their statically predicted number of structures can reach over 1 million possible cation/anion combinations. The amount of commonly used ILs are around 300 - 400 [60,61]. This gives a broad range of potential applications in many fields.

### 2.4.1. ILs as neat lubricants

The first IL ever synthesized was ethylammonium nitrate (EAN). Synthesized by Paul Walden in 1914, it is believed to be the earliest room-temperature ionic liquid with a melting point of  $12\text{ }^{\circ}\text{C}$  [62]. EAN is used as an electrically conductive solvent in electrochemistry, a protein crystallization agent, and it can form micelles and hydrogen bonds. In 1982, the first imidazolium-based IL was studied for its electrochemical behavior, which has potential applications for electrolytes in batteries, photoelectrochemical cells, and electroplating [63]. Years later, ILs were found to be effective solvents for both organic and inorganic compounds [13]. In 2001, ILs were first investigated as neat lubricants [64]. Since then, the tribological performance of ILs has been compared with conventional hydrocarbon base lubricants, for example, perfluoropolyether (PEPE) [64–68], polyalphaolefin (PAO) [68,69], and some mineral oils [69–71]. The studies propose ILs as a green alternative for conventional liquid lubricants due to the low-temperature fluidity, high-temperature stability, low vapor pressure, and excellent lubricity.

Typically, the cations are organic compounds having a large and asymmetric structure with a lengthy alkyl chain. The anions can be organic or inorganic compounds with smaller sizes and more symmetrical structures [14]. Selecting the cation and anion structure and elements are vital in designing ILs for lubricant applications. ILs need to be designed to adsorb and react with the surface to give a desirable tribological performance. In addition, ILs can be designed to be miscible in base lubricants, either polar or non-polar. Studies from friction modifiers and antiwear additives show that elements such as sulfur, phosphorus, boron, or fluorine can adsorb and react with tribosurfaces to form protective tribofilms. So ILs that have been used as neat lubricants typically consist of those elements. The typical cations and anions structures used as neat lubricants are shown

in **Figure 2-6** [14]. The type of cation and anion as well as the alkyl chain length will influence the tribological performance of ILs.

Early studies of ILs in tribology started with investigating the tribological performance of imidazolium-based ILs on steel on steel [64–67] and steel on aluminum tribo pairs [64,65,71–76]. These studies show better friction-reducing and antiwear abilities for ILs containing longer cations alkyl chains than the ones containing shorter alkyl chains [67,73,74,76]. It was believed that longer alkyl chains prevent the direct surface to surface contact due to the formation of thick, low-shear strength layers beneficial for friction and wear reduction, especially in the boundary lubrication condition. This mechanism is similar to the one provided by friction modifiers.

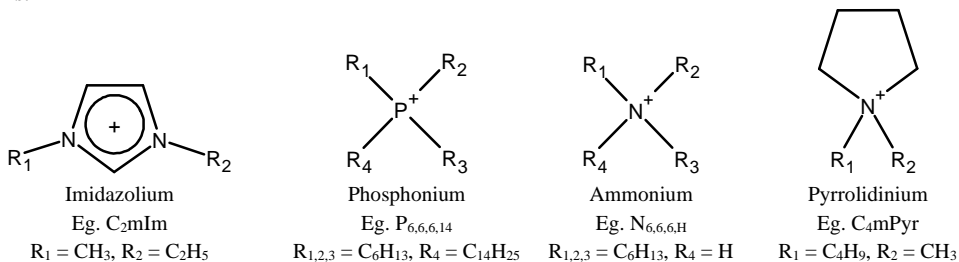
Functionalization of the cation by changing the hydrocarbon alkyl chain with other groups can improve the tribological properties of ILs. Phosphorus, one of the most common antiwear elements, can be used as a functional group for imidazolium cation in the form of phosphate. By changing the alkyl chain with a functional group, it is expected that the adsorption behavior would be increased. In a study performed on steel on aluminum tribopair, it was successfully shown that imidazolium functionalized with a phosphate group significantly improved friction and wear behavior compared to regular imidazolium [73,76].

As the availability of cation chemistries increases, the number of cations used in ILs for lubricants increases as well. The quaternary ammonium [68,70,77–80], quaternary phosphonium [80–87], and pyrrolidinium [84,86,88,89] based cations were studied as alternative to imidazolium cations. The research of the different types of cations concluded that ammonium-, phosphonium-, and pyrrolidinium-based ILs had better tribological properties than imidazolium-based ILs. It was found that increasing the alkyl chain length of ammonium, phosphonium, and pyrrolidinium cations also resulted in reducing friction and wear [70,82,86]. It seems that the influence of chain length on the tribological behavior apply to most IL systems.

In the early years of ILs' research as neat lubricants, tetrafluoroborate ( $\text{BF}_4^-$ ) and hexafluorophosphate ( $\text{PF}_6^-$ ) were frequently used as the anion part due to commercial availability at a reasonable price [20,90]. When tested individually,  $\text{BF}_4^-$  and  $\text{PF}_6^-$  combined with imidazolium cation showed lower friction and wear than the traditional lubricants phosphazene and perfluoropolyether [64,65].  $\text{BF}_4^-$  and  $\text{PF}_6^-$  are hydrophilic, which can lead to the formation of hydrogen fluoride (HF) in the presence of water contamination leading to an increase in friction [71,74,88,91]. To overcome this situation, other more hydrophobic fluorine-containing anions have been synthesized, i.e., bis(trifluoromethylsulfonyl)amide ( $\text{NTf}_2^-$ ) and trifluorotris(pentafluoroethyl)phosphate (FAP) [66,88]. The tribological tests showed that  $\text{NTf}_2^-$  has



**Cations:**



**Anions:**

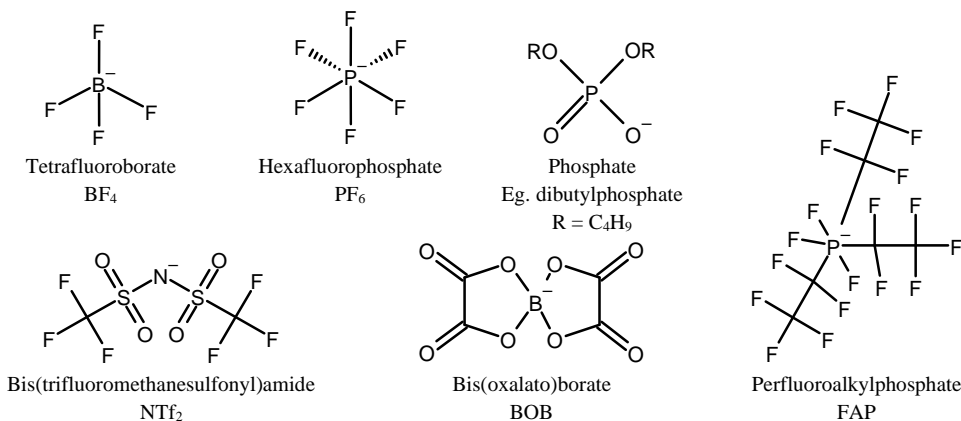


**Figure 2-6.** Typical ionic liquid cations and anions molecular structures. Figure adapted from [14].

better wear resistance but higher friction than BF<sub>4</sub><sup>-</sup> [66]. When the cation is the same, ILs composed of FAP are superior to NTf<sub>2</sub><sup>-</sup> in friction reduction and wear resistance for both steel on steel and steel on aluminum tribo pairs due to formation of metallic fluoride tribofilm on the worn surface [86,88].

It has been found that ILs in tribopairs form boron oxides, metallic fluorides, and metallic phosphates on the worn surfaces indicating that the anion part is the key in the mechanism of tribofilm formation [64,65,73,75]. To mimic the performance of classical antiwear additives like ZDDP, phosphate anions with hydrocarbon alkyl chains have been synthesized, i.e., dimethyl phosphate [83], diethyl phosphate [92], dibutyl phosphate [87], bisethylhexyl phosphate [87,93], diphenyl phosphate [86,87], in combination with imidazolium [92,93], or phosphonium cations [83,86,87]. It has been found that the tribological performance of phosphate anions is better than those anions containing fluor and boron due to the formation of metal phosphates on the tribosurfaces [83,86,87,92].

Although so much evidence suggests the important role of anions in tribofilm formation, the role of cations cannot be neglected. For example, aluminum lubricated with imidazolium cation functionalized with phosphate coupled to a BF<sub>4</sub><sup>-</sup> anion showed traces of boron oxide and -P-O-Al species on the worn surface which originated from the cation and anion part of the IL [73,76].

Therefore, both cation and anion decompose due to the localized high frictional temperature and eventually react with the nascent surface to form a protective tribofilm.

## 2.4.2. ILs as lubricant additives

Although the proven tribological efficiency, the use of ILs as base lubricant fluids is still limited due to the high production costs [14,20,59]. In most real applications, large volumes of lubricant are needed, and ILs as neat lubricants are unacceptable for most consumers. For that reason, research is being conducted to investigate the tribological behavior of ILs as lubricant additives in base lubricants such as mineral oils [70,75,94], synthetic oils [16,95,96], glycerol [10,97,98], and water-based lubricants [99,100]. Used as additives, ILs could be added to base lubricants up to 10 wt.% [70].

They can be used as antiwear and friction modifier additives for many reasons: (1) ILs can be tailored and tuned to meet certain properties; for example, longer alkyl chains are more soluble in oils, whereas shorter alkyl chains are more soluble in water [101]; (2) ILs have a double polar structure in which they can adsorb to tribosurfaces and form alternating anions-cations layers. This adsorption film can give similar behavior as graphite or MoS<sub>2</sub> layered structure [81]; (3) ILs can contain active elements such as fluorine, chlorine, sulfur, phosphorus, and boron, that with the assistance of localized high temperature, can decompose and react with the worn surface to form protective tribofilms [14]; (4) most ILs have a thermal decomposition temperature higher than conventional additives, and they can thus be used in higher temperature applications [80].

The first IL used as a lubricant additive can be traced back to 2003, in which P. Iglesias et al. studied 1 wt.% of n-dodecylammonium chloride (C<sub>12</sub>H<sub>25</sub>NH<sub>3</sub><sup>+</sup>Cl<sup>-</sup>) as an additive in a mineral oil [15]. Early studies of ILs as lubricant additives involve the use of non-polar hydrocarbon oils. Designing ILs as lubricant additives in non-polar hydrocarbon oils was challenging due to solubility, i.e., ions and non-polar molecules are typically immiscible. Although early research of ILs involved non-soluble ILs in non-polar oils, the results showed that the ILs could reduce friction and improve the tribological performance [70,74,75,94,102–104]. XPS analysis on the worn surfaces confirmed the presence of tribofilms containing different compounds depending on the active elements in ILs, for example, FeF<sub>3</sub>, B<sub>2</sub>O<sub>3</sub>, P<sub>2</sub>O<sub>5</sub>, or PO<sub>4</sub><sup>3-</sup>. The results also showed that phosphorus containing-ILs gave better friction and wear reduction.

ILs have also been investigated as lubricant additives in polar oils such as polyethylene glycol [96,105–109], glycerol [10,89,97,98,110], and ester oils [111–113]. The purpose of using these polar oils was to increase the solubility of ILs. For example, using polyethylene glycol as base lubricant increased the solubility of ILs having PF<sub>6</sub><sup>-</sup>, NTf<sub>2</sub><sup>-</sup>, and BF<sub>4</sub><sup>-</sup> as anions in more than 40 % (in the best

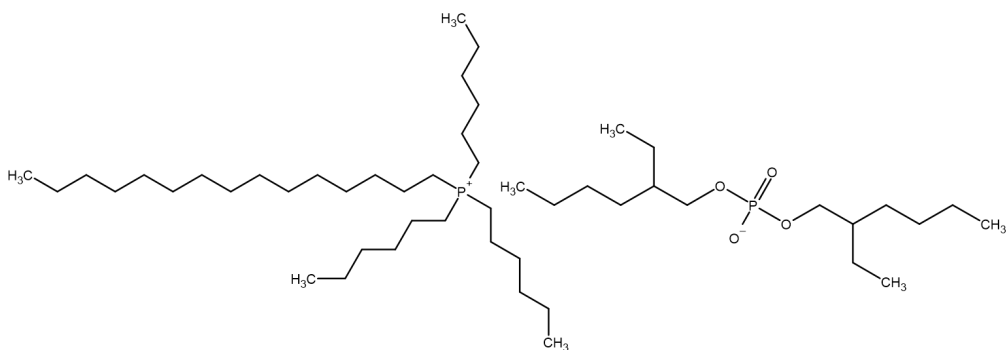


**Figure 2-7.** Chemical structure of trihexyltetradecylphosphonium bis(2-ethylhexyl) phosphate.

case) resulting in the best friction and wear results [105]. Surface analysis revealed the presence of tribofilms, being iron phosphate the predominant compound however, fluorine or other active elements were not commonly detected. It was deduced that physisorption rather than chemisorption played the most important role in the tribological performance. Another study performed using the same ILs but varying the cations as lubricant additive in polyethylene glycol showed a larger increase in solubility, more than 50 % in the best case [96]. The tribological performance was again very good, and the surface analysis showed fluorine on the worn steel surface. For the IL containing both phosphorus and fluorine, it was revealed that the worn surface also consisted of organic phosphine compounds and was the one with the best tribological performance [96].

Research of ILs focusing on their solubility in non-polar lubricant oils began in 2012, when Qu et al. synthesized for the first time a phosphonium cationic based IL, i.e., trihexyltetradecylphosphonium bis(2-ethylhexyl) phosphate, as shown in **Figure 2-7**, which is soluble with various hydrocarbon oils [16]. It was hypothesized that its high solubility is due to its 3D quaternary structure and long hydrocarbon chains. It was later revealed that six carbons are the critical minimum of each alkyl chain length to achieve high solubility of phosphonium cationic base ILs in polyalphaolefin 4 cSt base oils, regardless if the cation structure is symmetric or asymmetric [18]. However, a study by Minjin et al. shows conflicting results on the effect of cation symmetry on the solubility of ILs. Minjin et al. studied several different chain lengths of ammonium-based cationic ILs coupled with the same anion. They found that the solubility limit of these ILs in PAO10 increases with increasing the carbon chain length. The role of the 3D quaternary structures with high steric hindrance (long hydrocarbon chains) on the solubility of ILs in non-polar base oils can be explained by: (1) strong interionic interaction between cation and anion, which decreases the effective polarity of the IL thus leading to lower coordination of the molecules, and (2) increase of intermolecular London dispersion forces between hydrophobic moieties of the cations and the base oil molecules [16,18,114,115]. The tribological

performance of oil-soluble IL additives in non-polar base oils showed a lower coefficient of friction and wear rate of the tribomaterials [16,18,69,114–122]. Moreover, their antiwear and anti-scuffing properties were better compared to ZDDP [118,120,122]. In addition, oil-soluble phosphonium-based ILs showed a synergy effect with existing additives in fully formulated engine oils, enhancing the wear performance of the lubricants [16,114].

Nowadays, environmental issues receive greater attention in lubricant formulation. The UN sustainable goals for 2030 and the new green policies around the world are pushing the development of environmentally acceptable lubricants. Not only the base lubricants should be environmentally acceptable, but the additives as well. Therefore, developing environmentally friendly ILs free of halogen, phosphorus, and sulfur atoms are emerging [101]. Imidazolium and quaternary ammonium are chosen as the cation couple with ibuprofen, ricinoleic acid, and succinate [99,123,124]. Typical environmentally acceptable base oils are polar like synthetic esters, oils derived from vegetables, and water-based lubricants (containing glycols as organic phase). However, some non-polar short chain polyalphaolefins are also considered environmentally acceptable base lubricants. Water-based lubricants have several drawbacks that limit their use, such as low viscosity, high pour point, high corrosion, and poor tribological performance. To overcome this, ILs have been developed [101]: (1) shorter alkyl chain cation moieties coupled with a small anion, such as hexafluorophosphate [BF<sub>4</sub><sup>-</sup>] and tetrafluoroborate [PF<sub>6</sub><sup>-</sup>] [125,126]; (2) ILs using non-halogen anions, such as dialkyl phosphate, dialkyl phosphite, acesulfame, and gluconate, coupled with quaternary ammonium or phosphorous-nitrogen cations [100,127,128]. The results showed that these ILs as additives for water-based lubricants have good solubility and anticorrosion properties as well as improved friction reduction and antiwear performance [100,127,128].

## **2.5. Viscoelastic layers in a bulk liquid: Continuum mechanics approach**

Formulated lubricants contain additives to improve the tribological behavior of tribosystems by firstly forming adsorbed layers on the tribosurfaces. Therefore, the analysis of the viscoelastic behavior of the adsorbed layer becomes an important study in tribology because it can give a hint about the friction reduction function of additives and also its influence on the eventual tribofilm formation. The mechanical properties of an adsorbed layer can be determined from the frequency response of an oscillating quartz crystal in which these layers are deposited. This technique is known as the quartz crystal microbalance (QCM) technique [129].

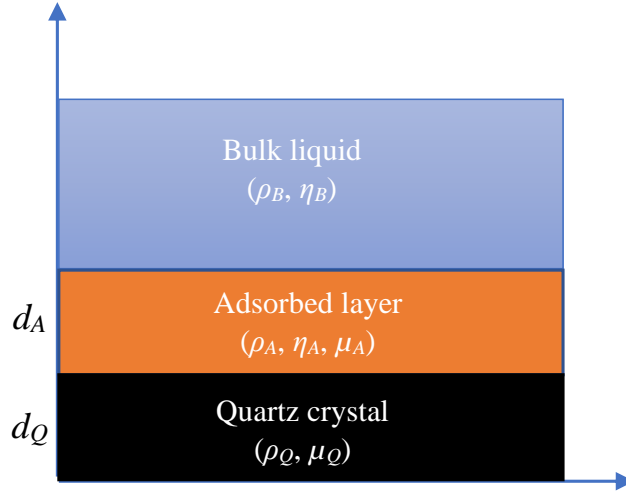


**Figure 2-8.** Quartz crystal covered by a viscoelastic adsorbed layer.

The QCM was first introduced by Gunter Sauerbrey in 1959 to measure adsorbed mass on a quartz sensor surface in a vacuum or gas medium [130]. Firstly, the quartz is oscillated at a defined frequency by applying an appropriate voltage, and any mass loading on the quartz surface changes its resonant frequency. The adsorption in vacuum or gas medium results in a rigid adsorbed layer that fully couples with the quartz oscillation; therefore, the change in adsorbed mass is linearly related to the change in the oscillation frequency. The relation between the frequency shift of the QCM sensor and the mass change was firstly proposed by Sauerbrey in the Sauerbrey equation:

$$\Delta f = -\frac{f_0}{\rho_Q d_Q} \left( \frac{\Delta m}{A_Q} \right) \quad (2-1)$$

where  $\Delta f$  and  $\Delta m$  are frequency shift (Hz) and mass change (kg). Whereas  $f_0$ ,  $\rho_Q$ ,  $d_Q$ , and  $A_Q$  are the fundamental frequency in vacuum or gas medium (Hz), density ( $\text{kg/m}^3$ ), thickness (m), and area of the quartz plate ( $\text{m}^2$ ), respectively.

In a liquid medium, the bulk liquid influences the adsorbed layer as an additional dynamic mass via direct hydration or entrapment within the adsorbed layer; as a result, the adsorbed layer possesses a viscoelastic behavior [131]. The resulting viscoelastic layer is not fully coupled with the quartz oscillation leading to dampening and energy loss of the oscillation. The energy loss in a QCM experiment can be obtained by measuring the dissipation factor ( $D$ ), which is inversely proportional with the decay time constant [132]:

$$D = \frac{1}{\pi f \tau} \quad (2-2)$$

where  $f$  is the resonant frequency and  $\tau$  is the decay time constant. The viscoelastic layer mass cannot be determined by the frequency shift alone as in the Saurbrey equation. Instead, both frequency shift and dissipation factors are needed in order to be able to quantify the adsorbed layer.

There are two theoretical approaches used to analyze the viscoelastic response of the adsorbed layer, i.e., the electrical circuit approach and the continuum mechanics approach [132,133]. The continuum mechanics approach has advantages over the electrical circuit approach due to its direct link with the physical parameters of the adsorbed layer. In the continuum mechanics approach, the mechanical properties of the viscoelastic layer are related to the energy storage and energy dissipation of the oscillating quartz. The Voigt model is used to describe the viscoelastic properties of the adsorbed layer, in which parallel arrangements of a spring and a dashpot are applied to represent the storage modulus (related with the shear elasticity modulus,  $\mu$ ) and loss modulus (related with the shear viscosity coefficient,  $\eta$ ).

The model of the continuum mechanics approach is shown in **Figure 2-8**, where a quartz crystal is covered by a viscoelastic adsorbed layer in a liquid medium. Hence  $d_Q$ ,  $\rho_Q$ , and  $\mu_Q$  are the thickness, density, and shear elasticity modulus of the quartz crystal, respectively. Whereas  $d_A$ ,  $\rho_A$ ,  $\eta_A$ , and  $\mu_A$  are thickness, density, shear viscosity coefficient, and shear elasticity modulus of the adsorbed layer. And  $\rho_B$  and  $\eta_B$  are the density and shear viscosity coefficient of the bulk liquid.

According to Voinova, the general solution for the wave function of the model in **Figure 2-8** oscillates at the fundamental frequency ( $f$ ) is as follows [133]:

$$\omega = 2 \cdot \pi \cdot f \quad (2-3)$$

$$\kappa_1 = \frac{\omega \cdot \eta_A - i \cdot \mu_A}{\omega} \text{ and } \kappa_2 = \eta_B \quad (2-4)$$

$$\zeta_1 = \sqrt{-\frac{\rho_A \cdot \omega^2}{\mu_A + i \cdot \omega \cdot \eta_A}} \text{ and } \zeta_2 = \sqrt{i \frac{\rho_B \cdot \omega}{\eta_B}} \quad (2-5)$$

$$\alpha = \frac{\kappa_1 \cdot \zeta_1 + \kappa_2 \cdot \zeta_2}{\kappa_1 \cdot \zeta_1 - \kappa_2 \cdot \zeta_2} \quad (2-6)$$

$$\beta = \kappa_1 \cdot \zeta_1 \cdot \frac{1 - \alpha \cdot e^{(2 \cdot \zeta_1 \cdot d_A)}}{1 + \alpha \cdot e^{(2 \cdot \zeta_1 \cdot d_A)}} \quad (2-7)$$

The imaginary part of the  $\beta$ -function corresponds to resonance frequency shift ( $\Delta f$ ), whereas the real part of the  $\beta$ -function corresponds to dissipation factor shift ( $\Delta D$ ) [132]:

$$\Delta f = \text{Im} \left( \frac{\beta}{2 \cdot \pi \cdot \rho_Q \cdot d_Q} \right) \text{ and } \Delta D = -\text{Re} \left( \frac{2 \cdot \beta}{2 \cdot \pi \cdot f \cdot \rho_Q \cdot d_Q} \right) \quad (2-8)$$

The frequency shift ( $\Delta f$ ) and dissipation factor shift ( $\Delta D$ ) in Equation 2-8 are measured with respect to the frequency and dissipation factors in vacuum or gas media, meaning the QCM experiment starts measuring the frequency and dissipation factor in air, followed by the introduction of bulk liquid containing the adsorbates. This kind of experiment is not practical in real situations. Normally, the experiment starts with a reference liquid (no adsorbates) followed by a bulk liquid containing adsorbates, so the frequency and dissipation factor shift is with respect to a reference liquid. Thus, the contribution of the reference liquid should be included in the equation as follows:

$$\kappa_R = \eta_R \quad (2-9)$$

$$\zeta_R = \sqrt{i \frac{\rho_R \cdot \omega}{\eta_R}} \quad (2-10)$$

$$\beta_R = \kappa_R \cdot \zeta_R \quad (2-11)$$

$$\Delta f = \text{Im} \left( \frac{\beta - \beta_R}{2 \cdot \pi \cdot \rho_Q \cdot d_Q} \right) \text{ and } \Delta D = -\text{Re} \left( \frac{\beta - \beta_R}{\pi \cdot f \cdot \rho_Q \cdot d_Q} \right) \quad (2-12)$$

By monitoring the real-time change in frequency, QCM can provide information regarding the amount of mass deposited on the quartz sensor and the rate of deposition (or removal) of adsorbed layers. Moreover, by monitoring both the frequency and dissipation factor shift, additional viscoelastic information, such as shear elasticity modulus and shear viscosity coefficient, can be obtained. This technique is called quartz crystal microbalance with dissipation (QCM-D).

*This page is intentionally left blank*



# Chapter 3

## Experimental

### 3.1. Materials and preparation

#### 3.1.1. Lubricants

Four different types of glycols were used in this Ph.D., i.e., monoethylene glycol, diethylene glycol, monopropylene glycol, and dipropylene glycol. Glycols were purchased from Acros Organics (Netherlands) with  $\geq 99\%$  purity. These glycols were mixed with water in a 1:1 proportion, and the following base lubricants were prepared: water-monoethylene glycol (WMEG), water-diethylene glycol (WDEG), water-monopropylene glycol (WMPG), and water-dipropylene glycol (WDPG). The water-glycol base lubricants were designed to study the behavior of ILs in polar media. For the study of ILs in non-polar media, polyalphaolefin 2 cSt and 8 cSt (PAO2 and PAO8) were used as the base lubricants. The PAOs were supplied by Chevron Phillips Chemical (Belgium) with 100% purity. The chemical formula, density, and chemical structure of all base lubricants used in this Ph.D. thesis are shown in **Table 3-1**.

The ILs used in this study were 1,3-dimethylimidazolium dimethylphosphate (IM), (2-hydroxyethyl) trimethylammonium dimethylphosphate (AM), tributylmethylphosphonium dimethylphosphate (PP), 1-butyl-1-methylpyrrolidinium tris(pentafluoroethyl) trifluorophosphate (BMP), trihexyltetradecylphosphonium bis(2,4,4-trimethylpentyl)phosphinate (PB), and trihexyltetradecylphosphonium decanoate (PC). The tribological behavior was compared with an organic friction modifier, i.e., dodecanoic acid (C12). PP ( $\geq 97\%$  purity) was purchased from Fluorochem (UK). IM ( $\geq 98\%$ ), AM ( $\geq 98\%$ ), BMP ( $\geq 98\%$ ), PB ( $\geq 90\%$  purity), PC ( $\geq 95\%$  purity), and C12 ( $\geq 99\%$ ) were purchased from Sigma-Aldrich (Germany). All chemicals were used as received. The chemical formula, density, and chemical structure of all additives used in this Ph.D. thesis are shown in **Table 3-2**. When formulating the lubricants, the base lubricants and additives were mixed using a magnetic stirrer for 4 hours at 50 °C and 70 °C for polar and non-polar media, respectively.

**Table 3-1.** Chemical formula, density, and chemical structure of all base lubricants

Abbr.	Chemical Name	Density (g/cm <sup>3</sup> )	Chemical Formula	Molecular Weight (g/mol)	Chemical Structure
MEG	Monoethylene glycol	1.115	C <sub>2</sub> H <sub>6</sub> O <sub>2</sub>	62.07	
DEG	Diethylene glycol	1.118	C <sub>4</sub> H <sub>10</sub> O <sub>3</sub>	106.12	
MPG	Monopropylene glycol	1.032	C <sub>3</sub> H <sub>8</sub> O <sub>2</sub>	76.1	
DPG	Dipropylene glycol	1.022	C <sub>6</sub> H <sub>14</sub> O <sub>3</sub>	134.2	
PAO2	Polyalphaolefin 2 cSt	0.798	C <sub>20</sub> H <sub>42</sub>	282.5	
PAO8	Polyalphaolefin 8 cSt	0.833	UVCB*	596**	

\* UVCB (unknown variable composition or biological substance) due to PAO8 results from polymerization of 1-decane.

\*\* This is calculated average molecular weight based on measurement using gas chromatography [29].

\*\*\* Molecular structure illustration after polymerization.

**Table 3-2.** Chemical formula, density, and chemical structure of all additives

Abbr.	Chemical Name	Density (g/cm <sup>3</sup> )	Chemical Formula	Molecular Weight (g/mol)	Chemical Structure
IM	1,3-dimethylimidazolium dimethylphosphate	1.277	C <sub>7</sub> H <sub>15</sub> N <sub>2</sub> O <sub>4</sub> P	222.18	
AM	(2-hydroxyethyl) trimethylammonium dimethylphosphate	1.186	C <sub>7</sub> H <sub>20</sub> NO <sub>5</sub> P	229.21	
PP	Tributylmethylphosphonium dimethylphosphate	1.004	C <sub>15</sub> H <sub>36</sub> O <sub>4</sub> P <sub>2</sub>	342.40	
BMP	1-butyl-1-methylpyrrolidinium tris(pentafluoroethyl) trifluorophosphate	1.647	C <sub>15</sub> H <sub>20</sub> F <sub>18</sub> NP	587.27	
PB	Trihexyltetradecylphosphonium bis(2,4,4-trimethylpentyl)phosphinate	0.895	C <sub>48</sub> H <sub>102</sub> O <sub>2</sub> P <sub>2</sub>	773.27	
PC	Trihexyltetradecylphosphonium decanoate	0.880	C <sub>42</sub> H <sub>87</sub> O <sub>2</sub> P	655.11	
C12	Dodecanoic acid	1.007	CH <sub>3</sub> (CH <sub>2</sub> ) <sub>10</sub> COOH	200.32	

**Table 3-3.** Chemical composition, microstructure, and hardness of AISI 52100 steel and AISI 316L stainless steel

	Chemical Composition (wt.%)									Microstructure	Equivalent Hardness
	Fe	Cr	Ni	Mo	Mn	Si	C	P	S		
<b>AISI 52100 steel</b>	Balance	1.3-1.6	-	-	0.25-0.45	0.15-0.30	0.98-1.10	≤0.025	≤0.025	Tempered martensite chromium carbide	746 HV
<b>AISI 316L stainless steel</b>	Balance	16-18	10-14	2.0-3.0	≤2.0	≤1.0	≤0.030	≤0.045	≤0.030	Austenite	217 HV

### 3.1.2. Steel specimens

Depending on the application, different types of steel were used with varied chemical composition, microstructure, and mechanical properties. Two steels were selected for this Ph.D. thesis, i.e., AISI 52100 bearing steel and AISI 316L stainless steel. Both steels were purchased from Smith Stål (Trondheim, Norway). The chemical composition, microstructure, and mechanical properties of these two steels are shown in **Table 3-3**. AISI 52100 steel is a high carbon and low alloyed chromium steel with a tempered martensite microstructure and chromium carbide precipitates leading to high hardness (60 HRC – Hardness Rockwell C scale, equivalent to 746 HV - Hardness Vickers). It can be hardened via the heat treatment process, i.e., quenching-tempering. AISI 52100 steel is mostly used in bearings, mill rolls, and vehicle parts thanks to its combination of strength, hardness, and workability. AISI 316L stainless steel is an austenitic stainless steel with low carbon content, high chromium, and contains molybdenum, making it more corrosion resistant than AISI 304 or 310 stainless steels. The high nickel content stabilizes the austenite at room temperature leading to high ductility and low hardness (217 HB – Hardness Brinell scale, equivalent to 217 HV – Hardness Vickers). AISI 316L has applications in pulp and paper equipment, heat exchangers, dyeing equipment, film processing equipment, pipelines, materials for exterior construction in coastal areas, food industry, biomedical industry, and many others. The elastic modulus and poisson ratio of both steels are 210 GPa and 0.29, respectively. These two steels were selected due to their wide applicability in tribological components, and to investigate the effect of chemical composition and mechanical properties on the lubricating mechanisms in polar and non-polar media. Tests on these steels were performed on disk specimens prepared from 30 mm diameter rods cut to a thickness of 6 mm. Surface preparation was done by following the procedure in the metalog guide provided by Struers for each material until it reached the surface finish of  $R_a = 0.090 \pm 0.003 \mu\text{m}$  [134]. After surface preparation, the sample disks were ultrasonically cleaned in distilled water-ethanol mixture (ca. 1:1) for 5 minutes, then rinsed with fresh ethanol and dried with pressurized air.

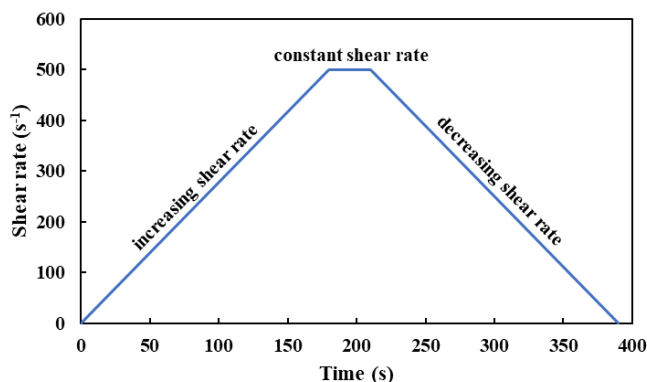


Figure 3-1. Dynamic viscosity measurement procedure.

## 3.2. Testing, statistical analysis and characterization

### 3.2.1. Density, conductivity, pH, and OCP

The density of the lubricants was measured by the constant fluid volume weighing method. The electrical conductivity of the lubricants was measured using a conductivity meter (Hanna Instruments HI-2300). The pH of the lubricants was measured using a pH meter (Radiometer analytical PHM220 or Hanna Instruments HI-2210). The open-circuit potential (OCP) was measured using a Gamry Interface 1000 Potentiostat with Ag/AgCl KCl saturated reference electrode for 4 hours.

### 3.2.2. Dynamic viscosity

The dynamic viscosity of the lubricants at 23 °C in humid air was measured by a rheometer (Haake Mars Rotational Rheometer with a CC27 cylinder measuring system, with the built-in Peltier element). Each measurement was performed by the procedure as shown in **Figure 3-1**. For the first step, the shear rate was increased from 0.01 to 500 s<sup>-1</sup> with a ramp time of 180 s. For the second step, the shear rate was held at a constant value of 500 s<sup>-1</sup> for 30 seconds. For the last step, the shear rate was decreased from 500 to 0.01 s<sup>-1</sup> with a ramp time of 180 seconds. The dynamic viscosity was calculated from the average value of 30 measurements taken during the second step.

### 3.2.3. Lubricant stability study

The stability of the lubricant mixtures was examined by a turbidity meter (Hanna Instruments HI-88713). Turbidity measures the appearance of lubricants by the degree of the light that has been

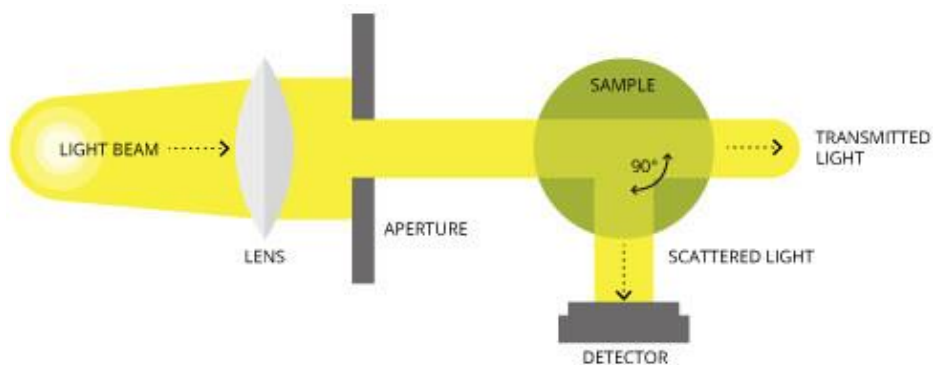


**Figure 3-2.** The principle of turbidity measurement [135].

scattered by the dispersed particles in the lubricant, as shown in **Figure 3-2**. With increasing in scattered light, the turbidity will be higher; thus, the turbidity unit (FNU) will be higher. The lubricants were put on a magnetic stirrer for 2 hours prior to the test. The reported FNU was measured by calculating the average value of 12 measurements taken from 2 hours test. High turbidity numbers indicate the mixture is not homogenous, representing a no fully soluble additive in the lubricant. By monitoring real-time turbidity evolution over a period of time, information about the stability of the lubricant mixture can be obtained.

### 3.2.4. Adsorption study

The adsorption studies were performed using a quartz crystal microbalance with dissipation (QCM-D) from Biolin Scientific. Iron (Fe) and stainless steel (SS) coated quartz crystals were used as sensors. The sensors were cleaned by the cleaning procedure provided by Biolin Scientific prior to the experiments. The experiment procedure is illustrated in **Figure 3-3** and consists of three steps. Real-time monitoring of frequency shift ( $\Delta f$ ) and dissipation shift ( $\Delta D$ ) at multiple harmonics was conducted during the experiments. For the first step, the reference (base) lubricant was injected into the sensor by a peristaltic pump for at least 30 minutes to obtain a steady baseline. For the second step, the reference lubricant was changed with a formulated lubricant (base lubricant and additives). During this step, the formulated lubricant was injected for 2 hours to observe the adsorption behavior of the additives on the sensor surface to form adsorbed layers. For the last step, the formulated lubricant was changed back to the reference lubricant for 1 hour to remove the adsorbed layers from the sensor surface. In this way, the weakly bonded adsorbed layer will be removed entirely from the sensor surface, and on the other hand, the strongly bonded adsorbed layers will remain on the sensor surface. The peristaltic pump flow rate was set to 50  $\mu\text{l}/\text{min}$  during the experiment.

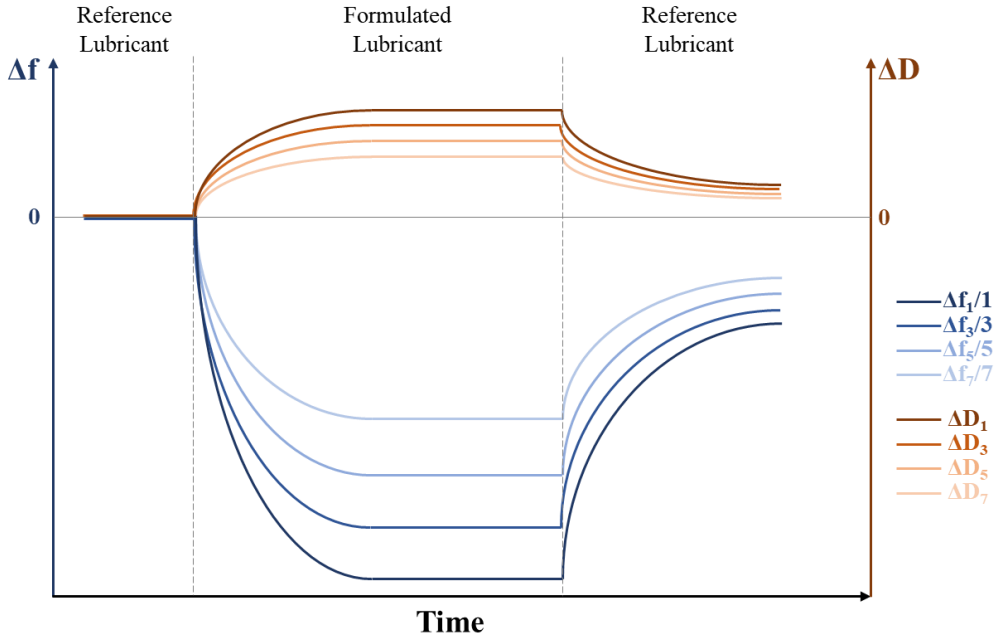


**Figure 3-3.** Measurement of frequency shift and dissipation shift at multiple harmonics.

From the frequency shift and dissipation shift at multiple harmonics, the adsorbed layer properties, such as thickness ( $d_A$ ), shear elasticity modulus ( $\mu_A$ ), and shear viscosity coefficient ( $\eta_A$ ), can be analyzed using MATLAB `fminsearch` function based on the Voigt-viscoelastic model by Voinova et al. [133]. A schematic illustration of the model and the detailed formulas are provided in **Figure 3-4**. In this model, the initial value of the adsorbed layer parameters ( $d_A$ ,  $\mu_A$ , and  $\eta_A$ ) is given in the beginning; then, the program will calculate  $\Delta f_n^c$  and  $\Delta D_n^c$  (c for calculated) from the selected overtones for each measurement time (minimum 3 overtones are required for the modeling). The MATLAB `fminsearch` function will find the minimum of the sum of squares of the scaled error ( $\chi^2$ ) between calculated ( $\Delta f_n^c$  and  $\Delta D_n^c$ ) and measured ( $\Delta f_n^m$  and  $\Delta D_n^m$ ) (m for measured) frequency and dissipation values by changing the initial value of the layer parameters ( $d_A$ ,  $\mu_A$ , and  $\eta_A$ ). The  $\sigma_{\Delta f_n^m}$  and  $\sigma_{\Delta D_n^m}$  values correspond to the standard deviations of the measured frequency and dissipation at the baseline, n denotes the number of overtone and k is the highest overtone number. To run the program, fixed parameters are needed, i.e., fundamental frequency ( $f_0$ ), density ( $\rho_Q$ ), and shear elasticity modulus ( $\mu_Q$ ) of the quartz crystal sensor, density ( $\rho_B$ ) and shear viscosity coefficient ( $\eta_B$ ) of the formulated lubricant, density ( $\rho_R$ ) and shear viscosity coefficient ( $\eta_R$ ) of the reference lubricant, and density of the adsorbed film ( $\rho_A$ ). Assumptions used for the film are rigidly attached (no slip), evenly distributed, and homogenous thickness, density, viscosity, and elasticity properties.

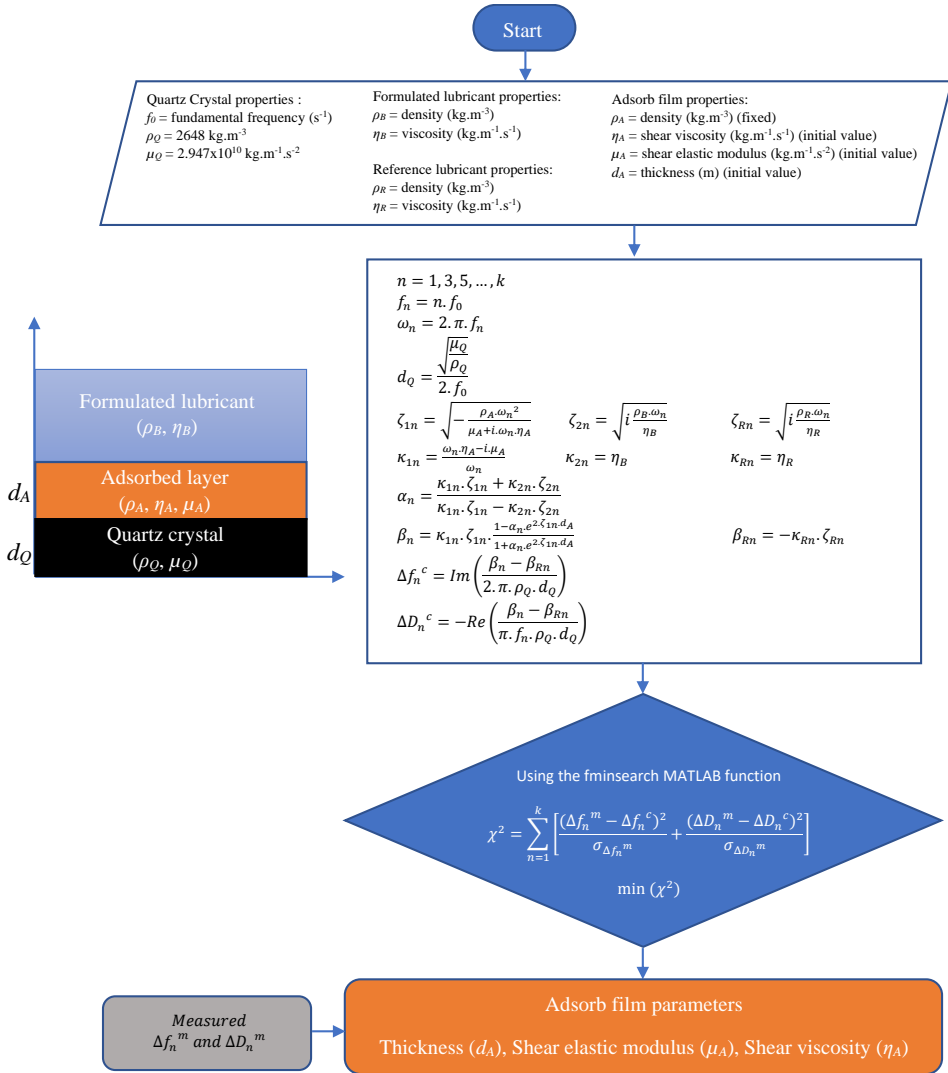
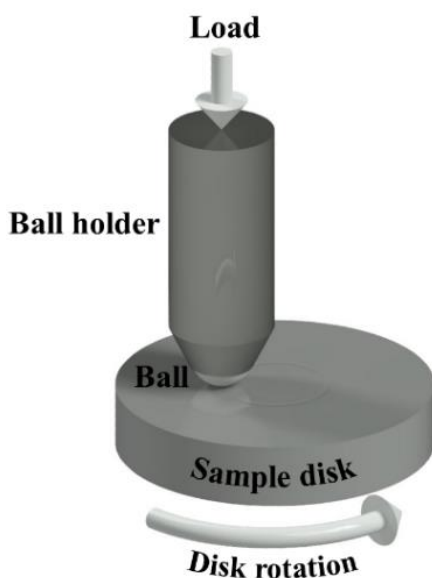


Figure 3-4. Schematic illustration of the viscoelastic model and formulae used in modelling.

### 3.2.5. Tribological tests

The tribological tests were performed using a unidirectional sliding ball-on-disk tribometer (Anton Paar with Phoenix tribology software) to evaluate the tribological performance of each lubricant on the steel samples. The tests were conducted by pushing a stationary alumina ball against a rotating disk sample under boundary lubricating conditions. The alumina ball (fused ceramic) was purchased from Precision Ball and Gauge Co. Ltd with an elastic modulus of 300 GPa and a poisson ratio of 0.21.



**Figure 3-5.** Illustration of tribological test setup.

The roughness of the alumina ball was 0.025  $\mu\text{m}$ . Alumina was chosen since this is an inert material with respect to the water base lubricant. It is important to avoid any electrical contact between the tribopair since the lubricants formulated with water and ILs are electrically conductive. The tribological tests are illustrated in **Figure 3-5**, and the test parameters are shown in **Table 3-4**. Two type of tests were performed, i.e., preliminary test and long-run test. At least two experiments were performed to verify the repeatability of the results for each condition. All reported friction values are referred to the testing materials pair (alumina on steel), and all the figures and tables captions avoid mentioning alumina for simplicity.

**Table 3-4.** Tribological test parameters

	Rotating ball-on-disk	
	Preliminary test	Long-run test
Disk	Steel	Steel
Ball	Alumina $\text{\O} 6$ mm	Alumina $\text{\O} 6$ mm
Force (N)	20	20
Maximum Hertzian contact pressure (GPa)	1.96	1.96
Rotational speed (rpm)	40	40
Track diameter (mm)	10	10
Sliding speed (m/s)	0.021	0.021
Sliding distance (m)	30	300
Number of cycles (n)	955	9550
Experiment duration (h)	$\sim 0.5$	$\sim 4$
Experimental temperature ( $^{\circ}\text{C}$ )	RT	RT



The lubrication conditions at the start of the test were defined for both water-glycol and PAO base lubricants by calculating the lambda ( $\lambda$ ) value which is the ratio between the minimum film thickness and the combined surface roughness of the two mating materials [22]:

$$\lambda = \frac{h_0}{(\sigma_{ball}^2 + \sigma_{disk}^2)} \quad (3-1)$$

where  $h_0$  is the minimum film thickness (m), and  $\sigma_{ball}$  and  $\sigma_{disk}$  are the surface roughness of the ball and disk, respectively. The minimum film thickness ( $h_0$ ) was calculated using the EHL Hamrock-Dowson formula [25]:

$$\frac{h_0}{R_x} = 3.63 \left( \frac{U\eta_0}{E'R_x} \right)^{0.68} (\alpha E')^{0.49} \left( \frac{W}{E'R_x^2} \right)^{-0.073} (1 - e^{-0.68k}) \quad (3-2)$$

where:

$k$  is the ellipticity parameter which the approximate value can be calculated using:

$$k = 1.0339 \left( \frac{R_y}{R_x} \right)^{0.636} \quad (3-3)$$

$R_x$  is the reduced radius of curvature in the sliding direction (m), i.e.:

$$\frac{1}{R_x} = \frac{1}{R_{ball,x}} + \frac{1}{R_{disk,x}} \quad (3-4)$$

where  $R_{ball,x}$  and  $R_{disk,x}$  are the radius of curvature in the sliding direction for the ball and disk, respectively.

$R_y$  is the reduced radius of curvature perpendicular to the sliding direction (m), i.e.:

$$\frac{1}{R_y} = \frac{1}{R_{ball,y}} + \frac{1}{R_{disk,y}} \quad (3-5)$$

where  $R_{ball,y}$  and  $R_{disk,y}$  are the radius of curvature perpendicular to the sliding direction for the ball and disk, respectively.

$E'$  is the reduced modulus of elasticity (Pa), i.e.:

$$\frac{1}{E'} = \frac{1}{2} \left[ \frac{1-\nu_{ball}}{E_{ball}} + \frac{1-\nu_{disk}}{E_{disk}} \right] \quad (3-6)$$

where  $E_{ball}$  and  $E_{disk}$  are the modulus of elasticity of the ball and disk, respectively. Whereas  $\nu_{ball}$  and  $\nu_{disk}$  are the Poisson's ratio of the ball and disk, respectively.

$U$  is the entraining surface velocity (m/s). i.e.:

$$U = \frac{U_{ball} + U_{disk}}{2} \quad (3-7)$$

where  $U_{ball}$  and  $U_{disk}$  refer to the velocities of ball and disk, respectively.

$\eta_0$  is the viscosity at atmospheric pressure of the lubricant (Pa.s).

$\alpha$  is the pressure-viscosity coefficient of the lubricant (Pa<sup>-1</sup>).

$W$  is the contact load (N).

**Table 3-5.** Lambda value calculation

Parameter	WMEG	WDEG	WMPG	WDPG	PAO2	PAO8
<b>Alumina Ball</b>						
Radius in x direction (mm)				3		
Radius in y direction (mm)				3		
Modulus of elasticity (MPa)				300		
Poisson's ratio				0.21		
Surface roughness (μm)				0.025		
Velocity (m/s)				0		
<b>Disk</b>						
Radius in x direction (mm)				∞		
Radius in y direction (mm)				∞		
Modulus of elasticity (MPa)				210		
Poisson's ratio				0.29		
Surface roughness (μm)				0.090		
Velocity (m/s)				0.021		
<b>Load (N)</b>				20		
<b>Lubricant</b>						
Pressure-viscosity coefficient (GPa <sup>-1</sup> )			4.5		11.49	13.00
Viscosity (mPa.s)	3.81	5.85	8.11	13.99	9.51	81.29
<b>Lambda value</b>	0.004	0.005	0.007	0.010	0.012	0.054

The lambda value of water-glycol and PAO base lubricants are shown in **Table 3-5** along with all needed parameters for calculation. The pressure-viscosity coefficient values for water-glycol, PAO2 and PAO8 are obtained from references [29,136,137]. The highest calculated lambda value is 0.054 for PAO8, and therefore the boundary lubrication condition is met for all lubricants. The addition of an additive to the base lubricant slightly changes the viscosity values, thus the lambda value still meets the boundary lubrication condition.

### 3.2.6. Wear analysis

The wear volume was quantified using an optical 3D microscope (Alicona Infinite Focus Microscope, IFM), followed by surface image analysis using MountainsMap software. For alumina ball, no wear or significant roughness changes were noticeable. In addition, no material transfer was observed. In the case of the steel, wear was observed. The wear area measurement of the steel was taken from four wind directions of the wear tracks, and the average wear area value was then calculated, as shown in **Figure 3-6**. After that, the specific wear rate was calculated by Archard's equation [138]:

$$SWR = \frac{\pi \cdot d \cdot \bar{A}}{N \cdot S} \quad (3-8)$$

$SWR$  is the specific wear rate (mm<sup>3</sup>/Nm),  $d$  is the wear track (mm),  $\bar{A}$  is the average wear area (mm<sup>2</sup>),  $N$  is the normal load (N), and  $S$  is the sliding distance (m). The average  $SWR$  value and the standard deviation were reported.

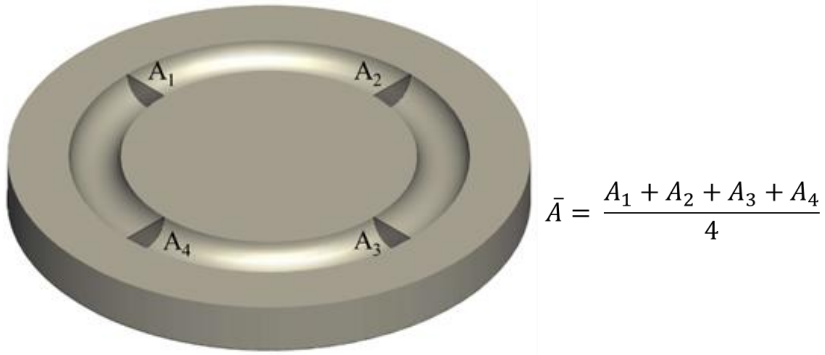


**Figure 3-6.** Illustration top surface of the sample and specific wear rate calculation.

In addition to SWR calculation, a detailed analysis of the wear cross-section profile was performed. An illustration of the wear cross-section profile is shown in **Figure 3-7**. During the test, not all the material is removed from the wear track (groove). Instead, some of the material is pushed to the track's side, forming ridges. As shown in **Figure 3-7**,  $A_{groove}$  is the cross-section area of a valley, and  $A_{ridges}$  is the cross-section area of side ridges; thus,  $A_{groove} - A_{ridges}$  corresponds to the actual wear loss. Then the degree of material loss ( $\beta$ ) could be calculated using the following formula [139]:

$$\beta = \frac{A_{groove} - A_{ridges}}{A_{groove}} \times 100 \quad (3-9)$$

$\beta$  becomes zero when the material loss is due to plastic deformation only ( $A_{groove} = A_{ridges}$ ), and  $\beta$  becomes unity when the material loss is due to abrasive wear only ( $A_{ridges} = 0$ ).

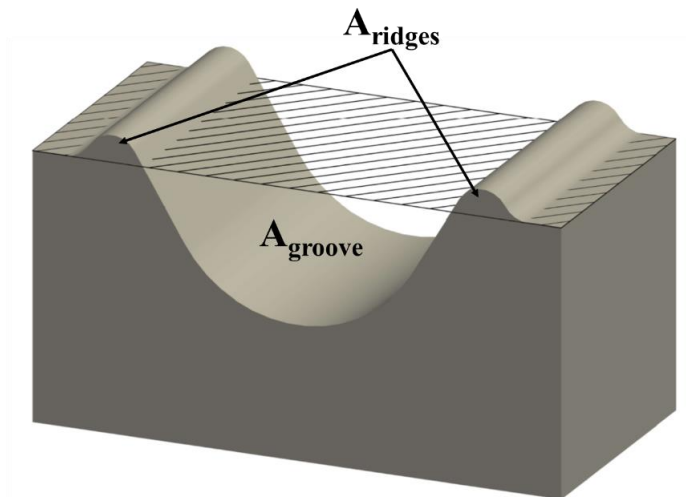


**Figure 3-7.** Illustration of wear cross-section profile.

### 3.2.7. Statistical analysis

#### 3.2.7.1. Two-way ANOVA analysis

The friction and wear data were analyzed using Two-way ANOVA with replication to determine the effect of two independent variables on friction and wear. OriginPro 2018b software was used to perform the Two-way ANOVA Analysis. In Two-way ANOVA, the null hypothesis is defined as the hypothesis where there is no significant difference in the result due to the independent variables. The output of Two-way ANOVA is the P-value for each variable. The P-value is the probability that the null hypothesis is true. To determine whether each independent variable is significant, the P-value for each variable is compared with the significant level to access the null hypothesis. The selected significant level used in this thesis is 0.05 (5%). The significant level is the tolerance limit for accepting the null hypothesis. If the P-value is smaller than the significant level, the null hypothesis is rejected, meaning that the effect of the variable is significant, and vice versa.

The steps for the Two-way ANOVA analysis are explained below, in which two independent variables (A and B) affect one dependent variable (Y) with three replications for each condition. Lubricant as a variable A with 3 number of levels (so  $a = 3$  with  $i = 1, 2,$  and  $3$ ), concentration as a variable B with 3 number of levels ( $b = 3$  with  $j = 1, 2,$  and  $3$ ), and the number of replication is assigned as  $n$  ( $n = 3$  with  $k = 1, 2,$  and  $3$  for three measurements). The dependent variable for each condition and measurement, for example COF value, is assigned as  $Y_{ijk}$ .

1. A matrix was set up with rows for variable A and columns for variable B. **Table 3-6** shows the matrix for the Two-way ANOVA with three replication.
2. The mean value was calculated. There were several mean values calculated, i.e., mean value for each cell ( $\bar{Y}_{ij}$ ), mean value each row ( $\bar{Y}_{Ai}$ ), mean value each column ( $\bar{Y}_{Bi}$ ), and total mean value ( $\bar{Y}_T$ ). The mean values calculation is shown in **Table 3-7**.
3. The degrees of freedom (DF) were calculated for each variable, their interaction, the error (within), and the total using the following equations [140]:

$$DF_A = a - 1 \quad (3-10)$$

$$DF_B = b - 1 \quad (3-11)$$

$$DF_{AB} = (a - 1)(b - 1) \quad (3-12)$$

$$DF_E = ab(n - 1) \quad (3-13)$$

$$DF_T = abn - 1 \quad (3-14)$$

where  $DF_A$ ,  $DF_B$ ,  $DF_{AB}$ ,  $DF_E$ , and  $DF_T$  are the degrees of freedom of variable A, variable B, Interaction between variable A and B, the error, and the total, respectively.

**Table 3-6.** Example of a Two-way ANOVA matrix

			Concentration (B)		
			Concentration 1	Concentration 2	Concentration 3
			$j = 1$	$j = 2$	$j = 3$
Lubricant (A)	Additive 1	$i = 1$	$Y_{111}$	$Y_{121}$	$Y_{131}$
			$Y_{112}$	$Y_{122}$	$Y_{132}$
			$Y_{113}$	$Y_{123}$	$Y_{133}$
	Additive 2	$i = 2$	$Y_{211}$	$Y_{221}$	$Y_{231}$
			$Y_{212}$	$Y_{222}$	$Y_{232}$
			$Y_{213}$	$Y_{223}$	$Y_{233}$
	Additive 3	$i = 3$	$Y_{311}$	$Y_{321}$	$Y_{331}$
			$Y_{312}$	$Y_{322}$	$Y_{332}$
			$Y_{313}$	$Y_{323}$	$Y_{333}$

**Table 3-7.** Two-way ANOVA matrix with all the mean values calculation

			Concentration (B)			Row mean value	
			Concentration 1 (B1)	Concentration 2 (B2)	Concentration 3 (B3)		
			$j = 1$	$j = 2$	$j = 3$		
Lubricant (A)	Additive 1 (A1)	$i = 1$	$Y_{111}$	$Y_{121}$	$Y_{131}$		
			$Y_{112}$	$Y_{122}$	$Y_{132}$		
			$Y_{113}$	$Y_{123}$	$Y_{133}$		
	Cell mean value			$\bar{Y}_{11}$	$\bar{Y}_{12}$	$\bar{Y}_{13}$	$\bar{Y}_{A1}$
	Additive 2 (A2)	$i = 2$	$Y_{211}$	$Y_{221}$	$Y_{231}$		
			$Y_{212}$	$Y_{222}$	$Y_{232}$		
			$Y_{213}$	$Y_{223}$	$Y_{233}$		
	Cell mean value			$\bar{Y}_{21}$	$\bar{Y}_{22}$	$\bar{Y}_{23}$	$\bar{Y}_{A2}$
	Additive 3 (A3)	$i = 3$	$Y_{311}$	$Y_{321}$	$Y_{331}$		
			$Y_{312}$	$Y_{322}$	$Y_{332}$		
			$Y_{313}$	$Y_{323}$	$Y_{333}$		
	Cell mean value			$\bar{Y}_{31}$	$\bar{Y}_{32}$	$\bar{Y}_{33}$	$\bar{Y}_{A3}$
Column mean value			$\bar{Y}_{B1}$	$\bar{Y}_{B2}$	$\bar{Y}_{B3}$		
Total mean value						$\bar{Y}_T$	

4. The sum of squares (SS) was calculated for each variable, their interaction, the error (within), and the total using the following equations [140]:

$$SS_A = bn \sum_{i=1}^a (\bar{Y}_{Ai} - \bar{Y}_T)^2 \quad (3-15)$$

$$SS_B = an \sum_{j=1}^b (\bar{Y}_{Bj} - \bar{Y}_T)^2 \quad (3-16)$$

$$SS_{AB} = n \sum_{i=1}^a \sum_{j=1}^b (\bar{Y}_{ij} - \bar{Y}_{Ai} - \bar{Y}_{Bj} + \bar{Y}_T)^2 \quad (3-17)$$

$$SS_E = \sum_{i=1}^a \sum_{j=1}^b \sum_{k=1}^n (Y_{ijk} - \bar{Y}_{ij})^2 \quad (3-18)$$

$$SS_T = \sum_{i=1}^a \sum_{j=1}^b \sum_{k=1}^n (Y_{ijk} - \bar{Y}_T)^2 \quad (3-19)$$

where  $SS_A$ ,  $SS_B$ ,  $SS_{AB}$ ,  $SS_E$ , and  $SS_T$  are the sum of squares of variable A, variable B, Interaction between variable A and B, the error, and the total, respectively.

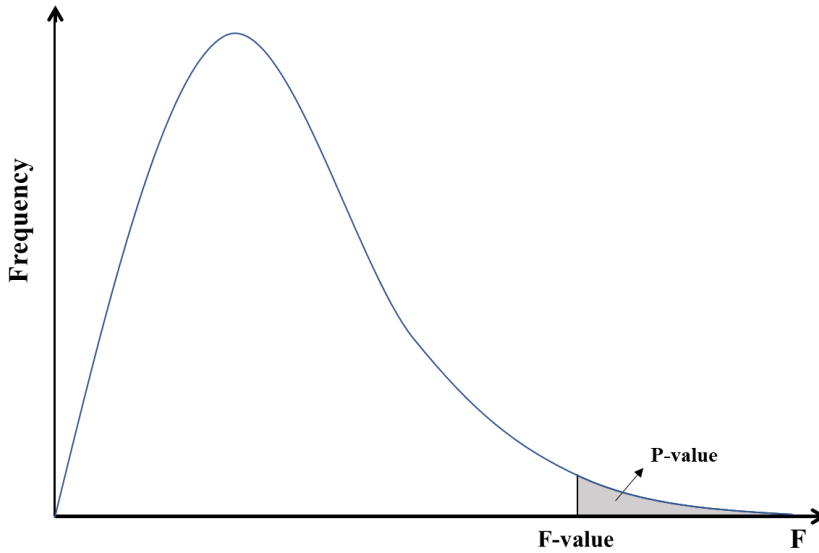


**Figure 3-8.** The F distribution showing the P-value.

5. The mean square (MS) was calculated for each variable, their interaction, and the error (within) using the following equations [140]:

$$MS_A = \frac{MS_A}{DF_A} \quad (3-20)$$

$$MS_B = \frac{MS_B}{DF_B} \quad (3-21)$$

$$MS_{AB} = \frac{MS_{AB}}{DF_{AB}} \quad (3-22)$$

$$MS_E = \frac{MS_E}{DF_E} \quad (3-23)$$

where  $MS_A$ ,  $MS_B$ ,  $MS_{AB}$ , and  $MS_E$  are the degrees of freedom of variable A, variable B, Interaction between variable A and B, and the error, respectively.

6. The F-value was calculated for each variable and their interaction using the following equations [140]:

$$F_A = \frac{MS_A}{MS_E} \quad (3-24)$$

$$F_B = \frac{MS_B}{MS_E} \quad (3-25)$$

$$F_{AB} = \frac{MS_{AB}}{MS_E} \quad (3-26)$$

where  $F_A$ ,  $F_B$ , and  $F_{AB}$  are the F-value of variable A, variable B, and Interaction between variable A and B, respectively.

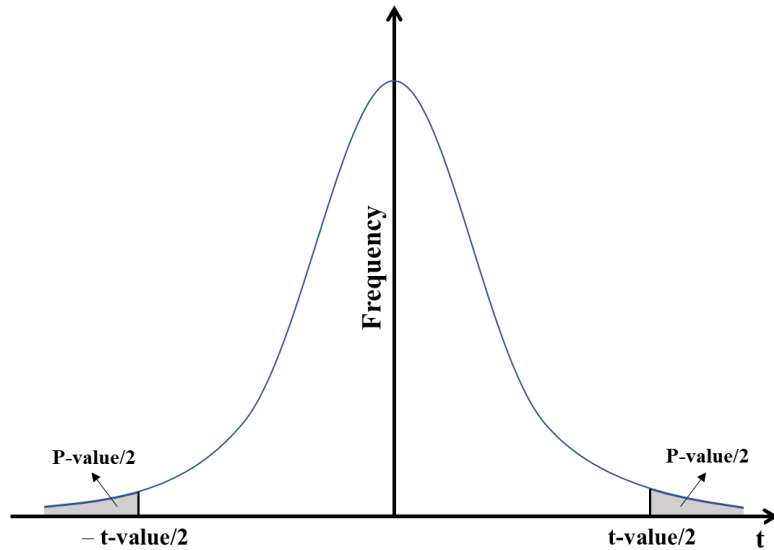


**Figure 3-9.** The t distribution showing the P-value.

7. P-value is defined as the probability of the F distribution to be above the F-value as illustrated in **Figure 3-8** and indicated by the following equation [141]:

$$\text{P-value} = P(F \geq F\text{-value}) \quad (3-27)$$

8. The obtained P-value was compared with significant level (0.05) to access the null hypothesis. If the P-value is smaller than the significant level, the null hypothesis is rejected, meaning that the effect of the variable is significant, and vice versa.

### 3.2.7.2. Post-Hoc test

A mean comparison test was performed to examine the differences between each level in one variable by comparing their mean value. The mean comparison test is performed as a continuation of the Two-way ANOVA test if there is a significant difference in the variable. The mean comparison test used in this thesis is the Fisher Least Significant Difference (LSD) test. The steps for the LSD test are explained below, in which mean comparison between lubricant with additive 1 (A1) and 2 (A2) is taken as an example.

1. The mean different (MD) between each lubricant was calculated using the following equation [140]:

$$MD = \bar{Y}_{A1} - \bar{Y}_{A2} \quad (3-28)$$

2. The standard error of mean different (SEMD) was calculated using the following equation [140]:

$$SEMD = \sqrt{\frac{2MS_E}{nb}} \quad (3-29)$$

3. The t-value was calculated using the following equation [140]:

$$t - value = \frac{MD}{SEMD} \quad (3-30)$$

4. P-value is defined as the probability of the t distribution to be above the t-value as illustrated in **Figure 3-9** and indicated by the following equation [141]:

$$P\text{-value} = P(t \geq t\text{-value}/2, t \leq -t\text{-value}/2) \quad (3-31)$$

5. Similar to Two-way ANOVA, the obtained P-value was compared with significant level (0.05) to access the null hypothesis. If the P-value is smaller than the significant level, the null hypothesis is rejected, meaning that the mean difference between each level is significant (significant number is 1), and vice versa (significant number is 0).

### 3.2.8. Surface topography and cross-section analysis

Surface imaging was performed using scanning electron microscopy (SEM). The principle of SEM is shown in **Figure 3-10**. The SEM components are electron source, anode, electromagnetic lenses, scanning coils, secondary electron (SE) detector, back-scattered electron (BSE) detector, and x-ray detector. The primary electrons generated by the electron gun are accelerated by the anode and focused by the lenses for hitting one point on the sample. Scanning coils are used for directing the primary beam for scanning the sample surface. These primary electrons interact with the atoms in the sample and create secondary electrons, back-scattered electrons, and x-rays collected by the sensors for image or chemical analysis. In this PhD thesis, the wear track morphology was observed using FEI Quanta FEG 650 Scanning Electron Microscopy. The wear track images were taken using the Everhart-Thornley secondary electron detector (ETD) at various magnifications.

The wear track cross-section was studied using FEI Helios Nanolab DualBeam scanning electron microscopy and focused ion beam (SEM-FIB). The cross-section was prepared at the center of the wear track and perpendicular to the sliding direction. A gallium liquid metal ion source was used for preparing the cross-section by deposition, regular cross-section, and cleaning cross-section procedure. The principle of SEM-FIB is illustrated in **Figure 3-11**.



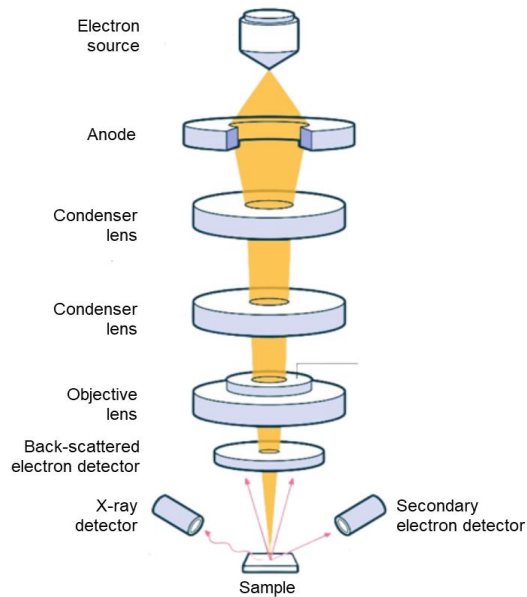


**Figure 3-10.** A working principle of SEM [142].

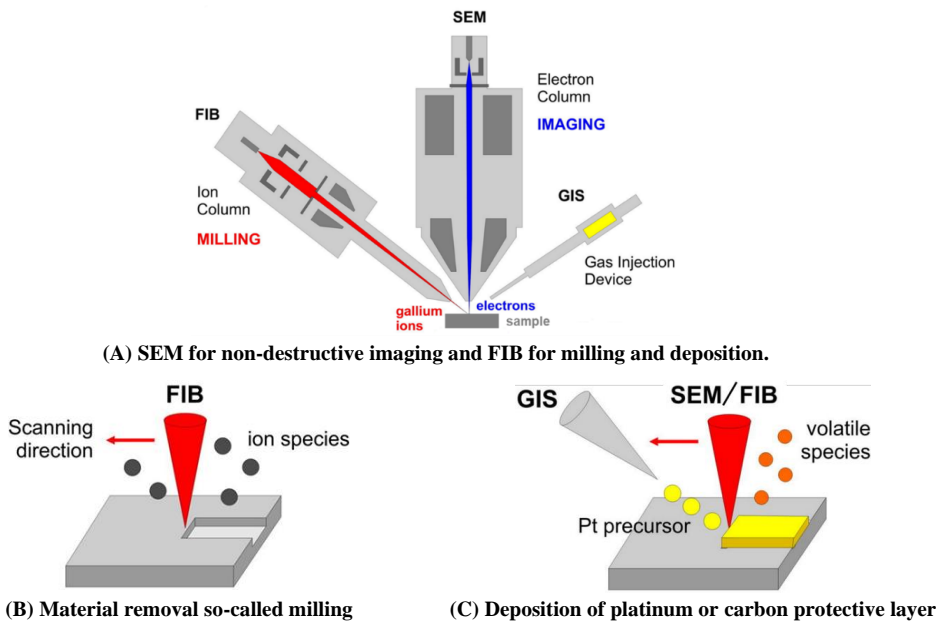


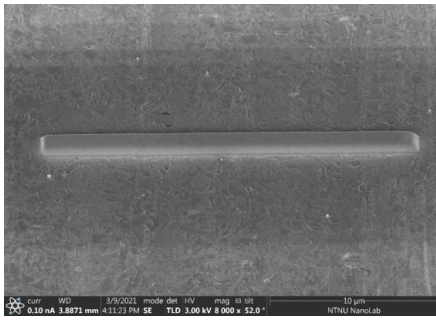
**Figure 3-11.** Imaging is performed by SEM, while milling and deposition are carried out by FIB (A). The high-energy ion beam collides with the surface atoms and causes the atoms to be ejected from the surface (B). Protective layer deposition using either electron or ion beam (C) [143].

To protect the wear track surface from damage, double layers of platinum or carbon were deposited in sequence prior to regular cross-section and cleaning cross-section processes. The first protective layer was deposited using an electron beam with a voltage of 3 kV and a current of 3.2 nA with a dimension of  $25\ \mu\text{m} \times 1.5\ \mu\text{m}$  and thickness of  $0.5\ \mu\text{m}$ . While the second protective layer was deposited using an ion beam with a voltage of 30 kV and a current of 0.26 nA with a dimension of  $25\ \mu\text{m} \times 1.5\ \mu\text{m}$  and thickness of  $3\ \mu\text{m}$ . The regular cross-section was carried out using the ion beam with a voltage of 30 kV and a current of 20 nA with a dimension of  $30\ \mu\text{m} \times 30\ \mu\text{m}$  with the depth of  $36\ \mu\text{m}$  in front of the protective layer and with a dimension of  $30\ \mu\text{m} \times 24\ \mu\text{m}$  with the depth of  $24\ \mu\text{m}$  in behind the protective layer. The cleaning cross-section procedure was done in two steps using the ion beam with a voltage of 30 kV and a current of 9.1 nA and 0.75 nA. The lower current was applied to minimize curtaining artifacts and maximum grain contrast. The secondary electron images of the cross-section were taken using the through lens detector (TLD). The images during first and second layer deposition, regular and cleaning cross-section processes were shown in **Figure 3-12** along with the example cross-section image.

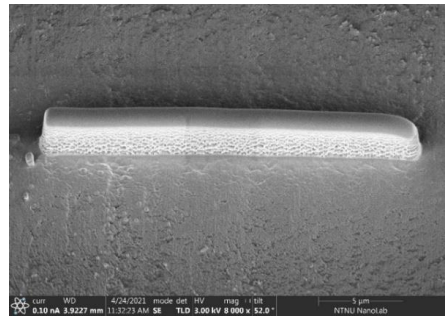
### **3.2.9. Tribo- and oxide film analysis**

#### **3.2.9.1. Scanning-transmission electron microscopy equipped with an x-ray energy dispersive spectroscopy (STEM/EDS)**

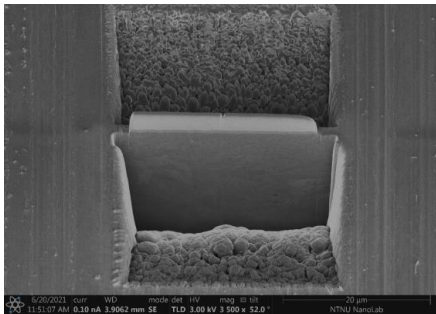
Scanning-transmission electron microscopy (STEM) is a type of transmission electron microscopy (TEM) in which the image is formed by electrons passing through a thin sample. Unlike standard TEM, in STEM, the electron beam is focused to a single point which is then scanned over the sample to make a complete image. The principle of STEM is illustrated in **Figure 3-13**. STEM is equipped with several detectors for imaging, such as secondary electron (SE), back-scattered electron (BSE), annular dark-field (ADF), high-angle annular dark-field (HAADF), and bright-field (BF). As in SEM, the SE detector collects secondary electrons that had been ejected from the sample when the incident electrons hit the sample. BSE detector collects incident electrons that had been scattered back by the strong Coulomb interaction with the atom nucleus. Dark-field detectors, ADF and HAADF, collect the scattered electrons in which HAADF collects larger angle scattered electrons, while ADF collects smaller angle scattered electrons. BF detector collects unscattered incident electrons from a point on the sample.



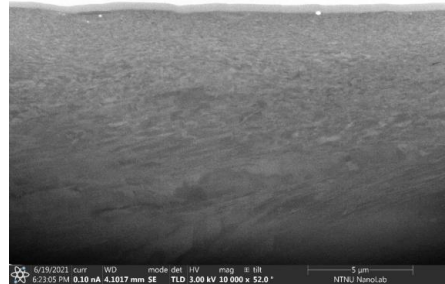
(A) First protective layer deposition by electron beam



(B) Second protective layer deposition by ion beam



(C) Regular and cleaning cross-section by ion beam



(D) Cross-section images taken using TLD detector

**Figure 3-12.** Images were taken during first layer deposition (A), second layer deposition (B), and regular and cleaning cross-section processes (C). Example of the cross-section image taken using TLD detector (D).

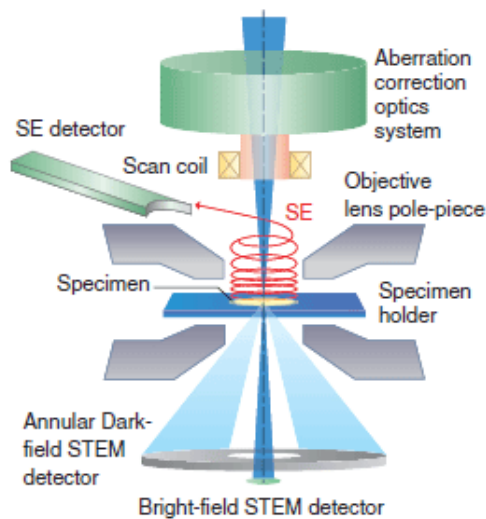


**Figure 3-13.** A working principle of STEM [144].

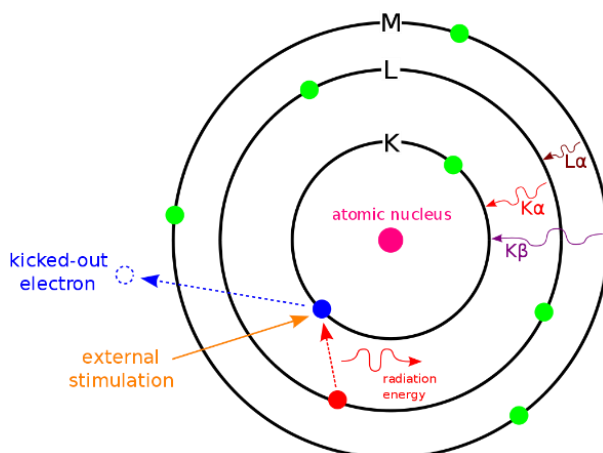
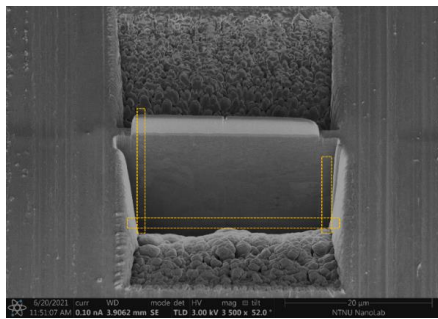


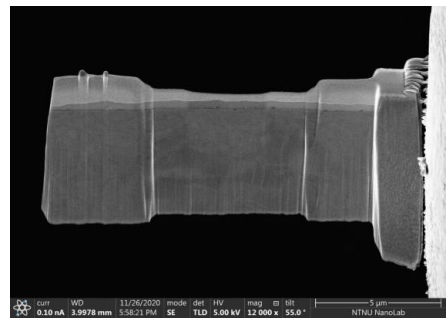
**Figure 3-14.** The principle of EDS [145].

In addition to imaging detectors, STEM can be equipped with an x-ray detector to collect emitted X-ray generated from the sample for chemical analysis. This technique is called energy-dispersive X-ray spectroscopy (EDS). The principle of EDS is illustrated in **Figure 3-14**. External stimulation, which is incident electrons, hits the inner shell electrons and ejects them from the atom. Removing these electrons will leave an empty hole that higher-energy electrons could fill. The transition from M to L or L to K shell is described as  $L_{\alpha}$  and  $K_{\alpha}$ , while a transition from M to K shell is described as  $K_{\beta}$ . Upon the transition from a higher energy state to a lower energy state, the electrons will release radiation energy, X-ray. The emitted energy of the X-ray can be measured by an energy-dispersive spectrometer. Due to the unique X-ray energy for each element on the periodic table, the measured X-ray energy can be used to identify what elements are present in the sample along with their proportion.

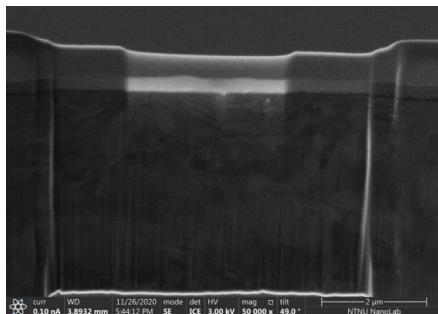
As mentioned before, STEM requires a very thin sample (lamella) to let electrons pass through the sample. Lamellae were U-cut after cross-section FIB imaging (see section 3.2.5) using an ion beam with a voltage of 30 kV and a current of 2.4 nA as shown in **Figure 3-15A**. Lamellae were then lifted and mounted on a TEM grid; subsequently, they were thinned in three steps using a current of 0.75 nA, 90 pA, and 41 pA with a voltage of 30 kV as shown in **Figure 3-15B**. Afterwards, the lamellae were cleaned using an ion beam with a current of 44 pA and a voltage of 2 kV. The resulted thin lamellae were transparent to the electron beam at a voltage of 3 kV and a current of 0.10 nA using an Ion Conversion and Electron (ICE) detector, as shown in **Figure 3-15C**. The volume interaction simulation using Casino software revealed that transparent steel lamellae at electron beam with a voltage of 3 kV and a current of 0.10 nA have a thickness of 40 nm. Here, the STEM lamellae sample preparation was complete.



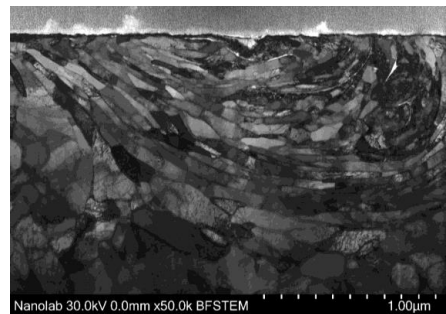
(A) Lamella U-Cut



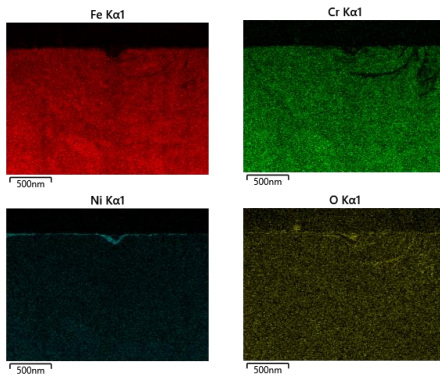
(B) Lamella mounting and thinning



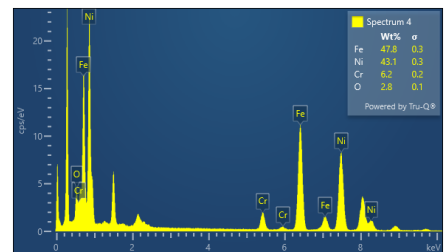
(C) Electron transparent lamella



(D) Cross-section TEM bright field images



(E) EDS elemental mapping



(F) EDS chemical point analysis of the tribofilm

**Figure 3-15.** Images were taken during thin lamella preparation: lamella U-cut (A), lamella mounting and thinning (B), and electron transparent lamella after thinning (C). Example of the cross-section TEM bright-field image (D), EDS elemental mapping of the cross-section (E), and EDS chemical point analysis of the tribofilm (F).

The thin lamellae were examined by the scanning-transmission electron microscope (STEM, Hitachi SU9000) equipped with an X-ray energy dispersive spectroscopy (EDS) detector (Ultim Extreme, Oxford Instruments) to analyze the tribo- or oxide films formed on the wear tracks after tribotests. An example of a STEM bright-field image is shown in **Figure 3-15D**. EDS was applied to obtain elemental mapping of the lamellae and to elemental point analyze the tribo- or oxide film as shown in **Figure 3-15E** and **Figure 3-15F**, respectively.

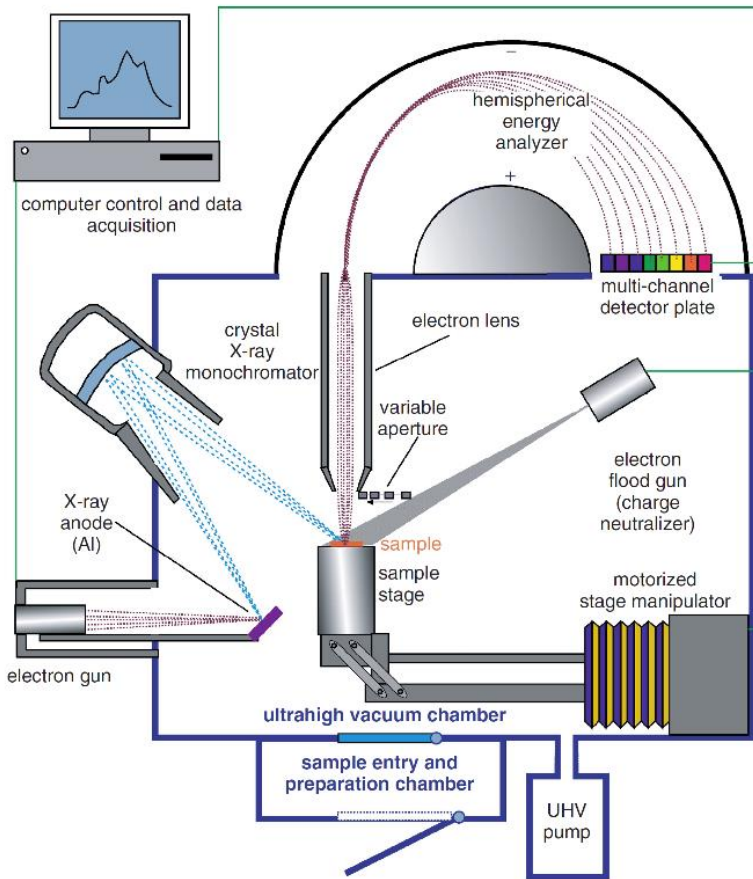


**Figure 3-16.** A schematic diagram of an XPS system using a monochromatized X-ray source [146].

### 3.2.9.2. X-ray photoelectron spectroscopy (XPS)

The principle of the XPS technique is illustrated in **Figure 3-16** [146]. An electron gun accelerates electrons which hit an aluminum (Al) anode that will emit X-rays. The emitted X-rays will be collected by a monochromator that directs the X-rays onto the sample surface. When the photons from the X-rays bombard the surface, some of the electrons will be excited and ejected from the surface. The emitted electrons are photoelectrons, and they only escape from a few nanometer depth from the surface. The kinetic energy of the photoelectrons will be measured, and the number of photoelectrons will be counted by an energy analyzer and a detector. The kinetic energy will be converted into binding energy using the following equation [146]:

$$BE = h \cdot \nu - KE - \Phi \quad (3-32)$$

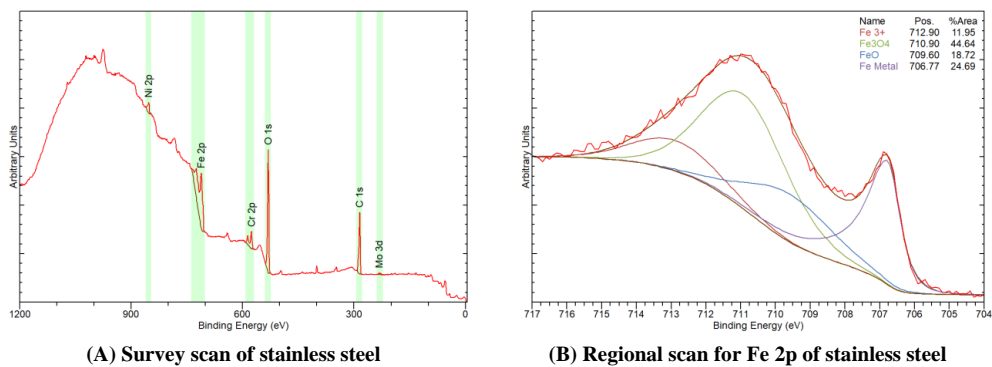


**Figure 3-17.** Survey scan of stainless steel and correspond regional scan for Fe 2p.

where  $BE$  is the binding energy of the photoelectrons,  $h\nu$  is the energy of the X-ray photons,  $KE$  is the kinetic energy of the photoelectrons, and  $\Phi$  is the work function of the spectrometer. The photoelectrons intensity versus binding energy is then plotted in XPS spectral lines. The peaks on the XPS spectral lines plot indicates from which shell the electron is ejected (1s, 2s, 2p, etc.), which provides information of the elemental and chemical state of the elements from the analyzed material [146].

In this PhD thesis, the inside and outside of the wear track were examined by XPS (Kratos Axis Ultra DLD) with monochromatic Al  $K\alpha$  as the X-ray source with 10 kV accelerating voltage and 10 mA current. The sample analysis chamber was set to vacuum with a pressure of  $9 \times 10^{-9}$  Torr during the acquisition. The electrostatic lens and hybrid lens were used for AISI 52100 steel and AISI 316L stainless steel samples, respectively.

Two different acquisitions were performed, i.e., survey scan and regional scan. A survey scan was performed first to collect elemental mapping of the surface by acquiring data over the whole binding energy spectra (from 1200 to 0 eV). A survey scan was performed with a pass energy of 160 eV and a step size of 1 eV. The pass energy is the potential applied in the energy analyzer, and it is related to resolution (the higher the pass energy, the lower the resolution). Using a pass energy of 160 eV, the survey scan has low resolution. An example of a survey scan for stainless steel is shown in **Figure 3-17A**. Afterwards, a regional scan was performed to obtain more detailed information about the chemical composition for selected elements by acquiring over a small range of binding energy spectra around the selected element peak. The regional scan was performed with a pass energy of 20 eV and a step size of 0.1 eV. Using small pass energy, the regional scan has high resolution. The lists of selected elements for the regional scan from higher to lower binding energy were nickel (Ni), iron (Fe), fluorine (F), chromium (Cr), oxygen (O), molybdenum (Mo), carbon (C) and phosphorus (P).

**Table 3-8.** Detailed curve-fitting modeling parameters used for XPS evaluation and quantification

Signal	Binding Energy ( $\pm 0.1$ eV)	FWHM ( $\pm 0.1$ eV)	Line Shape	Component	Reference
Ni 2p	855.9	1.8	GL(30)	Ni(OH) <sub>2</sub>	[147,148]
	853.7	1.8	GL(30)	NiO	
	852.7	0.9	GL(30)	Ni 2p <sub>3/2</sub>	
Fe 2p	714.4	2.9	GL(30)	FeF <sub>3</sub>	[104,149,150]
	712.8	2.9	GL(30)	Fe <sup>3+</sup>	
	712.6	2.9	GL(30)	FePO <sub>4</sub>	
	711.0	2.9	GL(30)	Fe <sub>3</sub> O <sub>4</sub>	
	709.5	2.9	GL(30)	FeO	
	706.8	0.9	LF(0.8,2,20,0)	Fe 2p <sub>3/2</sub>	
F 1s	684.9	1.6	GL(30)	F <sup>-</sup>	[104,151]
Cr 2p	578.7	1.5	GL(30)	CrO <sub>3</sub>	[149,150]
	577.3	1.5	GL(30)	Cr(OH) <sub>3</sub>	
	576.1	1.5	GL(30)	Cr <sub>2</sub> O <sub>3</sub>	
	573.9	1.2	LF(0.8,2,8,0)	Cr 2p <sub>3/2</sub>	
O 1s	533.3	1.8	GL(30)	O-C, O=C	[150,152]
	531.6	1.8	GL(30)	O-H	
	530.5	1.1	GL(30)	O-M	
Mo 3d	235.6	1.3	GL(30)	Mo <sup>6+(ox)</sup> 3d <sub>3/2</sub>	[153]
	232.4	1.3	GL(30)	Mo <sup>6+(ox)</sup> 3d <sub>5/2</sub>	
	234.2	1.6	GL(30)	Mo <sup>4+(hyd)</sup> 3d <sub>3/2</sub>	
	231.0	1.6	GL(30)	Mo <sup>4+(hyd)</sup> 3d <sub>5/2</sub>	
	232.3	0.9	GL(30)	Mo <sup>4+(ox)</sup> 3d <sub>3/2</sub>	
	229.1	0.9	GL(30)	Mo <sup>4+(ox)</sup> 3d <sub>5/2</sub>	
	230.6	0.7	LF(1.1,2.3,2,0)	Mo 3d <sub>3/2</sub>	
	227.6	0.7	LF(1.1,2.3,2,0)	Mo 3d <sub>5/2</sub>	
C 1s	289.3	1.3	GL(30)	O-C=O	[154–156]
	288.2	1.3	GL(30)	C=O	
	286.5	1.3	GL(30)	C-OH, C-O-C	
	285.4	1.0	GL(30)	C-N	
	285.0	1.0	GL(30)	C-C	
P 2p	133.7	1.6	GL(30)	(PO <sub>4</sub> <sup>3-</sup> )	

CasaXPS software was used for the evaluation and quantification of the survey and regional scans. Curve-fitting modeling deconvoluted each major peak obtained from the regional scan into many sub-peaks. Detail curve-fitting modeling parameters for different elements and chemical states are shown in **Table 3-8**. An example of a regional scan for Fe 2p of stainless steel from 717 eV to 704 eV is shown in **Figure 3-17B**, along with the deconvolution of the peaks, which shows the percentage of each component.

As mentioned before, XPS only obtains data from a few nanometers depth from the surface; thus, surface milling by argon ion sputtering is needed for XPS analysis far below the surface. Argon ion sputtering was performed at a pressure of  $4.4 \times 10^{-7}$  Torr, an energy of 4 kV, and a raster size of  $2.5 \times 2.5$  mm. The sputtering rate was calibrated using tantalum oxide (Ta<sub>2</sub>O<sub>5</sub>) of known thickness,



resulting in a 2 nm/min sputtering rate. For the selected samples, the sputtering times were 5, 15, 35, 85, 185, 685, and 1685 seconds. After each sputtering time, the survey and regional scans were performed, and the element composition change versus depth was obtained and plotted. In addition, detailed chemical compositions were obtained from each depth.

*This page is intentionally left blank*

## Chapter 4

# Preliminary studies of ionic liquids as lubricant additives in water-glycol and polyalphaolefin base lubricants

The preliminary studies of six ILs (IM, AM, PP, BMP, PB, and PC) as additives in water-glycol and PAO base lubricants were performed. The ILs were individually added to the water-glycol and PAO base lubricant with a concentration of 1 wt.%. The stability of the mixtures together with the tribological behavior of them were investigated. The solubility and stability of the lubricants were studied by turbidity test. The tribological tests were carried out on AISI 316L stainless steel disk against an alumina ball under boundary lubricating conditions. The rotation of the disk was set to 40 rpm with a track diameter of 10 mm. The tests were performed for 955 cycles giving a sliding distance of 30 m. The tribological performance of the lubricants was analyzed based on friction and specific wear rate. The main purpose of this preliminary study is to select the polar and non-polar base lubricants for the further tribological study of ionic liquids at longer sliding distances.

### 4.1. Mixture solubility and stability study

#### 4.1.1. Mixture solubility and stability of ionic liquids in water-glycol

In this study, four water-glycol mixtures were used as the base lubricants, i.e., WMEG, WDEG, WMPG, and WDPG. The mixture stability of ILs in all base lubricants was examined by turbidity meter, and the results are shown in **Figure 4-1**. All base lubricants indicate a low and stable turbidity numbers during the test. It is worth mentioning that all base lubricants are transparent, colorless, and without phase separation. The turbidity number of long-chain alkyl, i.e., PB and PC, show high turbidity values in several base lubricants, indicating phase separation. Moreover, the mixture of base lubricant and PB or PC has poor stability, as shown by the drop of turbidity numbers during the 2 hours test. In the case of short alkyl chain ILs, i.e., IM, AM, PP, and BMP, the turbidity numbers show low values similar to their base lubricants, indicating no phase separation. In addition, the mixture of base lubricant and short alkyl chain ILs shows high stability during the 2 hours test.

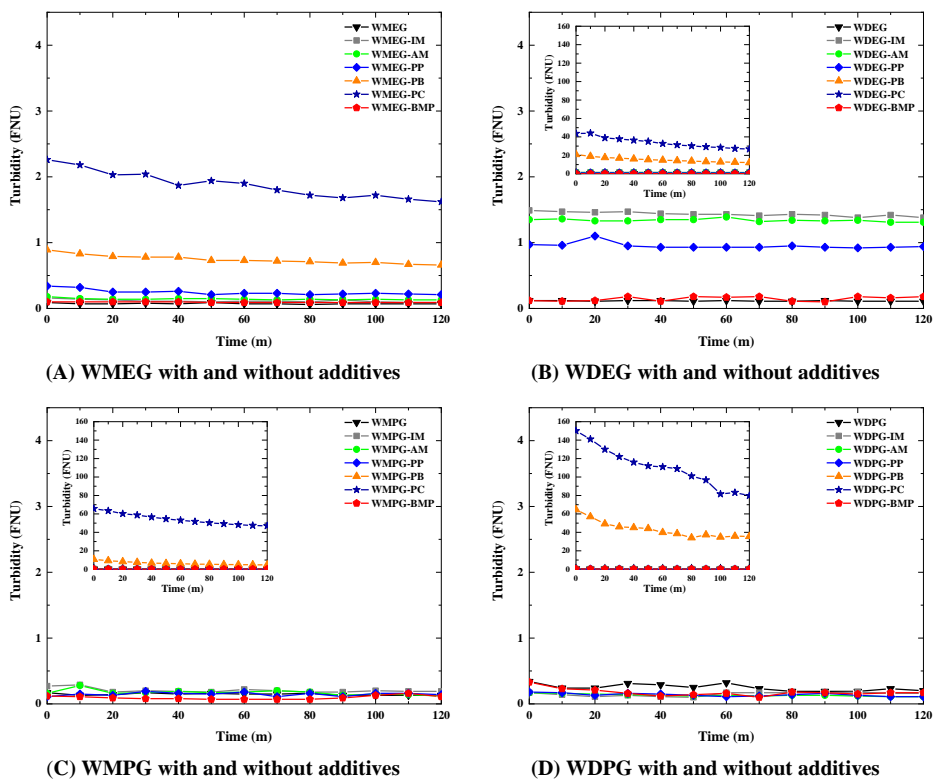


Figure 4-1. The turbidity measurement of ILs in WMEG, WDEG, WMPG, and WDPG base lubricants.

#### 4.1.2. Mixture solubility and stability of ionic liquids in PAO

In this study, two polyalphaolefins were used as the base lubricants, i.e., PAO2 and PAO8. The results of mixture stability of ILs in all base lubricants are shown in **Figure 4-2**. PAO2 and PAO8 base lubricants show low and stable turbidity numbers during the test indicating the lubricants are transparent, colorless, and without phase separation. The turbidity numbers of long alkyl chain PC show higher values in all base lubricants, indicating phase separation, however the mixture of base lubricant and PC has good stability during the 2 hours test. On the other hand, the turbidity of long alkyl chain PB shows a low value in PAO2 and PAO8, indicating no phase separation. In the case of short alkyl chain ILs, i.e., IM, AM, PP, and BMP, the turbidity numbers show low values similar to their base lubricants, indicating no phase separation. In addition, the mixture of base lubricant and short alkyl chain ILs shows high stability during the 2 hours test, except for PP in PAO2.

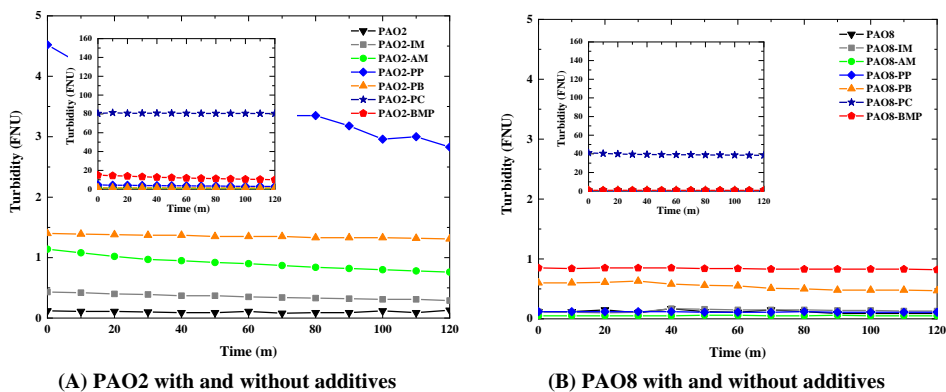


Figure 4-2. The turbidity measurement of ILs in PAO2 and PAO8 base lubricants.

## 4.2. Tribological behavior study

The effectiveness of ILs as lubricant additives were studied both in polar and non-polar media. Based on the turbidity results, long alkyl chain ILs, PB and PC, were discarded from this study due to the high turbidity numbers and the poor stability in the comparative study performed in polar and non-polar media. WMEG, WDEG, WMPG, and WDPG were selected as the base lubricants for polar media, while PAO2 and PAO8 were selected as the base lubricants for non-polar media.

### 4.2.1. Tribological performance of ionic liquids in water-glycol

The friction evolution of the AISI 316L stainless steel sliding against an alumina ball in the presence of all polar lubricants is presented in **Figure 4-3**. The friction evolution of WMEG, WDEG, WMPG, and WDPG base lubricants alone shows high friction at the start of the test, decreasing to a minimum value at 3 meters before it increases again and stabilizes. The addition of 1 wt.% ILs results in different friction behavior depending on the type of IL. From **Figure 4-3**, the influence of ILs in friction can be grouped into two categories.

The first category belongs to IM, AM, and PP, where they have similar high friction evolution during the running-in period. After the running-in period, the friction increases and stabilizes until the end of the test. **Figure 3-2** shows that IM, AM, and PP have the same anion moiety but are different in cations; thus, it seems that the anion controls the friction behavior of these ILs in water-glycol.

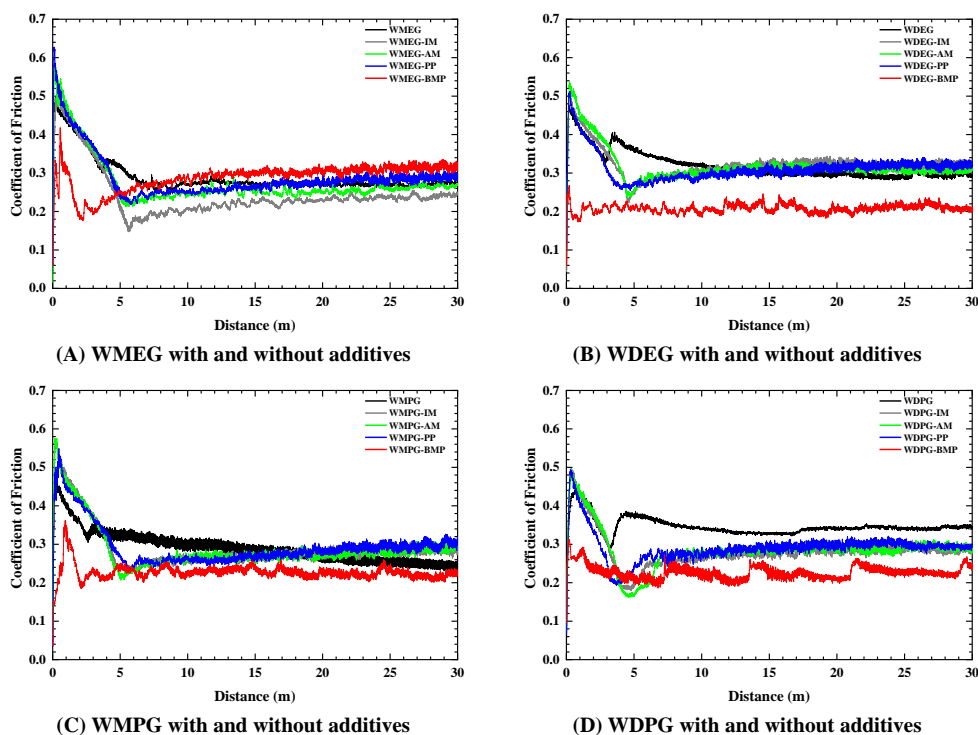


**Figure 4-3.** Friction evolution of AISI 316L stainless steel tested with different ILs in WMEG, WDEG, WMPG, and WDPG base lubricants.

The second category belongs to BMP, where lower friction than IM, AM, and PP during the running-in period is observed. After the running-in period, the friction evolution depends on the base lubricant, i.e., WMEG leads to continuous increase in friction, WDEG and WMPG show fluctuations in friction, and WDPG shows repeated decreases and increases in friction. **Figure 3-2** shows that BMP has different cation and anion moieties compared to IM, AM, and PP.

The influence of ILs on SWR of AISI 316L stainless steel is presented in **Figure 4-4** for all water-glycol lubricants. All short alkyl chain ILs (IM, AM, PP, and BMP) increase AISI 316L stainless steel SWR for all base lubricants.

#### 4.2.2. Tribological performance of ionic liquids in PAO

The friction evolution of the AISI 316L stainless steel sliding against an alumina ball in the presence of all non-polar lubricants is presented in **Figure 4-5**. Different friction evolution was observed for ILs as additives in PAO2 and PAO8. The friction evolution of PAO2 is characterized by a high COF

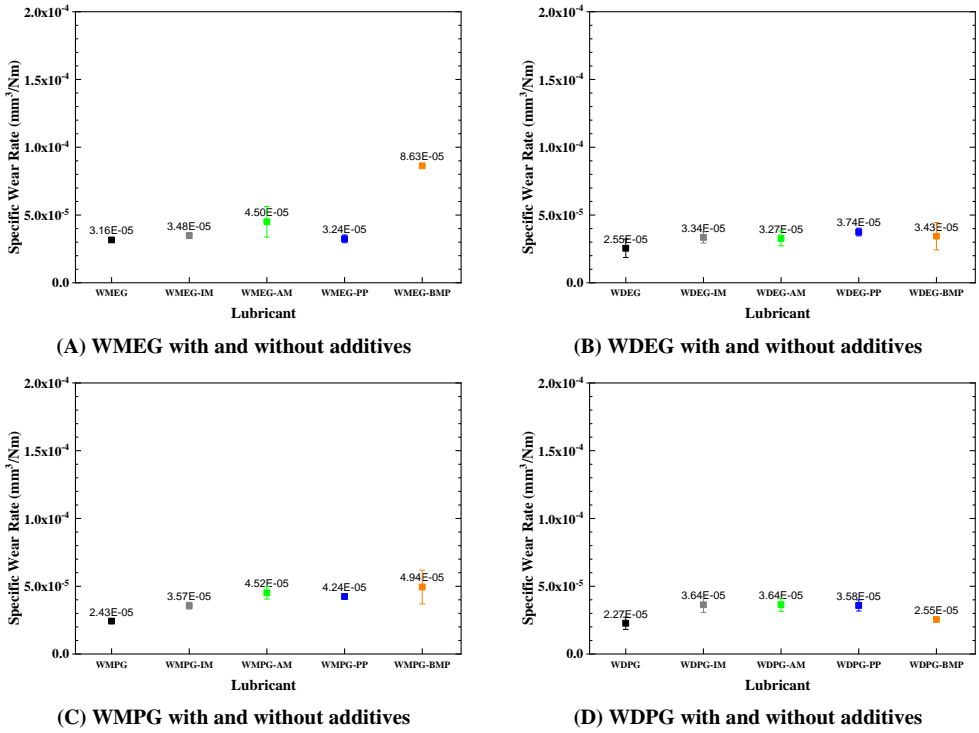
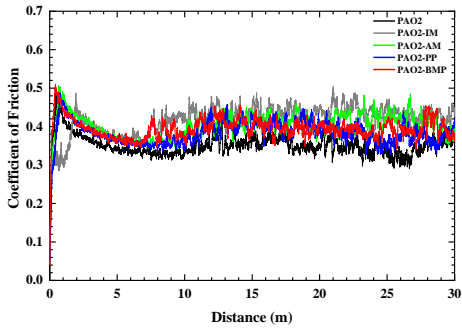


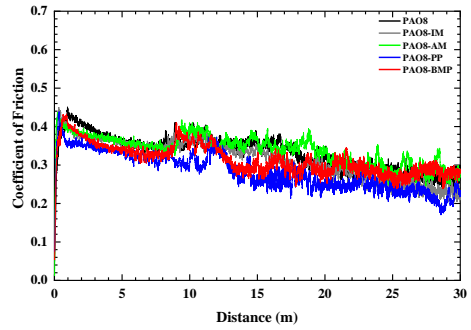
**Figure 4-4.** The specific wear rate (SWR) of AISI 316L stainless steel tested with different ILs in WMEG, WDEG, WMPG, and WDPG base lubricants.

of 0.50 at the beginning of the test and then decreases during the running-in period to 0.34 after 10 sliding meters. Afterwards, the friction fluctuates at around 0.34 for the rest of the test. The addition of 1 wt.% of ILs in the PAO2 base lubricant results in similar friction evolution but with higher value. The friction evolution of PAO8 alone shows a high COF of 0.45 at the beginning of the test and then decreases during the running-in period to 0.36 after 8 meters. After the running-in, the COF increases slightly, then it continuously decreases for the rest of the test. Similar friction evolution is also observed for PAO8 additivated with IM, AM, PP, and BMP, where ILs give slightly lower friction.

**Figure 4-6** shows the influence of ILs on the SWR of AISI 316L stainless steel both in PAO2 and PAO8 base lubricants. The SWR of PAO2 base lubricant alone is  $6.47 \times 10^{-5} \text{ mm}^3/\text{Nm}$ . The addition of individual ILs to the PAO2 base lubricant increases the SWR for all ILs, where BMP gives the highest SWR of  $1.06 \times 10^{-4} \text{ mm}^3/\text{Nm}$ . In the case of PAO8 alone, the SWR is  $6.20 \times 10^{-5} \text{ mm}^3/\text{Nm}$ , which is similar to PAO2 alone. The addition of the individual ILs to PAO8 base lubricant does not significantly change the SWR except for AM, where it increases by ca. 70%.

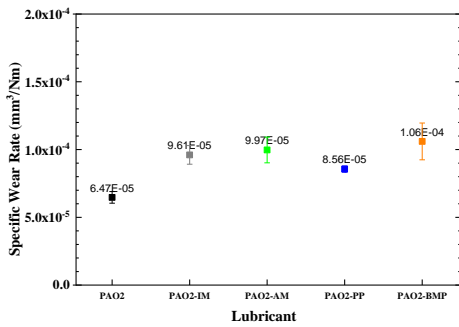


(A) PAO2 with and without additives

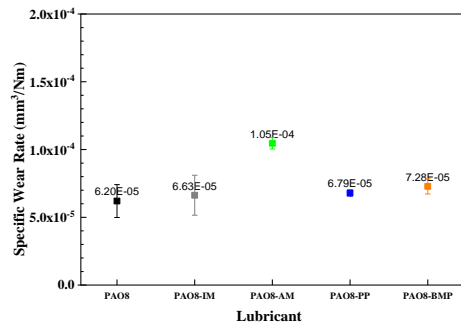


(B) PAO8 with and without additives

Figure 4-5. Friction evolution of AISI 316L stainless steel tested with different ILs in PAO2 and PAO8 base lubricants.



(A) PAO2 with and without additives



(B) PAO8 with and without additives

Figure 4-6. The specific wear rate (SWR) of AISI 316L stainless steel tested with different ILs in PAO2 and PAO8 base lubricants.

### 4.3. Conclusion

This chapter focused on preliminary studies of ILs as lubricant additives in several polar and non-polar base lubricants. These studies included mixture solubility and stability and tribological performance of ILs as lubricant additives. Six ILs with different cation, anion, and alkyl chain length were chosen during this study. The turbidity study shows that long alkyl chain ILs (PB and PC) result in high turbidity numbers and poor stability in several base lubricants thus, they were discarded from the tribological study. All four remaining ILs show wear increase compared to their respective base lubricant in both polar and non-polar base lubricant. In the case of friction, only WDPG-ILs and PAO8-ILs were able to bring lower friction evolution than the base lubricant. Therefore, the subsequent studies focused on the short alkyl chain ILs in WDPG and PAO8 base lubricants.



# Chapter 5

## Influence of ionic liquid concentration on the tribological performance

An investigation of the influence of ILs' concentration on the tribological performance of water-glycol and polyalphaolefin on AISI 316L stainless steel was performed to choose the optimal additive concentration for further tests and analysis. The results obtained in chapter 4 led to the selection of WDPG and PAO8 as base lubricants for further study. For simplicity, they will be called only WG and PAO, respectively. Also, from the results in chapter 4, the selected ILs were IM, AM, PP, and BMP. In this chapter, the optimal concentration of the additives will be established in WG and PAO. In some cases, the choice might not seem straight forward or justified, because a compromise between the two base fluids had to be made. Five different concentrations of ILs were studied 0.25, 0.5, 1, 2, and 4 wt.%. The tribological tests were performed at a disk rotation of 40 rpm with a track diameter of 10 mm. The tests were performed for 9550 cycles, giving a sliding distance of 300 m.

### 5.1. Study of ionic liquid concentration on the tribological performance in WG

**Table 5-1** shows the coefficient of friction (COF) values of AISI 316L stainless steel sliding against alumina ball lubricated by WG with and without ILs at different concentrations, while **Table 5-2** shows the resulting specific wear rate (SWR). Three repetitions are shown in each table (tests 1 to 3) for each condition.

The friction and wear values from **Table 5-1** and **Table 5-2** are analyzed using Two-way ANOVA. Two-way ANOVA is used to analyze the influence of two independent variables (type of lubricant and concentration) on friction and wear. Lubricant variables consist of five levels, i.e., WG, WG-IM, WG-AM, WG-PP, and WG-BMP, whereas the concentration variables consist of six levels, i.e., 0, 0.25, 0.5, 1, 2, and 4 wt.%. Here the COF value for Two-way ANOVA analysis is taken from the average COF from the start until the end of the test, whereas the wear value is taken from the SWR value, which represents the average specific wear rate during the test.

**Table 5-1.** The COF for all WG lubricants and concentrations

Test	WG	WG-0.25IM	WG-0.5IM	WG-1IM	WG-2IM	WG-4IM
1	0.171	0.201	0.229	0.209	0.216	0.206
2	0.175	0.194	0.224	0.213	0.215	0.186
3	0.174	0.195	0.212	0.216	0.200	0.206
Test	WG	WG-0.25AM	WG-0.5AM	WG-1AM	WG-2AM	WG-4AM
1	0.171	0.214	0.200	0.218	0.224	0.217
2	0.175	0.204	0.211	0.217	0.226	0.198
3	0.174	0.195	0.216	0.213	0.212	0.199
Test	WG	WG-0.25PP	WG-0.5PP	WG-1PP	WG-2PP	WG-4PP
1	0.171	0.207	0.221	0.228	0.214	0.196
2	0.175	0.191	0.224	0.228	0.218	0.188
3	0.174	0.214	0.222	0.210	0.213	0.194
Test	WG	WG-0.25BMP	WG-0.5BMP	WG-1BMP	WG-2BMP	WG-4BMP
1	0.171	0.166	0.173	0.173	0.175	0.173
2	0.175	0.174	0.174	0.179	0.163	0.174
3	0.174	0.164	0.168	0.173	0.168	0.173

**Table 5-2.** The SWR for all WG lubricants and concentrations

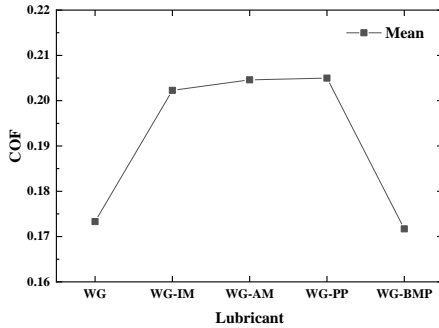
Test	WG	WG-0.25IM	WG-0.5IM	WG-1IM	WG-2IM	WG-4IM
1	9.02E-06	1.01E-05	1.24E-05	1.26E-05	1.25E-05	1.58E-05
2	7.06E-06	9.38E-06	2.06E-05	1.19E-05	1.23E-05	1.37E-05
3	7.40E-06	1.06E-05	1.19E-05	9.49E-06	1.04E-05	1.52E-05
Test	WG	WG-0.25AM	WG-0.5AM	WG-1AM	WG-2AM	WG-4AM
1	9.02E-06	1.02E-05	1.20E-05	1.28E-05	1.15E-05	1.20E-05
2	7.06E-06	8.28E-06	1.14E-05	1.25E-05	1.11E-05	1.18E-05
3	7.40E-06	8.65E-06	1.23E-05	1.25E-05	9.87E-06	1.19E-05
Test	WG	WG-0.25PP	WG-0.5PP	WG-1PP	WG-2PP	WG-4PP
1	9.02E-06	1.05E-05	8.84E-06	1.52E-05	1.41E-05	1.58E-05
2	7.06E-06	8.68E-06	1.45E-05	1.18E-05	1.48E-05	1.51E-05
3	7.40E-06	9.48E-06	1.56E-05	1.07E-05	1.39E-05	1.53E-05
Test	WG	WG-0.25BMP	WG-0.5BMP	WG-1BMP	WG-2BMP	WG-4BMP
1	9.02E-06	8.38E-06	8.28E-06	7.89E-06	7.96E-06	8.52E-06
2	7.06E-06	7.99E-06	8.12E-06	7.07E-06	7.62E-06	8.14E-06
3	7.40E-06	7.56E-06	7.80E-06	7.89E-06	8.35E-06	7.66E-06

### 5.1.1. The Two-way ANOVA analysis for the friction of WG lubricants

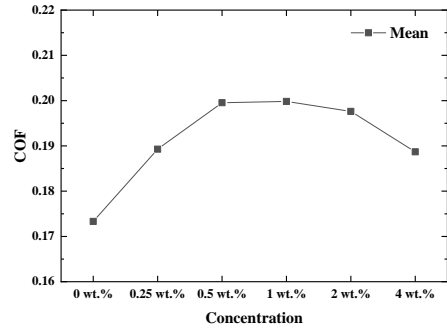
The results of the Two-way ANOVA test for the influence of the type of IL and concentration on friction are shown in **Table 5-3**. The results show that the P-value of the lubricant and concentration is less than 0.05, meaning that both lubricant type and concentration influence friction. In addition,

**Table 5-3.** Overall ANOVA results of friction for all WG lubricants and concentrations

	DF	SS	MS	F-Value	P-value
<b>Lubricant</b>	4	0.02146	5.37E-03	152.5517	1.02E-30
<b>Concentration</b>	5	0.00772	1.54E-03	43.9089	8.28E-19
<b>Interaction</b>	20	0.00635	3.17E-04	9.0259	1.44E-11
<b>Error</b>	60	0.00211	3.52E-05	--	--
<b>Corrected Total</b>	89	0.03764	--	--	--



**(A) Friction as a function of lubricant**



**(B) Friction as a function of concentration**

**Figure 5-1.** The friction of AISI 316L stainless steel influenced by WG lubricants and IL concentrations variables.

the P-value of interaction is less than 0.05, indicating the interaction effect between lubricant and concentration on friction are statistically significant.

The Two-way ANOVA analysis also generates a correlation graph on the friction value of each variable, as shown in **Figure 5-1**. The graph shows that WG gives low friction, and the addition of BMP does not influence the friction of the base lubricant. On the other hand, IM, AM, and PP increase friction. In the case of concentration, it shows that the addition of ILs increases the friction of WG base lubricant at any concentration, in which 0.5, 1, and 2 wt.% give the highest friction, whereas 0.25 and 4 wt.% of IL give lower friction.

A Fisher's LSD test was performed to evaluate the differences between each level in the lubricants and the concentrations in **Figure 5-1**. The result is shown in **Table 5-4** and **Table 5-5** for the mean test on lubricant and concentration, respectively. **Table 5-4** shows that WG-BMP and WG have a significant value of 0, indicating that WG-BMP and WG have similar friction values. The significant value between WG-IM, WG-AM, and WG-PP is also 0, meaning that WG-IM, WG-AM, and WG-PP have similar friction. In the case of concentration, **Table 5-5** shows that 0.5, 1, and 2 wt.% yields equal friction values, and 0.25 and 4 wt.% have similar friction values.

**Table 5-4.** Mean comparisons (LSD test) of friction between WG-IL lubricants

Lubricant	Lubricant	MD	SEMD	t-Value	P-Value	Alpha	Sig.
WG-IM	WG	0.02897	0.00198	14.6526	1.74E-21	0.050	1
WG-AM	WG	0.03128	0.00198	15.8239	4.40E-23	0.050	1
WG-PP	WG	0.03167	0.00198	16.0220	2.40E-23	0.050	1
WG-BMP	WG	-0.00161	0.00198	-0.8168	0.417	0.050	0
WG-AM	WG-IM	0.00232	0.00198	1.1713	0.246	0.050	0
WG-PP	WG-IM	0.00271	0.00198	1.3694	0.176	0.050	0
WG-BMP	WG-IM	-0.03058	0.00198	-15.4694	1.32E-22	0.050	1
WG-PP	WG-AM	0.00039	0.00198	0.1981	0.844	0.050	0
WG-BMP	WG-AM	-0.03290	0.00198	-16.6407	3.72E-24	0.050	1
WG-BMP	WG-PP	-0.03329	0.00198	-16.8388	2.07E-24	0.050	1

**Table 5-5.** Mean comparisons (LSD test) of friction between WG-IL concentrations

Concentration	Concentration	MD	SEMD	t-Value	P-Value	Alpha	Sig.
0.25 wt.%	0 wt.%	0.01596	0.00217	7.3720	5.80E-10	0.050	1
0.5 wt.%	0 wt.%	0.02622	0.00217	12.1067	9.44E-18	0.050	1
1 wt.%	0 wt.%	0.02652	0.00217	12.2449	5.80E-18	0.050	1
2 wt.%	0 wt.%	0.02430	0.00217	11.2209	2.28E-16	0.050	1
4 wt.%	0 wt.%	0.01537	0.00217	7.0974	1.71E-09	0.050	1
0.5 wt.%	0.25 wt.%	0.01025	0.00217	4.7347	1.38E-05	0.050	1
1 wt.%	0.25 wt.%	0.01055	0.00217	4.8729	8.40E-06	0.050	1
2 wt.%	0.25 wt.%	0.00834	0.00217	3.8490	2.90E-04	0.050	1
4 wt.%	0.25 wt.%	-0.00059	0.00217	-0.2745	0.785	0.050	0
1 wt.%	0.5 wt.%	0.00030	0.00217	0.1382	0.891	0.050	0
2 wt.%	0.5 wt.%	-0.00192	0.00217	-0.8858	0.379	0.050	0
4 wt.%	0.5 wt.%	-0.01085	0.00217	-5.0092	5.11E-06	0.050	1
2 wt.%	1 wt.%	-0.00222	0.00217	-1.0240	0.310	0.050	0
4 wt.%	1 wt.%	-0.01115	0.00217	-5.1475	3.08E-06	0.050	1
4 wt.%	2 wt.%	-0.00893	0.00217	-4.1235	1.17E-04	0.050	1

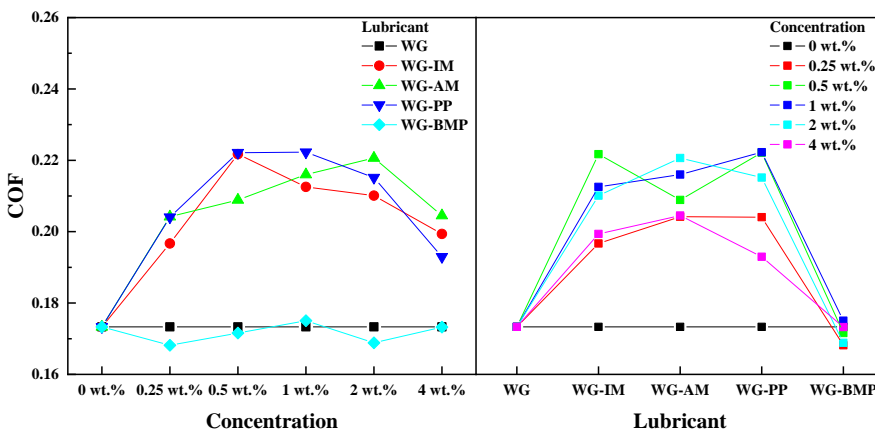
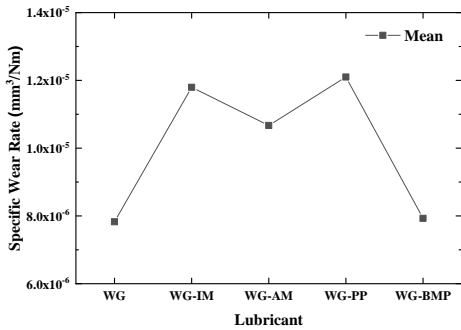


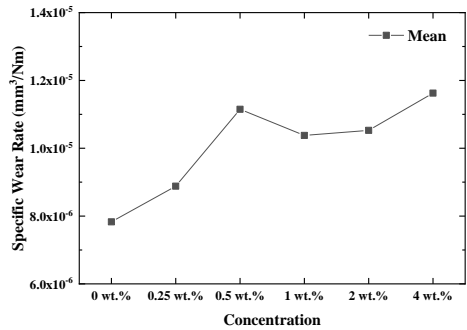
**Figure 5-2.** The Two-way ANOVA result of friction for the interaction between lubricant and concentration.

**Table 5-6.** Overall ANOVA results of wear for all WG lubricants and concentrations

	DF	SS	MS	F-Value	P-value
<b>Lubricant</b>	4	3.07E-10	7.68E-11	36.6442	1.74E-15
<b>Concentration</b>	5	1.55E-10	3.10E-11	14.7758	1.96E-09
<b>Interaction</b>	20	1.39E-10	6.93E-12	3.3067	1.77E-04
<b>Error</b>	60	1.26E-10	2.10E-12	--	--
<b>Corrected Total</b>	89	7.27E-10	--	--	--



**(A) Wear as a function of lubricant**



**(B) Wear as a function of concentration**

**Figure 5-3.** The wear of AISI 316L stainless steel influenced by WG lubricants and IL concentration variables.

As shown in the overall ANOVA results in **Table 5-3**, the interaction effect between lubricant and concentration on friction is statistically significant and it should therefore be considered. The Two-way ANOVA results for interaction between lubricant and concentration is shown in **Figure 5-2**. The results show that WG-BMP has a similar friction value with WG base lubricant at any concentration. On the other hand, IM, AM, and PP increase the friction of WG base lubricant, in which 0.5 wt.% of IM and PP and 2 wt.% of AM yield the highest friction.

### 5.1.2. The Two-way ANOVA analysis for the wear of WG lubricants

The results of the Two-way ANOVA test for the influence of the type of IL and concentration on wear are shown in **Table 5-6**. The results show that the P-value of the lubricant and concentration is less than 0.05, meaning that the lubricant and concentration influence the wear. In addition, the P-value of interaction is less than 0.05, indicating the interaction effect between lubricant and concentration on wear are statistically significant.

The Two-way ANOVA correlation graph between each variable on wear is shown in **Figure 5-3**. The graph shows that WG gives low wear, and the addition of BMP does not influence the wear of

**Table 5-7.** Mean comparisons (LSD test) of wear between WG-IL lubricants

Lubricant	Lubricant	MD	SEMD	t-Value	P-Value	Alpha	Sig.
WG-IM	WG	3.97E-06	4.83E-07	8.2252	2.02E-11	0.050	1
WG-AM	WG	2.84E-06	4.83E-07	5.8910	1.87E-07	0.050	1
WG-PP	WG	4.27E-06	4.83E-07	8.8493	1.77E-12	0.050	1
WG-BMP	WG	1.02E-07	4.83E-07	0.2104	0.834	0.050	0
WG-AM	WG-IM	-1.13E-06	4.83E-07	-2.3342	0.023	0.050	1
WG-PP	WG-IM	3.01E-07	4.83E-07	0.6241	0.535	0.050	0
WG-BMP	WG-IM	-3.87E-06	4.83E-07	-8.0149	4.62E-11	0.050	1
WG-PP	WG-AM	1.43E-06	4.83E-07	2.9584	0.004	0.050	1
WG-BMP	WG-AM	-2.74E-06	4.83E-07	-5.6806	4.17E-07	0.050	1
WG-BMP	WG-PP	-4.17E-06	4.83E-07	-8.6390	4.02E-12	0.050	1

**Table 5-8.** Mean comparisons (LSD test) of wear between WG-IL concentrations

Concentration	Concentration	MD	SEMD	t-Value	P-Value	Alpha	Sig.
0.25 wt.%	0 wt.%	1.05E-06	5.29E-07	1.9947	0.051	0.050	0
0.5 wt.%	0 wt.%	3.32E-06	5.29E-07	6.2804	4.16E-08	0.050	1
1 wt.%	0 wt.%	2.55E-06	5.29E-07	4.8226	1.01E-05	0.050	1
2 wt.%	0 wt.%	2.70E-06	5.29E-07	5.1061	3.58E-06	0.050	1
4 wt.%	0 wt.%	3.80E-06	5.29E-07	7.1842	1.21E-09	0.050	1
0.5 wt.%	0.25 wt.%	2.27E-06	5.29E-07	4.2858	6.70E-05	0.050	1
1 wt.%	0.25 wt.%	1.50E-06	5.29E-07	2.8279	0.006	0.050	1
2 wt.%	0.25 wt.%	1.64E-06	5.29E-07	3.1115	0.003	0.050	1
4 wt.%	0.25 wt.%	2.74E-06	5.29E-07	5.1895	2.63E-06	0.050	1
1 wt.%	0.5 wt.%	-7.71E-07	5.29E-07	-1.4579	0.150	0.050	0
2 wt.%	0.5 wt.%	-6.21E-07	5.29E-07	-1.1743	0.245	0.050	0
4 wt.%	0.5 wt.%	4.78E-07	5.29E-07	0.9037	0.370	0.050	0
2 wt.%	1 wt.%	1.50E-07	5.29E-07	0.2836	0.778	0.050	0
4 wt.%	1 wt.%	1.25E-06	5.29E-07	2.3616	0.021	0.050	1
4 wt.%	2 wt.%	1.10E-06	5.29E-07	2.0780	0.042	0.050	1

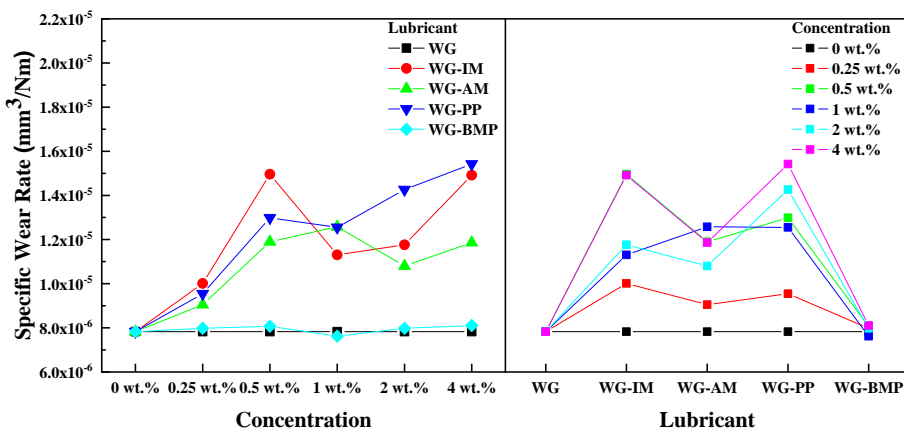


**Figure 5-4.** The Two-way ANOVA result of wear for the interaction between lubricant and concentration.

the base lubricant. On the other hand, IM, AM, and PP increase wear. In the case of concentration, it shows that the addition of ILs increases the wear of WG base lubricants at any concentration, where higher concentration gives higher wear.

A Fisher's LSD test was performed to evaluate the differences between each level in lubricants and concentrations in **Figure 5-3**. The result is shown in **Table 5-7** and **Table 5-8** for the mean test on lubricant and concentration, respectively. **Table 5-7** shows that WG-BMP and WG have a significant value of 0, indicating that WG-BMP and WG have similar wear values. The significant value between WG-IM and WG-PP is also 0, meaning that WG-IM and WG-PP have similar wear. In the case of concentration, **Table 5-8** shows that 0.5, 1, and 2 wt.% yields equal wear value, and 0 and 0.25 wt.% have similar wear values.

As shown in the overall ANOVA results in **Table 5-6**, the interaction between lubricant and concentration is statistically significant and it should therefore be considered. The Two-way ANOVA results for the interaction between lubricant and concentration is shown in **Figure 5-4**. The results show that WG-BMP has a similar wear value with WG base lubricant at any concentration. On the other hand, IM, AM, and PP increase the wear of WG base lubricant, where 0.5 wt.% of IM, 1 wt.% of AM, and 4 wt.% of PP yield the highest wear.

## **5.2. Study of ionic liquid concentration on the tribological performance in PAO**

**Table 5-9** shows the coefficient of friction (COF) values of AISI 316L stainless steel sliding against alumina ball lubricated by PAO with and without ILs at different concentrations. **Table 5-10** shows the resulting wear as specific wear rate (SWR). Three repetitions are shown in each table (tests 1 to 3) for each condition.

Two-way ANOVA was used to analyze the influence of two independent variables (type of lubricant and concentration) on friction and wear. Because the PAO-4AM data cannot be obtained due to its low solubility and symmetrical data is required for the Two-way ANOVA analysis, the Two-way ANOVA analysis is performed without all 4 wt.% data. Therefore, in this analysis, lubricant variables consist of five levels, i.e., WG, WG-IM, WG-AM, WG-PP, and WG-BMP, whereas the concentration variables consist of five levels, i.e., 0, 0.25, 0.5, 1, and 2 wt.%.

**Table 5-9.** The COF for all PAO lubricants and concentrations

Test	PAO	PAO-0.25IM	PAO-0.5IM	PAO-1IM	PAO-2IM	PAO-4IM
1	0.143	0.148	0.139	0.124	0.127	0.150
2	0.146	0.136	0.160	0.125	0.134	0.152
3	0.159	0.188	0.156	0.119	0.125	0.137
Test	PAO	PAO-0.25AM	PAO-0.5AM	PAO-1AM	PAO-2AM	PAO-4AM
1	0.143	0.174	0.139	0.128	0.125	--
2	0.146	0.195	0.134	0.129	0.131	--
3	0.159	0.198	0.123	0.130	0.126	--
Test	PAO	PAO-0.25PP	PAO-0.5PP	PAO-1PP	PAO-2PP	PAO-4PP
1	0.143	0.142	0.116	0.116	0.120	0.082
2	0.146	0.127	0.117	0.114	0.117	0.077
3	0.159	0.130	0.117	0.112	0.102	0.093
Test	PAO	PAO-0.25BMP	PAO-0.5BMP	PAO-1BMP	PAO-2BMP	PAO-4BMP
1	0.143	0.119	0.118	0.113	0.116	0.117
2	0.146	0.110	0.112	0.113	0.115	0.118
3	0.159	0.115	0.108	0.109	0.120	0.113

**Table 5-10.** The SWR for all PAO lubricants and concentrations

Test	PAO	PAO-0.25IM	PAO-0.5IM	PAO-1IM	PAO-2IM	PAO-4IM
1	1.60E-05	2.09E-05	1.77E-05	1.30E-05	1.49E-05	2.28E-05
2	1.68E-05	1.77E-05	2.36E-05	1.99E-05	1.77E-05	2.23E-05
3	1.76E-05	2.21E-05	2.35E-05	1.01E-05	1.46E-05	1.48E-05
Test	PAO	PAO-0.25AM	PAO-0.5AM	PAO-1AM	PAO-2AM	PAO-4AM
1	1.60E-05	2.13E-05	1.93E-05	1.59E-05	1.64E-05	--
2	1.68E-05	1.80E-05	1.68E-05	2.01E-05	1.57E-05	--
3	1.76E-05	3.03E-05	1.31E-05	1.78E-05	1.55E-05	--
Test	PAO	PAO-0.25PP	PAO-0.5PP	PAO-1PP	PAO-2PP	PAO-4PP
1	1.60E-05	1.90E-05	1.07E-05	1.29E-05	1.17E-05	1.02E-05
2	1.68E-05	1.88E-05	1.20E-05	1.31E-05	1.25E-05	9.35E-06
3	1.76E-05	1.39E-05	1.08E-05	9.48E-06	9.66E-06	1.19E-05
Test	PAO	PAO-0.25BMP	PAO-0.5BMP	PAO-1BMP	PAO-2BMP	PAO-4BMP
1	1.60E-05	6.70E-06	3.98E-06	3.61E-06	4.29E-06	3.88E-06
2	1.68E-05	5.67E-06	3.48E-06	3.45E-06	3.67E-06	4.09E-06
3	1.76E-05	8.28E-06	3.52E-06	1.92E-06	4.01E-06	5.66E-06

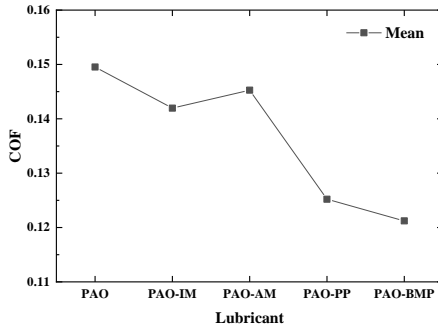
### 5.2.1. The Two-way ANOVA analysis for the friction of PAO lubricants

The results of the Two-way ANOVA test for the influence of IL type and concentration on friction are shown in **Table 5-11**. The results show that the P-value of the lubricant and concentration is less than 0.05, meaning that the type of lubricant and concentration influence friction. In addition,

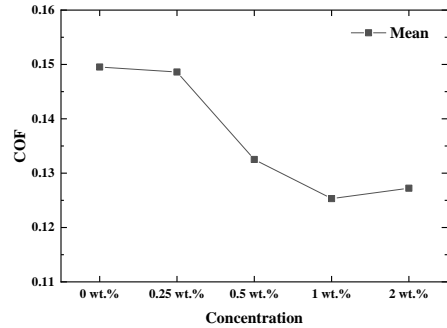


**Table 5-11.** Overall ANOVA results of friction for all PAO lubricants and concentrations

	DF	SS	MS	F-Value	P-value
<b>Lubricant</b>	4	0.00956	2.39E-03	29.2093	1.53E-12
<b>Concentration</b>	4	0.00814	2.04E-03	24.8806	2.25E-11
<b>Interaction</b>	16	0.00880	5.50E-04	6.7242	9.11E-08
<b>Error</b>	50	0.00409	8.18E-05	--	--
<b>Corrected Total</b>	74	0.03060	--	--	--



**(A) Friction as a function of lubricant**



**(B) Friction as a function of concentration**

**Figure 5-5.** The friction of AISI 316L stainless steel influenced by PAO lubricants and IL concentrations variables.

the P-value of interaction is less than 0.05, indicating the interaction effect between lubricant and concentration on friction are statistically significant.

The Two-way ANOVA correlation graph between each variable on the friction value is shown in **Figure 5-5**. The graph shows that PAO has the highest friction, and the addition of ILs decreases the friction. In the case of concentration, it shows that the addition of ILs decreases the friction of PAO base lubricant.

A Fisher's LSD test was performed to evaluate the differences between each level in lubricants and concentrations in **Figure 5-5**. The result is shown in **Table 5-12** and **Table 5-13** for the mean test on lubricant and concentration, respectively. **Table 5-12** shows that PAO-AM yields similar friction as PAO and PAO-IM, and PAO-PP yields similar friction as PAO-BMP. **Table 5-13** shows that 0.25 wt.% has a similar friction value with 0 wt.% (PAO base lubricant). In addition, 2 wt.% gives similar friction as 0.5 wt.% and 1 wt.%.

As shown in the overall ANOVA results in **Table 5-11**, the interaction between lubricant and concentration is statistically significant and should therefore be considered. The Two-way ANOVA results for interaction between lubricant and concentration are shown in **Figure 5-6**. The results show that IM and AM lower the friction of PAO base lubricant at higher concentrations only, while PP and BMP give lower friction at any concentration.

**Table 5-12.** Mean comparisons (LSD test) of friction between PAO-IL lubricants

Lubricant	Lubricant	MD	SEMD	t-Value	P-Value	Alpha	Sig.
PAO-IM	PAO	-0.00756	0.00330	-2.2877	0.026	0.050	1
PAO-AM	PAO	-0.00425	0.00330	-1.2872	0.204	0.050	0
PAO-PP	PAO	-0.02431	0.00330	-7.3606	1.64E-09	0.050	1
PAO-BMP	PAO	-0.02831	0.00330	-8.5697	2.21E-11	0.050	1
PAO-AM	PAO-IM	0.00330	0.00330	1.0005	0.322	0.050	0
PAO-PP	PAO-IM	-0.01676	0.00330	-5.0729	5.78E-06	0.050	1
PAO-BMP	PAO-IM	-0.02075	0.00330	-6.2820	7.96E-08	0.050	1
PAO-PP	PAO-AM	-0.02006	0.00330	-6.0734	1.68E-07	0.050	1
PAO-BMP	PAO-AM	-0.02405	0.00330	-7.2826	2.17E-09	0.050	1
PAO-BMP	PAO-PP	-0.00399	0.00330	-1.2091	0.232	0.050	0

**Table 5-13.** Mean comparisons (LSD test) of friction between PAO-IL concentrations

Concentration	Concentration	MD	SEMD	t-Value	P-Value	Alpha	Sig.
0.25 wt.%	0 wt.%	-0.00092	0.00330	-0.2783	0.782	0.050	0
0.5 wt.%	0 wt.%	-0.01701	0.00330	-5.1484	4.44E-06	0.050	1
1 wt.%	0 wt.%	-0.02420	0.00330	-7.3275	1.85E-09	0.050	1
2 wt.%	0 wt.%	-0.02230	0.00330	-6.7510	1.47E-08	0.050	1
0.5 wt.%	0.25 wt.%	-0.01609	0.00330	-4.8701	1.16E-05	0.050	1
1 wt.%	0.25 wt.%	-0.02328	0.00330	-7.0492	5.03E-09	0.050	1
2 wt.%	0.25 wt.%	-0.02138	0.00330	-6.4727	4.01E-08	0.050	1
1 wt.%	0.5 wt.%	-0.00720	0.00330	-2.1791	0.034	0.050	1
2 wt.%	0.5 wt.%	-0.00529	0.00330	-1.6026	0.115	0.050	0
2 wt.%	1 wt.%	0.00190	0.00330	0.5765	0.567	0.050	0

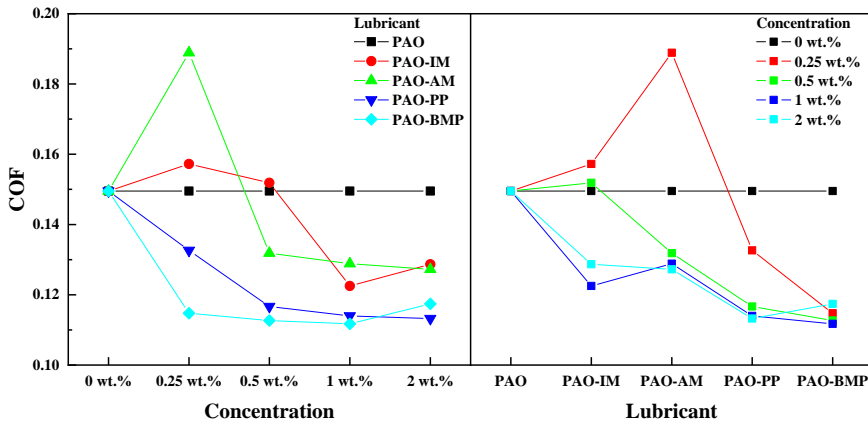


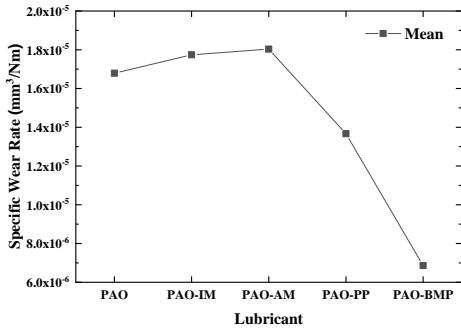
**Figure 5-6.** The Two-way ANOVA result of friction for the interaction between lubricant and concentration.

### 5.2.2. The Two-way ANOVA analysis for the wear of PAO lubricants

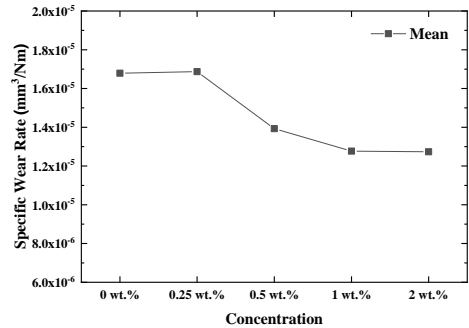
The results of the Two-way ANOVA test for the influence of IL and concentration on wear are shown in **Table 5-14**. The results show that the P-value of the type of lubricant and concentration is less than 0.05, meaning that the type of lubricant and concentration influence the wear. In addition, the P-value

**Table 5-14.** Overall ANOVA results of wear for all PAO lubricants and concentrations

	DF	SS	MS	F-Value	P-value
<b>Lubricant</b>	4	1.31E-09	3.27E-10	66.6327	2.03E-19
<b>Concentration</b>	4	2.58E-10	6.46E-11	13.1675	2.13E-07
<b>Interaction</b>	16	4.71E-10	2.94E-11	5.9993	4.81E-07
<b>Error</b>	50	2.45E-10	4.91E-12	--	--
<b>Corrected Total</b>	74	2.28E-09	--	--	--



(A) Wear as a function of lubricant



(B) Wear as a function of concentration

**Figure 5-7.** The wear of AISI 316L stainless steel influenced by PAO lubricants and IL concentrations variables.

of interaction is less than 0.05, indicating the interaction effect between lubricant and concentration on wear are statistically significant.

The Two-way ANOVA correlation graph between each variable on wear is shown in **Figure 5-7**. The graph shows that IM and AM increase the wear of PAO base lubricant; meanwhile, PP and BMP decrease it. In the case of concentration, it shows that the addition of 0.25 wt.% of IL does not influence the wear of PAO base lubricant. On the other hand, 0.5, 1, and 2 wt.% of IL decrease the wear of PAO base lubricant.

A Fisher's LSD test was performed to evaluate the differences between each level in lubricants and concentrations in **Figure 5-7**. The result is shown in **Table 5-15** and **Table 5-16** for the mean test on lubricant and concentration, respectively. **Table 5-15** shows that PAO, PAO-IM, and PAO-AM yield similar wear. In the case of concentration, **Table 5-16** shows that 0.25 wt.% has a similar friction value with 0 wt.% (PAO base lubricant), and 0.5, 1, and 2 wt.% gives similar wear.

As shown in the overall ANOVA results in **Table 5-14**, the interaction between lubricant and concentration is statistically significant and should therefore be considered. The Two-way ANOVA results for the interaction between lubricant and concentration are shown in **Figure 5-8**. The results

**Table 5-15.** Mean comparisons (LSD test) of wear between PAO-IL lubricants

Lubricant	Lubricant	MD	SEMD	t-Value	P-Value	Alpha	Sig.
PAO-IM	PAO	9.52E-07	8.09E-07	1.1769	0.245	0.050	0
PAO-AM	PAO	1.25E-06	8.09E-07	1.5401	0.130	0.050	0
PAO-PP	PAO	-3.12E-06	8.09E-07	-3.8598	3.26E-04	0.050	1
PAO-BMP	PAO	-9.93E-06	8.09E-07	-12.2720	1.06E-16	0.050	1
PAO-AM	PAO-IM	2.94E-07	8.09E-07	0.3632	0.718	0.050	0
PAO-PP	PAO-IM	-4.07E-06	8.09E-07	-5.0367	6.55E-06	0.050	1
PAO-BMP	PAO-IM	-1.09E-05	8.09E-07	-13.4489	3.10E-18	0.050	1
PAO-PP	PAO-AM	-4.37E-06	8.09E-07	-5.3999	1.84E-06	0.050	1
PAO-BMP	PAO-AM	-1.12E-05	8.09E-07	-13.8121	1.08E-18	0.050	1
PAO-BMP	PAO-PP	-6.80E-06	8.09E-07	-8.4122	3.86E-11	0.050	1

**Table 5-16.** Mean comparisons (LSD test) of wear between PAO-IL concentrations

Concentration	Concentration	MD	SEMD	t-Value	P-Value	Alpha	Sig.
0.25 wt. %	0 wt. %	8.34E-08	8.09E-07	0.1032	0.918	0.050	0
0.5 wt. %	0 wt. %	-2.86E-06	8.09E-07	-3.5387	8.79E-04	0.050	1
1 wt. %	0 wt. %	-4.02E-06	8.09E-07	-4.9674	8.32E-06	0.050	1
2 wt. %	0 wt. %	-4.05E-06	8.09E-07	-5.0118	7.14E-06	0.050	1
0.5 wt. %	0.25 wt. %	-2.95E-06	8.09E-07	-3.6418	6.42E-04	0.050	1
1 wt. %	0.25 wt. %	-4.10E-06	8.09E-07	-5.0705	5.82E-06	0.050	1
2 wt. %	0.25 wt. %	-4.14E-06	8.09E-07	-5.1150	4.99E-06	0.050	1
1 wt. %	0.5 wt. %	-1.16E-06	8.09E-07	-1.4287	0.159	0.050	0
2 wt. %	0.5 wt. %	-1.19E-06	8.09E-07	-1.4731	0.147	0.050	0
2 wt. %	1 wt. %	-3.60E-08	8.09E-07	-0.0445	0.965	0.050	0

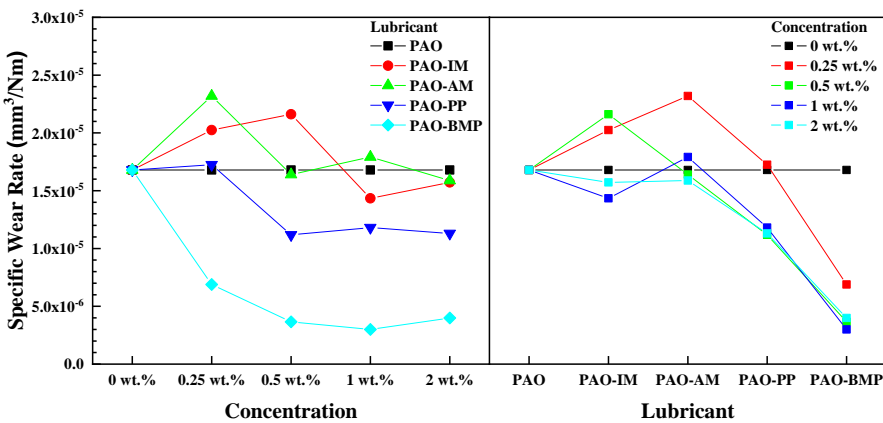


**Figure 5-8.** The Two-way ANOVA result of wear for the interaction between lubricant and concentration.

show that the concentration of IM and AM randomly influences wear. For PP, the concentration of 0.5 wt.% and higher decrease the wear of PAO base lubricant, while BMP gives lower wear than PAO base lubricant at any concentration, where 1 wt.% results in the lowest wear.

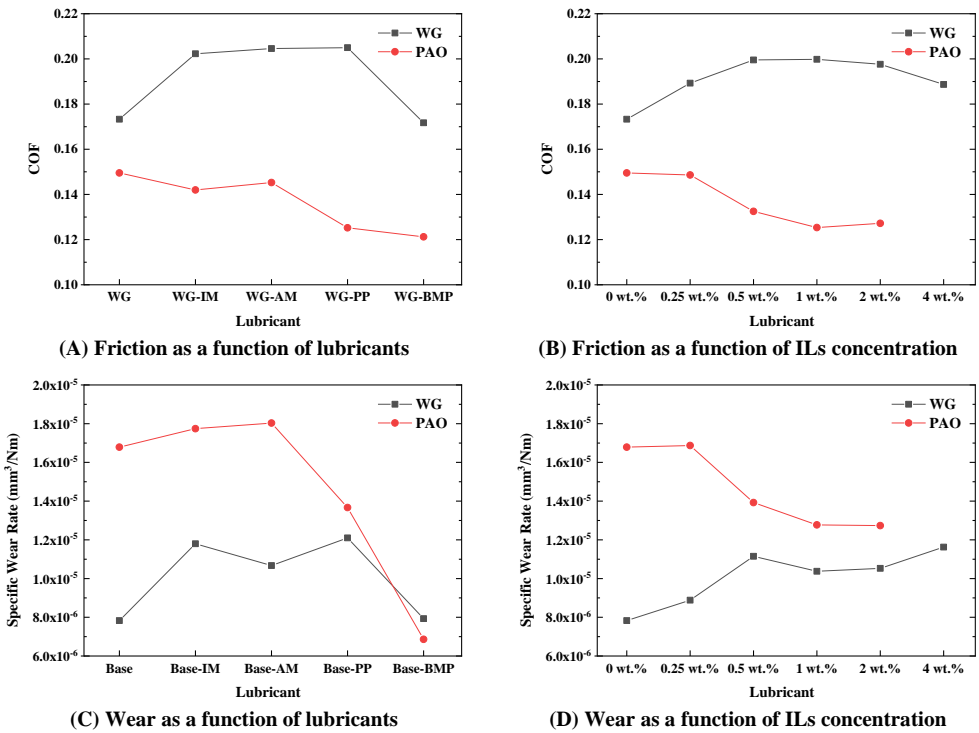


Figure 5-9. Summary of all ANOVA results.

### 5.3. Summary

Figure 5-9 shows a summary all ANOVA results obtained in this study. In WG base lubricant, IM, AM, and PP increase both friction and wear; however, BMP gives similar friction and wear as the WG base lubricant. For the effect of ILs concentration in WG lubricant, it shows that 0.5, 1, and 2 wt.% give the highest friction. Increasing the concentration further to 4 wt.% decreases friction even more. In the case of wear, an increase in concentration leads also to an increase of wear. However, according to interaction result in Figure 5-2 and Figure 5-4, these trends only occur for IM, AM, and PP. for BMP, similar friction and wear is obtained regardless of its concentration.

For PAO base lubricant, IM and AM slightly reduce the friction but slightly increase the wear. On the other hand, PP and BMP give lower friction and wear than the PAO base lubricant, where PP and BMP have similar friction values, but BMP gives much lower wear than PP. In the case of concentration, 0.25 wt.% gives similar friction and wear as PAO base lubricant, while 0.5 wt.% lower the friction and wear. The highest friction and wear reduction are achieved for 1 wt.% and 2 wt.% (both concentrations yield similar friction and wear values).

## 5.4. Conclusion

In this chapter, the influence of ILs and their concentration as lubricant additives in WG and PAO base lubricants on AISI 316L stainless steel was studied based on a statistical analysis of the friction and wear results. In the case of WG, both the type of ILs and their concentration increase the COF and wear of WG base lubricant, except for BMP. In the case of PAO, PP and BMP give lower COF and wear compared to PAO base lubricant. Similar trend is also obtained for 1 wt.% and 2 wt.%, where both concentrations give lower COF and wear compared to PAO base lubricant. These results were used as a basis for selecting the type of ILs and concentration for further studies.

For the selection of the type of ILs, it was obvious that BMP gives the best COF and wear results among all ILs, thus BMP was selected for further study. Due to the fact that IM, AM, and PP give similar COF and wear in WG lubricants, the selection of these ILs was based on their behavior in PAO. From **Figure 5-9**, PP lowers more efficiently the COF and wear of PAO, thus PP was selected for further study. Therefore, PP and BMP were the selected ILs for further study in WG and PAO.

For the concentration selection, a compromise was taken because opposite results were obtained in WG and PAO. An increase in concentration raises the COF and wear for WG lubricants but reduces the COF and wear for PAO lubricants. Since PAO was used as the criteria for choosing the type of IL, 1 wt.% was selected for further study because it was the optimal concentration in PAO.

# Chapter 6

## Adsorption study of ionic liquids additives in polar and non-polar media on iron and stainless steel coated sensors using Quartz Crystal Microbalance technique

(Parts of this chapter are published in paper 3)

Chapter 6 is dedicated to study the adsorption behavior of the additives in polar (WG) and non-polar (PAO) media. The adsorption study is performed using two surfaces, i.e., Fe and SS, which are deposited on quartz crystal sensors. QCM-D is used to perform the adsorption study by measuring the frequency shift and dissipation shift in real time. Based on the results obtained from chapter 5, PP and BMP were selected as additives and were individually mixed with WG and PAO base media with 1 wt.% concentration. The adsorption behavior of ionic liquids will be compared with a well-known organic friction modifier additive, i.e., carboxylic acid (C12). The C12 concentration used in this study is 0.1 wt.% based on a previous study performed in our group [42]. If 1 wt.% was chosen as concentration for C12, micelles will form when added to WG [42]. Therefore, the optimal concentration in WG was chosen for this additive despite the fact that this is lower than the concentration chosen for ILs and that it might not be the optimal one in PAO [42]. Again, a compromise had to be made for choosing the concentration of this additive. **Table 6-1** summarizes the dynamic viscosity, density, electrical conductivity, and pH of all solutions used in this study, as well as the OCP of the AISI 52100 steel and AISI 316L stainless steel in all solutions.

**Table 6-1.** Physical and electrical properties of all lubricants

Lubricants	Dynamic viscosity (mPa.s)	Density (kg/m <sup>3</sup> )	Electrical Conductivity* (μS/cm)	pH	OCP vs. Ag/AgCl (mV)	
					AISI 52100 steel	AISI 316L stainless steel
WG	13.99	1040	2.5	7.3	-537	20
WG-C12	13.53	1041	4.3	4.7	-396	30
WG-PP	13.76	1039	211.2	3.4	-588	70
WG-BMP	14.02	1045	109.3	7.0	-522	0
PAO	81.29	831.8	n.d.	n.d.	n.d.	n.d.
PAO-C12	83.13	840.8	n.d.	n.d.	n.d.	n.d.
PAO-PP	87.27	840.9	n.d.	n.d.	n.d.	n.d.
PAO-BMP	85.23	853.6	n.d.	n.d.	n.d.	n.d.

\* For comparison, the conductivity of tap water is ca 500 μS/cm and for seawater is ca 5000 μS/cm

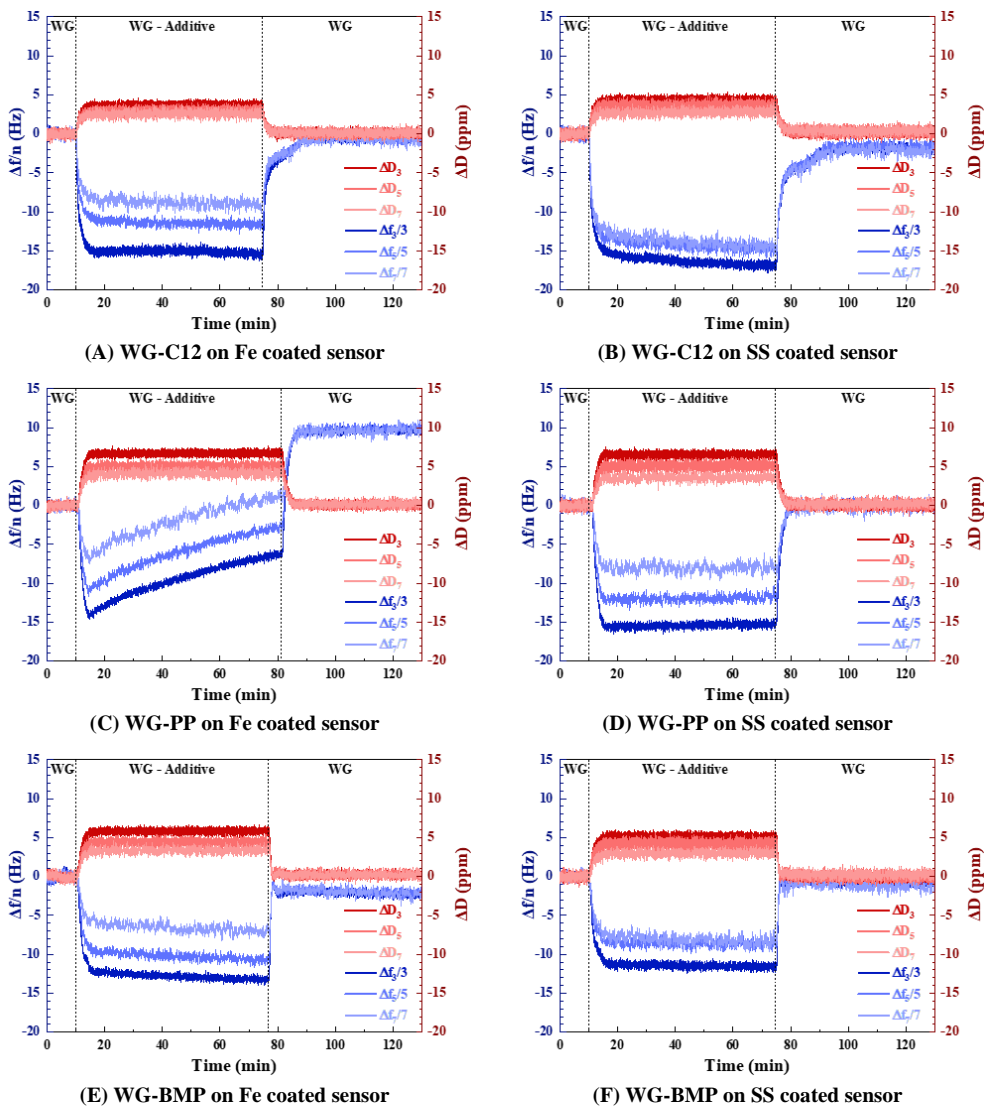


**Figure 6-1.** The frequency and dissipation evolution during QCM testing using Fe and SS coated sensors for additivated WG lubricants at room temperature.

## 6.1. Adsorption study of ionic liquids additives in polar media (WG)

**Figure 6-1** shows the frequency and dissipation evolution obtained from QCM-D for C12, PP, and BMP as additives in WG. Only 3<sup>rd</sup>, 5<sup>th</sup>, and 7<sup>th</sup> overtones are shown in each figure whereas the first overtone is discarded due to high edge effect of the sensor. Three steps were performed during the tests: (1) introduction of WG base for the first 30 minutes (only last 10 minutes are shown in



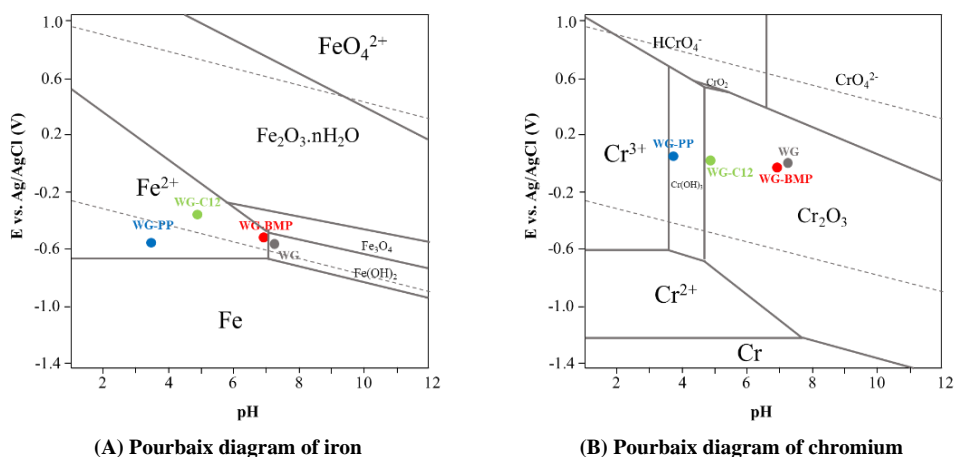
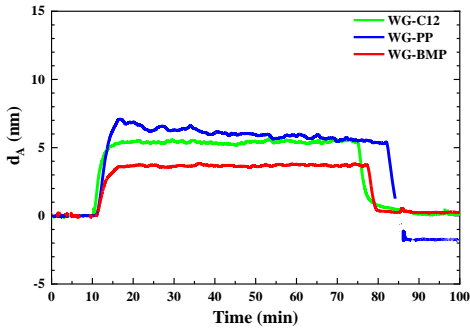


**Figure 6-2.** Pourbaix diagram of iron and chromium at 25 °C [157]. The studied lubricants are located in the diagram based on their measured OCP and pH from **Table 6-1**.

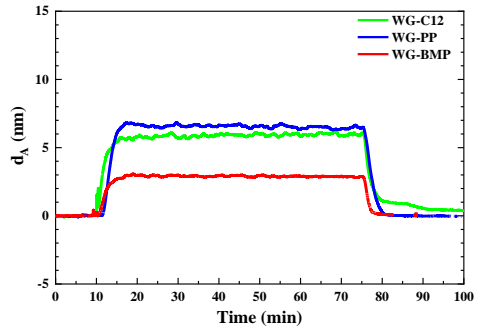
the figure), (2) introduction of additivated WG for the next 1 hour, and (3) rinsing using the same WG base for the last 1 hour.

From **Figure 6-1**, the first 10 minutes are the reference for the frequency and dissipation evolution. For all solutions, there is a frequency drop during the introduction of the additivated solution indicating there is an adsorption of the additive onto the sensor surface. In addition, the dissipation is increasing as the frequency decreases indicating that the adsorbed layer is not fully rigid and has viscoelastic properties. Among all solutions and surface combinations, WG-PP on Fe coated sensor behaves differently from the others, where the frequency continuously increases with time during the introduction of WG-PP on the sensor surface. Moreover, the final frequency during the third step (after rinsing with WG) increases above the zero-reference point, indicating weight loss during the experiment. This weight loss is due to the low pH and high electrical conductivity of WG-PP (**Table 6-1**) that corrodes the Fe coated sensor. No corrosion is observed for WG-PP on the SS coated sensor meaning that the passive film on the stainless steel prevented the corrosion attack. No corrosion is observed for WG-BMP both on Fe and SS coated sensors.

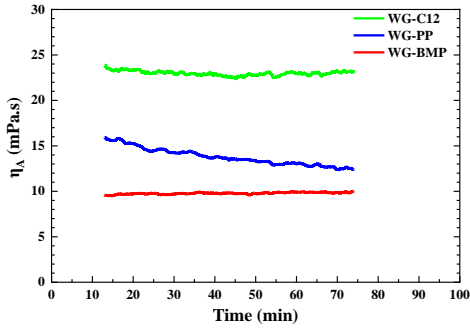
The corrosion behavior of the solutions towards the sensor surface can be explained by the Pourbaix diagram, as shown in **Figure 6-2**. The solutions are plotted in the Pourbaix diagram based on their measured OCP and pH from **Table 6-1**. From the Pourbaix diagram of iron, iron dissolution ( $\text{Fe}^{2+}$ ) is expected to occur for WG-PP and WG-C12, however as shown in the QCM result, only WG-PP causes corrosion on the Fe coated sensor. This could be explained by the higher electrical conductivity of WG-PP compared to WG-C12. In the case of WG and WG-BMP, they are in the border between iron dissolution ( $\text{Fe}^{2+}$ ) and iron oxide ( $\text{Fe}_3\text{O}_4$ ) formation, as a result the iron dissolution is limited.



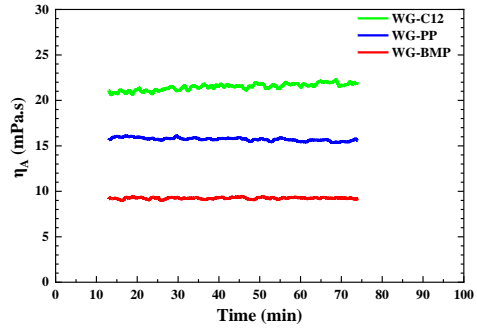
(A) Adsorbed layer thickness on Fe coated sensor



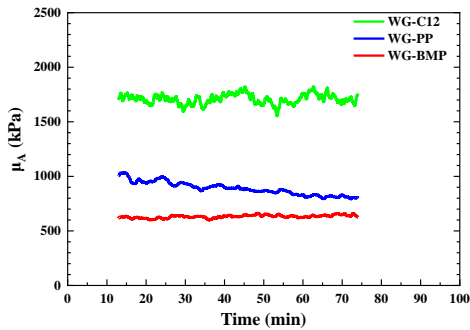
(B) Adsorbed layer thickness on SS coated sensor



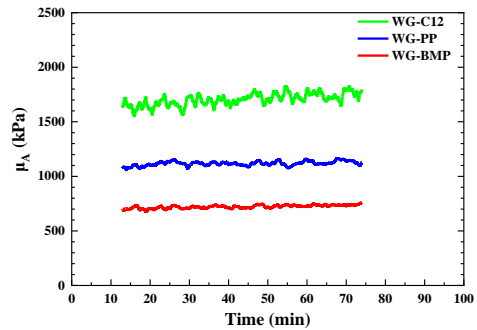
(C) Adsorbed layer viscosity on Fe coated sensor



(D) Adsorbed layer viscosity on SS coated sensor



(E) Adsorbed layer modulus elasticity on Fe coated sensor



(F) Adsorbed layer modulus elasticity on SS coated sensor

**Figure 6-3.** Viscoelastic properties of adsorbed layer on Fe and SS coated sensor derived from modelling.

In the case of the SS coated sensor, the Pourbaix diagram for chromium shows that chromium oxide ( $\text{Cr}_2\text{O}_3$ ) stable phase is expected to be the dominant phase for WG and WG-BMP, whereas chromium hydroxide ( $\text{Cr}(\text{OH})_3$ ) is expected to be the dominant phase for WG-PP. In the case of WG-C12, the system is in the border between chromium oxide and chromium hydroxide. None of the solutions lay in the active dissolution of chromium ( $\text{Cr}^{2+}$  or  $\text{Cr}^{3+}$ ), indicating that no corrosion occurred for SS coated sensor in any lubricant solution.

To analyze the viscoelastic properties of the adsorbed layers, a simulation based on the Voigt model proposed by Voinova et al. is used [133]. The logics and the general mathematic equations used in the modelling is shown in **Figure 3-4**. In this simulation, the density of the adsorbed layer was firstly defined as an input, where it is assumed the same density as in its pure form, as shown in **Table 3-2**. The outputs of this simulation are the thickness, shear viscosity, and shear elasticity modulus as shown in **Figure 6-3**.

**Figure 6-3** shows that PP gives the highest thickness and BMP gives the lowest thickness of adsorbed layer both on Fe and SS coated sensors. Comparing the adsorbed layer on Fe and SS coated sensor, PP and C12 have similar thickness whereas BMP is thicker on Fe coated sensor. In the case of shear viscosity and shear elasticity modulus, C12 gives the highest value followed by PP, and BMP. There is no significant difference between the shear viscosity and shear elasticity modulus values on Fe and SS coated sensor. Shear viscosity and shear elasticity modulus of WG-PP adsorbed layer on Fe coated sensor show a decrease due to the corrosion effect on the sensor.

Due to their ionic nature and high dipole moment, ILs have a higher tendency to be adsorbed on the metal surfaces to form a single- or multi-layer adsorbed films [116]. Based on a calculation from the MarvinSketch software, the length of one molecule of each additive is 1.9, 2.03, and 2.11 nm, for C12, PP, and BMP, respectively. Taking these values into account and comparing them to the thickness obtained from the simulation in **Figure 6-3**, it can be assumed that the additives form multi-layer films, being ca. 3 layers, 4 layers, 2 layers for C12, PP and BMP respectively. The tendency of C12 and PP to form thicker layers could be due to the dissociation of C12 and PP in water (as shown by the pH drop in the solution in **Table 6-1**). Consequently, species with higher polar moment are found for WG-PP and WG-C12 compared to WG-BMP, which in turn results in thicker, more viscous, and more rigid adsorbed layer.

## **6.2. Adsorption study of ionic liquids additives in non-polar media (PAO)**

**Figure 6-4** shows the evolution of frequency and dissipation from QCM-D for C12, PP, and BMP as additives in PAO. Only the frequency and dissipation change of the fundamental frequency (1<sup>st</sup> overtone) could be recorded because the viscosity of the tested lubricants was high enough to dampen the quartz crystal, resulting in a high noise-to-peak ratio at higher overtones. Three steps of experiments were performed during the test, i.e., introduction of PAO alone for the first 30 minutes

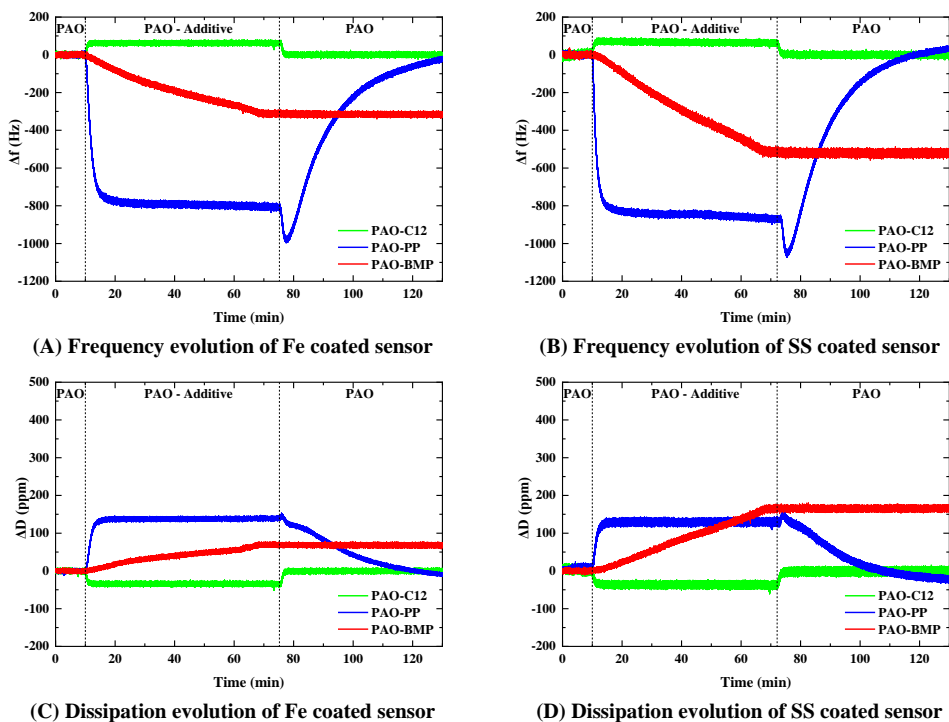


**Figure 6-4.** The frequency and dissipation evolution during QCM-D testing using Fe and SS coated sensors for additivated PAO lubricants at room temperature.

(only last 10 minutes was shown in the figure), introduction of additivated PAO for the next 1 hour, and rinsing using PAO alone for the last 1 hour.

From **Figure 6-4**, by comparing the frequency evolution during the experiment, three phenomena are found: (1) the frequency change rate during the introduction of the additivated solution, (2) the extent of the frequency shift, and (3) whether frequency returns back to zero after rinsing. The frequency change rate or the slope is related to the adsorption kinetics of the additive onto the sensor surface, whereas the extent of the frequency shift is correlated with the amount of initially adsorbed layer. The frequency shift during the rinsing is related to the bonding strength of the adsorbed layer. A strongly adsorbed layer will remain on the surface during rinsing leaving no changes in the frequency, whereas a loosely bonded adsorbed layer will be removed from the surface during rinsing resulting the frequency shift to zero.

Due to the fact that only the first overtone is obtained during these experiments, a quantitative analysis to obtain the viscoelastic properties of the adsorbed layers could not be performed, instead, a qualitative analysis will be performed based on the frequency and dissipation shift. In addition, due to the unexpected frequency shift of C12 towards positive values and the dissipation shift towards

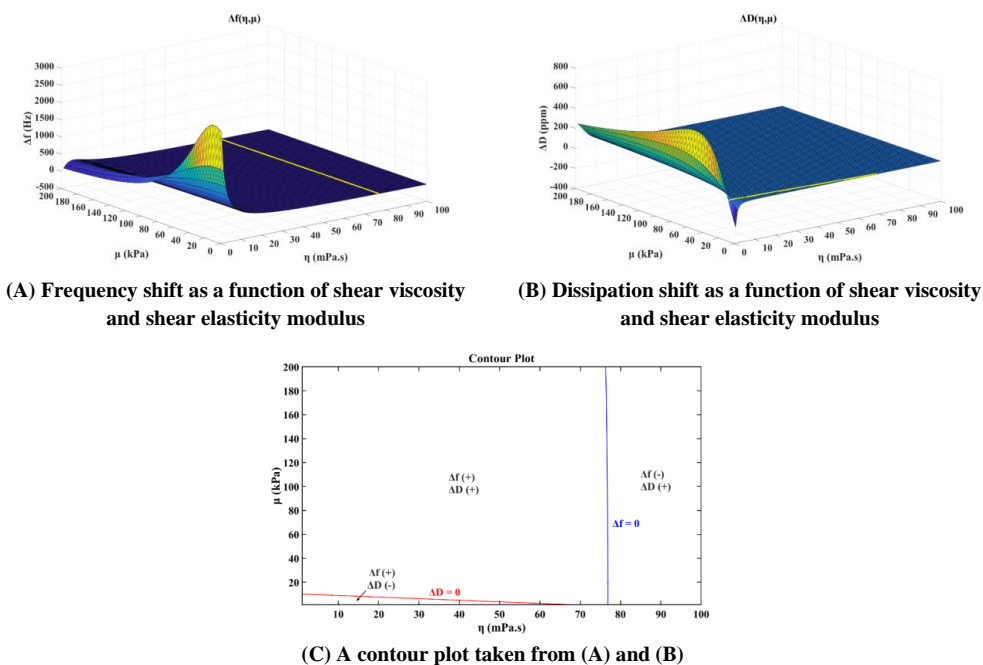


**Figure 6-5.** The numerical simulation of the frequency shift (A) and the dissipation shift responses (B) as a function of the shear elasticity modulus and the shear viscosity coefficient of the thin viscoelastic layer for PAO-C12. A contour plot is taken from (A) and (B), showing the different regions of  $\Delta f$  and  $\Delta D$  value (C).

negative values, the adsorption behavior of C12 will be analyzed separately with the help of numerical simulation. As shown in **Figure 6-4**, PP has a higher slope and frequency shift compared to BMP, indicating PP has faster adsorption kinetics and larger amount of adsorbed material on the sensor surface. However, after rinsing, the frequency and dissipation of PP shifted back to zero indicating the adsorbed layer is completely removed from the surface. In contrast, the frequency and dissipation of BMP is not affected by the rinsing indicating the adsorbed layer of BMP remained on the surface. Comparing the adsorption behavior of PP and BMP on Fe and SS coated sensors it is found that the adsorption behavior of PP is not affected by the surface chemistry whereas BMP shows faster adsorption kinetics. After rinsing the SS coated sensor, there is more initially and strongly adsorbed layer than on the Fe coated sensor.

In order to understand the adsorption behavior of C12 on the Fe and SS coated sensors, a simulation approach has been taken. The illustration of the simulation is similar to **Figure 3-4** except that the input for the shear viscosity and shear elasticity modulus of the adsorbed layer is changed from 0 to 100 and 0 to 200, respectively. The C12 adsorbed layer has a thickness of 10 nm and a density of 880 kg/m<sup>3</sup>. The thickness of 10 nm for the analysis of C12 was selected based on the thickness measured using atomic force microscopy (AFM) [42]. In addition, the sensor is oscillated at a frequency of

5 MHz in PAO-C12 solution with a density of 840.8 kg/m<sup>3</sup> and a shear viscosity of 83.13 mPa.s. The result is a plot of the frequency and dissipation shift as a function of shear viscosity and shear elasticity modulus (**Figure 6-5A** and **Figure 6-5B**). In the plots, the zero-value line (yellow line) is presented and becomes the basis for constructing **Figure 6-5C**.

In order to explain the acoustic response in **Figure 6-5**, the simplified equations are provided by considering one thin viscoelastic layer under bulk liquid and keep only the first-order approximation [133]:

$$\Delta f \approx -\frac{1}{2\pi\rho_Q d_Q} \left\{ \frac{\eta_B}{\delta_B} + d_A \rho_A \omega - 2d_A \left( \frac{\eta_B}{\delta_B} \right)^2 \frac{\eta_A \omega^2}{\mu_A^2 + \eta_A^2 \omega^2} \right\} \quad (6-1)$$

$$\Delta D \approx \frac{1}{2\pi f_0 \rho_Q d_Q} \left\{ \frac{\eta_B}{\delta_B} + 2d_A \left( \frac{\eta_B}{\delta_B} \right)^2 \frac{\mu_A \omega}{\mu_A^2 + \eta_A^2 \omega^2} \right\} \quad (6-2)$$

$$\delta_B = \sqrt{\frac{2\eta_B}{\rho_B \omega}} \quad (6-3)$$

$$\omega = 2\pi f_0 \quad (6-4)$$

where  $\rho_B$  and  $\eta_B$  are the density (kg/m<sup>3</sup>) and viscosity (Pa.s) of bulk liquid, whereas  $d_A$ ,  $\rho_A$ ,  $\mu_A$ , and  $\eta_A$  are the thickness (m), density (kg/m<sup>3</sup>), shear elasticity modulus (Pa), and shear viscosity coefficient (Pa.s) of the adsorbed layer. From Equation 6-1, the resonance frequency shift depends on the bulk liquid term ( $\eta_B$  and  $\delta_B$ ), and the difference between the layer mass contribution ( $d_A$ ,  $\rho_A$ , and  $\omega$ ) and layer viscoelastic contribution ( $\mu_A$  and  $\eta_A$ ). Whereas from Equation 6-2, the resonance dissipation shift depends on the bulk liquid term  $\eta_B/\delta_B$  and layer viscoelastic contribution ( $\mu_A$  and  $\eta_A$ ). Note that Equation 6-1 and Equation 6-2 take the reference from the vacuum, meaning the bulk liquid contribution is relative to the vacuum. In a liquid medium, the contribution of the reference liquid should be included in the equations as follows:

$$\Delta f \approx -\frac{1}{2\pi\rho_Q d_Q} \left\{ \left( \frac{\eta_B}{\delta_B} - \frac{\eta_R}{\delta_R} \right) + d_A \rho_A \omega - 2d_A \left( \frac{\eta_B}{\delta_B} \right)^2 \frac{\eta_A \omega^2}{\mu_A^2 + \eta_A^2 \omega^2} \right\} \quad (6-5)$$

$$\Delta D \approx \frac{1}{2\pi f_0 \rho_Q d_Q} \left\{ \left( \frac{\eta_B}{\delta_B} - \frac{\eta_R}{\delta_R} \right) + 2d_A \left( \frac{\eta_B}{\delta_B} \right)^2 \frac{\mu_A \omega}{\mu_A^2 + \eta_A^2 \omega^2} \right\} \quad (6-6)$$

$$\delta_R = \sqrt{\frac{2\eta_R}{\rho_B \omega}} \quad (6-7)$$

where  $\rho_R$  and  $\eta_R$  are the density (kg/m<sup>3</sup>) and viscosity (Pa.s) of the reference liquid. In the case of similar density and viscosity between reference and bulk liquids, the influence between those two can be canceled:

$$\Delta f \approx -\frac{1}{2\pi\rho_Q d_Q} \left\{ d_A \rho_A \omega - 2d_A \left( \frac{\eta_B}{\delta_B} \right)^2 \frac{\eta_A \omega^2}{\mu_A^2 + \eta_A^2 \omega^2} \right\} \quad (6-8)$$

$$\Delta D \approx \frac{1}{2\pi f_0 \rho_Q d_Q} \left\{ 2d_A \left( \frac{\eta_B}{\delta_B} \right)^2 \frac{\mu_A \omega}{\mu_A^2 + \eta_A^2 \omega^2} \right\} \quad (6-9)$$

It is worth noticing that due to the approximation, the layer mass contribution is neglected in Equation 6-9 thus it seems that  $\Delta D$  will only have positive value. However, from the simulation in **Figure 6-5B** and **Figure 6-5C** (without approximation), there is a region with a negative dissipation value when the layer has low shear elasticity modulus with the shear viscosity lower than the shear viscosity of the bulk. Thus, the different frequency and dissipation shift of C12 is because of the very low shear modulus and shear viscosity of the adsorbed layer created by C12 on the sensor surface.

Looking at the experimental results in **Figure 6-4**, PP and BMP have negative frequency shift and positive dissipation shift, indicating that the layer adsorption mass has more influence than the layer viscoelastic properties, according to Equation 6-8. In addition, the adsorbed layers of PP and BMP must have higher shear viscosity than the bulk liquid in order to shift the frequency negatively and dissipation positively. On the other hand, C12 has a positive frequency shift and a negative dissipation shift, indicating that the layer viscoelastic properties have more influence than the layer adsorption mass, according to Equation 6-8. Moreover, according to the results obtained in **Figure 6-5C**, C12 adsorbed layer must have lower shear viscosity and lower shear elasticity modulus than the bulk.

The adsorption of additives on active surfaces is influenced by the polarity of the additives, the polarity of the base lubricant, the surface chemistry, and the surface electrical charge [47,116,158,159]. In the adsorption study performed with QCM using polar and non-polar media, different adsorption behaviors were found. From the large frequency shift observed in **Figure 6-4**, ILs are expected to form multi-layer structures with PP forming a thicker film than BMP. Comparing the frequency shift between polar and non-polar media (**Figure 6-1** and **Figure 6-4**), ILs in non-polar media are expected to form thicker multi-layer structures than in polar media.

Generally speaking, ILs in non-polar media, such as PAO, exhibit no ionic dissociation, keeping the dipole moment in the molecule. As shown in **Figure 6-4**, the BMP layer strongly adsorbs to the surface after rinsing with PAO, indicating that the adsorption of BMP on the QCM sensor surface is strong enough to overcome the molecular interaction with PAO. The strong adsorption of BMP indicates a chemisorption process, which promotes the formation of a tribofilm. In addition, the presence of high electronegative atoms (fluorine for BMP) promotes strong adsorption to the metallic surface. On the other hand, PP weakly adsorbs to the surface showing that it undergoes

**Table 6-2.** Summary of the adsorbed layer properties on both Fe and SS coated sensors for WG lubricants

Additive	Adsorption Kinetics	Initially adsorbed layer	Strongly Adsorbed layer	Thickness	Shear viscosity	Shear elasticity modulus
SS-PP	Fast	Medium-high	No	Medium-high	Medium	Medium
Fe-PP	Fast	Medium-high	No	Medium-high	Medium	Medium
SS-BMP	Medium	Low	No	Low	Low	Low
Fe-BMP	Medium	Low	No	Low	Low	Low
SS-C12	Fast	Medium	No	Medium	High	High
Fe-C12	Fast	Medium	No	Medium	High	High

**Table 6-3.** Summary of the adsorbed layer properties on both Fe and SS coated sensors for PAO lubricants

Additive	Adsorption Kinetics	Initially adsorbed layer	Strongly Adsorbed layer	Mass layer contribution	Shear viscosity (Compared to bulk liquid)	Shear elasticity modulus
SS-PP	Medium-high	Very high	No	Very high	High	High
Fe-PP	Medium	High	No	High	High	High
SS-BMP	Slow	Medium-high	Yes	Medium-high	High	High
Fe-BMP	Very slow	Medium	Yes	Medium	High	High
SS-C12	Very fast	Very low	No	Very low	Low	Low
Fe-C12	Very fast	Very low	No	Very low	Low	Low

a physisorption process. The anion of PP has a smaller negative charge density than BMP and its smaller size generates a weaker interaction with the metal surface.

In the case of C12, the simulation work (**Figure 6-5**) shows that C12 forms an adsorbed layer with lower shear elasticity modulus and lower density than PAO, due to the replacement of long PAO molecules with shorter C12 molecules on the sensor surface, therefore a less durable adsorbed layer is formed. This effect was the same for iron and stainless steel surfaces.

### 6.3. Summary

**Table 6-2** summarizes the adsorbed layer properties on both Fe and SS coated sensors for WG lubricants. There was no significant difference in the adsorption behavior of the additives on Fe and SS coated sensors except that PP in polar media generates corrosion on the Fe coated sensor surface.

**Table 6-3** summarizes the adsorbed layer properties on both Fe and SS coated sensors for PAO lubricants. For C12, there was no significant difference in the adsorption behavior of the additives on Fe and SS coated sensor. However, for PP and BMP, there are higher adsorption kinetics and initially adsorbed layer on the SS coated sensor than on the Fe coated sensor.



## 6.4. Conclusion

The adsorption behavior of additives was studied by QCM-D in polar and non-polar media using Fe and SS coated sensors. The viscoelastic properties of the adsorbed layers in polar media were analyzed by MATLAB simulations. The results show that PP forms the thickest adsorbed layer with medium shear viscosity and shear elasticity modulus, and BMP forms the thinnest layer with low shear viscosity and shear elasticity modulus. On the other hand, C12 forms a medium thickness adsorbed layer with the highest shear viscosity and shear elasticity modulus. None of the additives created a strongly adsorbed layer with the sensor surface, indicating a competition with the polar molecules of the base lubricant for the surface sites.

Unfortunately, the viscoelastic properties of the adsorbed layer in non-polar media could not be quantified due to the high noise at higher overtones. The qualitative analysis shows that PP forms thicker adsorbed layers than BMP, however both PP and BMP show viscous, and rigid adsorbed layer. In addition, BMP forms strongly adsorbed layers due to the high electronegativity of fluorine, which bonded to the sensor surface overcoming the molecular interaction with the non-polar media. On the other hand, C12 forms the thinnest layer with low shear viscosity and shear elasticity modulus.

Comparing adsorption behavior in polar and non-polar media, the results show that the polarity of the media influences the adsorption behavior of the additives. PP and BMP form thinner multi-layer structure in polar media compared to non-polar media due to the dissociation of the ILs in water and surface adsorption competition between ILs and water, which limits building up thicker layers. In the case of C12, the results show that C12 forms a thicker, more viscous, and more rigid adsorbed layer in polar media compared to non-polar media.

*This page is intentionally left blank*

# Chapter 7

## A tribological study of ionic liquids as boundary additives in a polar base lubricant

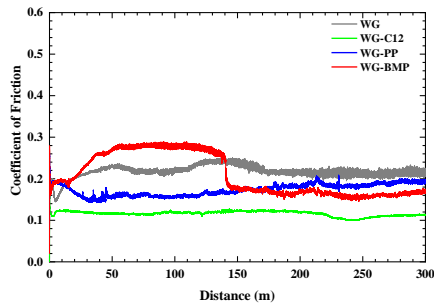
(Parts of this chapter are published in paper 1 and 2)

Chapter 7 is dedicated to study the influence of ILs as lubricant additives in water-glycol on the tribological performance of AISI 52100 bearing steel and AISI 316L stainless steel. In this study, PP and BMP were studied as lubricant additives in WG, and their tribological behavior were compared with a carboxylic acid (dodecanoic acid, C12). The selected concentrations were 1 wt.% and 0.1 wt.% for ILs and C12, respectively, and the reasons behind were explained earlier. In this study, the boundary lubricating conditions were met as explained in section 3. The tests were performed for 9550 cycles which give a sliding distance of 300 m. A detailed surface analysis was performed using a range of advanced analytical tools, such as FIB-SEM, STEM-EDS and XPS.

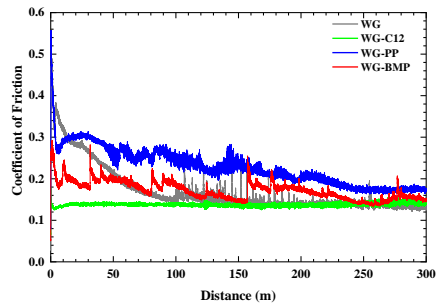
### 7.1. Friction and wear performance in water-glycol

**Figure 7-1** shows the friction evolution of AISI 52100 steel and AISI 316L stainless steel lubricated by WG base lubricant alone and WG additivated with PP, BMP, or C12. For AISI 52100 steel, WG base lubricant alone shows a COF of 0.21 and slightly fluctuates for the rest of the test as shown in **Figure 7-1A**. The addition of 1 wt.% of PP to the base lubricant shows a COF of 0.16 after the running-in period, followed by a steady increment to 0.19 at the end of the test. The friction evolution of WG-BMP shows two distinct regions: (1) high COF of 0.28 after the running-in period for ca. 100 meters of sliding distance and lower COF of 0.18 until the end of the test. The base lubricant additivated with C12 shows a very short running-in period followed by stable friction at 0.12. The resulted wear of AISI 52100 steel is shown in **Figure 7-1C**, in which WG base lubricant alone gives the highest SWR of  $9.98 \times 10^{-6} \text{ mm}^3/\text{Nm}$ , followed by BMP, C12, and PP with SWR of  $9.53 \times 10^{-6}$ ,  $4.45 \times 10^{-6}$ , and  $1.95 \times 10^{-6} \text{ mm}^3/\text{Nm}$ , respectively.

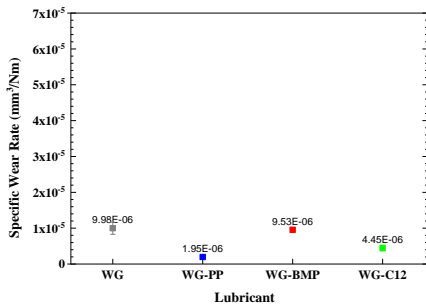
In the case of AISI 316L stainless steel, the friction evolution of WG base lubricant alone is characterized by high friction at the start followed by a continuous decrease reaching steady friction values of 0.14 after ca. 100 m as shown in **Figure 7-1B**. The addition of 1 wt.% of PP to WG affects



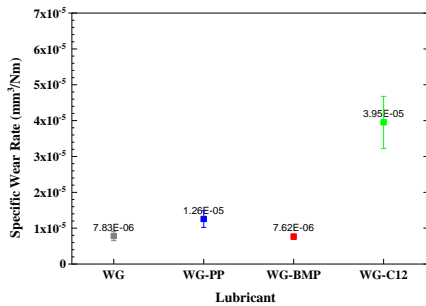
(A) Friction evolution of AISI 52100 steel



(B) Friction evolution of AISI 316L stainless steel



(C) Specific wear rate of AISI 52100 steel



(D) Specific wear rate of AISI 316L stainless steel

**Figure 7-1.** Friction evolution and wear rates of AISI 52100 steel and AISI 316L stainless steel lubricated by WG with and without additives.

the friction evolution of this base lubricant, in which there is a sudden drop at the start of the test (ca. 5 m) and continue decreasing until the end of the test with some abrupt increments in some distances. The friction evolution of WG-BMP has similar behavior as WG-PP except that it occurs at a lower friction values. The addition of 0.1 wt.% of C12 suppresses the running-in period and keeps the friction at 0.14. The resulted wear of AISI 316L stainless steel is shown in **Figure 7-1D**, where the WG base lubricant alone gives a SWR of  $7.83 \times 10^{-6} \text{ mm}^3/\text{Nm}$ , followed by BMP, C12, and PP with SWR of  $7.62 \times 10^{-6}$ ,  $3.95 \times 10^{-5} \text{ mm}^3/\text{Nm}$ , and  $1.26 \times 10^{-5} \text{ mm}^3/\text{Nm}$ , respectively.

**Figure 7-2** shows the SEM images of the wear track surface after the tribological testing. The wear track morphology of AISI 52100 steel lubricated by the WG base lubricant alone shows a smooth surface with little signs of plastic deformation. Completely different wear track morphology is observed for WG-PP sample, where many surface cracks are found, resulting in surface detachment in some areas. The wear track morphology of WG-BMP sample shows a smooth surface with no signs of plastic deformation. In the case of WG-C12 sample, the wear track shows a smooth surface with some surface cracks.

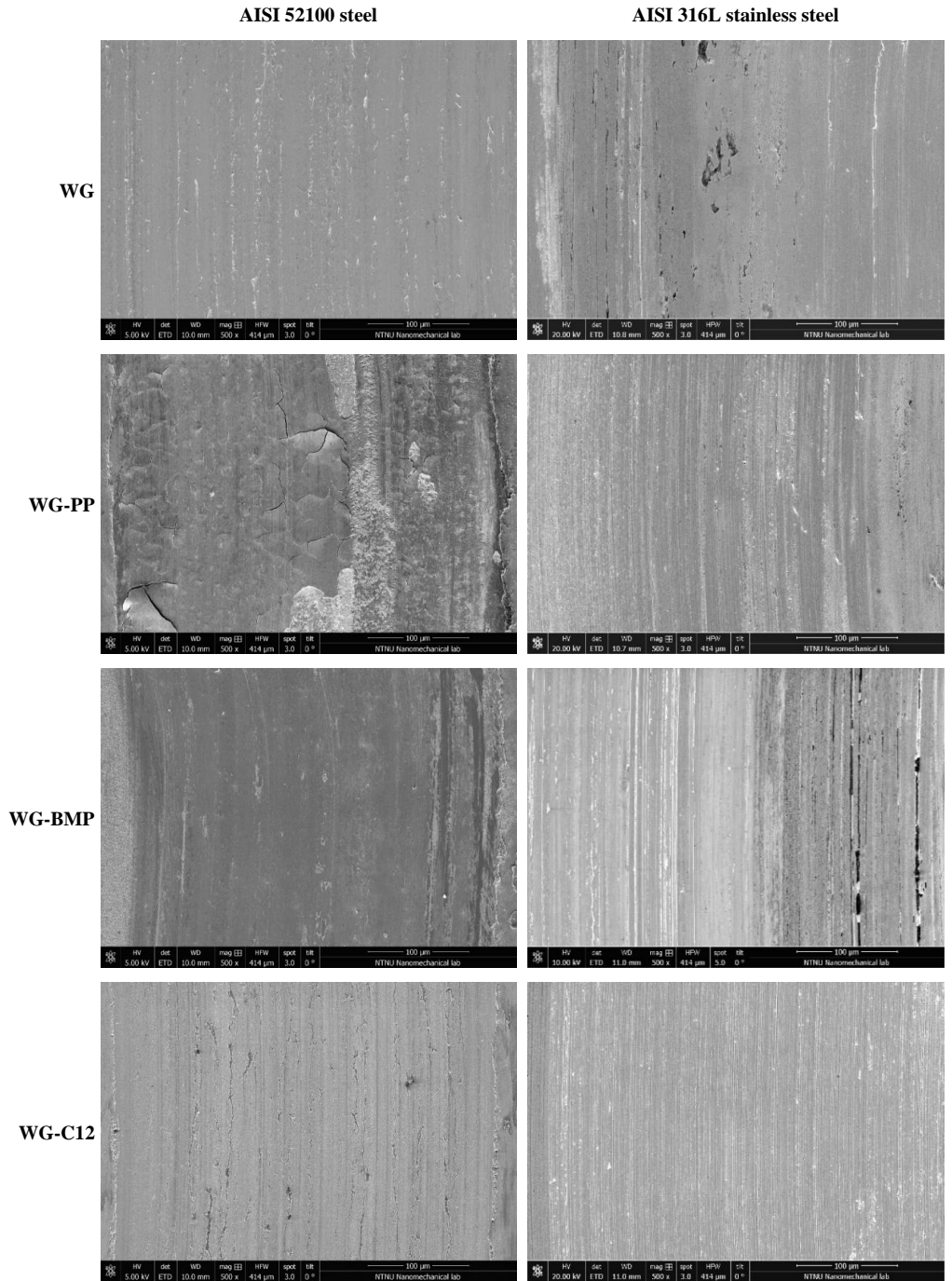
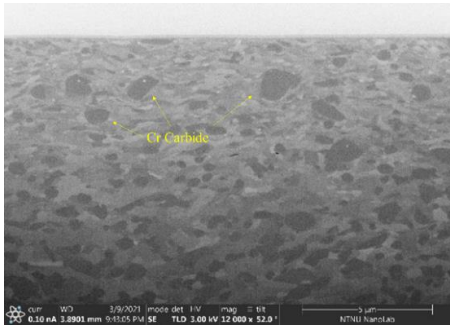


**Figure 7-2.** SEM images of the wear tracks of AISI 52100 steel and AISI 316L stainless steel disks tested in WG with and without additives.

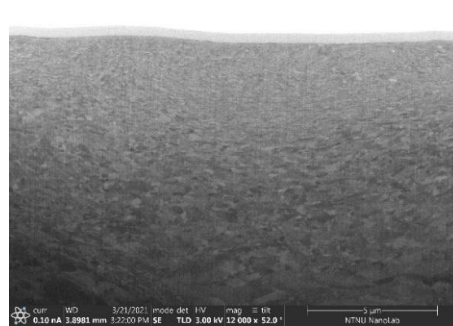
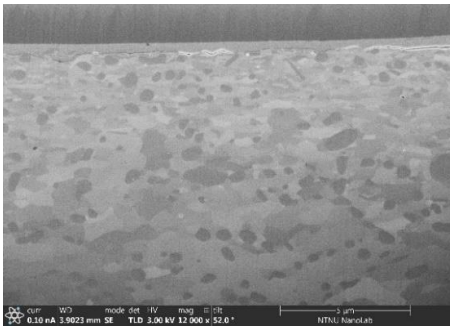
**AISI 52100 steel**

**AISI 316L stainless steel**

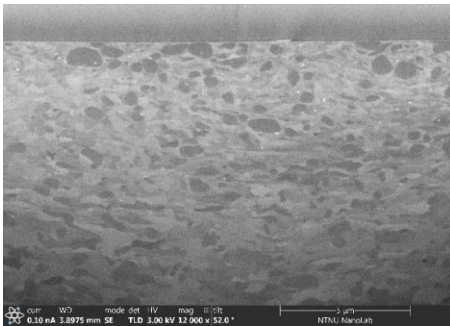
**WG**



**WG-PP**



**WG-BMP**



**WG-C12**

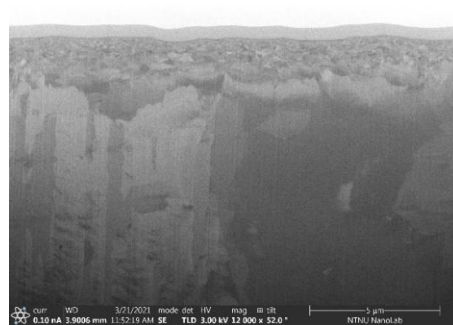
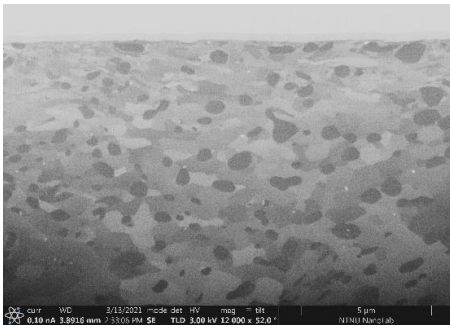


**Figure 7-3.** FIB cross-section images of the wear tracks of AISI 52100 steel and AISI 316L stainless steel disks tested in WG with and without additives.

For AISI 316L stainless steel, the wear track morphology of the WG sample shows a smooth surface with signs of wear and pits in several locations. The wear track surfaces for WG-PP, WG-BMP, and WG-C12 samples show similar wear morphology, where abrasive wear with little signs of plastic deformation is found.

The influence of friction on the subsurface microstructures is shown in **Figure 7-3** on cross-sections prepared with SEM-FIB. The microstructure of AISI 52100 steel consists of chromium carbides (dark round particles) with various degree of deformed grains and plastic deformation in all cases. WG and WG-BMP have similar degree of recrystallization and plastic deformation, whereas WG-PP and WG-C12 show lower degree of recrystallization and plastic deformation, which is in agreement with the friction results.

For AISI 316L stainless steel, a higher degree of recrystallization and plastic deformation is observed compared to AISI 52100 steel due to its lower hardness. WG and WG-BMP have similar degree of recrystallization and plastic deformation, whereas WG-PP shows higher degree of recrystallization and plastic deformation. In the case of WG-C12, a lower degree of recrystallization and plastic deformation is found with thinner subsurface recrystallization area. These results are also in agreement with the friction results.

## **7.2. The effect of additives and surface chemistry on tribofilm formation**

In order to investigate the tribofilms created on the wear tracks, the cross-section of all samples was examined by STEM. Lamellae with a thickness of about 60 nm from each sample were prepared using SEM-FIB. The STEM images and the EDS elemental mapping are presented in **Figure 7-4** and **Figure 7-5** for AISI 52100 steel and AISI 316L stainless steel, respectively. The chosen elements for mapping are iron, chromium, nickel, oxygen, and phosphorous, which are present in the bulk material and the ILs. Oxygen is an indicator of the presence of oxides. Although BMP contains fluorine, this element was not detected by EDS mapping due to the close energy for F K $\alpha$  and Fe L $\alpha$ .

For AISI 52100 steel samples, as shown in **Figure 7-4**, the sample lubricated by WG shows a thin tribofilm on the surface with a thickness of less than 10 nm (measured from higher magnification images). A very thick tribofilm is observed for the WG-PP sample of 400 – 900 nm thickness. In addition, wear debris is observed in the tribofilm, as indicated from the STEM and Fe mapping images. The tribofilm is not fully adhered to the base material, as indicated by a crack at the interface

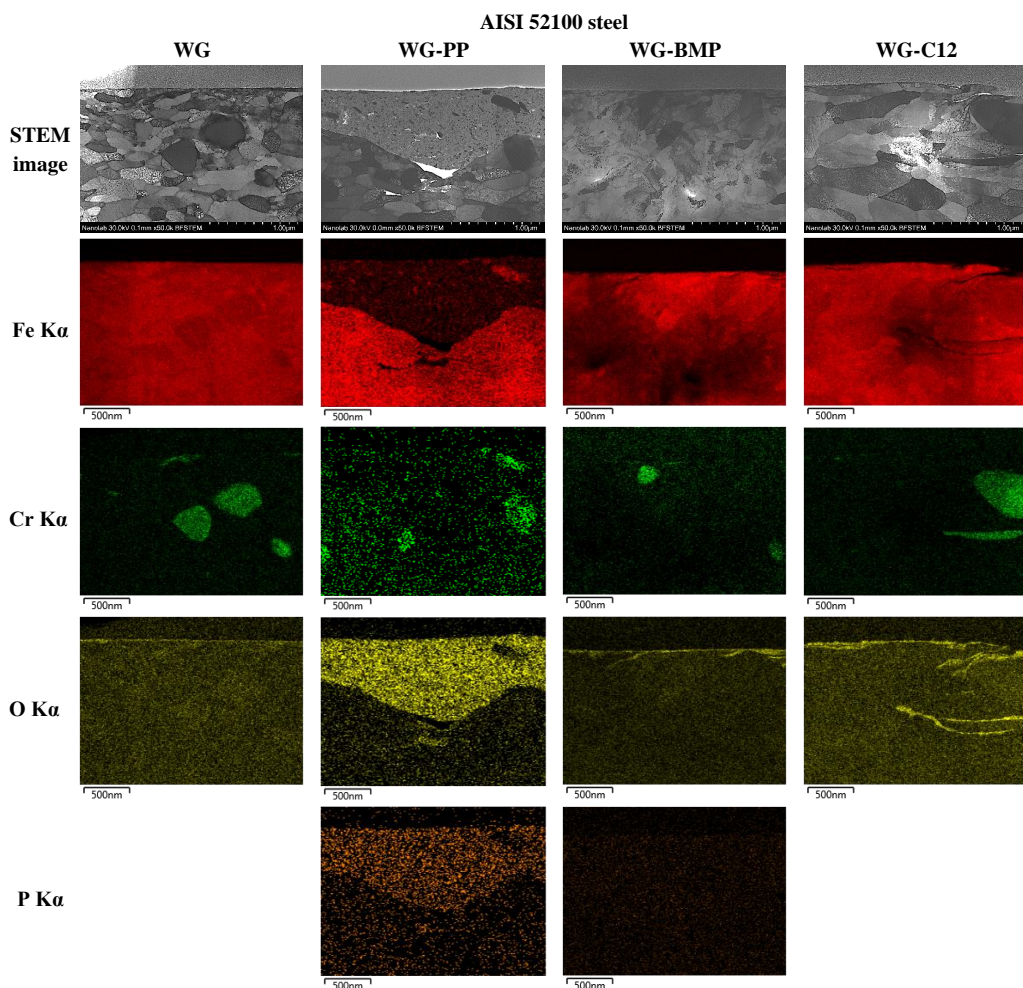


**Figure 7-4.** STEM cross-section images and EDS elemental mapping of the wear tracks on AISI 52100 steel tested in WG with and without additives.

with the base material. For WG-BMP and WG-C12 samples, a thin tribofilm is observed with a thickness of ca. 20 nm. EDS elemental mapping of the cross-sections shows high oxygen levels in the tribofilms of all samples, indicating they consist mainly of oxides. Only an additional element, phosphorous, is detected in the WG-PP sample, indicating that PP is involved in the formation of the tribofilm.

For AISI 316L stainless steel samples, the sample lubricated with WG shows a thick tribofilm on the surface with a thickness of 50 – 100 nm as shown in **Figure 7-5**, being much thicker than the tribofilm formed on AISI 52100 steel lubricated with WG. This indicates the role of the tribosurface chemistry on the tribofilm formation. The STEM image of WG-PP sample shows dissolution of Fe and Cr on



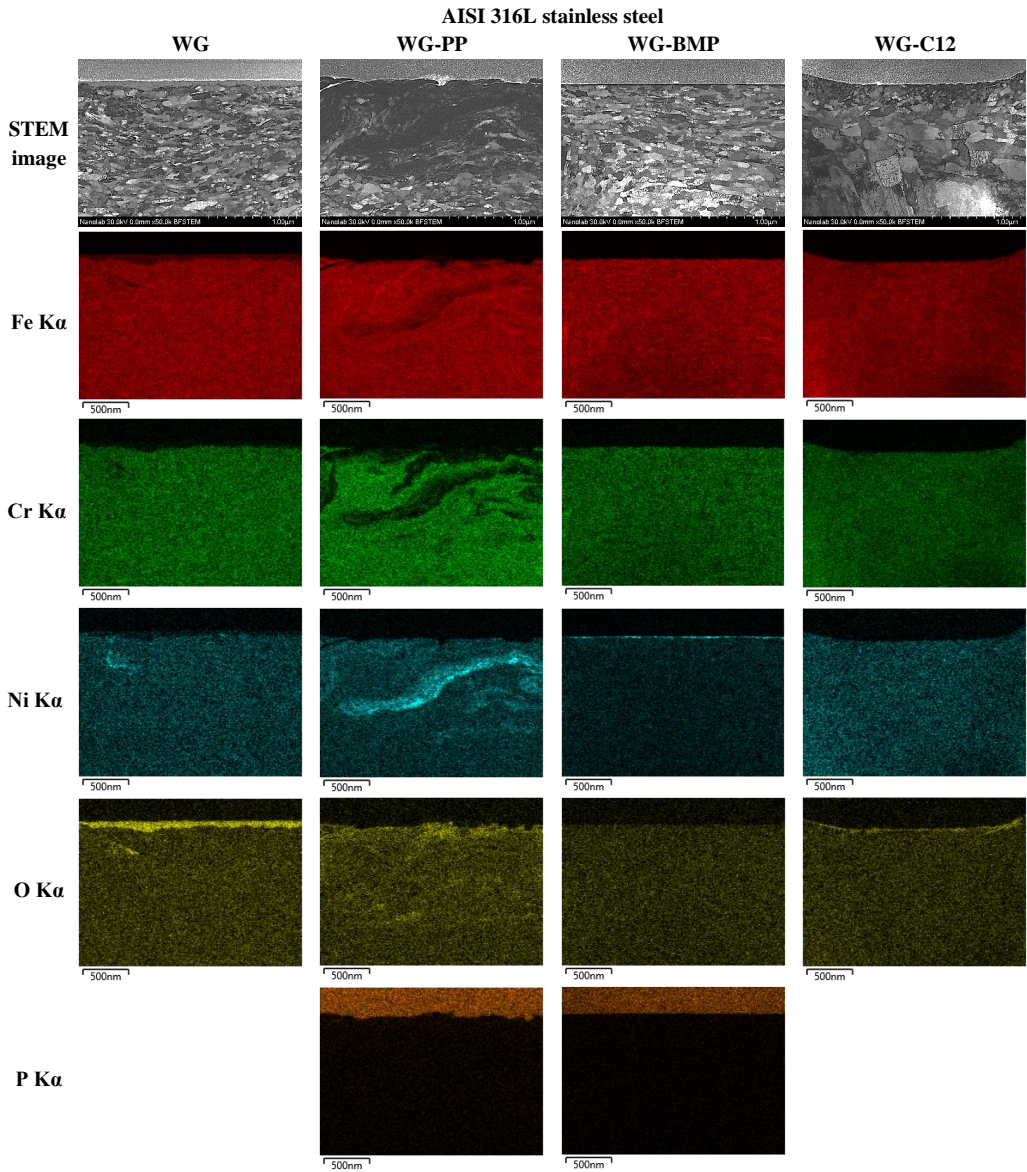


**Figure 7-5.** STEM cross-section images and EDS elemental mapping of the wear tracks on AISI 316L stainless steel tested in WG with and without additives.

the surface. In addition, the tribofilm is only found in some surface areas. The dissolution of Fe and Cr is a result of the corrosion attack due to the low pH of the WG-PP lubricant solution. In the case of WG-BMP sample, the oxide film on the surface is not found as shown in the oxygen elemental mapping. Instead, a thin layer of nickel with a thickness of 20 nm is observed. For WG-C12 sample, a thin tribofilm with a thickness of 20 nm is observed.

**Table 7-1.** EDS chemical composition analysis of the tribofilms tested in WG with and without additives (at.%)

Sample	Lubricant	Tribofilm thickness (nm)	Elemental concentration in tribofilm (at.%)				
			Fe	Cr	Ni	O	P
AISI 52100 steel	WG	< 10	57.81	0	-	42.19	-
	WG-PP	400 – 900	29.46	0	-	64.60	5.94
	WG-BMP	20	49.67	0	-	50.33	0
	WG-C12	20	42.60	0	-	57.40	-
AISI 316L stainless steel	WG	50 – 100	35.56	3.16	3.92	57.36	-
	WG-PP	< 10	31.83	7.40	2.27	52.37	6.13
	WG-BMP	20	33.50	2.88	40.51	23.11	0
	WG-C12	20	42.00	7.04	1.65	49.32	-

**Table 7-2.** Wear track chemical composition after XPS analysis for Fe spectra tested in WG-PP and WG-BMP

Sample	Lubricant	XPS chemical analysis (at.%)					Fe oxides / Fe <sup>0</sup> Ratio
		Fe <sup>0</sup>	FeO	Fe <sub>3</sub> O <sub>4</sub>	FePO <sub>4</sub>	FeF <sub>3</sub>	
AISI 52100 steel	WG-PP	29.67	44.70	18.05	5.50	-	2.11
	WG-BMP	19.31	55.43	20.12	0	0	3.91
AISI 316L stainless steel	WG-PP	40.28	35.73	13.93	4.08	-	1.23
	WG-BMP	25.40	53.91	10.09	0	0.54	2.51

A detailed chemical composition of the tribofilm is taken by means of EDS and the results are shown in **Table 7-1**. In the case of all AISI 52100 steel samples, the tribofilm consists of iron and oxygen, in addition phosphorous is detected for the WG-PP sample, indicating a reaction with the worn surface. On the other hand, no traces of phosphorous are found for WG-BMP sample. Chromium is not detected in the tribofilm because it formed stable chromium carbides. In the case of all AISI 316L samples, the tribofilm consists of iron, chromium, nickel, and oxygen. It is worth noticing that WG-BMP tribofilm consists of large amounts of nickel. Phosphorous is detected for the WG-PP sample, and it is not detected for WG-BMP sample as it happened for the AISI 52100 steel.

In order to examine the chemical composition and chemical bonding state of the elements in the tribofilms, XPS analysis is performed. Moreover, XPS is used to study in detail the presence of phosphorous and fluorine to overcome the drawbacks of the EDS analysis. The detailed analysis of the XPS results is shown in **Figure 7-6** for both AISI 52100 steel and AISI 316L stainless steel. WG-PP produces a tribofilm consisting of metal oxides and hydroxides. In addition, phosphorous is found both in AISI 52100 steel and AISI 316L stainless steel samples, indicating that PP reacts with the worn surfaces. In the case of WG-BMP, XPS shows that the tribofilm consists of metal oxides and hydroxides for both AISI 52100 steel and AISI 316L stainless steel. However, fluorine it is only found in AISI 316L stainless steel sample, indicating that BMP only reacts with AISI 316L stainless steel but not with AISI 52100 steel. Further XPS analyses found that P created iron phosphate (FePO<sub>4</sub>), whereas F formed iron fluoride (FeF<sub>3</sub>).

**AISI 52100 steel**

**AISI 316L stainless steel**

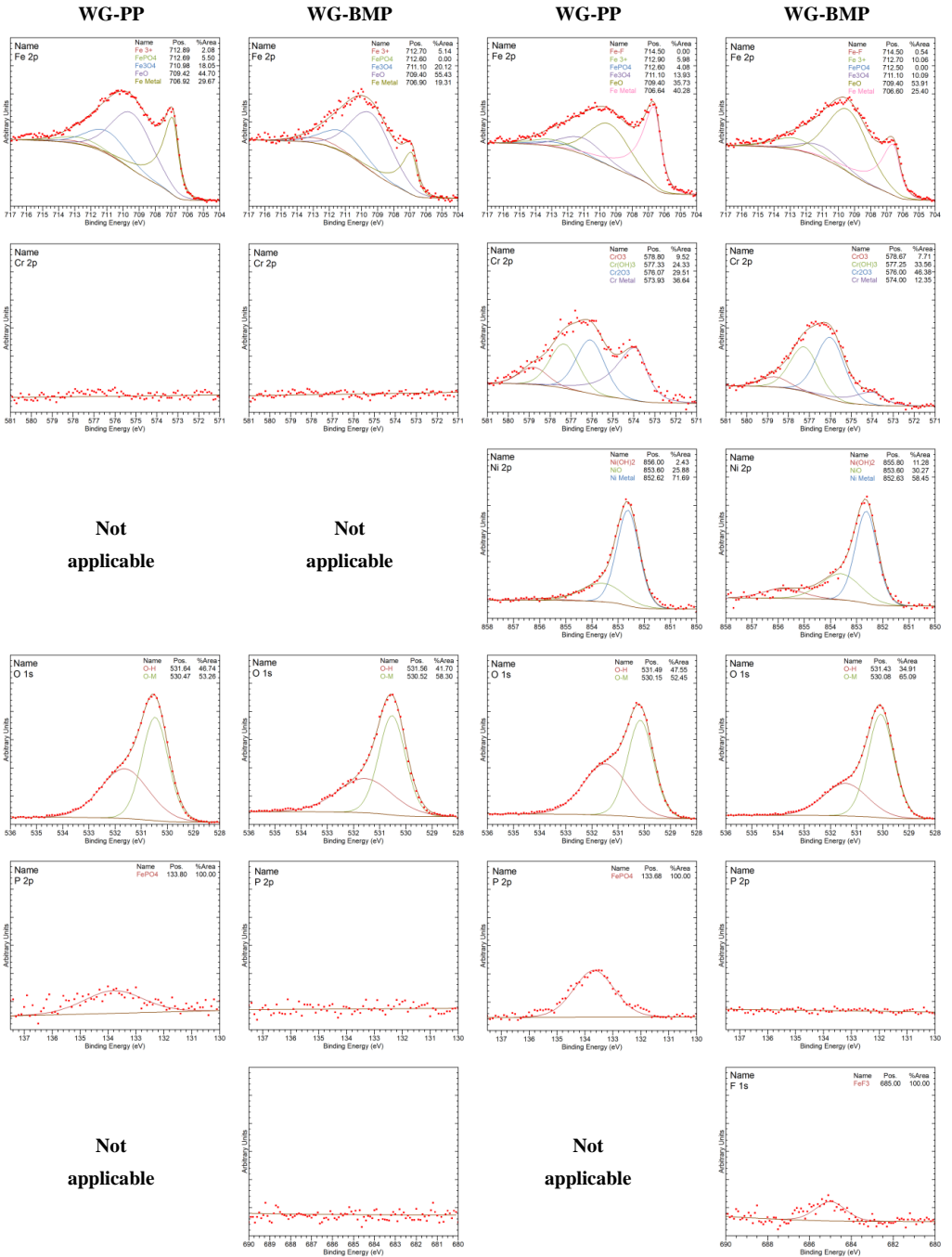


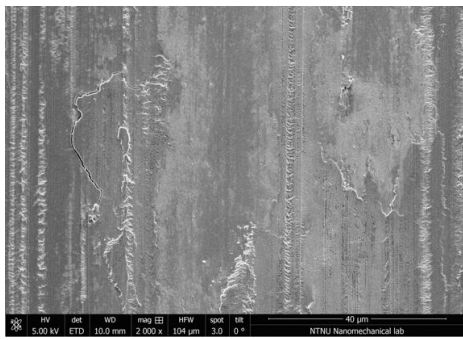
**Figure 7-6.** XPS spectra inside the tribofilm of the AISI 52100 steel and AISI 316L stainless steel lubricated by WG-PP and WG-BMP.

The differences in pH and electrical conductivity have an effect on the chemistry of the metal surface and, therefore, on the tribofilm formation. **Table 7-2** shows the wear track chemical composition after XPS analysis for Fe spectra, along with the Fe oxides to metal ratio. The Fe oxides to metal ratio is an indicator of the relative number of oxides inside the tribofilm. Low pH and high electrical conductivity lead to metal dissolution resulting in lower oxide to metal ratio as shown in WG-PP for both AISI 52100 steel and AISI 316L stainless steel. The corrosion process with WG-PP leads to the formation of phosphates in the tribofilm for both steels.

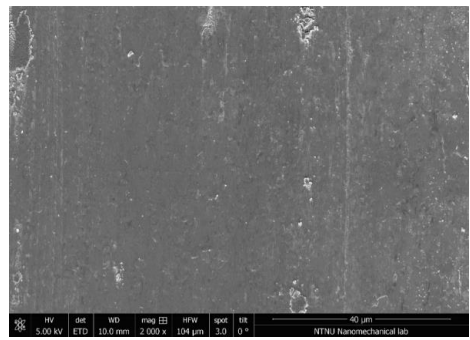
### 7.3. The effect of adsorbed layer and tribofilm on friction

For AISI 52100 steel, the friction evolution of WG at the end of the test was the highest, and friction decreased by adding the ILs, as shown in **Figure 7-1A**. The friction evolution of ILs was controlled by the presence of a thick tribofilm, which increases the friction due to the increase in the effective roughness of the worn surface. This behavior is shown by higher friction evolution of WG-PP compared to WG-BMP at the end of the test as shown in **Figure 7-1A**, regardless of the PP adsorbed layer is thicker, or has higher shear viscosity and shear elasticity modulus compared to BMP adsorbed layer (**Figure 6-3**). In the absence of a thick tribofilm, the friction is controlled by surface adsorption. For example, by adding C12 into WG base lubricant, the friction reduces drastically as shown in **Figure 7-1A**. According to literature, the friction reduction of carboxylic acids in polar media is due to the formation of a thin oxide film and the adsorption of carboxylic acid onto the rubbing surface [35,130]. Furthermore, the QCM-D study showed that C12 forms medium-thick, viscous, and rigid adsorbed layers (**Figure 6-3**), resulting in low and steady friction throughout the test. WG-BMP at the end of the test shows higher friction evolution than WG-C12 due to BMP adsorbed layer having a lower thickness, shear viscosity and shear elasticity modulus than C12 (**Figure 6-3**).

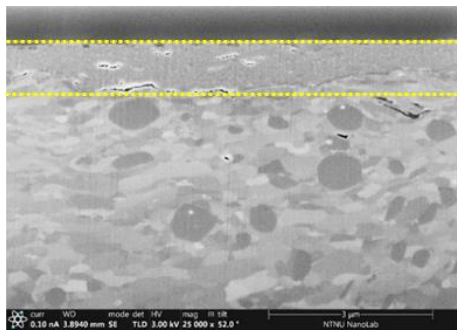
As shown in **Figure 7-1**, the friction evolution of WG-BMP consists of two distinct behaviors: (1) high friction at the first half of the test and (2) lower friction at the second half of the test. To further understand the influence of tribofilm formation on friction, a shorter test was performed for WG-BMP on AISI 52100 steel (terminated after 100 m of sliding distance, before the transition). The top view of the worn surface, wear cross-section FIB image and STEM image with elemental mapping of WG-BMP 100 m are shown in **Figure 7-7**, along with WG-BMP 300 m sample for comparison. The WG-BMP 300 m wear track shows a smooth surface, whereas a rougher surface is observed for the WG-BMP 100 m as a result of the formation of a thick tribofilm. These wear surface morphologies are in agreement with the friction evolution of WG-BMP on AISI 52100 steel in **Figure 7-1A**,



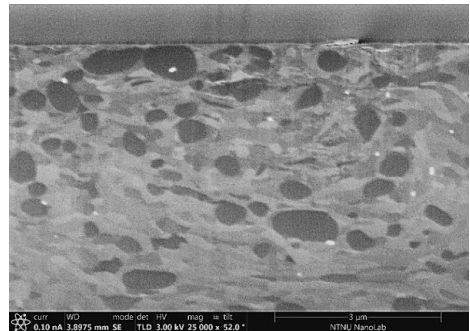
(A) Worn surface top view WG-BMP 100 m



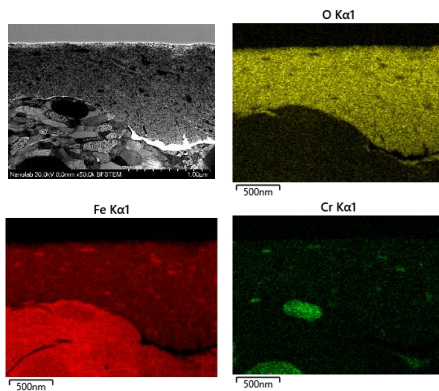
(B) Worn surface top view WG-BMP 300 m



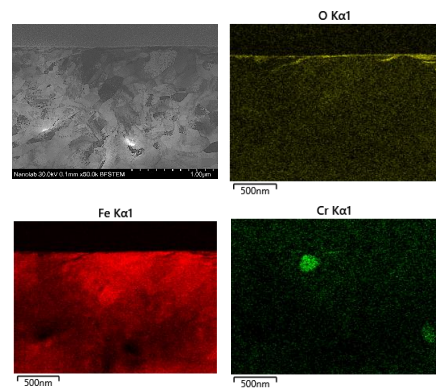
(C) Worn cross-section WG-BMP 100 m



(D) Worn cross-section WG-BMP 300 m



(E) STEM image WG-BMP 100 m



(F) STEM image WG-BMP 300 m

**Figure 7-7.** The top view, cross-section, and STEM image with elemental mapping of AISI 52100 steel worn surface lubricated by WG-BMP tested for 100 m and 300 m (tribofilm is indicated between two dashed yellow lines).

where a rougher surface results in higher friction and vice versa. Therefore, in this case, a thick oxide tribofilm is responsible for the higher friction.

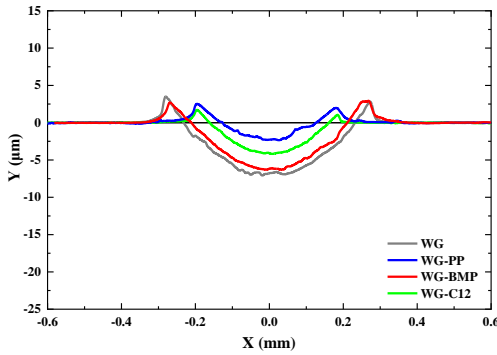
Comparing the friction evolution of WG-PP and WG-BMP at the first half of the test, when a very thick tribofilm is present for both cases, lower friction is found for WG-PP. This behavior could be

due to three reasons. Firstly, the adsorbed layer of PP is thicker and has higher shear viscosity and shear elasticity modulus than the BMP adsorbed layer. Secondly, the low pH of the WG-PP leads to more active dissolution ( $\text{Fe}^{2+}$ ) of the tribosurface decreasing the Fe oxide to metal ratio (**Table 7-2**). And lastly, the presence of iron phosphate in the tribofilm of PP which alters the tribofilm properties.

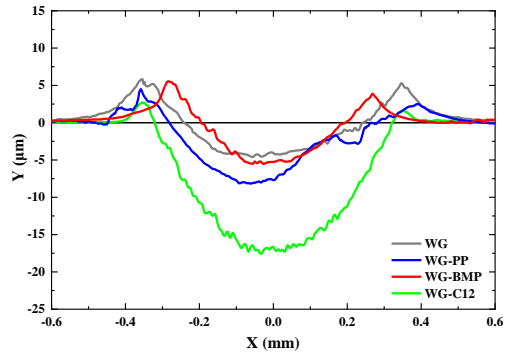
In the case of AISI 316L stainless steel, WG base lubricant gives high friction at the start of the test and gradually decreases to a steady friction condition with a COF of 0.14 that slightly fluctuates until the end of the test. Surprisingly, the STEM images show that WG alone in AISI 316L stainless steel is able to form a thick tribofilm (**Figure 7-5**). Therefore, thick tribofilms might not be the main factor controlling the friction in the case of AISI 316L stainless steel compared to AISI 52100 steel. However, the chemical composition of the tribofilm might be the controlling factor on AISI 316L stainless steel, which consists of other metal elements than only Fe (**Table 7-1**). Adding C12 to WG suppresses the running-in period in the case of AISI 316L stainless steel, and the friction evolution stabilizes at low a COF of 0.14. Thus, in the absence of thick tribofilms, friction evolution is controlled by the adsorbed layer, where the thicker, more viscous, and more rigid C12 adsorbed layer decreases friction. There is no significant difference in the friction evolution of WG-C12 on AISI 316L stainless steel and AISI 52100 steel, indicating the hardness of the substrate does not play important role in friction for WG.

Interestingly for AISI 316L stainless steel, WG-PP and WG-BMP show different friction behavior compared to WG alone or WG-C12. Friction evolution in WG-ILs is controlled by other factors than surface adsorption. The ILs increase the electrical conductivity of the lubricant and trigger a tribocorrosion process on the surface of a passive metal such as the AISI 316L stainless steel. In a tribocorrosion process, the removal of the passive film and the repassivation of the wear track occur in a cyclic manner. This tribocorrosion process has a clear detrimental effect in the frictional behavior resulting in the fluctuation of the friction evolution as shown in **Figure 7-1B**. The fluctuations in WG-PP and WG-BMP are to be understood as depassivation-repassivation events due to the high electrical conductivity of the lubricant. The higher friction evolution of WG-PP compared to WG-BMP is due to stronger tribocorrosion effect leading to higher metal dissolution. Resulting in higher surface roughness as shown in STEM image in **Figure 7-5**. In addition, the tribofilm chemical composition difference between WG-PP and WG-BMP, it shows that the WG-PP tribofilm is rich in oxides and phosphate whereas the WG-BMP tribofilm is rich in nickel. It seems that a more metal-based tribofilm has a more beneficial effect on friction compared to an oxide-based tribofilm. Moreover, the effect of pH and electrical conductivity is opposite in the case of AISI 52100 steel, since for this non-passive metal alloy a tribocorrosion process is not expected [160].

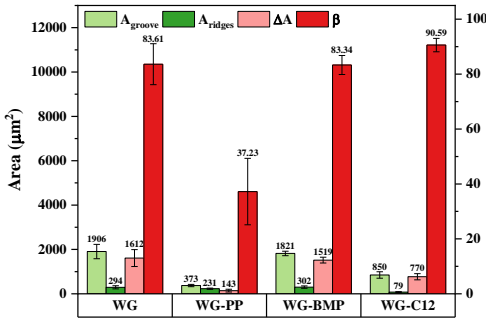




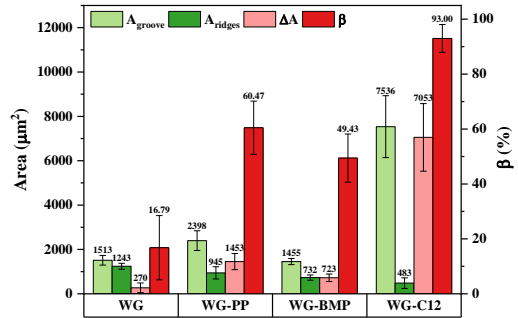
(A) Wear profile of AISI 52100 steel



(B) Wear profile of AISI 316L stainless steel



(C) Calculated wear area of AISI 52100 steel



(D) Calculated wear area of AISI 316L stainless steel

**Figure 7-8.** Wear cross-section profile and the calculated wear area of AISI 52100 steel and AISI 316L stainless steel lubricated by WG with and without additives.

## 7.4. The effect of adsorbed layer and tribofilm on wear

The influence of the additives on wear was studied more in detail by analyzing the wear tracks' cross section. As shown in **Figure 7-8A** and **Figure 7-8B**, the wear profiles from each lubricant condition show the formation of ridges along the sides of the wear groove. These ridges are a good indicator for plastic deformation, and the difference between the area of the worn groove and the area of the ridges give the real material loss. The ridges area ( $A_{ridges}$ ), groove area ( $A_{groove}$ ), and real material loss ( $\Delta A$ ) are presented in **Figure 7-8C** and **Figure 7-8D** along with the degree of material loss ( $\beta$ ).

In the case of AISI 52100 steel, **Figure 7-8C** shows that samples tested in the polar media (WG) have high  $\beta$  value, indicating a more abrasive wear mechanism. Looking at the  $\Delta A$  and the  $\beta$  value of WG-PP, the importance of tribofilm becomes obvious, where a very thick tribofilm results in low material loss and also changes the wear mechanism towards more plastic deformation. Moreover, the WG-PP

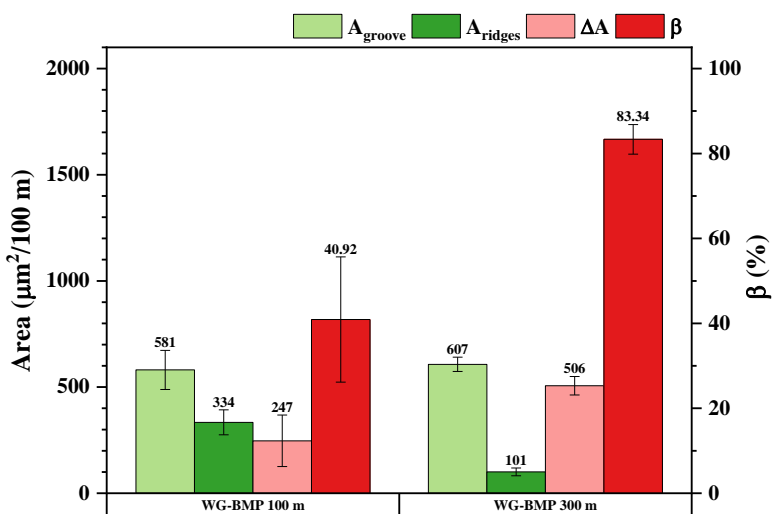


**Figure 7-9.** The calculated wear area of AISI 52100 steel lubricated by WG-BMP tested for 100 m and 300 m.

tribofilm also contains iron phosphate (**Figure 7-6** and **Table 7-1**), enhancing its antiwear properties. Comparing WG and WG-C12, **Figure 7-8C** shows that they have a comparable  $\beta$  value, indicating a similar wear mechanism, which corresponds to more abrasive wear. This might be due to the fact that they do not create thick tribofilms (**Figure 7-4**). However, WG-C12 has lower material loss than WG indicating the importance of the adsorbed layer. Thus, in the absence of a thick tribofilm (in the case of WG-C12), the wear reduction is mainly influenced by the adsorbed layer, which has medium-thick, viscous, and rigid adsorbed layer (**Figure 6-3**).

As shown in the STEM images in **Figure 7-7**, WG-BMP 100 m produces a very thick tribofilm, whereas it has been removed in WG-BMP 300 m. The effect of this tribofilm removal on the wear resistance of AISI 52100 steel lubricated by WG-BMP has been further analyzed and it is shown in **Figure 7-9**. The measured areas are normalized to 100 m for easier comparison. This was observed that WG-BMP 100 m sample shows lower area loss ( $\Delta A$ ) than WG-BMP 300 m due to thick tribofilm. Therefore, the formation of a thick tribofilm has a beneficial effect on the wear reduction of the AISI 52100 steel in polar media. However, when looking at the wear track surface and the FIB cross-sections, the thickest tribofilms (WG-PP and WG-BMP 100 m) have poor adhesion to the metal (**Figure 7-2**, **Figure 7-3**, and **Figure 7-7**) that can have a detrimental effect on the tribofilm integrity. The different mechanical properties of the tribofilm and the metal might be responsible for this behavior, where under pressure, the ductile metal tends to plastically deform leading to cracking and detachment of the more brittle oxide tribofilm at the interface.



In the case of AISI 316L stainless steel, **Figure 7-8D** shows that WG alone has a low  $\beta$  value, indicating more plastic deformation. This might be due to the fact that WG alone forms a thick tribofilm. AISI 316L stainless steel protects itself from corrosion by creating a stable passive (chromium oxide) film on the surface due to its high content in chromium. During the tribotest, when the sliding process starts, this passive film is removed by the mechanical action of the counterpart and the pristine metal alloy (depassivated wear track) will be then exposed to the lubricant. If the lubricant contains oxygen and is electrically conductive, the passive film will reform almost instantaneously (i.e., repassivation process). This process (tribocorrosion) will continue in a cyclic manner until the mechanical action is stopped, leading to an increase in the wear rate of the material [161]. Looking at the  $\Delta A$  and  $\beta$  values of WG-PP, PP increases the  $\Delta A$  and  $\beta$  values of the WG base lubricant, suffering more abrasive wear. This is in agreement with the fact that tribocorrosion and active dissolution have taken place in WG-PP resulting in a higher material removal rate. In the case of WG-BMP, the neutral pH lowers the metal dissolution, and the intermediate electrical conductivity lowers the tribocorrosion. In addition, BMP created a metal-based tribofilm thus leading to lower  $\Delta A$  and  $\beta$  values as shown in **Figure 7-8D**. In the case of WG-C12, C12 gives the lowest electrical conductivity in WG (**Table 6-1**) yet it creates the highest area loss as shown in **Figure 7-8D**. In addition, WG-C12 gives high  $\beta$  value, indicating more abrasive wear mechanism. This might be because C12 does not create thick tribofilms (**Figure 7-4**).

Comparing AISI 52100 steel and AISI 316L stainless steel lubricated by WG, it shows that AISI 316L stainless steel has lower  $\Delta A$  and  $\beta$  values, indicating that the presence of a thick tribofilm plays an important role on reducing wear (**Figure 7-4** and **Figure 7-5**). In the absence of a thick tribofilm, comparing AISI 52100 steel and AISI 316L stainless steel lubricated by WG-C12, it shows that both samples have similar  $\beta$  value, resulting similar abrasive wear mechanism. However, the area loss of AISI 316L stainless steel is much larger than AISI 52100 steel, indicating that the hardness of the substrate plays a significant role in wear reduction. Therefore, in the case of AISI 316 stainless steel, the factor controlling wear is the tribofilm thickness and the hardness of the substrate.

## 7.5. Summary

A summary of the tribological study of ionic liquids and carboxylic acid as boundary additives in water-glycol is illustrated in **Figure 7-10** and **Figure 7-11** for AISI 52100 steel and AISI 316L stainless steel, respectively.

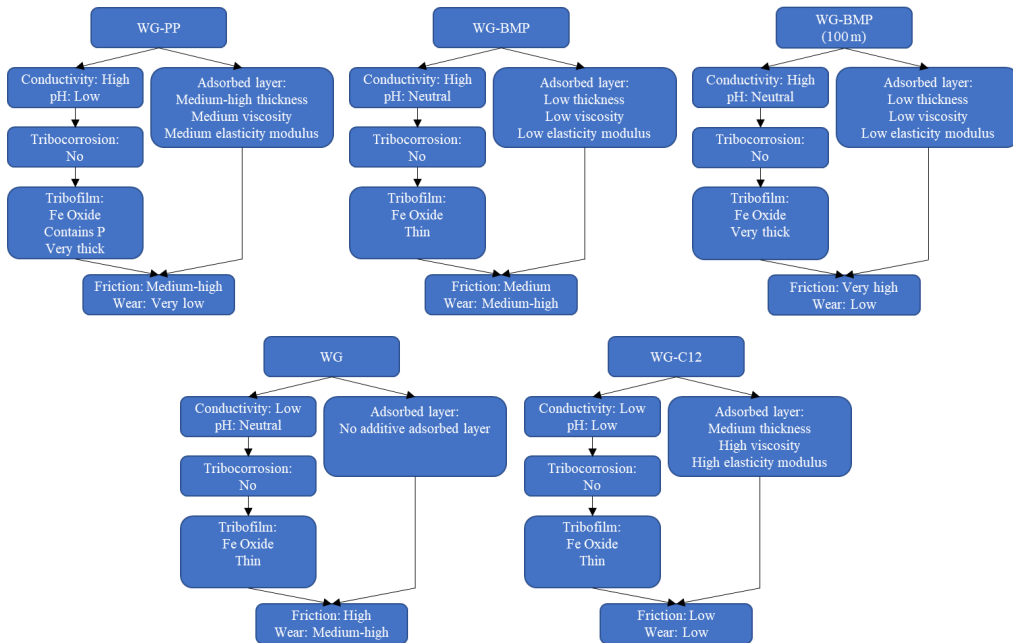


**Figure 7-10.** The summary of the tribological study of ionic liquids and carboxylic acid as boundary additives in water-glycol for a non-passive and hard metal (AISI 52100 steel).

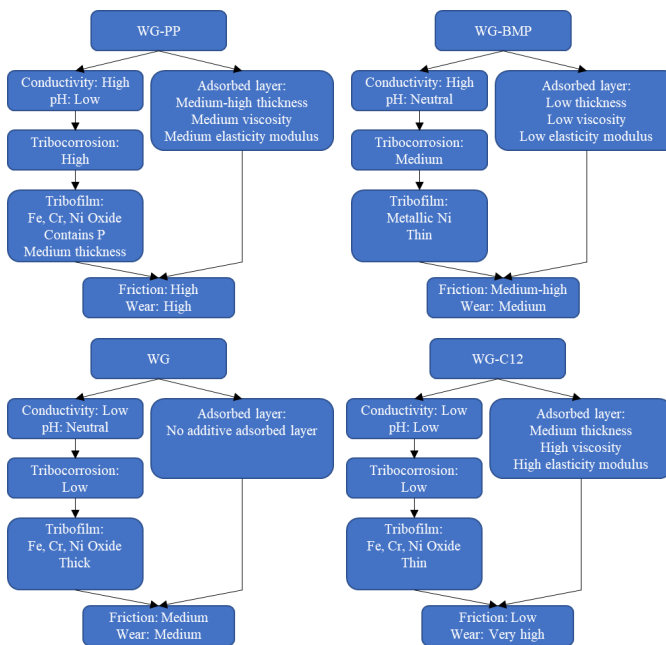


**Figure 7-11.** The summary of the tribological study of ionic liquids and carboxylic acid as boundary additives in water-glycol for a passive and soft metal (AISI 316L stainless steel).

## 7.6. Conclusion

The tribological behavior of ILs in polar media was studied in detail by analyzing the effect of surface adsorption and tribofilm formation on friction and wear. In this study, two metals, i.e., non-passive (AISI 52100) and passive (AISI 316L), were used to examine the effect of surface chemical composition on the tribological behavior of ILs in a polar medium (water-glycol).

Comparing AISI 52100 steel and AISI 316L stainless steel lubricated by WG alone shows that the tribofilm chemical composition and thickness plays a significant role in reducing friction and wear. In addition, the absence of functional additives makes it difficult to influence friction and wear. Clearly, the use of additives in WG results in a better friction and wear control, however, the type of additive and the chemical composition and mechanical properties of the tribomaterial play an important role.

In the case of the non-passive metal (AISI 52100), the friction and wear were controlled by the presence of tribofilms, resulting in high friction and low wear for thick tribofilm formation (WG-PP and WG-BMP 100 m). WG-PP resulted in lower friction and wear compared to WG-BMP 100 m, which was due to the metal dissolution on the surface and the presence of iron phosphate in the tribofilm which stabilized the tribofilm formation. In addition, PP produced thicker, more viscous and more rigid adsorbed layer compared to BMP influencing the frictional and antiwear properties. In the absence of a thick tribofilm, the friction and wear were controlled by the additive's adsorbed layer, where the thicker, more viscous, and more rigid C12 adsorbed layer gave the lowest friction and wear (comparing WG-C12, WG-BMP and WG).

In the case of the passive metal (AISI 316L), thick tribofilms could not be formed due to the tribocorrosion process in the lubricant additivated with ILs, which leads to a cyclic and continuous tribofilm formation and removal (as seen in the fluctuating friction evolution, **Figure 7-1**). Hence, the frictional and wear behavior of ILs were controlled by the tribocorrosion process rather than by the additive's surface adsorption. The tribocorrosion process was driven by the electrical conductivity and the pH of the lubricant, where the higher electrical conductivity and lower pH of WG-PP enhanced the process, leading to high friction and wear compared to WG-BMP. In the absence of tribocorrosion, friction is controlled by the additive's adsorbed layer whereas wear is controlled by the tribofilm formation, where the thicker, more viscous, and more rigid C12 adsorbed layer resulted in the lowest friction. However, the lack of thick tribofilm (C12) resulted in the highest wear.

*This page is intentionally left blank*

# Chapter 8

## A tribological study of ionic liquids as boundary additives in a non-polar base lubricant

(Parts of this chapter are published in paper 3)

Chapter 8 is dedicated to study the influence of ILs used as lubricant additives in polyalphaolefin (PAO) on the tribological performance of AISI 52100 bearing steel and AISI 316L stainless steel. In this study, PP and BMP were studied as lubricant additives in PAO, and their tribological behavior was compared with a carboxylic acid additive, C12. The selected concentrations were 1 wt.% and 0.1 wt.% for ILs and C12, respectively, and are the same as in previous chapters. As described in section 3, the boundary lubricating conditions were used for the tribological tests. The tests were performed for 9550 cycles which gave a distance of 300 m. A detailed surface analysis was performed using a range of advanced analytical tools, such as FIB-SEM, STEM-EDS and XPS.

### 8.1. Friction and wear performance in PAO

**Figure 8-1** shows the friction evolution of AISI 52100 steel and AISI 316L stainless steel lubricated by PAO base lubricant and PAO additivated with PP, BMP, and C12. The friction evolution of AISI 52100 steel lubricated with PAO alone shows a COF of 0.1 at the beginning of the test, followed by a steady increase after 20 m to reach a COF of 0.19 at 70 m as shown in **Figure 8-1A**. Afterwards, the friction continuously declines to 0.14 until the end of the test. The addition of ILs in PAO delays the friction increase to 30 m and 100 m for PP and BMP, respectively. In addition, BMP not only delays further the friction increment but also decreases friction until the end of the test. The addition of C12 in PAO results in a steadier friction evolution at ca. 0.12 without any friction increase. It is worth noticing that the friction of PAO, PAO-PP, and PAO-BMP is lower than PAO-C12 before any friction increase takes place. The wear of AISI 52100 steel is shown in **Figure 8-1C**, PAO base lubricant gives the highest SWR of  $5.70 \times 10^{-6} \text{ mm}^3/\text{Nm}$ , followed by PP, BMP, and C12, with  $5.30 \times 10^{-6}$ ,  $3.63 \times 10^{-6}$ , and  $2.89 \times 10^{-6} \text{ mm}^3/\text{Nm}$ , respectively.

In the case of AISI 316L stainless steel, the friction evolution of PAO alone is characterized by high friction at the beginning of the test, followed by a steady decrease in friction at ca. 50 m until reaching 0.14 as shown in **Figure 8-1B**. The addition of PP in PAO significantly reduces the running-in period

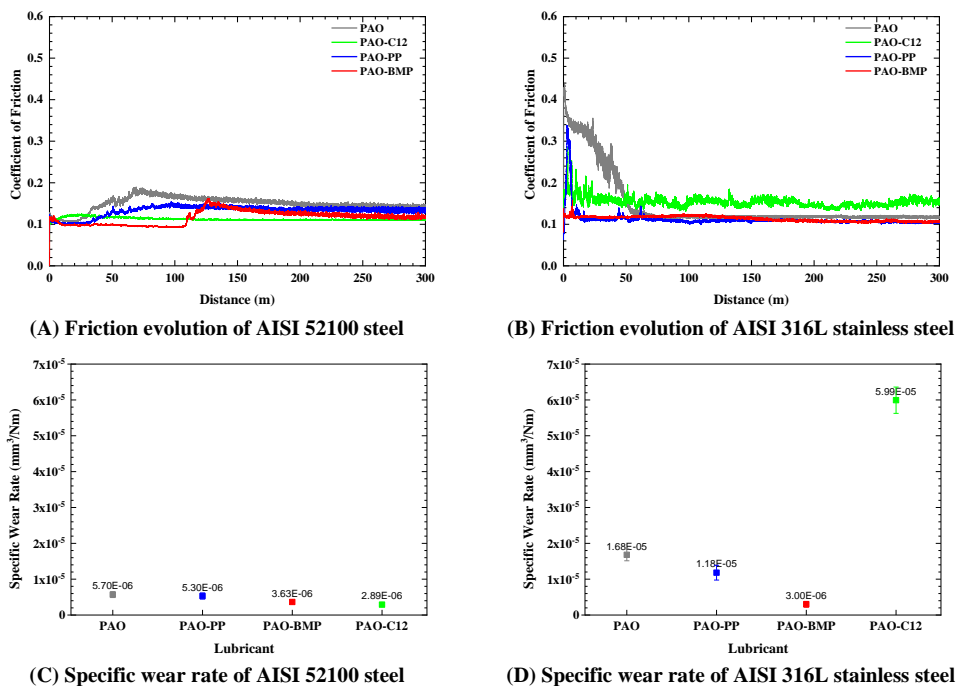


**Figure 8-1.** Friction evolution and wear rates of AISI 52100 steel and AISI 316L stainless steel lubricated by PAO with and without additives.

and maintains a steady friction after the running-in slightly lower than PAO alone. BMP in PAO reduces more efficiently the running-in period than PP, completely suppressing it. After the running-in, the COF of PAO-BMP is comparable to PAO-PP. C12 in PAO increases friction to 0.15 and fluctuates during the whole test, indicating unstable friction. The wear of AISI 316L stainless steel is shown in **Figure 8-1D**, PAO alone gives a SWR of  $1.68 \times 10^{-5} \text{ mm}^3/\text{Nm}$ . ILs reduce the SWR to  $1.18 \times 10^{-5}$  and  $3.00 \times 10^{-6} \text{ mm}^3/\text{Nm}$  for PP and BMP, respectively. The SWR of PAO-C12 is  $5.99 \times 10^{-5} \text{ mm}^3/\text{Nm}$ , which is ca. 3.5 times higher than the SWR of PAO alone.

**Figure 8-2** shows the SEM images of the wear track surface after tribo testing. The wear track morphology of AISI 52100 steel lubricated by PAO alone shows abrasive wear marks with minor plastic deformation. In the case of PAO-PP and PAO-BMP, the wear tracks of AISI 52100 steel have similar morphology, where abrasive wear with minor plastic deformation is observed. On the other hand, a smooth wear surface with no plastic deformation is observed on AISI 52100 steel lubricated by PAO-C12, which is in agreement with the friction evolution and wear results.

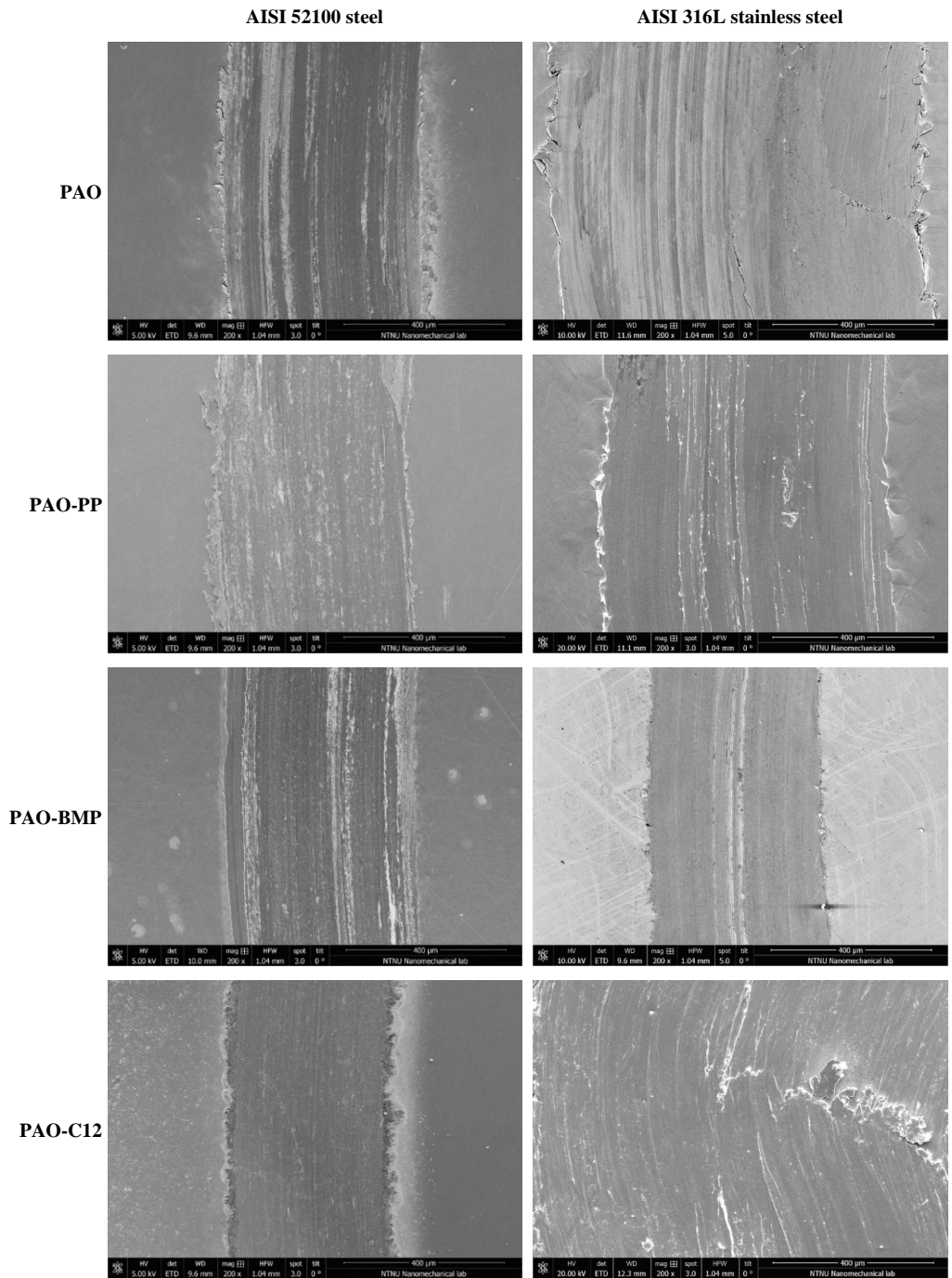
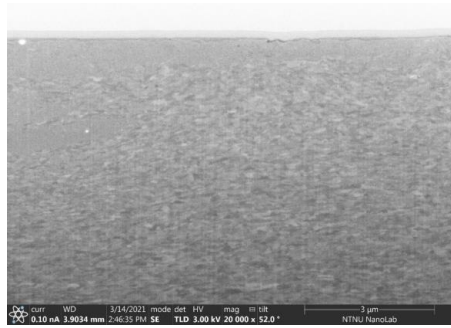
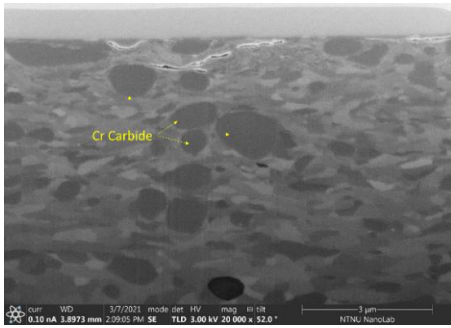


**Figure 8-2.** SEM images of the wear tracks of AISI 52100 steel and AISI 316L stainless steel disks tested in PAO with and without additives.

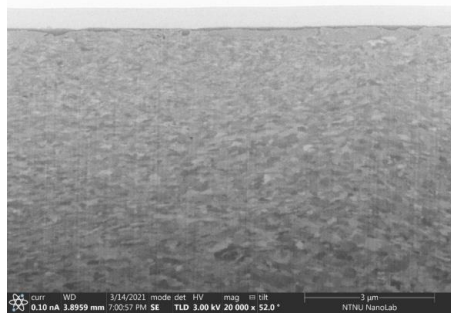
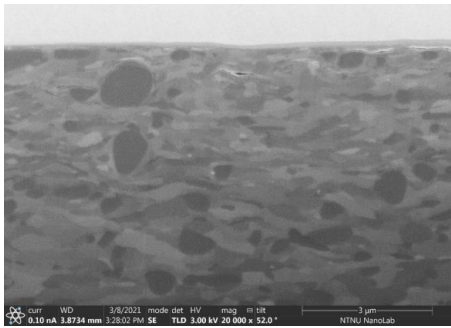
**AISI 52100 steel**

**AISI 316L stainless steel**

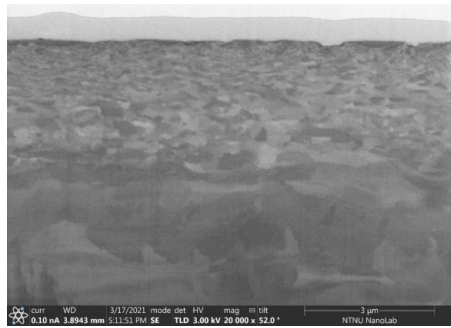
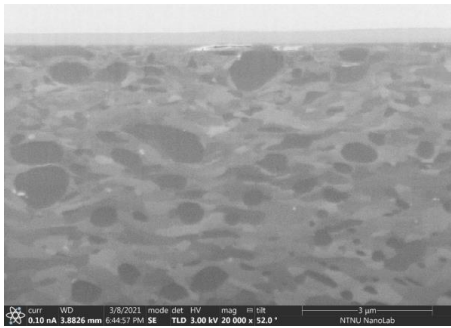
**PAO**



**PAO-PP**



**PAO-BMP**



**PAO-C12**

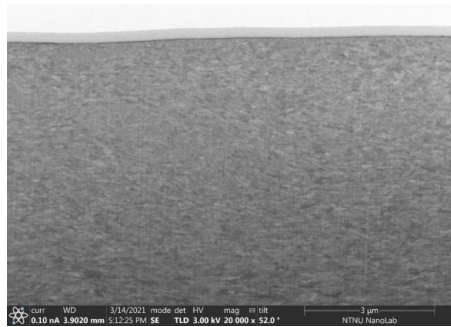
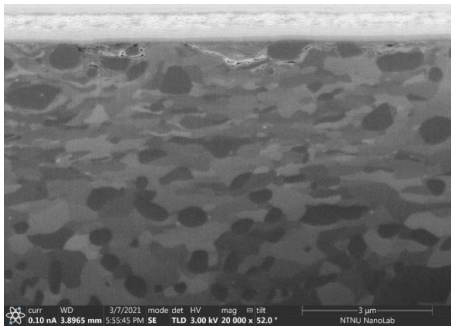


**Figure 8-3.** FIB cross-section images of the wear tracks of AISI 52100 steel and AISI 316L stainless steel disks tested in PAO with and without additives.



The wear morphology of AISI 316L stainless steel lubricated with PAO alone shows a smooth wear surface with signs of abrasive wear and plastic deformation. In the case of AISI 316L stainless steel lubricated with PAO-PP, the wear track shows plowing with signs of plastic deformation and delamination in some areas. On the other hand, PAO-BMP shows a smooth surface and abrasive grooves with no signs of plastic deformation. PAO-C12 shows delamination, wear flakes, and severe plastic deformation inside the wear track.

The influence of friction on the subsurface microstructure of the steels is shown in **Figure 8-3**. The length of the cross-section was 20  $\mu\text{m}$  and was taken from the center of the wear track and perpendicular to the sliding direction and prepared using SEM-FIB. The microstructure of AISI 52100 steel lubricated by all lubricants consists of chromium carbides (dark round particles) with some deformed grains and plastic deformation. PAO, PAO-PP, and PAO-BMP samples have similar degree of recrystallization and plastic deformation, whereas PAO-C12 samples show lower degree of recrystallization and plastic deformation, which is in agreement with the low friction evolution.

For AISI 316L stainless steel, a higher degree of recrystallization and plastic deformation is observed compared to AISI 52100 steel due to its lower hardness. PAO, PAO-PP and PAO-C12 have similar degree of recrystallization and plastic deformation. In the case of PAO-BMP, lower degree of recrystallization and plastic deformation is found, together with a thinner subsurface recrystallization area, which is in agreement with its low friction evolution.

## **8.2. The effect of additives and surface chemistry on tribofilm formation**

In order to investigate the tribofilms, the cross-section of all wear tracks was examined by STEM. The STEM images and the EDS elemental mapping are presented in **Figure 8-4** and **Figure 8-5** for AISI 52100 steel and AISI 316L stainless steel, respectively. The chosen elements for mapping were iron, chromium, nickel, oxygen, and phosphorous, which are present in the bulk material and the ILs. The oxygen is an indicator of the presence of oxides. Although BMP contains fluorine, this element was not selected for EDS mapping due to the close energy of F  $K\alpha$  and Fe  $L\alpha$ .

For AISI 52100 steel samples, the samples lubricated by PAO, PAO-PP, and PAO-BMP show a thick tribofilm on the wear track surface with a thickness of 50 – 250 nm. In addition, cracks are found in the subsurface area for PAO and PAO-PP, however no visible subsurface cracks are observed for PAO-BMP. In the case of PAO-C12, a thin tribofilm is observed with a thickness of ca. 15 nm.

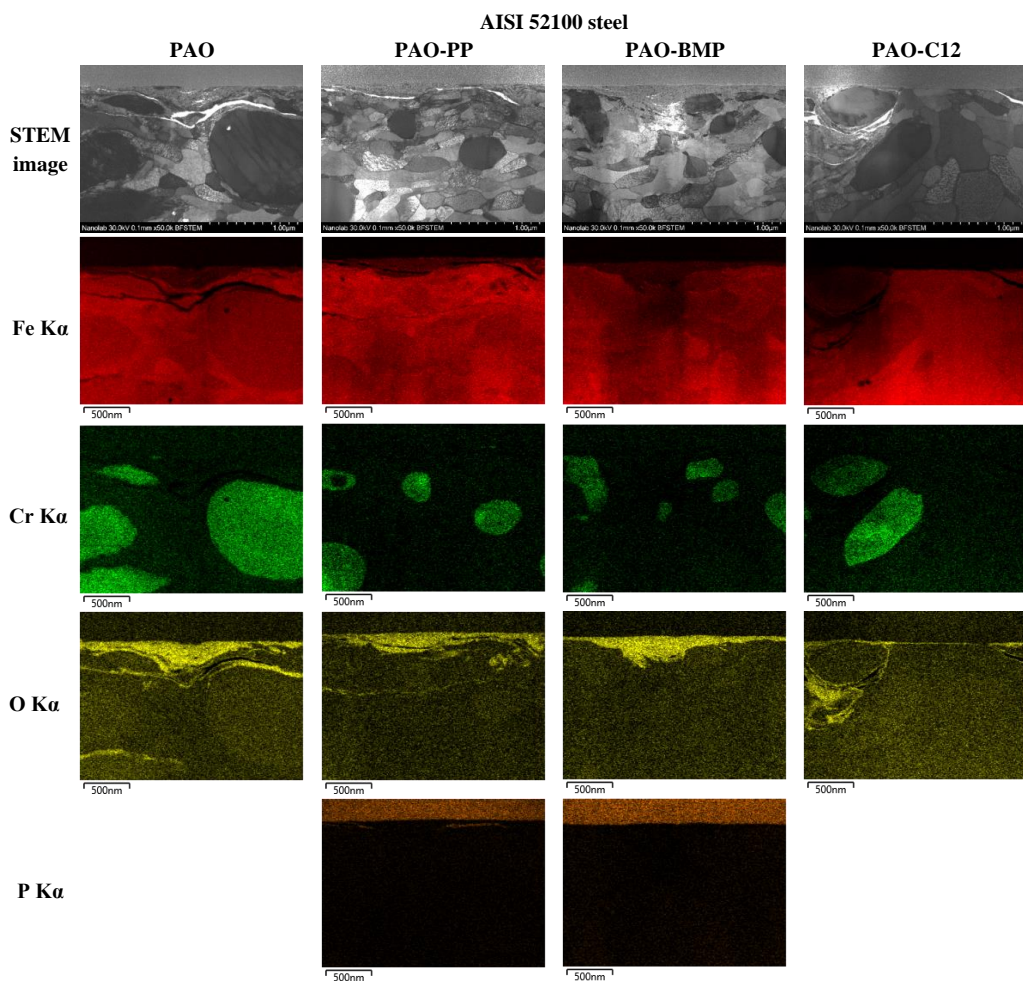


**Figure 8-4.** STEM cross-section images and EDS elemental mapping of the wear tracks on AISI 52100 steel tested in PAO with and without additives.

In addition, cracks are found in the vicinity of the carbides and on the surface. EDS elemental mapping of the cross-sections shows high oxygen levels in the tribofilms of all samples, indicating they consist mainly of oxides. No phosphorous is detected in the tribofilm of PAO-PP and PAO-BMP samples indicating that the ILs are not involved in the tribofilm formation.

For AISI 316L stainless steel, the samples lubricated by PAO, PAO-PP, and PAO-BMP show a thick tribofilm on the surface with a thickness of 50 – 300 nm. No visible subsurface cracks are observed for the samples lubricated by PAO, PAO-PP, and PAO-BMP. In the case of PAO-C12, a thin tribofilm is observed with a thickness of ca. 15 nm. In addition, signs of smeared surface material into the subsurface region are observed. EDS elemental mapping of the cross-sections shows high oxygen

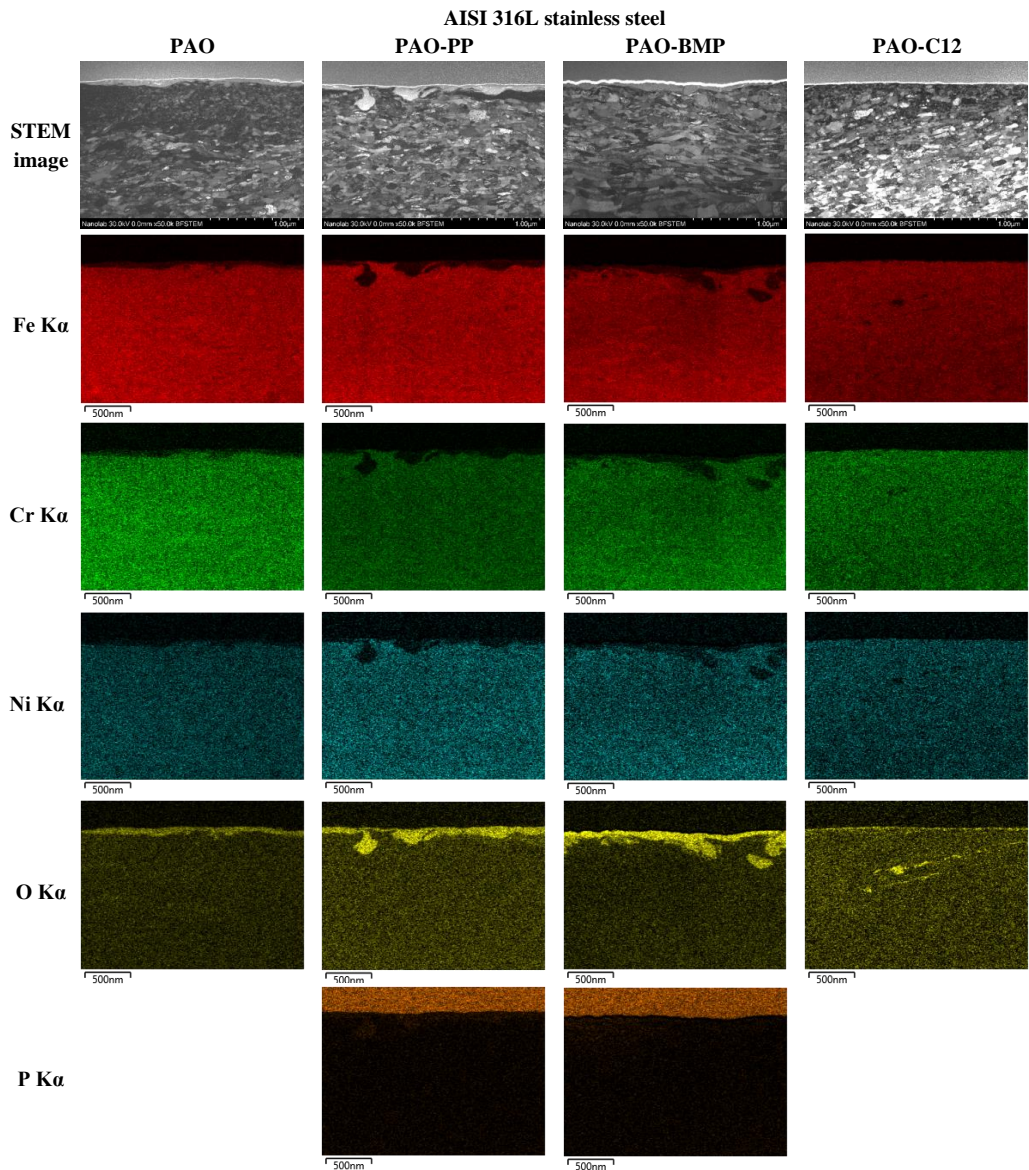


**Figure 8-5.** STEM cross-section images and EDS elemental mapping of the wear tracks on AISI 316L stainless steel tested in PAO with and without additives.

levels in the tribofilms of all samples, indicating they consist mainly of oxides. In addition, phosphorous is detected in PAO-PP, indicating that PP is involved in the tribofilm formation. In the case of PAO-BMP, no clear indication of phosphorus is found in the tribofilm.

A detailed chemical composition of the tribofilms is taken by means of EDS and the results are shown in **Table 8-1**. In the case of all AISI 52100 steel samples, the tribofilms consist of iron and oxygen.

**Table 8-1.** EDS chemical composition analysis of the tribofilms tested in PAO with and without additives (at.%)

Sample	Lubricant	Tribofilm thickness (nm)	Elemental concentration in tribofilm (at.%)				
			Fe	Cr	Ni	O	P
AISI 52100 steel	PAO	50 – 250	46.49	0	-	53.51	-
	PAO-PP	50 – 250	48.87	0	-	51.13	0
	PAO-BMP	50 – 250	44.60	0	-	55.40	0
	PAO-C12	15	40.31	0	-	59.69	-
AISI 316L stainless steel	PAO	50 – 100	31.06	8.23	3.46	57.25	-
	PAO-PP	100 – 200	25.59	5.79	3.02	60.36	5.24
	PAO-BMP	100 – 300	21.54	5.18	2.74	69.91	0.63
	PAO-C12	15	37.92	10.42	5.28	46.38	-

Chromium is not detected in the tribofilm because it forms stable chromium carbide. In the case of all AISI 316L samples, the tribofilms consist of iron, chromium, nickel, and oxygen. In addition, phosphorous is detected for both PAO-PP and PAO-BMP samples.

XPS analysis was performed to analyze the tribofilm of AISI 52100 steel and AISI 316L stainless steel lubricated by PAO-PP and PAO-BMP. With XPS, the presence of phosphorous and fluorine will be studied in detail to overcome the drawbacks of the EDS analysis. The detailed XPS spectra are shown in **Figure 8-6** for both AISI 52100 steel and AISI 316L stainless steel.

XPS results for AISI 52100 steel lubricated by PAO-PP show the presence of Fe and O in the tribofilm. No Cr or P is found in the tribofilm, indicating that the stable Cr carbide and the PP moieties did not contribute to the tribofilm formation, which is in agreement with the EDS data. The detailed Fe spectra deconvolution shows the presence of Fe metal ( $\text{Fe}^0$ ), Fe oxides ( $\text{FeO}$ ,  $\text{Fe}_3\text{O}_4$ ,  $\text{Fe}_2\text{O}_3$ ), and Fe hydroxides ( $\text{FeOOH}$  and  $\text{Fe}(\text{OH})_3$ ). In the case of PAO-BMP, only Fe and O are detected with no Cr, P, or F in the tribofilm. The absence of P and F indicates that the BMP moieties did not contribute to the tribofilm formation. Therefore, metallic Fe and Fe oxides and hydroxides are the main constituents of the tribofilm of PAO-BMP.

In the case of AISI 316L stainless steel lubricated by PAO-PP, XPS shows Fe, Cr, Ni, O, and P in the tribofilm. The Fe and Cr spectra deconvolution shows that the tribofilms mainly consist of metallic elements and metal oxides and hydroxides. In addition, P is detected in the tribofilm in the form of iron phosphate, indicating the PP moieties react with the worn surface and contribute to the tribofilm formation, which is in agreement with the EDS data. For PAO-BMP, XPS shows the presence of Fe, Cr, Ni, O, P, and F in the tribofilm. The P spectrum has a smaller peak indicating less phosphorous species for PAO-BMP than PAO-PP, which is in agreement with the EDS data. In addition, F is detected in the tribofilm indicating both BMP moieties react with the worn surface and contribute to the tribofilm formation.

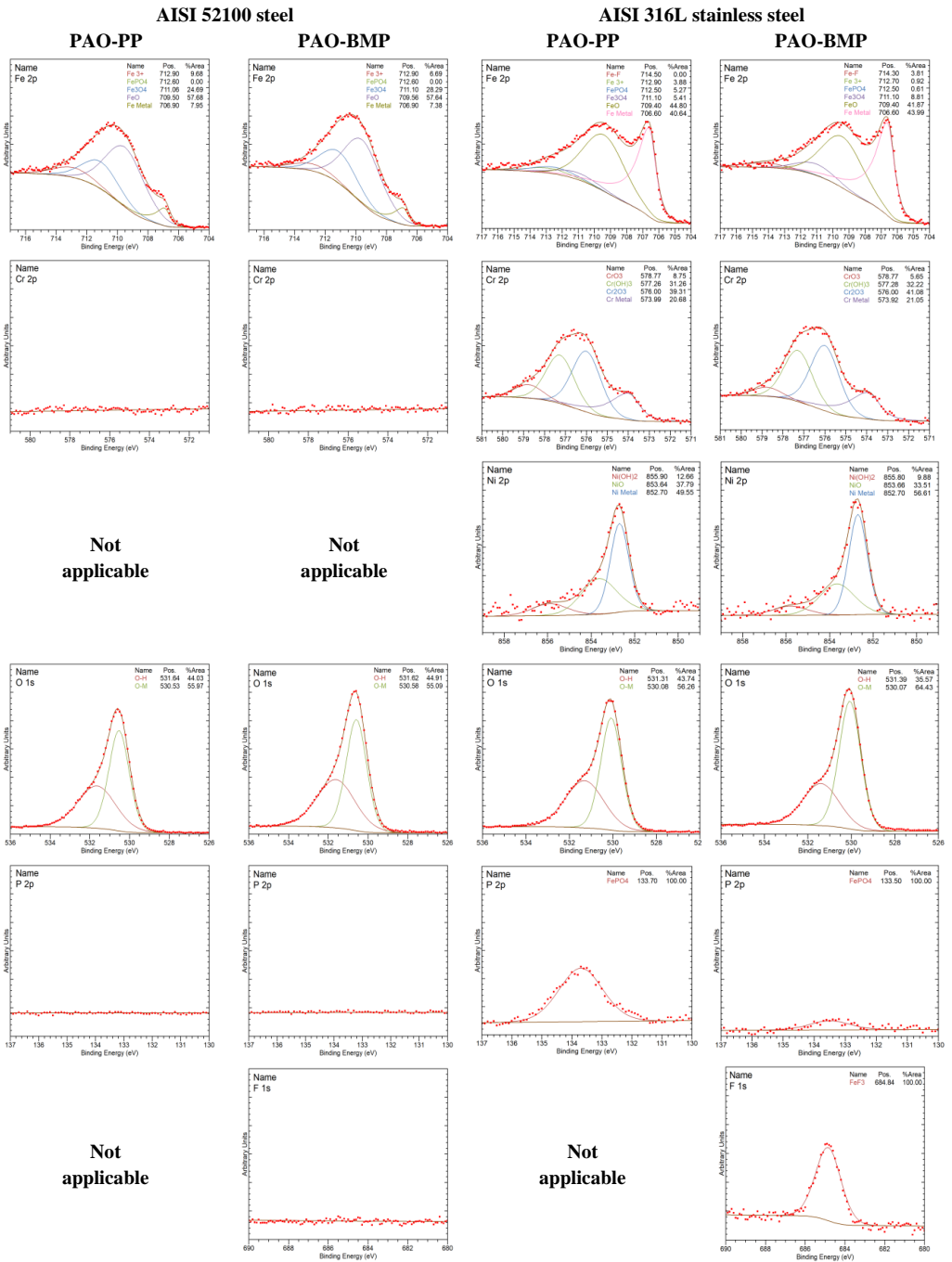


**Figure 8-6.** XPS spectra inside the tribofilm of the AISI 52100 steel and AISI 316L stainless steel lubricated by PAO-PP and PAO-BMP.

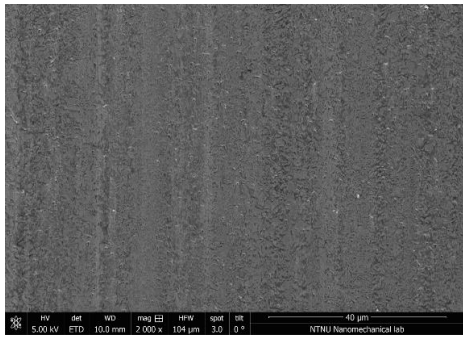
### 8.3. The effect of adsorbed layer and tribofilm on friction

For AISI 52100 steel, **Figure 8-1A** shows that there is an increase in friction after some sliding cycles for PAO, PAO-PP, and PAO-BMP resulting in higher friction than PAO-C12. As shown in **Figure 8-4**, thick tribofilms are formed for PAO, PAO-PP, and PAO-BMP, whereas a thin tribofilm is formed for PAO-C12. The formation of thick tribofilms can increase the friction due to the increase in effective surface roughness as shown in **Figure 8-2**, where PAO, PAO-PP, and PAO-BMP have rougher worn surfaces than PAO-C12. The friction evolution of PAO-BMP is lower than the friction of PAO-PP despite the QCM-D study shows that BMP creates a thinner adsorbed layer compared to PP (**Table 6-3**). However, this layer is strongly adsorbed on the surface, playing a significant role in reducing friction. In the case of PAO-C12, the friction is maintained at a low level despite C12 creates an adsorbed layer with low thickness, low shear viscosity and low shear elasticity modulus (**Table 6-3**). Thus, the friction evolution of AISI 52100 steel is highly influenced by tribofilm formation.

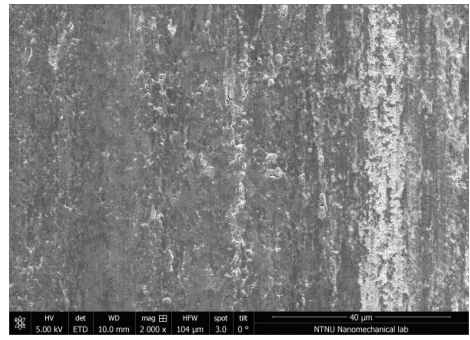
To further understand the influence of tribofilm on friction, a shorter test was performed for PAO-BMP on AISI 52100 steel. Shorter tests terminated after 100 m sliding distance. As shown in **Figure 8-1A**, the friction evolution of PAO-BMP consists of two distinct regions: (1) low friction for the first 100 m of the test and (2) high friction for the rest of the test. The top view of the worn surface, wear cross-section FIB image and STEM image with elemental mapping of PAO-BMP 100 m are shown in **Figure 8-7**, along with PAO-BMP 300 m sample for comparison. The PAO-BMP 100 m sample wear track shows a smooth surface, whereas a rougher surface is observed for the PAO-BMP 300 m as a result of a thick tribofilm formation. These wear surface morphologies are in agreement with the friction evolution of PAO-BMP on AISI 52100 steel in **Figure 8-1A**, where a rougher surface results in higher friction and vice versa. Therefore, the thicker oxide tribofilm is responsible for the higher friction.

Interestingly, the friction evolution before friction increases shows that PAO, PAO-PP and PAO-BMP give lower friction than PAO-C12 (**Figure 8-1A**). The order of friction from high to low is PAO-C12, PAO, PAO-PP, and PAO-BMP. In the absence of a thick tribofilm (in the case of PAO-C12), the friction evolution is controlled by the additive's surface adsorption. Here PAO-C12 gives higher friction than PAO alone due to the thin C12 adsorbed layer with low shear viscosity and shear elasticity modulus, which replaces the long and big PAO molecules resulting in a non-durable adsorbed layer (chapter 6). Whereas for PAO-PP and PAO-BMP, thick, viscous, and rigid adsorbed layers result in low friction (**Table 6-3**). In addition, the strongly adsorbed layer of BMP produces a more durable adsorbed layer resulting in lower friction at longer distances than the PP adsorbed layer.

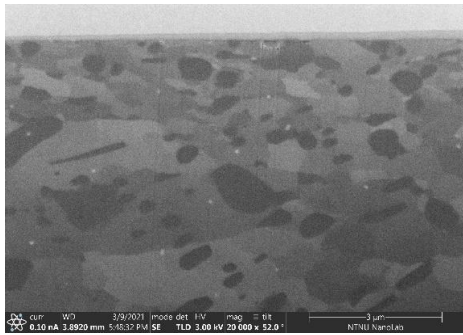




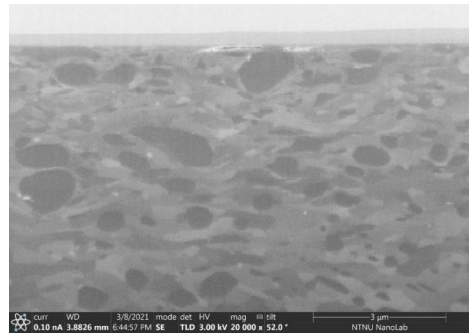
(A) Worn surface top view PAO-BMP 100 m



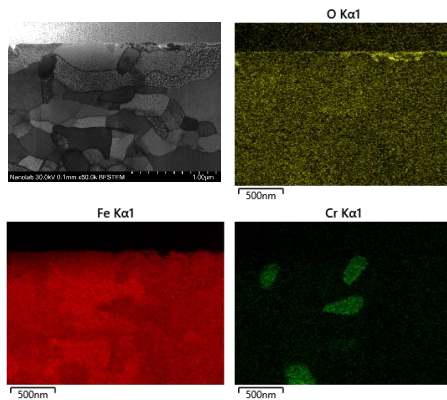
(B) Worn surface top view PAO-BMP 300 m



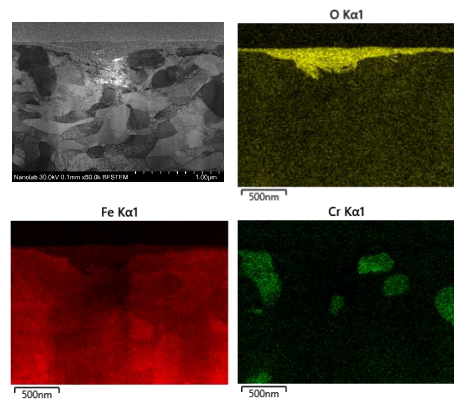
(C) Worn cross-section PAO-BMP 100 m



(D) Worn cross-section PAO-BMP 300 m



(E) STEM image PAO-BMP 100 m



(F) STEM image PAO-BMP 300 m

**Figure 8-7.** The top view, cross-section, and STEM image with elemental mapping of AISI 52100 steel worn surface lubricated by PAO-BMP tested for 100 m and 300 m.

In the case of AISI 316L stainless steel, a friction increase due to thick tribofilm formation is not observed. As shown in **Figure 8-1B** and **Figure 8-5**, the friction evolution of the AISI 316L stainless steel lubricated by PAO, PAO-PP, and PAO-BMP shows low values even though a thick tribofilm was formed, implying that a thick tribofilm might not be the factor playing the most important role

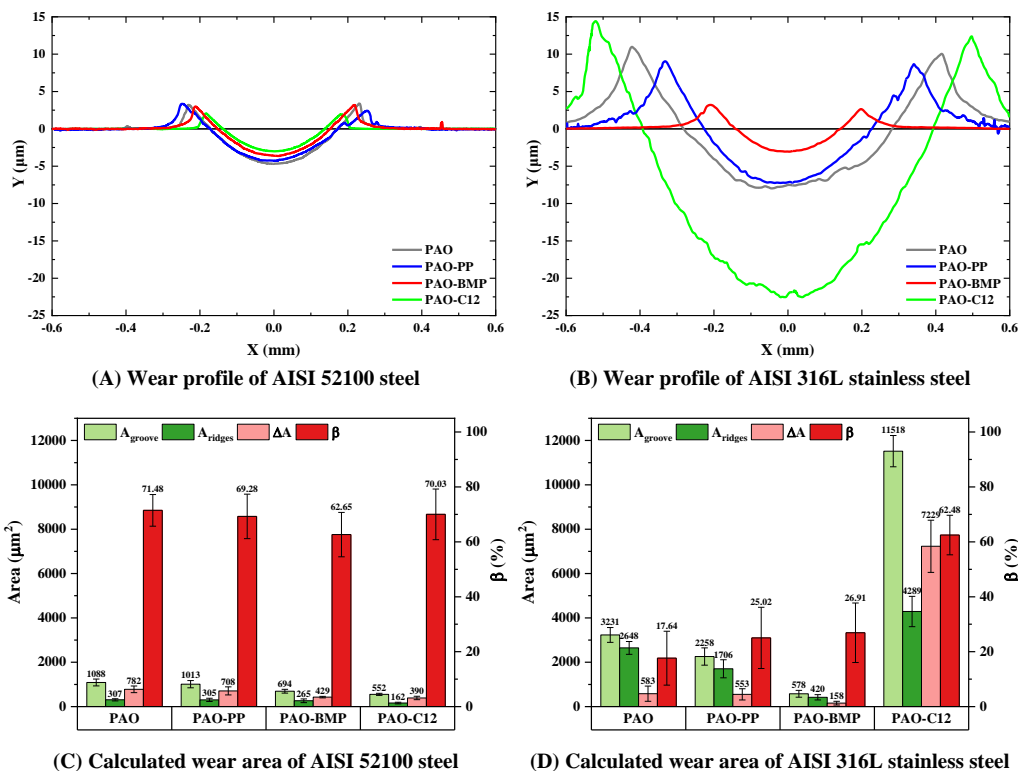


**Figure 8-8.** Wear cross-section profile and the calculated wear area of AISI 52100 steel and AISI 316L stainless steel lubricated by PAO with and without additives.

for stainless steel. As shown in **Figure 8-6**, the tribofilm formed on stainless steel contains oxides and hydroxides from different metals, whereas the tribofilm on AISI 52100 steel only contains Fe oxides and hydroxides. In addition, iron phosphate and fluoride were formed in the tribofilm of stainless steel. Therefore, the chemical composition of the tribofilm influences its mechanical properties, resulting in a different frictional response. Looking at the friction evolution at the running-in period, it is seen that BMP has a significant effect on it, which is in agreement with the surface adsorption data (chapter 6). The durable BMP adsorbed layer reduces the running-in period significantly thus leading to the thinnest recrystallization region (**Figure 8-3**).

However, different friction behavior is observed in the case of a thin tribofilm and a less durable adsorbed layer formed by PAO-C12, both on AISI 52100 steel and AISI 316L stainless steel. PAO-C12 shows steady and low friction evolution on AISI 52100 steel (**Figure 8-1A**); in contrast, higher friction with high fluctuation is observed for AISI 316L stainless steel (**Figure 8-1B**). Both tribofilms on AISI 52100 steel and AISI 316L stainless steel are thin oxide layers (**Table 8-1**), and the QCM study indicates that C12 formed a less durable adsorbed layer both on Fe and SS coated sensors



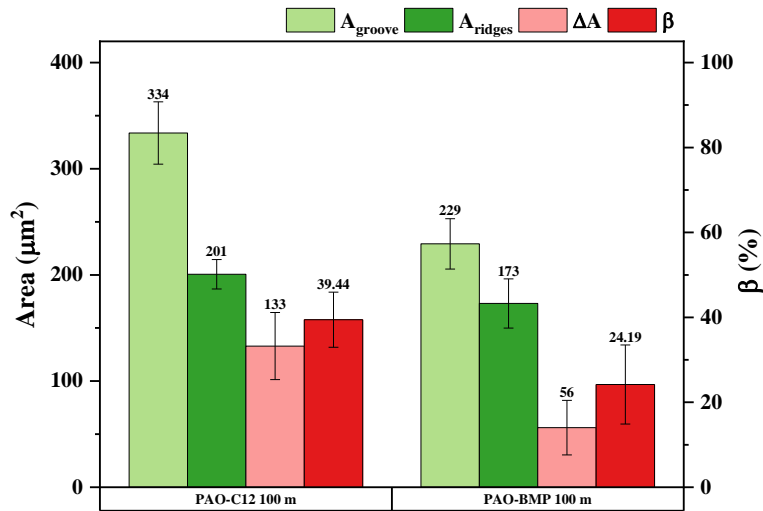


**Figure 8-9.** The calculated wear area of AISI 52100 steel lubricated by PAO-C12 and PAO-BMP tested for 100 m.

(**Table 6-3**). The main difference remains in the mechanical properties of the substrate, where AISI 52100 steel has a higher hardness than AISI 316L stainless steel. For a soft tribosurface (AISI 316L) lubricated by PAO-C12, the less durable adsorbed layer and thin tribofilm cannot withstand the applied boundary lubricating conditions, resulting in plastic deformation, as shown in **Figure 8-2**. On the other hand, a less durable adsorbed layer and thin tribofilm on a high hardness substrate (AISI 52100) withstands the applied boundary lubricating condition, thus maintaining low friction.

#### 8.4. The effect of adsorbed layer and tribofilm on wear

The influence of the additives on wear is studied in more detailed by analyzing the wear cross section. As shown in **Figure 8-8A** and **Figure 8-8B**, wear profiles from each lubricant condition show the formation of ridges along the side of the wear groove. The ridges area ( $A_{ridges}$ ), groove area ( $A_{groove}$ ), and area loss ( $\Delta A$ ) are presented in **Figure 8-8C** and **Figure 8-8D** along with the degree of material loss ( $\beta$ ) for AISI 52100 steel and AISI 316L stainless steel, respectively.

In the case of AISI 52100 steel, **Figure 8-8C** shows that all additives reduce the area loss ( $\Delta A$ ). Interestingly, the  $\beta$  value of all lubricants is comparable (60 to 70%) indicating a similar abrasive wear mechanism. Similar to the friction behavior, wear is also highly influenced by the presence of a tribofilm and adsorbed layer. As the tribofilms have similar thickness and chemical composition for PAO-PP and PAO-BMP, the wear reduction is mainly affected by the adsorbed layer, where a durable adsorbed layer (BMP) gives lower wear. To further understand the influence of the adsorbed layer,

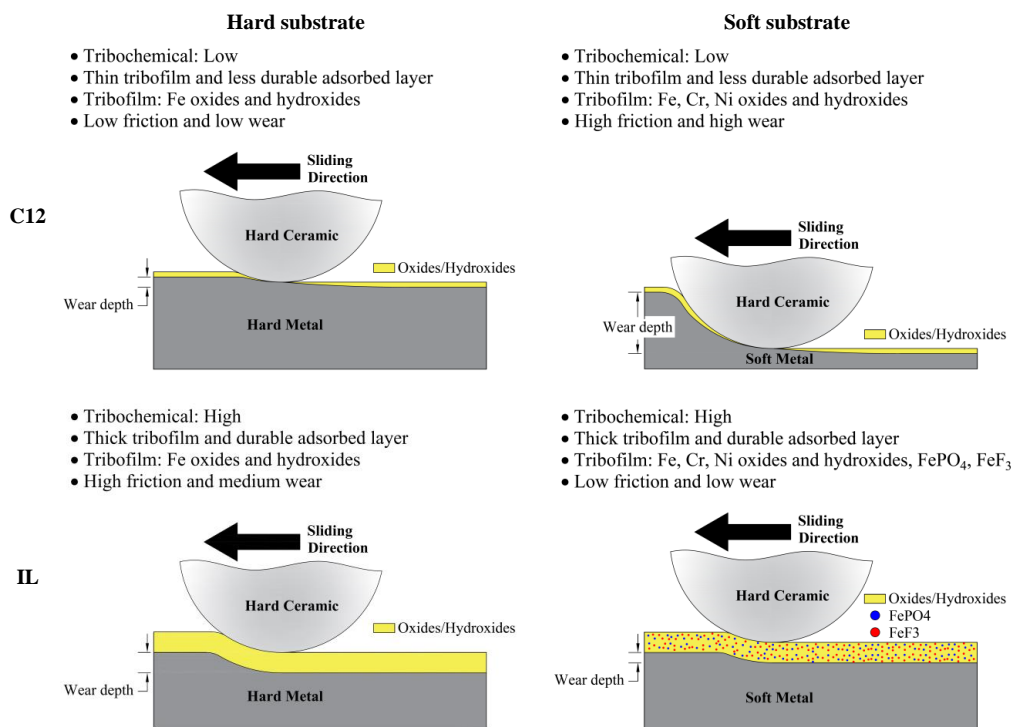


**Figure 8-10.** Schematic illustration of the wear mechanism of hard versus soft substrate lubricated by PAO-C12 and PAO-IL.

a shorter test was performed for PAO-C12 and PAO-BMP (i.e., terminated after 100 m sliding, right before the thick tribofilm formation). A detailed wear analysis is performed, and the results are shown in **Figure 8-9**. The results show that the  $\Delta A$  for PAO-BMP 100 m is ca. 50% lower than PAO-C12 100 m. In addition, the  $\beta$  value is smaller for PAO-BMP 100 m indicating more plastic deformation, suggesting that in the absence of a thick tribofilm, the durable adsorbed layer of BMP has better abrasion resistance than the less durable adsorbed layer of C12.

In the case of AISI 316L stainless steel lubricated by PAO, PAO-PP, and PAO-BMP, a thick tribofilm also forms on the wear track, as shown in **Table 8-1**. These tribofilms contain metallic oxides and hydroxides of iron, chromium, and nickel. Moreover, the tribofilm formed by PAO-PP contains iron phosphate, whereas the tribofilm formed by PAO-BMP contains iron fluoride and iron phosphate, yielding durable tribofilms. **Figure 8-8D** shows that PAO, PAO-PP, and PAO-BMP have similar low  $\beta$  values indicating similar wear mechanisms, i.e., more plastic deformation, probably due to the lower hardness of the substrate. Interestingly the wear of PAO-BMP is the lowest among all tested lubricant-metal combinations, suggesting the combination of a thick tribofilm with a durable adsorbed layer significantly reduces wear regardless of the hardness of the substrate. For PAO-C12 on AISI 316L

stainless steel, abrasive wear is the main mechanism as shown in **Figure 8-8D**. Similar to AISI 52100 steel, C12 creates a thin tribofilm and a less durable adsorbed layer. However, C12 produces the higher wear on AISI 316L stainless steel than on AISI 52100 steel, indicating the substrate hardness plays an important role in this case again.

## 8.5. Summary

A significant influence of substrate (tribomaterial) hardness on wear is found in this study, where a harder substrate gives lower wear. Interestingly, the formation of a tribofilm on a soft tribomaterial significantly reduces friction and wear; on the other hand, the formation of a tribofilm on a hard tribomaterial increases friction and wear. Therefore, surface properties such as adsorption and chemistry, both of the lubricant and the tribosurface, are factors as important as the mechanical properties of the tribomaterial to control friction and wear of lubricated tribosystems. **Figure 8-10** summarizes the wear mechanisms of the two metals studied in this work lubricated with C12 and ILs in PAO.

## 8.6. Conclusion

The tribological behavior of ILs in non-polar media was studied in detail by analyzing the effect of surface adsorption and tribofilm formation on friction and wear. In this study, two metals, i.e., hard AISI 52100 steel and soft AISI 316L stainless steel, were used to examine the effect of surface hardness and chemical composition on the tribological behavior of ILs and C12.

In the case of the harder metal, the friction and wear behavior of ILs resulted in two different scenarios. In the absence of a thick tribofilm, friction and wear were controlled by the additive surface adsorption, where a durable adsorbed layer resulted in low friction and wear. The presence of a thick tribofilm results in higher friction and wear than a thin tribofilm. Comparing within thick tribofilm samples, friction and wear are controlled by the additive's surface adsorption, where a durable adsorbed layer results in lower friction and wear.

In the case of the softer metal, the friction and wear behavior of ILs were controlled by the tribofilm formation. The tribofilm in AISI 316L steel consisted of metal and oxides from iron, chromium, and nickel. Thick tribofilms on a soft tribomaterial increase the wear resistance. In the presence of a thick tribofilm, the friction evolution is controlled by the additives' surface adsorption, where a durable adsorbed layer results in the lowest friction.

In the case of PAO-C12, thin tribofilms are formed on both AISI 52100 steel and AISI 316L stainless steel. Moreover, the C12 adsorbed layer has low shear viscosity and low shear elasticity modulus leading to a non-durable adsorbed layer. Therefore, the friction and wear evolution of C12 are mostly controlled by the hardness of the substrate, i.e., PAO-C12 on a harder substrate led to low friction and wear.

# Chapter 9

## Conclusions and future work

### 9.1. Conclusions

In this Ph.D. thesis, ionic liquids with different cation and anion moieties and alkyl chain length were compared to investigate their role as lubricant additives in low viscosity polar and non-polar base fluids. The tribological behavior and adsorption mechanisms of lubricants containing ionic liquids applied on stainless steel and bearing steel surfaces have been investigated and compared with a well-known carboxylic acid as reference additive.

Preliminary studies performed by turbidity meter showed that the alkyl chain influences the solubility of the ionic liquids in the base fluid. The study showed that long alkyl chain ILs were not fully soluble in water-glycol, while they were fully soluble in polyalphaolefin. Interestingly, the long alkyl chain ILs with non-3D anion structure were not fully soluble in neither water-glycol, nor polyalphaolefin lubricants.

In the polar base lubricant, ionic liquids alter the electrical conductivity and pH of the base fluid. All ionic liquids investigated in this Ph.D. thesis increase the electrical conductivity of water-glycol; however, only PP significantly reduce the pH of water-glycol to acidic values, whereas the others resulted in a similar pH value as the base fluid. For the non-polar base lubricant, the electrical conductivity and pH of the lubricants could not be measured due to the lack of the electrical charge mobility in the fluid.

For the polar base lubricant, studying the effect of concentration of ILs in friction and wear of AISI 316L stainless steel showed that increasing the concentration increased wear, where 4 wt.% ILs gave the highest wear due to tribocorrosion. In the case of friction, a parabolic result was found in which 1 and 2 wt.% of ILs gave the highest friction and a further increase of the concentration decreased friction. The metal dissolution at higher concentration helps in reducing friction. For the non-polar base lubricant, low concentration of ILs (0.25 wt.%) did not influence friction and wear. The friction and wear reduction were observed from 0.5 wt.% concentration, reaching a plateau at 1 wt.% where further increase in the concentration gave similar results as 1 wt.%. Here, in the absence of

tribocorrosion, the tribological behavior depended mostly on the adsorption and tribochemical reaction of the ILs with the tribosurface.

The adsorption study of the ILs and C12 by QCM-D showed that the polarity of the additives, polarity of the lubricant, pH of the lubricant, and tribosurface type played an important role on the adsorption of the additives to the sensor surface. The active molecular interaction and competitive adsorption between the ILs and the polar lubricant molecules limits the adsorbed layer formation resulting in a thinner adsorbed layer compared to the non-polar lubricant. In addition, corrosion on the steel coated sensor was observed for PP. For the stainless steel coated sensor, no corrosion was observed for any additive.

Further studies of ILs as lubricant additives were conducted by comparing the influence of tribosurface hardness. This study was performed on a bearing steel (AISI 52100) and a stainless steel (AISI 316L). The tribological behavior of the steels was investigated in the presence of ILs as lubricant additives in a polar (water-glycol) and a non-polar (PAO) base lubricant. As mentioned before, ILs in water-glycol increase the electric conductivity and alter the pH of the base fluid. Tribological tests on the hard metal revealed none or little tribocorrosion on the surface leading to a thick tribofilm formation. The formation of a thick tribofilm enhanced the wear reduction; however, the chemical composition of the tribofilm (mainly consisting of hard Fe oxides) led to a friction increase. Thus, friction and wear of a hard metal, which is also actively corroding (non-passive) in the polar medium, are controlled by tribofilm formation. Water-glycol additivated with ILs tested on a passive and soft metal resulted in a tribocorrosion process on the surface leading to the formation of a thin tribofilm. In addition, the low pH in the case of PP dissolved the passive film resulting in further thinning of the tribofilm thus leading to high friction and wear. Thus, for a passive and soft metal, the friction and wear were controlled by tribocorrosion in the polar lubricant.

The tribological behavior of the two steels were also investigated in a non-polar (polyalphaolefin) base lubricant additivated with ILs and C12. As mentioned before, due to the lack of ionic mobility in the lubricant, the conductivity and pH cannot be measured. For the harder metal, friction and wear were controlled by tribofilm formation where the presence of hard Fe oxides increased friction and wear. In the case of the passive and soft metal, tribocorrosion did not occur due to the lack of electrical conductivity in the lubricant. Thus, friction and wear were controlled by the additives' adsorbed layer properties and the tribofilm thickness, where a strongly adsorbed layer and a thick tribofilm led to excellent friction-reducing and antiwear performance.

Consequently, in this Ph.D. thesis it was found that the most important factors controlling friction and wear are the thickness and viscoelastic properties of the adsorbed layer, the thickness and

chemical composition of the tribofilm, and the hardness and chemical composition of the steel. Thus, the surface material, the lubricant and the additives, and their interaction need to be considered in order to understand the tribological behavior of the system.

In this Ph.D. thesis, the potential of ILs as lubricant additives in low viscosity base lubricants was assessed. The results showed that ILs can be used as lubricant additives for low viscosity lubricants, but several parameters need to be considered, such as, the solubility of the ILs in the base lubricant, the pH of the ILs for polar media (need to maintain a neutral pH on the lubricant), the ability of ILs to form thick and durable adsorbed layers, the ability of ILs to form thick oxide tribofilms (alloying elements in the metal surface are needed), and the ability of ILs to provide with no or mild corrosion and tribocorrosion (this can also be achieved by modifying the tribosurface composition).

## **9.2. Future work**

This Ph.D. thesis has studied the potential of ILs as lubricant additives in low viscosity base lubricants and provides with some understanding of their influence on surface adsorption and tribological behavior. However, some areas still remain for further study:

- Although the surface adsorbed layer of the additives could be analyzed by QCM-D, further analysis with a more physical approach could give better understanding about the adsorbed layer. This can be done by AFM with both surface mapping and force-distance curves. Surface mapping by AFM will provide with the actual topography of the adsorbed layer and the force-distance curves will provide the bonding strength of the adsorbed layers at the surface.
- This Ph.D. thesis showed that a durable tribofilm is needed for better friction reduction and antiwear performance; however, the study of the actual mechanical properties of the tribofilms is missing. This could be done by nanoindentation technique.
- As shown from the XPS study, the tribofilms consist of different type of oxides, thus further analysis by TEM can provide more details about the tribofilm composition bringing further understanding of the correlation between the tribofilm's composition and properties.
- Element mapping for AISI 316L stainless steel lubricated by WG-BMP showed the formation of a nickel-rich tribofilm, however a more detailed analysis needs to be done. The use of high resolution TEM can provide better understanding of this tribofilm and the reasons why nickel preferentially segregates with BMP only.

- Two types of steels were studied in this Ph.D. thesis, i.e., hard and non-passive metal and soft and passive metal. The opposite combination of properties should be tested for further understanding, i.e., soft and non-passive metal and hard and passive metal.
- Investigating the tribological performance of the fully formulated lubricant to examine the synergy effect between ionic liquid and other additives. This study can be performed both in boundary and hydrodynamic lubricating conditions.



# Chapter 10

## References

- [1] Mathieu L. *Electric surge: Carmakers' electric car plans across Europe 2019-2025*. <https://www.transportenvironment.org/discover/electric-surge-carmakers-electric-car-plans-across-europe-2019-2025/> (2019)
- [2] Chen Y, Jha S, Raut A, Zhang W, Liang H. Performance Characteristics of Lubricants in Electric and Hybrid Vehicles: A Review of Current and Future Needs. *Frontiers in Mechanical Engineering* **6**: 1–19 (2020)
- [3] European Environment Agency. CO2 emissions from cars: facts and figures. <https://www.europarl.europa.eu/news/en/headlines/society/20190313STO31218/co2-emissions-from-cars-facts-and-figures-infographics> (2019)
- [4] Holmberg K, Erdemir A. The impact of tribology on energy use and CO2 emission globally and in combustion engine and electric cars. *Tribology International* **135**: 389–396 (2019)
- [5] Van Rensselar J. The tribology of electric vehicles. *Tribology & Lubrication Technology* **75**: 34–43 (2019)
- [6] Narita K, Takekawa D. Lubricants Technology Applied to Transmissions in Hybrid Electric Vehicles and Electric Vehicles. *SAE Technical Papers* (2019)
- [7] Zhang X *et al.* Synthesis of Ultrathin WS2 Nanosheets and Their Tribological Properties as Lubricant Additives. *Nanoscale Research Letters* **11**: (2016)
- [8] Yi M, Zhang C. The synthesis of two-dimensional MoS2 nanosheets with enhanced tribological properties as oil additives. *RSC Advances* **8**: 9564–9573 (2018)
- [9] Zhang B M, Sun J L. Tribological performances of multilayer-MoS2 nanoparticles in water-based lubricating fluid. *IOP Conference Series: Materials Science and Engineering* **182**: 012023 (2017)
- [10] Arshad M S, Kovač J, Cruz S, Kalin M. Physicochemical and tribological characterizations of WDLC coatings and ionic-liquid lubricant additives: Potential candidates for low friction under boundary-lubrication conditions. *Tribology International* **151**: (2020)
- [11] Earle M J, Seddon K R. Ionic liquids. Green solvents for the future. *Pure and Applied*

*Chemistry* **72**: 1391–1398 (2000)

- [12] Zhao H. Innovative applications of ionic liquids as ‘green’ engineering liquids. *Chemical Engineering Communications* **193**: 1660–1677 (2006)
- [13] Welton T. Room-Temperature Ionic Liquids. Solvents for Synthesis and Catalysis. *Chemical Reviews* **99**: 2071–2084 (1999)
- [14] Somers A E, Howlett P C, MacFarlane D R, Forsyth M. A review of ionic liquid lubricants. *Lubricants* **1**: 3–21 (2013)
- [15] Iglesias P, Bermúdez M D, Carrión F J, Martínez-Nicolás G. Friction and wear of aluminium-steel contacts lubricated with ordered fluids-neutral and ionic liquid crystals as oil additives. *Wear* **256**: 386–392 (2004)
- [16] Qu J *et al.* Antiwear performance and mechanism of an oil-miscible ionic liquid as a lubricant additive. *ACS Applied Materials and Interfaces* **4**: 997–1002 (2012)
- [17] Zhang S, Hu L, Qiao D, Feng D, Wang H. Vacuum tribological performance of phosphonium-based ionic liquids as lubricants and lubricant additives of multialkylated cyclopentanes. *Tribology International* **66**: 289–295 (2013)
- [18] Barnhill W C *et al.* Phosphonium-organophosphate ionic liquids as lubricant additives: Effects of cation structure on physicochemical and tribological characteristics. *ACS Applied Materials and Interfaces* **6**: 22585–22593 (2014)
- [19] Amde M, Liu J F, Pang L. Environmental Application, Fate, Effects, and Concerns of Ionic Liquids: A Review. *Environmental Science and Technology* **49**: 12611–12627 (2015)
- [20] Xiao H. Ionic Liquid Lubricants: Basics and Applications. *Tribology Transactions* **60**: 20–30 (2017)
- [21] Jost P. *A report on the present position and industry’s needs.* (1966)
- [22] Dowson D. *History of tribology.* London (UK): Addison-Wesley Longman Limited, 1978.
- [23] Czichos H. *Tribology: A Systems Approach to the Science and Technology of Friction, Lubrication and Wear.* Amsterdam (Netherlands): Elsevier Scientific Publishing Company, 1978.
- [24] Mang T, Dresel W. *Lubricants and Lubrication.* Weinheim (Germany): Wiley-VCH Verlag GmbH & Co. KGaA, 2007.

- [25] Stachowiak G W, Batchelor A W. *Engineering Tribology*. Oxford (UK): Elsevier, 2014.
- [26] Minami I. Molecular science of lubricant additives. *Applied Sciences (Switzerland)* **7**: (2017)
- [27] Gosvami N N *et al.* Mechanisms of antiwear tribofilm growth revealed in situ by single-asperity sliding contacts. *Science* **348**: 102–106 (2015)
- [28] Pawlak Z. *Tribochemistry of Lubricating Oils*. Amsterdam (Netherlands): Elsevier B.V., 2003.
- [29] Rudnick L R. *Synthetics, Mineral Oils, and Bio-Based Lubricants*. Boca Raton, Florida (USA): CRC Press, 2020.
- [30] Monoethylene Glycol Physical Properties. <https://www.meglobal.biz/products/monoethylene-glycol/physicalproperties/>
- [31] Diethylene Glycol Physical Properties. <https://www.meglobal.biz/products/diethylene-glycol/physicalproperties/>
- [32] Propylene Glycol (PG) Industrial Grade. <https://www.dow.com/en-us/pdp.propylene-glycol-pg-industrial-grade.70511z.html>
- [33] Dipropylene Glycol (DPG) Regular Grade. <https://www.dow.com/en-us/pdp.dipropylene-glycol-dpg-regular-grade.21603z.html>
- [34] Blok H. The flash temperature concept. *Wear* **6**: 483–494 (1963)
- [35] Kapsa P, Martin J M. Boundary lubricant films: a review. *Tribology International* **15**: 37–42 (1982)
- [36] Morina A, Neville A. Tribofilms: Aspects of formation, stability and removal. *Journal of Physics D: Applied Physics* **40**: 5476–5487 (2007)
- [37] Jacobson S, Hogmark S. Tribofilms – On the crucial importance of tribologically induced surface modifications. *Recent Developments in Wear Prevention, Friction and Lubrication* **661**: 197–225 (2010)
- [38] Sahoo R R, Biswas S K. Frictional response of fatty acids on steel. *Journal of Colloid and Interface Science* **333**: 707–718 (2009)
- [39] Jahanmir S, Beltzer M. An adsorption model for friction in boundary lubrication. *ASLE Transactions* **29**: 423–430 (1986)
- [40] Okabe H, Masuko M, Sakurai K. Dynamic behavior of surface-adsorbed molecules under boundary lubrication. *ASLE Transactions* **24**: 467–473 (1981)

- [41] Mukerjee P, Mysels K J. *Critical Micelle Concentrations of Aqueous Surfactant Systems*. Washington D.C. (USA): National Bureau of Standards, 1972.
- [42] Bernat S, Armada S, Espallargas N. Friction Mechanisms by Carboxylic Acids in Aqueous Lubricants. *Tribology Letters* **66**: 1–15 (2018)
- [43] Spikes H. Friction Modifier Additives. *Tribology Letters* **60**: 1–26 (2015)
- [44] Guegan J, Southby M, Spikes H. Friction Modifier Additives, Synergies and Antagonisms. *Tribology Letters* **67**: 1–12 (2019)
- [45] Graham J, Spikes H, Korcek S. The friction reducing properties of molybdenum dialkyldithiocarbamate additives: part i — factors influencing friction reduction. *Tribology Transactions* **44**: 626–636 (2001)
- [46] Khaemba D N, Jarnias F, Thiebaut B, Neville A, Morina A. The role of surface roughness and slide-roll ratio on the decomposition of MoDTC in tribological contacts. *Journal of Physics D: Applied Physics* **50**: aa5905 (2017)
- [47] Khanmohammadi H, Wijanarko W, Espallargas N. Ionic Liquids as Additives in Water-Based Lubricants: From Surface Adsorption to Tribofilm Formation. *Tribology Letters* **68**: 130 (2020)
- [48] Spikes H. Low- and zero-sulphated ash, phosphorus and sulphur anti-wear additives for engine oils. *Lubrication Science* **20**: 103–136 (2008)
- [49] Spikes H. The history and mechanisms of ZDDP. *Tribology Letters* **17**: 469–489 (2004)
- [50] Sarin R, Tuli D K, Verma A S, Rai M M, Bhatnagar A K. Additive-additive interactions: Search for synergistic FM-EP-AW composition. *Wear* **174**: 93–102 (1994)
- [51] Sarin R, Tuli D K, Rai Faridabad (India); and others] M M [Indian O C. Titanium dithiophosphates: A new class of multifunctional lubricant additives. (1995)
- [52] Zhang J, Liu W, Xue Q, Wang Q. Investigation of the friction and wear behaviors of Cu(I) and Cu(II) dioctyldithiophosphates as additives in liquid paraffin. *Wear* **216**: 35–40 (1998)
- [53] Boshui C, Junxiu D, Guoxu C. Tribochemistry of gadolinium dialkyldithiophosphate. *Wear* **196**: 16–20 (1996)
- [54] Nicholls M A, Do T, Norton P R, Kasrai M, Bancroft G M. Review of the lubrication of metallic surfaces by zinc dialkyl-dithiophosphates. *Tribology International* **38**: 15–39 (2005)

- [55] Yamaguchi E S, Ryason P R. Inelastic electron tunneling spectra of lubricant oil additives on native aluminum oxide surfaces. *Tribology Transactions* **36**: 367–374 (1993)
- [56] Martin J M. Antiwear mechanisms of zinc dithiophosphate: A chemical hardness approach. *Tribology Letters* **6**: 1–8 (1999)
- [57] Canter N. Special Report: ZDDP's uncertain future. [https://www.stle.org/files/TLTArchives/2019/09\\_September/Tech\\_Beat.aspx](https://www.stle.org/files/TLTArchives/2019/09_September/Tech_Beat.aspx) (2019)
- [58] THE EUROPEAN COMMISSION. COMMISSION REGULATION (EU) No 136/2014. *Official Journal of the European Union* (2014)
- [59] Amiril S A S, Rahim E A, Syahrullail S. A review on ionic liquids as sustainable lubricants in manufacturing and engineering: Recent research, performance, and applications. *Journal of Cleaner Production* **168**: 1571–1589 (2017)
- [60] Li X, Zhao D, Fei Z, Wang L. Applications of functionalized ionic liquids. *Science in China, Series B: Chemistry* **49**: 385–401 (2006)
- [61] Palacio M, Bhushan B. A review of ionic liquids for green molecular lubrication in nanotechnology. *Tribology Letters* **40**: 247–268 (2010)
- [62] Koel M. Ionic liquids in chemical analysis. *Critical Reviews in Analytical Chemistry* **35**: 177–192 (2005)
- [63] Wilkes J S, Levisky J A, Wilson R A, Hussey C L. Dialkylimidazolium chloroaluminate melts: a new class of room-temperature ionic liquids for electrochemistry, spectroscopy and synthesis. *Inorganic Chemistry* **21**: 1263–1264 (1982)
- [64] Ye C, Liu W, Chen Y, Yu L. Room-temperature ionic liquids: a novel versatile lubricant. *Chemical communications (Cambridge, England)* **21**: 2244–5 (2001)
- [65] Liu W, Ye C, Gong Q, Wang H, Wang P. Tribological performance of room-temperature ionic liquids as lubricant. *Tribology Letters* **13**: 81–85 (2002)
- [66] Lu Q, Wang H, Ye C, Liu W, Xue Q. Room temperature ionic liquid 1-ethyl-3-hexylimidazolium- bis(trifluoromethylsulfonyl)-imide as lubricant for steel-steel contact. *Tribology International* **37**: 547–552 (2004)
- [67] Wang H, Lu Q, Ye C, Liu W, Cui Z. Friction and wear behaviors of ionic liquid of alkyylimidazolium hexafluorophosphates as lubricants for steel/steel contact. *Wear* **256**: 44–48 (2004)

- [68] Kamimura H, Kubo T, Minami I, Mori S. Effect and mechanism of additives for ionic liquids as new lubricants. *Tribology International* **40**: 620–625 (2007)
- [69] Somers A E *et al.* Ionic liquids as antiwear additives in base oils: Influence of structure on miscibility and antiwear performance for steel on aluminum. *ACS Applied Materials and Interfaces* **5**: 11544–11553 (2013)
- [70] Qu J, Truhan J J, Dai S, Luo H, Blau P J. Ionic liquids with ammonium cations as lubricants or additives. *Tribology Letters* **22**: 207–214 (2006)
- [71] Jiménez A E, Bermúdez M D. Ionic liquids as lubricants for steel-aluminum contacts at low and elevated temperatures. *Tribology Letters* **26**: 53–60 (2007)
- [72] Chen *et al.* Tribological performance of an ionic liquid as a lubricant for steel/aluminium contacts. *Journal of Synthetic Lubrication* **20**: 217–225 (2003)
- [73] Mu Z, Zhou F, Zhang S, Liang Y, Liu W. Effect of the functional groups in ionic liquid molecules on the friction and wear behavior of aluminum alloy in lubricated aluminum-on-steel contact. *Tribology International* **38**: 725–731 (2005)
- [74] Jiménez A E, Bermúdez M D, Iglesias P, Carrión F J, Martínez-Nicolás G. 1-N-alkyl -3-methylimidazolium ionic liquids as neat lubricants and lubricant additives in steel–aluminium contacts. *Wear* **260**: 766–782 (2006)
- [75] Jiménez A E, Bermúdez M D, Carrión F J, Martínez-Nicolás G. Room temperature ionic liquids as lubricant additives in steel-aluminium contacts: Influence of sliding velocity, normal load and temperature. *Wear* **261**: 347–359 (2006)
- [76] Mu Z *et al.* Investigation of tribological behavior of Al-Si alloy against steel lubricated with ionic liquids of 1-diethylphosphonyl-n-propyl-3-alkylimidazolium tetrafluoroborate. *Journal of Tribology* **130**: 3–7 (2008)
- [77] Qu J *et al.* Tribological characteristics of aluminum alloys sliding against steel lubricated by ammonium and imidazolium ionic liquids. *Wear* **267**: 1226–1231 (2009)
- [78] Lawes S D A, Hainsworth S V., Blake P, Ryder K S, Abbott A P. Lubrication of steel/steel contacts by choline chloride ionic liquids. *Tribology Letters* **37**: 103–110 (2010)
- [79] Fan M *et al.* The ecotoxicity and tribological properties of choline monocarboxylate ionic liquid lubricants. *Lubrication Science* **32**: 1–9 (2020)
- [80] Sharma V, Doerr N, Aswath P B. Chemical-mechanical properties of tribofilms and their

relationship to ionic liquid chemistry. *RSC Advances* **6**: 22341–22356 (2016)

- [81] Liu X Q, Zhou F, Liang Y M, Liu W M. Tribological performance of phosphonium based ionic liquids for an aluminum-on-steel system and opinions on lubrication mechanism. *Wear* **261**: 1174–1179 (2006)
- [82] Weng L J, Liu X Q, Liang Y M, Xue Q J. Effect of tetraalkylphosphonium based ionic liquids as lubricants on the tribological performance of a steel-on-steel system. *Tribology Letters* **26**: 11–17 (2007)
- [83] Minami I, Inada T, Sasaki R, Nanao H. Tribo-chemistry of phosphonium-derived ionic liquids. *Tribology Letters* **40**: 225–235 (2010)
- [84] Otero I *et al.* Ionic liquids based on phosphonium cations As neat lubricants or lubricant additives for a steel/steel contact. *ACS Applied Materials and Interfaces* **6**: 13115–13128 (2014)
- [85] Totolin V *et al.* Tribological investigations of ionic liquids in ultra-high vacuum environment. *Lubrication Science* **26**: 514–524 (2014)
- [86] Somers A E *et al.* A comparison of phosphorus and fluorine containing IL lubricants for steel on aluminium. *Physical Chemistry Chemical Physics* **14**: 8224–8231 (2012)
- [87] Somers A E, Howlett P C, Sun J, MacFarlane D R, Forsyth M. Phosphonium ionic liquids as lubricants for aluminium-steel. *WIT Transactions on Engineering Sciences* **66**: 273–283 (2010)
- [88] Minami I, Kita M, Kubo T, Nanao H, Mori S. The tribological properties of ionic liquids composed of trifluorotris(pentafluoroethyl) phosphate as a hydrophobic anion. *Tribology Letters* **30**: 215–223 (2008)
- [89] Pejaković V *et al.* Pyrrolidinium sulfate and ammonium sulfate ionic liquids as lubricant additives for steel/steel contact lubrication. *Proceedings of the Institution of Mechanical Engineers, Part J: Journal of Engineering Tribology* **226**: 923–932 (2012)
- [90] Minami I. Ionic liquids in tribology. *Molecules (Basel, Switzerland)* **14**: 2286–2305 (2009)
- [91] Sanes J, Carrión F J, Bermúdez M D, Martínez-Nicolás G. Ionic liquids as lubricants of polystyrene and polyamide 6-steel contacts. Preparation and properties of new polymer-ionic liquid dispersions. *Tribology Letters* **21**: 121–133 (2006)
- [92] Zhang L, Feng D, Xu B. Tribological characteristics of alkylimidazolium diethyl phosphates

- ionic liquids as lubricants for steel-steel contact. *Tribology Letters* **34**: 95–101 (2009)
- [93] Jiang D, Hu L, Feng D. Crown-type ionic liquids as lubricants for steel-on-steel system. *Tribology Letters* **41**: 417–424 (2011)
- [94] Qu J, Blau P J, Dai S, Luo H, Meyer H M. Ionic Liquids as Novel Lubricants and Additives for Diesel Engine Applications. *Tribology Letters* **35**: 181–189 (2009)
- [95] Jiménez A E, Bermúdez M D. Imidazolium ionic liquids as additives of the synthetic ester propylene glycol dioleate in aluminium-steel lubrication. *Wear* **265**: 787–798 (2008)
- [96] Cai M *et al.* Imidazolium ionic liquids as antiwear and antioxidant additive in poly(ethylene glycol) for steel/steel contacts. *ACS Applied Materials and Interfaces* **2**: 870–876 (2010)
- [97] Kronberger M, Pejaković V, Gabler C, Kalin M. How anion and cation species influence the tribology of a green lubricant based on ionic liquids. *Proceedings of the Institution of Mechanical Engineers, Part J: Journal of Engineering Tribology* **226**: 933–951 (2012)
- [98] Mahrova M *et al.* Pyridinium based dicationic ionic liquids as base lubricants or lubricant additives. *Tribology International* **82**: 245–254 (2015)
- [99] Wang Y *et al.* Ibuprofen-Based Ionic Liquids as Additives for Enhancing the Lubricity and Antiwear of Water–Ethylene Glycol Liquid. *Tribology Letters* **65**: (2017)
- [100] Zheng G *et al.* Tribological properties and surface interaction of novel water-soluble ionic liquid in water-glycol. *Tribology International* **116**: 440–448 (2017)
- [101] Cai M, Yu Q, Liu W, Zhou F. Ionic liquid lubricants: When chemistry meets tribology. *Chemical Society Reviews* **49**: 7753–7818 (2020)
- [102] Battez A H *et al.* Tribological behaviour of two imidazolium ionic liquids as lubricant additives for steel/steel contacts. *Wear* **266**: 1224–1228 (2009)
- [103] Zhang C *et al.* Tribological behavior of 1-methyl-3-hexadecylimidazolium tetrafluoroborate ionic liquid crystal as a neat lubricant and as an additive of liquid paraffin. *Tribology Letters* **46**: 49–54 (2012)
- [104] Viesca J L *et al.* FAP- anion ionic liquids used in the lubrication of a steel-steel contact. *Tribology Letters* **52**: 431–437 (2013)
- [105] Yao M, Liang Y, Xia Y, Zhou F. Bisimidazolium Ionic Liquids as the High-Performance Antiwear Additives in Poly(ethylene glycol) for Steel–Steel Contacts. *ACS Applied Materials*



& *Interfaces* **1**: 467–471 (2009)

- [106] Zhang H, Xia Y, Yao M, Jia Z, Liu Z. The influences of methyl group at C2 position in imidazolium ring on tribological properties. *Tribology Letters* **36**: 105–111 (2009)
- [107] Gusain R, Singh R, Sivakumar K L N, Khatri O P. Halogen-free imidazolium/ammonium-bis(salicylato)borate ionic liquids as high performance lubricant additives. *RSC Advances* **4**: 1293–1301 (2014)
- [108] Gusain R, Khatri O P. Halogen-free ionic liquids: Effect of chelated orthoborate anion structure on their lubrication properties. *RSC Advances* **5**: 25287–25294 (2015)
- [109] Khatri P K, Joshi C, Thakre G D, Jain S L. Halogen-free ammonium-organoborate ionic liquids as lubricating additives: The effect of alkyl chain lengths on the tribological performance. *New Journal of Chemistry* **40**: 5294–5299 (2016)
- [110] Pejaković V, Kronberger M, Kalin M. Influence of temperature on tribological behaviour of ionic liquids as lubricants and lubricant additives. *Lubrication Science* **26**: 107–115 (2014)
- [111] Gusain R, Dhingra S, Khatri O P. Fatty-Acid-Constituted Halogen-Free Ionic Liquids as Renewable, Environmentally Friendly, and High-Performance Lubricant Additives. *Industrial and Engineering Chemistry Research* **55**: 856–865 (2016)
- [112] Zhu L, Zhao G, Wang X. Investigation on three oil-miscible ionic liquids as antiwear additives for polyol esters at elevated temperature. *Tribology International* **109**: 336–345 (2017)
- [113] Zheng G *et al.* Surface analysis of tribofilm formed by phosphorus-nitrogen (P-N) ionic liquid in synthetic ester and water-based emulsion. *Tribology International* **115**: 212–221 (2017)
- [114] Yu B *et al.* Oil-miscible and non-corrosive phosphonium-based ionic liquids as candidate lubricant additives. *Wear* **289**: 58–64 (2012)
- [115] Fan M, Yang D, Wang X, Liu W, Fu H. DOSS- Based QAILs: As both neat lubricants and lubricant additives with excellent tribological properties and good detergency. *Industrial and Engineering Chemistry Research* **53**: 17952–17960 (2014)
- [116] Huang G, Yu Q, Ma Z, Cai M, Liu W. Probing the lubricating mechanism of oil-soluble ionic liquids additives. *Tribology International* **107**: 152–162 (2017)
- [117] Yu Q *et al.* Task-Specific Oil-Miscible Ionic Liquids Lubricate Steel/Light Metal Alloy: A Tribochemistry Study. *Advanced Materials Interfaces* **5**: 1–12 (2018)

- [118] Qu J *et al.* Comparison of an oil-miscible ionic liquid and ZDDP as a lubricant anti-wear additive. *Tribology International* **71**: 88–97 (2014)
- [119] Qiao D, Wang H, Feng D. Tribological performance and mechanism of phosphate ionic liquids as additives in three base oils for steel-on-aluminum contact. *Tribology Letters* **55**: 517–531 (2014)
- [120] Cai Z bing *et al.* Comparison of the tribological behavior of steel-steel and Si<sub>3</sub>N<sub>4</sub>-steel contacts in lubricants with ZDDP or ionic liquid. *Wear* **319**: 172–183 (2014)
- [121] Anand M *et al.* Ionic liquids as tribological performance improving additive for in-service and used fully-formulated diesel engine lubricants. *Wear* **334–335**: 67–74 (2015)
- [122] Fu X, Sun L, Zhou X, Li Z, Ren T. Tribological Study of Oil-Miscible Quaternary Ammonium Phosphites Ionic Liquids as Lubricant Additives in PAO. *Tribology Letters* **60**: (2015)
- [123] Zheng D, Wang X, Zhang M, Ju C. Synergistic Effects Between the Two Choline-Based Ionic Liquids as Lubricant Additives in Glycerol Aqueous Solution. *Tribology Letters* **67**: 1–13 (2019)
- [124] Avilés M D, Carrión-Vilches F J, Sanes J, Bermúdez M D. Diprotic Ammonium Succinate Ionic Liquid in Thin Film Aqueous Lubrication and in Graphene Nanolubricant. *Tribology Letters* **67**: (2019)
- [125] Phillips B S, Zabinski J S. Ionic liquid lubrication effects on ceramics in a water environment. *Tribology Letters* **17**: 533–541 (2004)
- [126] Xie G, Liu S, Guo D, Wang Q, Luo J. Investigation of the running-in process and friction coefficient under the lubrication of ionic liquid/water mixture. *Applied Surface Science* **255**: 6408–6414 (2009)
- [127] Wang Y, Yu Q, Cai M, Zhou F, Liu W. Halide-free PN ionic liquids surfactants as additives for enhancing tribological performance of water-based liquid. *Tribology International* **128**: 190–196 (2018)
- [128] Dong R *et al.* Towards superior lubricity and anticorrosion performances of proton-type ionic liquids additives for water-based lubricating fluids. *Chemical Engineering Journal* **383**: (2020)
- [129] Johannsmann D. *The Quartz Crystal Microbalance in Soft Matter Research*. Cham: Springer International Publishing, 2015.
- [130] Sauerbrey G. Verwendung von Schwingquarzen zur Wägung dünner Schichten und zur

Mikrowägung. *Zeitschrift für Physik* **155**: 206–222 (1959)

- [131] Höök F *et al.* Variations in coupled water, viscoelastic properties, and film thickness of a Mefp-1 protein film during adsorption and cross-linking: A quartz crystal microbalance with dissipation monitoring, ellipsometry, and surface plasmon resonance study. *Analytical Chemistry* **73**: 5796–5804 (2001)
- [132] Rodahl M, Kasemo B. On the measurement of thin liquid overlayers with the quartz-crystal microbalance. *Sensors and Actuators A: Physical* **54**: 448–456 (1996)
- [133] Voinova M V, Rodahl M, Jonson M, Kasemo B. Viscoelastic Acoustic Response of Layered Polymer Films at Fluid-Solid Interfaces: Continuum Mechanics Approach. *Physica Scripta* **59**: 391–396 (1999)
- [134] Bjerregaard L, Geels K, Ottesen B, Rückert M. *Metalog Guide: Your Guide to the Perfect Metallographic Structure*. Rødovre (Denmark): Struers A/S, 2020.
- [135] Turbidity Analyzer Working Principle. <https://instrumentationtools.com/turbidity-analyzer-working-principle/>
- [136] Totten, George E., De Negri V J. *Handbook of Hydraulic Fluid Technology*. Boca Raton, Florida (USA): CRC Press, 2012.
- [137] Mathas D *et al.* Evaluation of Methods for Viscosity Simulations of Lubricants at Different Temperatures and Pressures: A Case Study on PAO-2. *Tribology Transactions* **64**: 1138–1148 (2021)
- [138] Archard J F. Contact and rubbing of flat surfaces. *Journal of Applied Physics* **24**: 981–988 (1953)
- [139] Bruce R W. *Handbook of lubrication and tribology, Volume II: Theory and Design*. Boca Raton, Florida (USA): CRC Press, 2012.
- [140] Montgomery D C. *Design and Analysis of Experiments*. New Jersey (USA): John Wiley and Sons, Inc., .
- [141] Illowsky B, Dean S. *Introductory Statistics*. Houston, Texas (USA): 2013.
- [142] SEM vs TEM. <https://www.technologynetworks.com/analysis/articles/sem-vs-tem-331262>
- [143] Rigort A, Plitzko J M. Cryo-focused-ion-beam applications in structural biology. *Archives of Biochemistry and Biophysics* **581**: 122–130 (2015)

- [144] The principle of SE detection. <https://www.hitachi-hightech.com/global/science/products/microscopes/electron-microscope/tem/hd2700.html>
- [145] Energy-Dispersive X-ray Spectroscopy (EDS). [https://chem.libretexts.org/Courses/Franklin\\_and\\_Marshall\\_College/Introduction\\_to\\_Materials\\_Characterization\\_\\_CHM\\_412\\_Collaborative\\_Text/Spectroscopy/Energy-Dispersive\\_X-ray\\_Spectroscopy\\_\(EDS\)](https://chem.libretexts.org/Courses/Franklin_and_Marshall_College/Introduction_to_Materials_Characterization__CHM_412_Collaborative_Text/Spectroscopy/Energy-Dispersive_X-ray_Spectroscopy_(EDS))
- [146] *Surface Analysis: The Principal Techniques, 2nd Edition*. John Wiley and Sons, Ltd, 2009.
- [147] Casella I G, Guascito M R, Sannazzaro M G. Voltammetric and XPS investigations of nickel hydroxide electrochemically dispersed on gold surface electrodes. *Journal of Electroanalytical Chemistry* **462**: 202–210 (1999)
- [148] Lei Y, Jiang J, Bi T, Du J, Pang X. Tribological behavior of: In situ fabricated graphene-nickel matrix composites. *RSC Advances* **8**: 22113–22121 (2018)
- [149] Fredriksson W, Malmgren S, Gustafsson T, Gorgoi M, Edström K. Full depth profile of passive films on 316L stainless steel based on high resolution HAXPES in combination with ARXPS. *Applied Surface Science* **258**: 5790–5797 (2012)
- [150] Zavieh A H, Espallargas N. The effect of friction modifiers on tribocorrosion and tribocorrosion-fatigue of austenitic stainless steel. *Tribology International* **111**: 138–147 (2017)
- [151] Yu B *et al.* Tribological evaluation of  $\alpha$ , over( $\omega$ ,')-diimidazoliumalkylene hexafluorophosphate ionic liquid and benzotriazole as additive. *Tribology International* **41**: 797–801 (2008)
- [152] Long Y, Bouchet M-I D B, Lubrecht T, Onodera T, Martin J M. Superlubricity of glycerol by self-sustained chemical polishing. *Scientific Reports* **9**: 6286 (2019)
- [153] Marcus P, Bussell M E. XPS study of the passive films formed on molybdenum-implanted austenitic stainless steels. *Applied Surface Science* **59**: 7–21 (1992)
- [154] Ding Y *et al.* Synthesis of short-chain passivated carbon quantum dots as the light emitting layer towards electroluminescence. *RSC Advances* **7**: 28754–28762 (2017)
- [155] Li H *et al.* Tuning the Chemical Hardness of Boron Nitride Nanosheets by Doping Carbon for Enhanced Adsorption Capacity. *ACS Omega* **2**: 5385–5394 (2017)
- [156] Urtis L A *et al.* Influence of water on tribolayer growth when lubricating steel with a

fluorinated phosphonium dicyanamide ionic liquid. *Lubricants* **7**: (2019)

- [157] Pourbaix M. *Atlas of electrochemical equilibria in aqueous solutions*. Houston, Texas (USA): National Association of Corrosion Engineers, 1974.
- [158] He S, Meng Y, Tian Y. Correlation between adsorption/desorption of surfactant and change in friction of stainless steel in aqueous solutions under different electrode potentials. *Tribology Letters* **41**: 485–494 (2011)
- [159] Losada-Pérez P, Khorshid M, Renner F U. Interactions of aqueous imidazolium-based ionic liquid mixtures with solid-supported phospholipid vesicles. *PLoS ONE* **11**: 1–15 (2016)
- [160] López-Ortega A, Arana J L, Bayón R. On the comparison of the tribocorrosion behavior of passive and non-passivating materials and assessment of the influence of agitation. *Wear* **456–457**: (2020)
- [161] Igual Munoz A, Espallargas N, Mischler S. *Tribocorrosion*. Cham (Switzerland): Springer International Publishing, 2020.

*This page is intentionally left blank*

## **Paper I**

Ionic liquids as boundary additives in water-based and PAO lubricants

W. Wijanarko, H. Khanmohammadi, and N. Espallargas

Friction 2021

DOI: [10.1007/s40544-021-0550-0](https://doi.org/10.1007/s40544-021-0550-0)

*This page is intentionally left blank*



# Ionic liquids as boundary additives in water-based and PAO lubricants

Wahyu WIJANARKO<sup>1,2,\*</sup>, Hamid KHANMOHAMMADI<sup>1</sup>, Nuria ESPALLARGAS<sup>1,\*</sup>

<sup>1</sup> Norwegian Tribology Center, Department of Mechanical and Industrial Engineering, Norwegian University of Science and Technology (NTNU), Trondheim 7491, Norway

<sup>2</sup> Department of Mechanical Engineering, Sepuluh Nopember Institute of Technology (ITS), Surabaya 6011, Indonesia

Received: 11 March 2021 / Revised: 29 April 2021 / Accepted: 23 August 2021

© The author(s) 2021.

**Abstract:** Ionic liquids have been widely discussed as potential lubricants, however, their properties make them also very good potential candidates as lubricant additives (e.g., friction modifiers and anti-wear). In this work, the tribological study of two ionic liquids (tributylmethylphosphonium dimethylphosphate (PP), and 1-butyl-1-methylpyrrolidinium tris(pentafluoroethyl)trifluorophosphate (BMP)) as lubricant additives has been performed on stainless steel (AISI 316L) exposed to polar (water-glycol) and non-polar (polyalphaolefin) based lubricants under boundary lubricating conditions. The performance of these ionic liquids as lubricant additives has been compared to a classical organic friction modifier (dodecanoic acid (C12)). The water-glycol lubricant formulated with the two ionic liquids showed friction values higher than the same base lubricant formulated with dodecanoic acid, however, opposite results were observed for polyalphaolefin (PAO). A detailed surface chemical analysis using X-ray photoelectron spectroscopy (XPS) revealed differences in the passive/tribofilm thickness and chemical composition of the stainless steel surface tested in all lubricants. In the case of the polar lubricant additivated with ionic liquids, the tribochemical reaction accompanied by a tribocorrosion process led to the formation of an unstable passive/tribofilm resulting in high friction and wear. However, in the absence of tribocorrosion process (polyalphaolefin base lubricant), the tribochemical reaction led to the formation of a stable passive/tribofilm resulting in low friction and wear. A detailed surface and subsurface investigation of the microstructure using scanning electron microscopy equipped with a focused ion beam (SEM-FIB) showed that high wear rates resulted in thicker recrystallization region under the wear track surface. Among all lubricant additives tested in this work, BMP in non-polar lubricant media showed the best tribological performance.

**Keywords:** water lubricant; polyalphaolefin (PAO); ionic liquids; tribochemistry; tribocorrosion; tribofilm

## 1 Introduction

In this modern era, energy efficiency has become a significant issue in automotive and industrial sectors worldwide. In system components consisting of moving parts, wear and friction play a significant role in the energy consumption. A recent study shows that 23% of the world's total energy consumption was lost in tribological contacts to overcome friction (20%)

and to repair the worn parts due to wear or wear-related failures (3%) [1]. Lubrication is needed in moving parts to provide low-friction and wear-protective boundary films to protect surfaces. Lubricants consists of about 70%–99% base oil and 30%–1% chemical additives depending on the application and use of the lubricant. Base oils have two main sources, biological (animal or vegetable sources) and non-biological (mineral or synthetic oils produced by the

\* Corresponding authors: Wahyu WIJANARKO, E-mail: wahyu.wijanarko@ntnu.no, wijanarko@me.its.ac.id; Nuria ESPALLARGAS, E-mail: nuria.espallargas@ntnu.no

distillation and cracking process of crude oil) leading to a broad variety of hydrocarbons that can be polar and non-polar. For some specific applications where fire safety is the main requirement, water-based lubricants are also formulated (i.e., typically ca. 1:1 mixture of water and glycols or any other polar hydrocarbon that helps increasing viscosity). The primary function of the base oil is to lubricate and act as a carrier of additives. Additives are chemical compounds that improve the performance of base oils and are meant for enhancing an already existing property (viscosity, pour point, oxidation resistance, etc.) or to add a new property (cleaning/suspending ability, antiwear performance, corrosion control, friction control, etc.). Each additive or group of additives have a function in different or several lubricating regimes (i.e., boundary, mixed, and hydrodynamic regimes). Friction modifiers and anti-wear additives are most critical in the boundary/mixed lubricating conditions and are the focus of this work due to their relevance for future applications in low and ultra-low viscosity lubricants used in, for example, electric vehicles [2].

Commonly used friction modifiers are carboxylic acids which have a polar head and a non-polar hydrocarbon tail. They are commonly known as organic friction modifiers (OFMs). They have been used since the 1920s and due to their amphiphilic molecular structure, the OFMs can be dissolved in polar and non-polar media [3]. The polar head tends to adsorb on metal surfaces while the non-polar tail stretches out to the lubricant base preventing contact between adjacent sliding surfaces thus providing low friction. There are two main parameters limiting the functionality of carboxylic acids, i.e., high temperature and high pressure [4]. When the mechanical conditions in a tribological system become severe (very high pressure in the boundary lubricating regime), the friction modifier on the moving surface tends to desorb. In this extreme boundary lubricating condition, anti-wear additives are then required to preserve the integrity of the surfaces in contact. A well-known anti-wear additive is zinc dialkyldithiophosphate (ZDDP), which was developed in the 1940s as an antioxidant, but its ability to reduce wear was soon discovered [3]. The ability of ZDDP to overcome wear lies on its capability to form a protective film on the metal surface through tribochemical reactions [5].

However, the degradation products of ZDDP pose environmental risks thus its use needs to be reduced to meet the Euro 5 and Euro 6 standards [6, 7]. Therefore, current trends in industry to maintain low friction and wear protection in systems working in boundary lubricating conditions (e.g., electric vehicles using low and ultra-low viscosity lubricants) are pushing the need to find new friction and anti-wear additives with a greener perspective as well, for example, ionic liquids.

Ionic liquids (ILs) are organic salts, containing a positive (cation) and a negative (anion) part, that are liquid at low temperature (usually  $<100$  °C). Ionic liquids are considered as “green” substances due to their extremely low volatility (not emitting hazardous volatile compounds) [8, 9]. But they offer other benefits as well, such as low melting points (liquid at room temperature), chemical and thermal stability (high-temperature operation), non-flammability, high ionic conductivity, high heat capacity, high thermal conductivity (facilitating the removal of excessive heat), and high polarity (highly surface active and adsorbing) [10–12]. Their chemical and physical properties can be tuned by changing the anion and cation composition to obtain task-specific ILs structures. This flexibility makes ILs ideal candidates for lubricants for extreme conditions, such as high shear and high loads, extreme temperatures, and even ultra-high vacuum [13, 14]. In addition, some research works performed on ILs as lubricant additives have proven that ILs have excellent friction-reduction and anti-wear properties [13, 15–17].

The mechanisms by which ILs are potential good candidates as lubricant additives are still not clear in literature and this can be due to the vast amount of chemistries available, making it difficult to find a unique distinctive trend. Two main lubricating mechanisms for ILs are proposed/found in literature: (1) ILs form an adsorbed layer on the metal surface, and (2) ILs form a protective layer (tribofilm) on the metal surface by a tribochemical process [18]. For the first lubricating mechanism, the anions of ILs are attracted by the positively charged metal surface during the rubbing action, subsequently, cations are attracted by anions. Depending on the attraction force between the ions, a monolayer or multilayer structure of anions-cations can be formed originating from the

metal surface towards the bulk lubricant [19–21]. This structure has low shear strength properties thus reduces the friction between the two sliding surfaces [22]. For the second mechanism, ILs between two mating surfaces will be broken down or decomposed due to the localized high temperature and high pressure. The highly active IL anions will eventually react with the metal surface during the rubbing action. A protective tribofilm will be formed as a product of this tribochemical reaction which will eventually increase the wear resistance [23–26].

Since the possibilities for ILs as lubricant additives are many and the trend of low viscosity and environmentally friendly lubricants is increasing, this research work was initiated with the aim to study ILs as potential green additives in two low viscosity lubricant media (one polar and one non-polar). The non-polar lubricant media was a low viscosity and low conductivity polyalphaolefin (PAO). The polar lubricant media chosen was a water–glycol mixture due to its clear compatibility with the environment, but it was also chosen because of its high electrical conductivity with the aim of studying the effect of conductivity in the performance of ILs as lubricant additives. More precisely, the effect of electrical conductivity and the corrosion performance of the ILs were assessed in this work. In this respect, a hybrid tribocorrosion-tribochemical mechanism has been proposed. The tribological performance of the two ILs has been compared with a well-known OFM, dodecanoic acid (C12). The tribological material chosen for this study has been an austenitic stainless steel (AISI 316L) due to its good corrosion resistance. This metal alloy also allows to study the ionic reactivity of ILs towards the

properties of the passive/tribofilm. The tribological performance of the different additives is discussed based on a detailed XPS analysis inside and outside the wear tracks, and a microstructural analysis of the wear track subsurface cross-section.

## 2 Experimental procedure

### 2.1 Materials

In this work, two ionic liquids were used as lubricant additives in polar and non-polar media. As a reference, a commonly used organic friction modifier (OFM) was chosen. The ionic liquids (ILs) were the following: tributylmethylphosphonium dimethylphosphate (PP) (97% purity and a molar mass of  $342.40 \text{ g}\cdot\text{mol}^{-1}$ ) purchased from Fluorochem, and 1-butyl-1-methylpyrrolidinium tris(pentafluoroethyl) trifluorophosphate (BMP) ( $\geq 98\%$ ,  $587.27 \text{ g}\cdot\text{mol}^{-1}$ ) purchased from Sigma-Aldrich. The OFM was a carboxylic acid (dodecanoic acid, abbreviated C12) ( $\geq 99\%$ ,  $200.32 \text{ g}\cdot\text{mol}^{-1}$ ) purchased from Sigma-Aldrich. The chemical structures of all the additives used in this work are presented in Fig. 1. The additives were dissolved in two different media: (1) a polar media consisting of a mixture of water and dipropylene glycol (WG), and (2) a non-polar media consisting of a polyalphaolefin with an aliphatic hydrocarbon chain of 10 carbons (PAO). Dipropylene glycol ( $\geq 99\%$ ,  $134.18 \text{ g}\cdot\text{mol}^{-1}$ ) was purchased from Acros Organics, and the polyalphaolefin was obtained from Chevron Phillips Chemical. All chemicals in these experiments were used as received without further purification. The mixture of the base lubricant with the additives

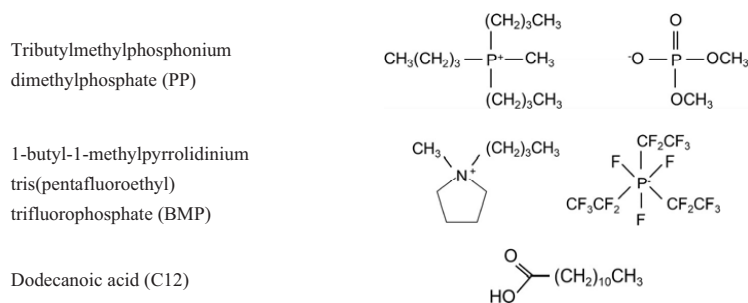


**Fig. 1** Molecular structures of the ionic liquids and dodecanoic acid.

was made using a magnetic stirrer for 4 hours at 50 °C and 70 °C for polar and non-polar media, respectively. The additive concentrations used for the tribological studies were 1 wt% and 0.1 wt% for ILs and a carboxylic acid, respectively. In a previous study performed in our research group, the optimal concentration for C12 in the same base lubricants was found to be 0.1 wt% [27]. Therefore, for the present work, 0.1 wt% of C12 was chosen as a reference. In an independent study, we have tested the ILs in both base lubricants at different concentrations (0.25, 0.5, 1, 2, and 4 wt%). In that study, it was found that for the water-based lubricant, the ILs were fully soluble at all concentrations and friction was stable at concentrations equal and above 1 wt%. For the case of PAO, the solubility of ILs varied depending on the IL type. For PP, it was at the same level as in water-glycol and BMP was not fully soluble at any concentration due to its high electronegativity. Therefore, a concentration of 1 wt% was chosen for the ILs in both base lubricants.

Stainless steel 316L samples were cut from a 30 mm diameter stainless steel bar purchased from Smith Stål (Trondheim, Norway) to create disks of 5 mm thickness for tribological testing. The disks were ground using SiC paper and polished using diamond paste to obtain a surface finish of  $R_a = 0.090 \pm 0.003 \mu\text{m}$ . The roughness was measured using a Mitutoyo SJ-301 surface roughness stylus profilometer. The average surface roughness ( $R_a$ ) in 0°, 90°, 180°, and 270° directions was chosen to describe the roughness. After grinding and polishing, disks were ultrasonically cleaned in a 1:1 mixture of ethanol and distilled water for 5 minutes. Subsequently, disks were rinsed with ethanol and dried with hot air before testing.

## 2.2 Testing and characterization methods

Rheometer (Haake Mars Rotational Rheometer with a CC27 cylinder measuring system, with the built-in Peltier element) was used to measure the dynamic viscosity 23 °C in humid air. Each measurement was performed by increasing the shear rate from 0.01 to 500  $\text{s}^{-1}$  with a ramp time of 180 seconds, then held at a constant shear rate of 500  $\text{s}^{-1}$  for 30 seconds, and continued by decreasing the shear rate from 500 to 0.01  $\text{s}^{-1}$  with a ramp time of 180 seconds. The dynamic

viscosity was reported from the average value of 30 measurements taken during the lubricant was held at a constant shear rate of 500  $\text{s}^{-1}$ . The dynamic viscosity values are presented in Table 1. There is a significant difference in dynamic viscosity between WG and PAO. However, adding the additives does not significantly change the dynamic viscosity of any of these two base lubricants.

A turbidity meter (Hanna Instruments HI-88713) was used to examine the stability of the lubricant mixture at room temperature. Turbidity measures the appearance of lubricants by the degree of light that has been scattered by the insoluble additives in the lubricant. With increasing in scattered light, the turbidity will be higher; i.e., higher Formazin Nephelometric Units (FNU). The lubricants were put on a magnetic stirrer for 2 hours prior to the test. The reported FNU was measured by calculating the average value of 12 measurements taken from 2 hours test. Turbidity values are shown in Table 1. WG and PAO base lubricants have stable turbidity numbers of 0.25 and 0.1 FNU, respectively, being transparent and without phase separation. Lubricants with additives show similar turbidity number and stable values as their base lubricant, except for PAO-BMP, which increases turbidity number to 0.84 FNU and shows a cloudy appearance, indicating that it is not fully soluble in PAO.

The conductivity of the lubricants was measured using a conductivity meter (Hanna Instruments HI-2300). The pH of the lubricant was measured using a pH meter from Radiometer analytical (PHM220 Lab

**Table 1** Physical and electrical properties of all lubricants.

Lubricants	Dynamic viscosity (mPa·s)	Turbidity (FNU)	Conductivity ( $\mu\text{S}/\text{cm}$ )*	pH
WG	13.99	0.25	2.5	7.3
WG-C12	13.53	0.25	4.3	4.7
WG-PP	13.76	0.13	211.2	3.4
WG-BMP	14.02	0.17	109.3	7.0
PAO	81.29	0.12	n.d.	n.d.
PAO-C12	83.13	0.21	n.d.	n.d.
PAO-PP	87.27	0.12	n.d.	n.d.
PAO-BMP	85.23	0.84	n.d.	n.d.

\* For comparison, the conductivity of tap water is ca. 500  $\mu\text{S}/\text{cm}$  and for seawater is ca. 5,000  $\mu\text{S}/\text{cm}$ .

pH Meter). These measurements only apply to polar lubricants (WG) with and without additives, since the non-polar lubricant (PAO) has non-detectable conductivity or pH due to the lack of sufficient ionic species. Conductivity and pH results are presented in Table 1. C12 does not significantly increase the conductivity of the base lubricant compared to ionic liquids. Ionic liquids increase the conductivity in 2 orders of magnitude. Among the ILs, PP presents the highest conductivity compared to BMP. Adding C12 and PP to WG changes the pH towards acidic values, with PP having the greatest effect. However, BMP does not change the pH value of the base lubricant.

A unidirectional ball-on-disk tribometer (Phoenix tribology) was used to evaluate the tribological performance of the lubricant under boundary conditions. An alumina (fused ceramic) ball with a diameter of 6 mm, purchased from Precision Ball and Gauge Co., Ltd., was pushed against the stainless steel 316L disk with a free-weight load of 20 N, which corresponds to a maximum Hertzian contact pressure of 1.96 GPa. The rotation of the disk was set to 40 rpm with a track diameter of 10 mm, which gives a sliding speed of 2.09 cm/s. The calculated lambda ( $\lambda$ ) value, according to the EHL Hamrock-Dowson formula, is 0.016 and 0.088 for WG and PAO, respectively, and therefore the boundary lubrication condition is met for both lubricants. The addition of an additive to the base lubricant slightly changes the viscosity value, but the lambda value still meets the boundary lubrication condition. Testing WG and PAO with C12 additive served as the reference. All lubricants were tested at room temperature. The distance of the tribological test was set to 300 meters (4 hours duration). Three experiments were performed to verify the repeatability of the results for each condition.

The wear volume was quantified with Alicona Infinite Focus optical 3D microscope and MountainsMap surface imaging, analysis, and metrology software. The wear volume was measured from four locations of the wear track for each sample and the average value was then calculated. Subsequently, from three samples for each condition, Archard's equation was used to calculate the average specific wear rate (SWR) [28]:

$$\text{SWR} = \frac{V}{N \cdot S}$$

where SWR is a specific wear rate ( $\text{mm}^3/(\text{N} \cdot \text{m})$ ),  $V$  is the volume loss ( $\text{mm}^3$ ),  $N$  is the normal load (N), and  $S$  is the sliding distance (m).

The wear track morphology was observed using FEI Quanta FEG 650 Scanning Electron Microscopy (SEM) and the wear track cross sections were prepared and observed with FEI Helios Nanolab DualBeam focused ion beam (FIB) and SEM. Gallium liquid metal ion source was used for deposition, milling, and polishing. Prior to milling, a platinum layer of  $24 \mu\text{m} \times 7 \mu\text{m} \times 5 \mu\text{m}$  was deposited on the wear track's surface to protect the surface from damage during the ion milling process. In FIB images, this platinum layer will be seen as a black layer on top of the surface. Milling was carried out to the depth of  $15 \mu\text{m}$  using the gallium source with a voltage of 30 kV and a current of 21 nA in the right, front, and left of the protective platinum layer. The cross section cleaning procedure was done in two steps using a current of 6.5 nA and 0.92 nA with a voltage of 30 kV. The lower current was applied to minimize artifacts such as curtaining and to get maximum grain contrast. Grain contrast of wear track cross section was revealed in SEM mode using through-lens-detector (TLD).

X-ray photoelectron spectroscopy (XPS) was used to perform detail chemical analysis of the inside and outside of the wear tracks by a Kratos Axis Ultra DLD machine using monochromatic Al  $K\alpha$  source (10 mA, 10 kV). The sample analysis chamber was set to a vacuum of  $9 \times 10^{-9}$  Torr during the acquisition. A survey scan was performed to collect the elemental map of the surface using pass energy of 160 eV and step size of 1 eV. From the elemental map, several elements were selected for further detailed high resolution scan, i.e., nickel (Ni), iron (Fe), chromium (Cr), molybdenum (Mo), carbon (C), oxygen (O), phosphorus (P), and fluorine (F), using pass energy of 20 eV and step size of 0.1 eV. Depth profile chemical analysis was performed to study the tribofilm. Sputtering was performed using Argon ion gun with a pressure of  $4.4 \times 10^{-7}$  Torr, an energy of 4 kV, and a raster size of  $2.5 \times 2.5$  mm. The selected sputtering times were 0, 5, 15, 35, 85, 185, 685, and 1685 seconds. CasaXPS software was used for evaluation and quantification. Detail curve-fitting parameters for different compounds used for evaluation and quantification are shown in Table 2.

**Table 2** Detail curve-fitting parameters of compounds detected outside and inside the wear track of the stainless steel after tribo-testing.

Signal	Binding energy ( $\pm 0.1$ eV)	FWHM ( $\pm 0.1$ eV)	Line shape	Assignment	Reference
Ni 2p	855.9	1.8	GL(30)	Ni(OH) <sub>2</sub>	[29, 30]
	853.7	1.8	GL(30)	NiO	
	852.7	0.9	GL(30)	Ni 2p <sub>3/2</sub>	
Fe 2p	714.4	2.9	GL(30)	FeF <sub>3</sub>	[16, 31, 32]
	712.8	2.9	GL(30)	Fe <sup>3+</sup>	
	712.6	2.9	GL(30)	FePO <sub>4</sub>	
	711.0	2.9	GL(30)	Fe <sub>3</sub> O <sub>4</sub>	
	709.5	2.9	GL(30)	FeO	
	706.7	0.9	LF(0.8,2,20,0)	Fe 2p <sub>3/2</sub>	
F 1s	684.9	1.6	GL(30)	F <sup>-</sup>	[16, 33]
Cr 2p	578.7	1.5	GL(30)	CrO <sub>3</sub>	[31, 32]
	577.3	1.5	GL(30)	Cr(OH) <sub>3</sub>	
	576.1	1.5	GL(30)	Cr <sub>2</sub> O <sub>3</sub>	
	573.9	1.2	LF(0.8,2,8,0)	Cr 2p <sub>3/2</sub>	
O 1s	533.3	1.8	GL(30)	O–C, O=C	[32, 34]
	531.4	1.8	GL(30)	O–H	
	530.1	1.1	GL(30)	O–M	
Mo 3d	235.6	1.3	GL(30)	Mo <sup>6+(ox)</sup> 3d <sub>3/2</sub>	[35]
	232.4	1.3	GL(30)	Mo <sup>6+(ox)</sup> 3d <sub>5/2</sub>	
	234.2	1.6	GL(30)	Mo <sup>4+(hyd)</sup> 3d <sub>3/2</sub>	
	231.0	1.6	GL(30)	Mo <sup>4+(hyd)</sup> 3d <sub>5/2</sub>	
	232.3	0.9	GL(30)	Mo <sup>4+(ox)</sup> 3d <sub>3/2</sub>	
	229.1	0.9	GL(30)	Mo <sup>4+(ox)</sup> 3d <sub>5/2</sub>	
	230.6	0.7	LF(1.1,2.3,2,0)	Mo 3d <sub>3/2</sub>	
	227.6	0.7	LF(1.1,2.3,2,0)	Mo 3d <sub>5/2</sub>	
C 1s	289.3	1.3	GL(30)	O–C=O	[36–38]
	288.2	1.3	GL(30)	C=O	
	286.5	1.3	GL(30)	C–OH, C–O–C	
	285.4	1.0	GL(30)	C–N	
	285.0	1.0	GL(30)	C–C	
P 2p	133.6	1.6	GL(30)	(PO <sub>4</sub> <sup>3-</sup> )	[38, 39]

### 3 Results

#### 3.1 Tribological testing

Sliding tests were performed on stainless steel under the boundary lubricating regime conditions to study the influence of ionic liquids as boundary lubricant additives in polar and non-polar base lubricants.

Figures 2(a) and 2(b) show the friction evolution over the whole distance for the base lubricants, base lubricants with ionic liquids (PP and BMP), and base lubricants with reference additive (C12) in polar (WG) and non-polar (PAO) media, respectively. Friction evolution of WG and PAO base lubricants alone are characterized by a long running-in distance with high friction, reaching steady friction values of 0.145



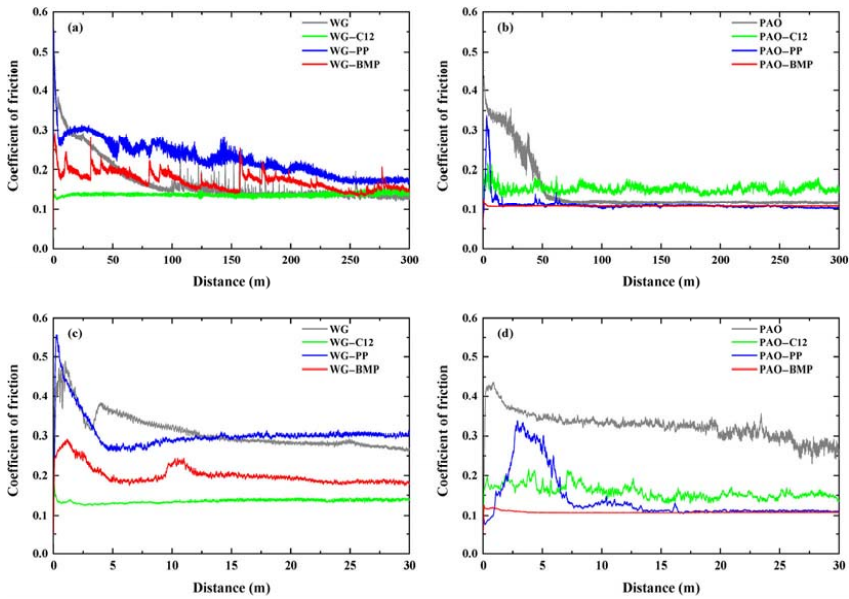


**Fig. 2** The friction evolution at room temperature for (a) WG with and without additive, (b) PAO with and without additive, (c) the running-in period for WG and (d) running-in period for PAO. Only one friction evolution graph is shown for each test due to the excellent repeatability of the results.

and 0.112 for WG and PAO after ca. 100 and 50 m sliding distance, respectively. Adding C12 to WG suppresses the running-in sliding distance (Fig. 2(c)) and keeps friction similar to the WG base lubricant alone after running-in. C12 in PAO shortens the running-in sliding distance to 10 m (Fig. 2(d)) but increases the friction to 0.15 with respect to the base lubricant alone. The addition of 1 wt% of ILs to WG significantly affects the friction evolution of this base lubricant. There is a sudden drop in friction at the start of the test (5 m sliding distance, Fig. 2(c)) and then the friction continues decreasing with time with some abrupt increments in some places until a sliding distance of 200 m (Fig. 2(a)). The ionic liquids in PAO reduce the running-in sliding distance (Fig. 2(d)), and friction after running-in is almost similar to the PAO base lubricant alone. Among the two ILs, BMP is the best in reducing the running-in period in PAO and it gives the lowest friction evolution in WG.

The specific wear rate (SWR) was calculated from the volume loss measured by 3D optical microscope, and the results are shown in Fig. 3. The SWR value of the base lubricants (WG and PAO) alone are

$7.83 \times 10^{-6} \text{ mm}^3/(\text{N}\cdot\text{m})$  and  $1.68 \times 10^{-5} \text{ mm}^3/(\text{N}\cdot\text{m})$ , respectively. The carboxylic acid increases the SWR in approximately 5 and 4 times as compared to the base lubricants alone. PP in WG doubles the SWR, whereas BMP gives a similar SWR value as the WG base lubricant alone. The presence of ILs in PAO decreases the SWR with respect to PAO alone. The highest reduction occurs with BMP by approximately 82% compared to PAO alone.

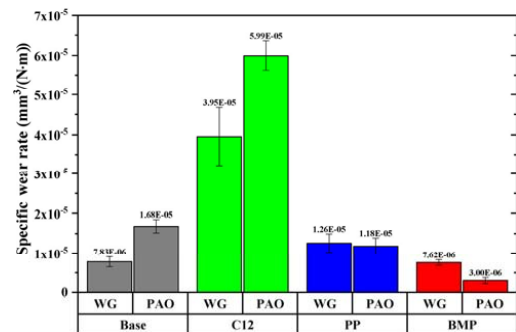


**Fig. 3** The influence of carboxylic acid and ionic liquids on the wear rate of stainless steel.

### 3.2 Wear track morphology

Figure 4 shows the SEM images of the wear tracks on stainless steel disk lubricated by polar and non-polar base lubricant with and without additives. The wear track morphology for stainless steel lubricated by WG base lubricant alone shows a smooth surface with signs of wear and pits in several locations. These pits indicate cracks that propagate through the surface

leading to material detachment. The material lubricated by PAO base lubricant alone, shows a smooth wear track surface with signs of abrasive wear and plastic deformation. When using carboxylic acid as additive, very fine wear scars with no signs of plastic deformation are observed in WG–C12. On the other hand, severe plastic deformation is observed on the surface lubricated by PAO with C12 additive.

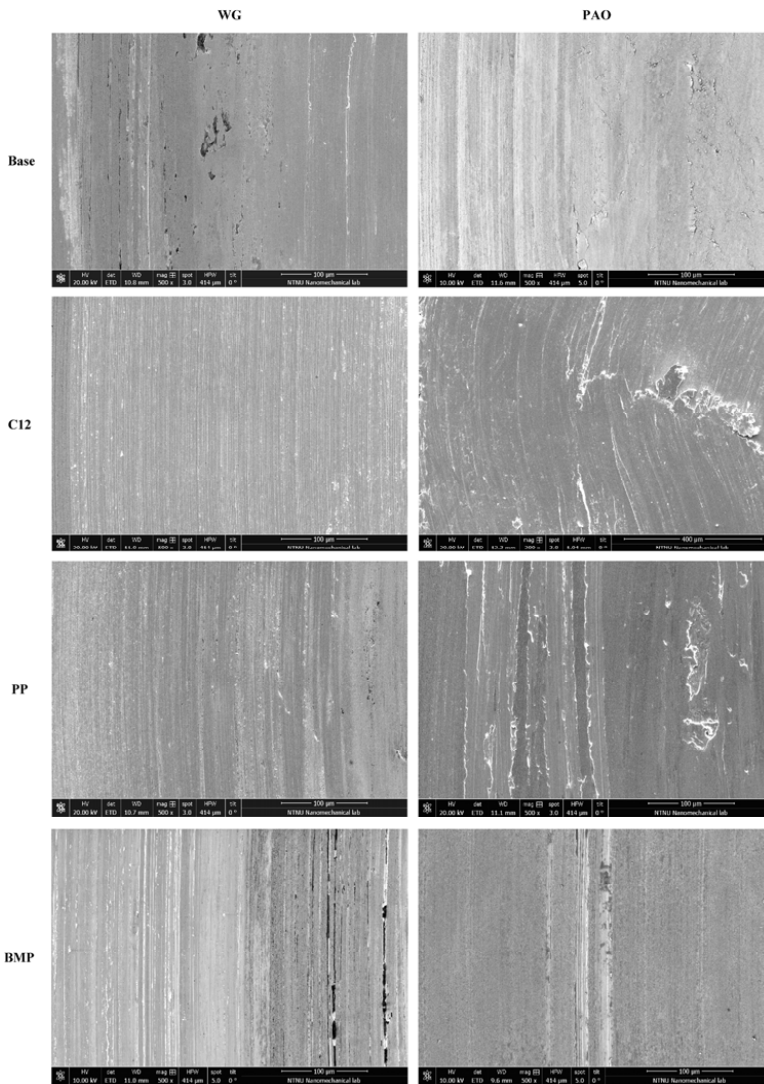


**Fig. 4** SEM images of the wear tracks on stainless steel disk tested in different lubricants at room temperature. Pictures were taken with 500x magnification except for PAO–C12 with 200× magnification.



The wear tracks of stainless steel lubricated by WG-PP and WG-BMP show similar wear morphology, i.e., abrasive wear with little signs of plastic deformation with WG-BMP having the smoothest surface. Stainless steel lubricated by PAO-PP shows plowing with signs of plastic deformation and some delaminated areas. On the other hand, different wear mechanism is found for stainless steel lubricated by PAO-BMP. In this case, a smoother surface and abrasive grooves

with no signs of plastic deformation can be found. From the wear track images, BMP seems to give a better effect on wear morphology than PP both in polar and non-polar base lubricant, which is in agreement with the friction evolution and SWR results.

The cross section subsurface microstructures prepared by FIB are shown in Fig. 5. The images were taken at the center of the wear track and perpendicular to the sliding direction. For all samples, the subsurface

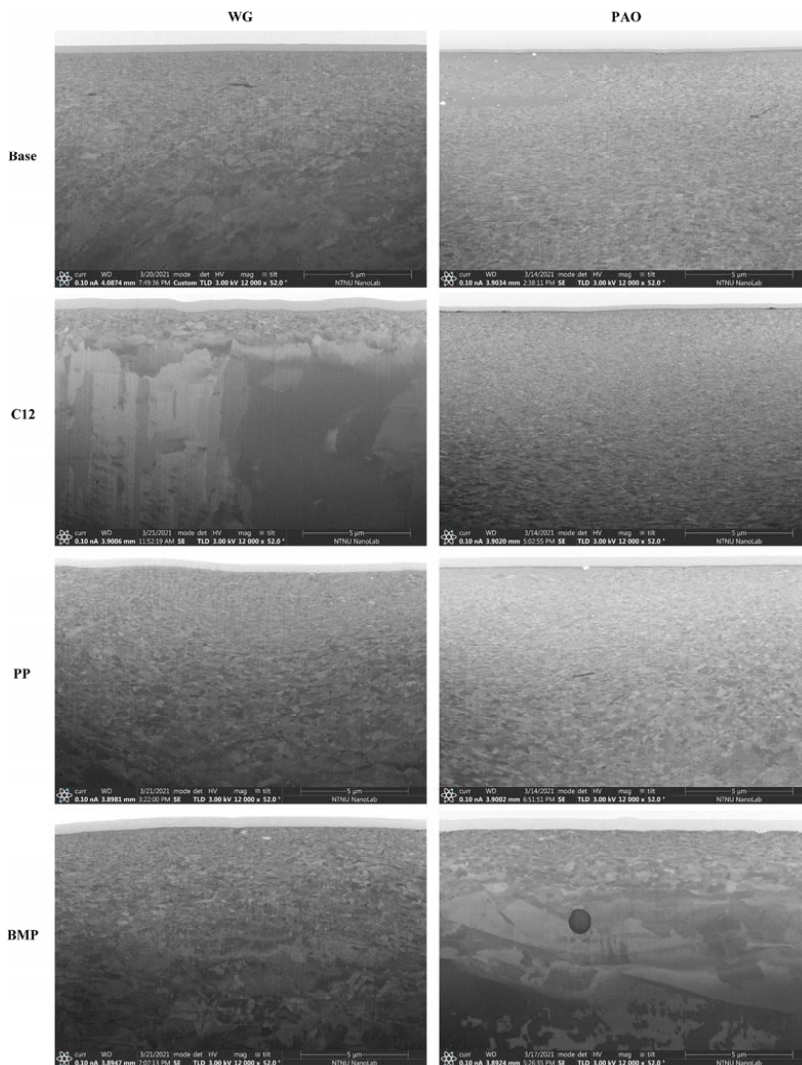


**Fig. 5** FIB cross-sections of the wear tracks of stainless steel tested with different lubricants at room temperature.

microstructure of stainless steel exhibited different extents of grain refinement and plastic deformation. When testing with the base lubricant alone, finer grain recrystallization deeper along the cross section was observed for stainless steel lubricated by PAO compared to WG. Adding C12 to the base lubricant resulted in very different subsurface grain features. C12 in WG gives a thinner subsurface recrystallization area, whereas C12 in PAO resulted in a thicker subsurface recrystallization area with finer grains. This is in line with the higher friction evolution of PAO–C12 (Fig. 2), which gives higher shear forces resulting in higher shear strain at the surface and subsurface areas.

Comparing the subsurface microstructures of stainless steel lubricated by WG–PP and WG–BMP, similar grain refinement or recrystallization has occurred. On the other hand, different subsurface microstructures were observed for stainless steel lubricated by PAO–PP and PAO–BMP. In the case of PAO–PP, very fine grain structure close to the surface in nanometer size can be observed. Contrary, thinner recrystallization area was observed for stainless steel lubricated by PAO–BMP, indicating lower shear strain occurring in the subsurface region. This result is in agreement with lower friction and wear during the test.

### 3.3 Passive film thickness and surface chemical composition

Surface chemical composition inside and outside the wear tracks was studied by X-ray photoelectron spectroscopy (XPS) for base lubricant with additives and untested 316L stainless steel served as a reference. Argon sputtering was applied to perform depth profiling in order to study the passive/tribofilm thickness and its chemical composition. For each sputtering time, the percentage of atomic concentration was calculated based on peak areas obtained from the high resolution XPS spectra of each element (graphs are not shown in this paper). For all test conditions, a decrease in oxygen concentration and an increase in metallic concentration as sputtering time increased were observed, getting close to the chemical composition of the bulk stainless steel. The oxygen peak versus sputtering time was used to calculate the passive film thickness. Passive film thickness can be defined by sputtering time when the oxygen peak concentration reaches 50% of the maximum value

[40]. To calibrate the sputtering rate with passive film thickness, tantalum oxide ( $\text{Ta}_2\text{O}_5$ ) with known thickness was sputtered with the same procedure. The obtained sputter rate was 2 nm per minute for  $\text{Ta}_2\text{O}_5$ . Table 3 shows the passive film thickness inside and outside of the wear track calculated with respect to  $\text{Ta}_2\text{O}_5$ . The passive film thickness of untested 316L was 1.87 nm, which is in agreement with the results obtained from other authors [41–43]. Thicker passive film thickness outside the wear track was observed for all stainless steel tested with WG with respect to the reference sample, however, in the case of PAO thicker passive film was only observed using C12 as additive. Comparing inside and outside of the wear track (i.e., ratio inside/outside), thicker passive film thickness was observed for all lubricant formulations, except for PAO–C12.

A detailed XPS analysis was made to study the passive film composition from the high resolution XPS spectra inside and outside of the wear tracks, and on the reference sample. Curve-fitting parameters in Table 2 were used in CasaXPS software to quantify the relative concentration of the compounds. A detailed procedure for calculating the relative concentration between compounds can be found elsewhere [44]. Figure 6 shows the subsurface relative atomic concentration of the passive film component from high resolution XPS spectra of chromium (Cr) and iron (Fe) inside and outside of the wear tracks and on the reference sample. Cr peaks consist of  $\text{Cr}^0$ ,  $\text{Cr}_2\text{O}_3$ ,  $\text{Cr}(\text{OH})_3$ , and  $\text{CrO}_3$ , and Fe peaks consist of  $\text{Fe}^0$ ,  $\text{FeO}$ ,  $\text{Fe}_3\text{O}_4$ ,  $\text{Fe}^{3+}$  (i.e.,  $\text{FeOOH}$  and  $\text{Fe}(\text{OH})_3$ ),  $\text{FePO}_4$ , and  $\text{FeF}_3$ . It can be seen that the passive film formed on the stainless steel surface when tested in lubricants

**Table 3** Passive film thickness inside and outside of the wear track.

		Passive film thickness (nm)		
Untested SS316L		1.87		
Base lubricant	Position	Additive		
		C12	PP	BMP
WG	Outside	3.30	3.67	2.43
	Inside	3.47	8.50	13.50
	Ratio inside/outside	1.05	2.32	5.55
PAO	Outside	2.97	1.83	1.87
	Inside	2.60	11.63	10.17
	Ratio inside/outside	0.88	6.36	5.44

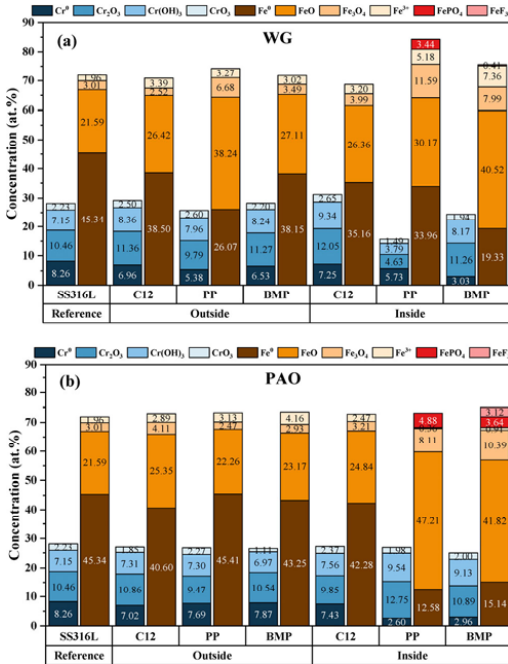


**Fig. 6** Relative atomic concentration of Cr and Fe species inside and outside the wear track of the stainless steel tested with different lubricant formulations, (a) in WG and (b) in PAO (taken from sputtering time 35 seconds).

with C12 additive inside the wear track consists of oxides and hydroxides only. However, phosphate and fluoride were found in the passive films inside the wear track of the stainless steel material tested with lubricant containing ionic liquid additives indicating a tribochemical reaction during the rubbing action. Moreover, iron hydroxides were suppressed in

the presence of phosphate and fluoride for non-polar lubricant.

## 4 Discussion

### 4.1 Effect of the base fluid polarity and tribo-corrosion on friction

The reference lubricant additive used in this work was a classical organic friction modifier (OFM), dodecanoic acid (C12). When this additive was added to the polar (WG) and non-polar (PAO) lubricant, different friction values and evolution with time were obtained. C12 in WG fully suppressed the running-in period and it shortened the running-in period from 50 to 10 meters in PAO as compared to the base lubricant alone. The lowest and more stable friction evolution was obtained in WG, which can be attributed to the surface coverage of this additive to the metal surface. Before rubbing starts, C12 instantaneously adsorbs onto the metal surface. Indeed, it was found that more adsorption to the metal surface for WG-C12 (19.35 at%) compared to PAO-C12 (15.39 at%) when considering the relative concentration of O=C=O and C=O bonds found by XPS (Fig. 7). Most studies of carboxylic acids used as lubricant additives are performed in non-polar base lubricants (mineral or synthetic oils). For these types of base lubricants, two adsorption mechanisms of carboxylic acids to metal surfaces have been proposed in literature: (1) carboxylic acid molecules and surface oxide or hydroxide form a hydrogen bond, or (2) formation of metal carboxylates [45–47]. However, when polar lubricants (mostly water-based) are used, the adsorption of carboxylic

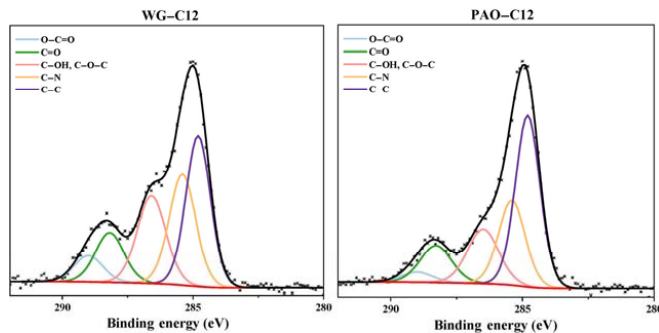


**Fig. 7** C 1s spectra on the stainless steel surface outside the wear track lubricated by WG-C12 and PAO-C12.

acid to the metal surface is different due to the deprotonation of the carboxylic head in water. In a previous study, it was found that the carboxylic acid C12 in water-based lubricant has a tendency to form a multilayer brush structure, efficiently separating the two mating sliding surfaces thus reducing friction in a more efficient way than in non-polar lubricant [27]. In addition, this mechanism depends on the concentration of the additive (for WG) and on the length of the carboxylic chain (for PAO). In WG, when the carboxylic acid concentration is higher than the critical micelle concentration (CMC), the deprotonated carboxylic acids form micelles separating the sliding surfaces even more efficiently, and in non-polar media (PAO) the longer the carboxylic chain the more efficient the surface separation is [27]. Therefore, in this work the very short chain of C12 was not sufficient in PAO to keep an efficient separation of the sliding surfaces and friction was higher than in WG where a multilayer of additive kept a very efficient separation of the surfaces decreasing friction. These differences in friction are evident from the FIB cross sections of the wear tracks, where the recrystallized region in WG–C12 is thinner than the one in PAO–C12 (Fig. 5).

Due to the sliding action, the adsorbed carboxylic acid reacts with the metal to form a tribofilm [32, 47]. The passive film thickness inside the wear track was analyzed by XPS and values of 3.47 and 2.60 nm were found for WG–C12 and PAO–C12, respectively (Table 3). The passive films inside the wear tracks are tribofilms mostly composed of oxides and hydroxides (Fig. 6) since the stainless steel material is oxidized on the surface (i.e., passive film) and the carboxylic

acid mostly contains C, H, and O. A further analysis of the XPS results has been performed to calculate the oxide and hydroxide to metal ratios (Cr and Fe) inside and outside the wear tracks (Fig. 8). Comparing these ratios inside the wear track, it can be seen that more oxide and hydroxide are present for WG–C12 than for PAO–C12. This is in agreement with more additive adsorption on the surface and a thicker passive/tribofilm, thus leading to a more efficient friction reduction for WG–C12 than for PAO–C12.

Interestingly, the ILs show different friction results than the reference additive (C12), being lowest for PAO–ILs and highest for WG–ILs. Clearly, the passive/tribofilms inside the wear track are thicker when the base lubricants are additivated with ILs (Table 3) and this effect is also seen outside the wear track for WG. These differences in passive/tribofilm thickness are accompanied by different surface chemistry as compared to C12, i.e., higher oxide and hydroxide to metal ratio is found together with P and F (Figs. 6 and 8). In addition, the Fe oxide to metal ratio significantly increases inside the wear track for all ILs, and outside the wear track for PP only. Worth noticing is that the Fe oxide to metal ratio remained constant both inside and outside the wear track for C12. The presence of F<sup>-</sup> and PO<sub>4</sub><sup>3-</sup> compounds (Figs. 6 and 9) make the passive film thicker, being ILs the triggers for a tribochemical reaction that promotes the formation of Cr and Fe ions that further react with oxygen, phosphorous and fluorine (Figs. 8 and 9). This surface tribochemical reaction has a clear detrimental effect in WG by creating fluctuations in the friction evolution, whereas in PAO it creates a

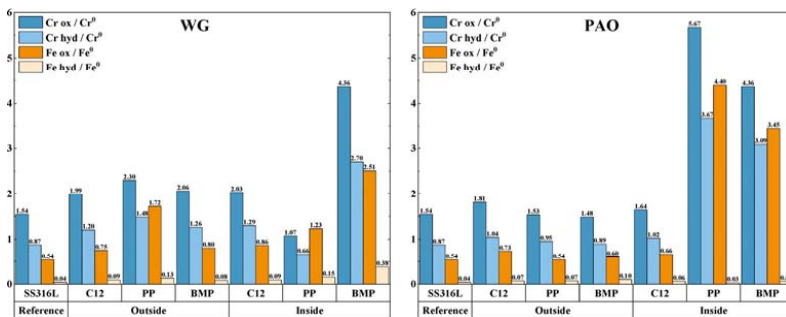


**Fig. 8** The intensity ratio of oxide and hydroxide with respect to the metallic part for Cr and Fe for all lubricants inside and outside the wear track.

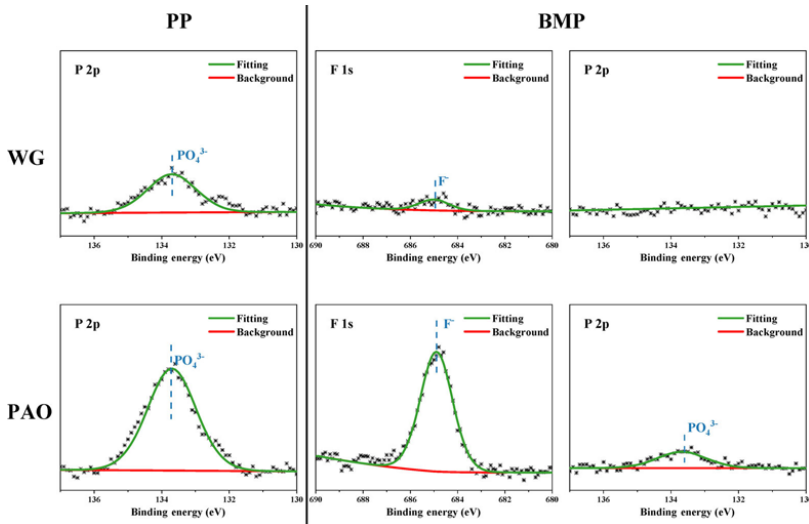


**Fig. 9** F 1s and P 2p spectra inside the wear track of the stainless steel lubricated by WG–PP, WG–BMP, PAO–PP, and PAO–BMP (taken from sputtering time 35 seconds).

thick and durable tribofilm that stabilizes friction (Fig. 1). The fluctuations in WG are to be understood as depassivation–repassivation events due to the high electrical conductivity of the media. Therefore, friction evolution in WG is mainly controlled by tribocorrosion [48], whereas in PAO it is controlled by the tribochemical reaction that creates a thick and durable tribofilm. The lowest friction was obtained for PAO–BMP and WG–BMP for each base lubricant and their respective tribofilms contained mostly  $\text{FeF}_3$  (Figs. 6 and 9). Therefore, F contributes to the tribochemical reaction enhancing the tribofilm formation [49]. However, this process is more efficient in PAO since, due to the lack of electrical conductivity, it does not compete with tribocorrosion. Thus, more  $\text{FeF}_3$  and some traces of  $\text{FePO}_4$  are found in PAO–BMP, whereas in WG–BMP only traces of  $\text{FeF}_3$  are found (Fig. 9).

A special case is PP, which creates a tribofilm of mostly  $\text{FePO}_4$  in both WG and PAO (Fig. 9). Indeed, big differences in the Fe and Cr oxides both inside and outside the wear tracks are found for PP. An increase in the amount of Fe and Cr oxide outside the wear track and a significant decrease inside the wear track are found in WG with respect to PAO. In addition, PP leads to the lowest inside/outside passive film thickness ratio for WG among all ILs mixtures tested (Table 3).

This is in agreement with its highest conductivity and lowest pH in WG (Table 1). Due to the high conductivity, fast repassivation kinetics for PP are to be expected in the wear track during the sliding action in water. However, the very low pH leads to a high (active) metal dissolution resulting in lower oxide and hydroxide to metal ratio compared to outside the wear track (Fig. 8). BMP has an electrical conductivity in the same order of magnitude as PP, however due to the neutral pH of the solution, the dissolution of Cr and Fe oxide was slower in WG (Fig. 8). The higher electrical conductivity and the lowest pH of PP resulted in a thinner tribofilm and therefore in higher friction for WG–PP than WG–BMP. Since PAO is a non-conductive medium, tribocorrosion does not take place and therefore the friction evolution only depends on the tribochemical reaction of the additives with the metal surface. Indeed, more  $\text{FePO}_4$  and  $\text{FeF}_3$  are always found in the wear tracks of PAO (Fig. 6).

#### 4.2 Effect of tribocorrosion and pH on wear

Wear rates in the different lubricants varied significantly, being the highest wear rate for the lubricants additivated with C12 (Fig. 3). A detailed investigation of the metal subsurface microstructure in the wear track shows a high recrystallization region for all



testing conditions, but with varying depth (Fig. 5), which is a well-known phenomenon in tribology [50–52]. This subsurface investigation revealed thicker recrystallization region when wear rate was higher for same additive in different media. This effect is clear comparing WG–C12 with PAO–C12 and WG–BMP with PAO–BMP, however, the causes for each pair are different. The adsorption of C12 on the stainless steel surface depended on the polarity of the media leading to a thinner tribofilm in the case of PAO–C12 resulting in thicker recrystallization region and higher wear. For PAO–BMP, a thick and durable tribofilm was formed on the metal surface resulting in limited subsurface recrystallization and the lowest material removal of all studied base and additive pairs. In the case of PP, the wear rate has been mostly controlled by electrical conductivity and pH (i.e., tribocorrosion and metal dissolution).

Further analysis of the wear track cross sections revealed the formation of ridges adjacent to the wear groove as shown in Figs. 10(a) and 10(b). The ridges are to be understood as material displacement to the sides of the wear track indicating signs of plastic deformation. The measured areas of the wear groove

( $A_{groove}$ ) and ridges ( $A_{ridges}$ ) are presented in Fig. 10(c) and Fig. 10(d) for WG and PAO with and without additive, respectively, along with the degree of material loss ( $\beta$ ). The degree of material loss is defined as the ratio of material loss to the volume of the wear track groove and it has been calculated by using the following equation [53]:

$$\beta = \frac{A_{groove} - A_{ridges}}{A_{groove}} \times 100\%$$

$\beta$  becomes zero when the material loss is due to plastic deformation only ( $A_{groove} = A_{ridges}$ ), and  $\beta$  becomes unity when the material loss is due to abrasive wear ( $A_{ridges} = 0$ ). Indeed, when the WG lubricants are additivated with ILs, they suffer more abrasive wear characterized by higher  $\beta$  values compared to PAO–ILs (Fig. 10). This effect is clearer for PP and it is aggravated by the low pH values (i.e., PP shows the largest values of  $A_{groove}$ ). This is in agreement with the fact that the tribocorrosion mechanism in WG has competed with the tribofilm formation resulting in higher material removal rates. The corrosiveness of polar media on metals is mainly dependent on oxygen

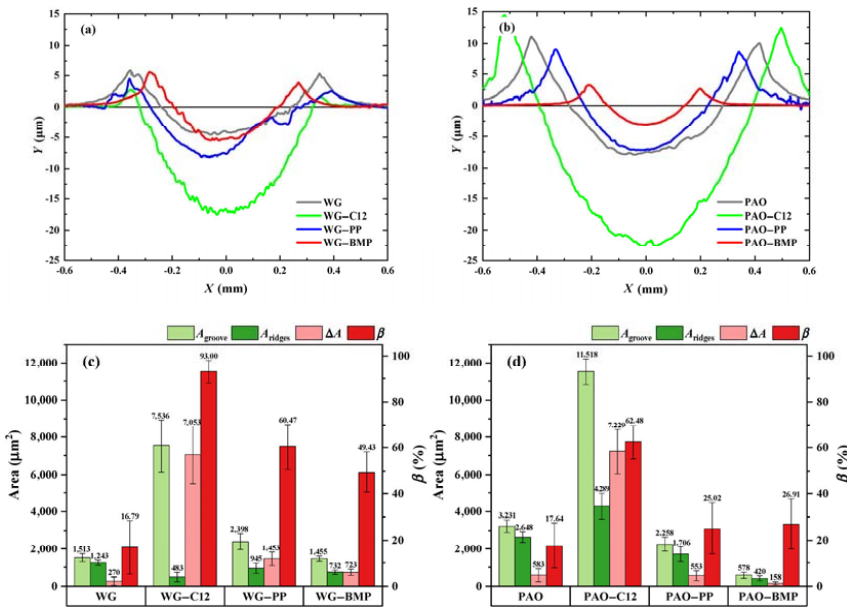


**Fig. 10** Wear cross section profile for (a) WG with and without additive, (b) PAO with and without additive, (c) calculated area of (a), and (d) calculated area of (b).

content, electrical conductivity, temperature, and pH. Stainless steel 316L protects itself from corrosion by creating a passive film (chromium oxide) on the surface due to the high content in Cr. During the tribotest, when rubbing starts, this passive film is removed by the mechanical action of the counterpart and the pristine metal alloy (depassivated wear track) will be then exposed to the lubricant. If the lubricant contains oxygen and is electrically conductive, the passive film will reform almost instantaneously (i.e., repassivation process). This process (tribocorrosion) will continue in a cyclic manner until the mechanical action is stopped, leading to an increase in the wear rate of the material [48].

A very interesting case is C12, which has the lowest conductivity in WG and therefore it should be expected to suffer of more plastic deformation. The very low conductivity of WG–C12 slowed down the repassivation kinetics (absence of tribocorrosion) and produced a thin passive film that resulted in higher wear than otherwise expected. In addition, the acidic pH that this additive brings to the WG lubricant (4.7) has played the most important role in the wear process. This very low pH accelerates the active dissolution of the metal in the contact area and therefore very high values of  $A_{\text{groove}}$  (abrasive wear) and little signs of plastic deformation are found for WG–C12. Indeed, the opposite was found in similar tests performed previously at higher pH (ca. 8) for C12 in WG, where lower wear rates and thicker passive films were found [32, 54].

The passive/tribofilm thickness has also played an important role in the wear performance of the additives. Indeed, this work shows that ILs can function as anti-wear additives in both WG and PAO, whereas C12 can only function as friction modifier. For the ILs, the passive/tribofilm thickness inside the wear track was very thick (Table 3). Comparing WG and PAO additivated with ILs, a competition effect between electrical conductivity and pH is observed. The higher conductivity enhanced the repassivation kinetics for both ILs resulting in a thicker tribofilm as compared to C12. But on the other hand, the low pH of PP increased the metal dissolution thinning the tribofilm for WG–PP, whereas PP in PAO–PP did not have any detrimental effect on the wear rate or on the tribofilm thickness. The polarity of the base lubricant has played a crucial role for PP, dissociating in

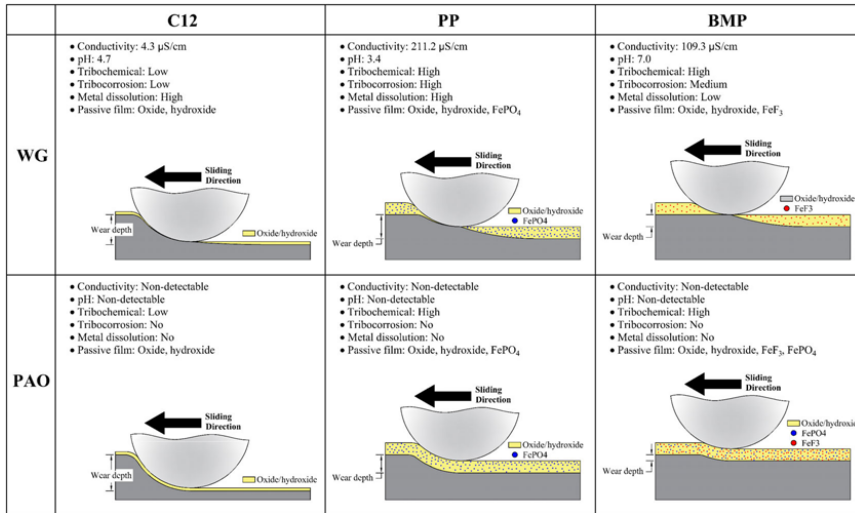
water (i.e., increasing the electrical conductivity and decreasing pH) and remaining intact in PAO (i.e., enhancing a tribochemical reaction with the metal). In addition, the presence of  $\text{FePO}_4$  and  $\text{FeF}_3$  compounds inside the wear tracks (Figs. 6 and 8) contributed to keeping a very low wear rate due to the creation of thicker and more durable films on the metal surface. This effect is more evident in PAO since the absence of electrical conductivity (i.e., very low ion mobility) mostly promotes the adsorption of the additive on the surface and the subsequent tribochemical reaction with the metal.

Figure 11 summarizes the frictional and wear mechanisms of PP and BMP in polar (water-based) and non-polar (PAO) lubricants as studied in this work. Worth noticing is the tribocorrosion process that occurred in the polar lubricant and the tribochemical process that occurred in the non-polar lubricant. The interplay of these two effects was driven by the polarity of the medium, the electrical conductivity, and the pH leading to different friction and wear results.

## 5 Conclusions

The effect of ionic liquids on friction and wear of 316L stainless steel tested in both polar and non-polar lubricants has been investigated and compared with carboxylic acid (C12) as reference additive. The following conclusions can be drawn from this work:

- The carboxylic acid (C12) in the polar lubricant showed lower friction than that in the non-polar lubricant due to higher adsorption on the metal surface and thicker passive film. However, the lower conductivity of the lubricants additivated with C12 resulted in thinner passive film compared to lubricants additivated with ionic liquids thus leading to high wear (i.e., the main role of C12 main is as a friction modifier).
- Ionic liquids contribute to a higher electrical conductivity and therefore tribocorrosion played the most important role in the frictional evolution in WG. This effect was suppressed in PAO and therefore friction values depended mostly on the adsorption and tribochemical reaction of the additives with the metal surface.
- Ionic liquids form a thicker passive/tribofilm that results in lower wear for the non-polar base



**Fig. 11** Schematic illustration of the wear mechanism of SS316L in different lubricating conditions.

lubricant. In addition, the passive/tribofilm created on the surface contains  $\text{FePO}_4$  and  $\text{FeF}_3$ , which contributes both to thickening the tribofilm and to keeping low friction and wear.

- In the polar lubricant, the pH played an important role, the lower pH dissolves the passive film resulting in thinner passive/tribofilm thus leading to higher friction and wear. This effect was suppressed in the non-polar lubricant.
- Among all additives tested, BMP shows the best wear and frictional performance in both polar and non-polar lubricants. In the case of the polar lubricant, the neutral pH resulted in less metal dissolution and the intermediate electrical conductivity resulted in a mild tribocorrosion process keeping  $\text{FeF}_3$  in the passive/tribofilm thus decreasing wear and friction. In the case of the non-polar lubricant, tribocorrosion is absent and the tribochemical reaction leads to the formation of a thick P and F containing tribofilm that decreases friction and wear.

with Project Number 4153, and the Norwegian Micro- and Nano-fabrication facility, NorFab, for providing the characterization facilities.

**Open Access** This article is licensed under a Creative Commons Attribution 4.0 International License, which permits use, sharing, adaptation, distribution and reproduction in any medium or format, as long as you give appropriate credit to the original author(s) and the source, provide a link to the Creative Commons licence, and indicate if changes were made.

The images or other third party material in this article are included in the article's Creative Commons licence, unless indicated otherwise in a credit line to the material. If material is not included in the article's Creative Commons licence and your intended use is not permitted by statutory regulation or exceeds the permitted use, you will need to obtain permission directly from the copyright holder.

To view a copy of this licence, visit <http://creativecommons.org/licenses/by/4.0/>.

## Acknowledgements

The authors would like to acknowledge the financial support from Indonesia Endowment Fund for Education (LPDP), M-ERA.NET GreenCOAT project

## References

- [1] Holmberg K, Erdemir A. Influence of tribology on global energy consumption, costs and emissions. *Friction* 5(3): 263–284 (2017)



- [2] Farfan-Cabrera L I. Tribology of electric vehicles: A review of critical components, current state and future improvement trends. *Tribol Int* **138**: 473–486 (2019)
- [3] Spikes H. Friction modifier additives. *Tribol Lett* **60**(1): 5 (2015)
- [4] Guegan J, Southby M, Spikes H. Friction modifier additives, synergies and antagonisms. *Tribol Lett* **67**(3): 83 (2019)
- [5] Barnes A M, Bartle K D, Thibon V R A. A review of zinc dialkyldithiophosphates (ZDDPS): Characterisation and role in the lubricating oil. *Tribol Int* **34**(6): 389–395 (2001)
- [6] Spikes H. The history and mechanisms of ZDDP. *Tribol Lett* **17**(3): 469–489 (2004)
- [7] Commission Regulation (EU) No. 136/2014 of 11 February 2014. <https://eur-lex.europa.eu/eli/reg/2014/136/oj>.
- [8] Earle M J, Seddon K R. Ionic liquids. Green solvents for the future. *Pure Appl Chem* **72**(7): 1391–1398 (2000)
- [9] Zhao H. Innovative applications of ionic liquids as “green” engineering liquids. *Chem Eng Commun* **193**(12): 1660–1677 (2006)
- [10] Seddon K R. Ionic liquids for clean technology. *J Chem Tech Biotechnol* **68**(4): 351–356 (1997)
- [11] Welton T. Room-temperature ionic liquids. Solvents for synthesis and catalysis. *Chem Rev* **99**(8): 2071–2084 (1999)
- [12] Wasserscheid P, Welton T. *Ionic Liquids in Synthesis*. Weinheim (Germany): Wiley-VCH Verlag GmbH & Co. KGaA, 2002.
- [13] Bermúdez M D, Jiménez A E, Sanes J, Carrión F J. Ionic liquids as advanced lubricant fluids. *Molecules* **14**(8): 2888–2908 (2009)
- [14] Palacio M, Bhushan B. A review of ionic liquids for green molecular lubrication in nanotechnology. *Tribol Lett* **40**(2): 247–268 (2010)
- [15] Somers A E, Khemchandani B, Howlett P C, Sun J Z, MacFarlane D R, Forsyth M. Ionic liquids as antiwear additives in base oils: Influence of structure on miscibility and antiwear performance for steel on aluminum. *ACS Appl Mater Interfaces* **5**(22): 11544–11553 (2013)
- [16] Viesca J L, García A, Battez A H, González R, Monge R, Fernández-González A, Hadfield M. FAP<sup>-</sup> anion ionic liquids used in the lubrication of a steel-steel contact. *Tribol Lett* **52**(3): 431–437 (2013)
- [17] Song Z H, Liang Y M, Fan M J, Zhou F, Liu W M. Ionic liquids from amino acids: Fully green fluid lubricants for various surface contacts. *RSC Adv* **4**(37): 19396–19402 (2014)
- [18] Xiao H P. Ionic liquid lubricants: Basics and applications. *Tribol Trans* **60**(1): 20–30 (2017)
- [19] Atkin R, Abedin S Z E, Hayes R, Gasparotto L H S, Borisenko N, Endres F. AFM and STM studies on the surface interaction of [BMP]TFSA and [EMIm]TFSA ionic liquids with Au(111). *J Phys Chem C* **113**(30): 13266–13272 (2009)
- [20] Perkin S, Albrecht T, Klein J. Layering and shear properties of an ionic liquid, 1-ethyl-3-methylimidazolium ethylsulfate, confined to nano-films between mica surfaces. *Phys Chem Chem Phys* **12**(6): 1243–1247 (2010)
- [21] Foulston R, Gangopadhyay S, Chiutu C, Moriarty P, Jones R G. Mono- and multi-layer adsorption of an ionic liquid on Au(110). *Phys Chem Chem Phys* **14**(17): 6054–6066 (2012)
- [22] Zhou F, Liang Y M, Liu W M. Ionic liquid lubricants: Designed chemistry for engineering applications. *Chem Soc Rev* **38**(9): 2590–2599 (2009)
- [23] Qu J, Bansal D G, Yu B, Howe J Y, Luo H M, Dai S, Li H Q, Blau P J, Bunting B G, Mordukhovich G, et al. Antiwear performance and mechanism of an oil-miscible ionic liquid as a lubricant additive. *ACS Appl Mater Interfaces* **4**(2): 997–1002 (2012)
- [24] Zhou Y, Dyck J, Graham T W, Luo H M, Leonard D N, Qu J. Ionic liquids composed of phosphonium cations and organophosphate, carboxylate, and sulfonate anions as lubricant antiwear additives. *Langmuir* **30**(44): 13301–13311 (2014)
- [25] Barnhill W C, Qu J, Luo H M, Meyer III H M, Ma C, Chi M F, Papke B L. Phosphonium-organophosphate ionic liquids as lubricant additives: Effects of cation structure on physicochemical and tribological characteristics. *ACS Appl Mater Interfaces* **6**(24): 22585–22593 (2014)
- [26] González R, Bartolomé M, Blanco D, Viesca J L, Fernández-González A, Battez A H. Effectiveness of phosphonium cation-based ionic liquids as lubricant additive. *Tribol Int* **98**: 82–93 (2016)
- [27] Bernat S, Armada S, Espallargas N. Friction mechanisms by carboxylic acids in aqueous lubricants. *Tribol Lett* **66**(3): 83 (2018)
- [28] Archard J F. Contact and rubbing of flat surfaces. *J Appl Phys* **24**(8): 981–988 (1953)
- [29] Casella I G, Guascito M R, Sannazzaro M G. Voltammetric and XPS investigations of nickel hydroxide electrochemically dispersed on gold surface electrodes. *J Electroanal Chem* **462**(2): 202–210 (1999)
- [30] Lei Y, Jiang J L, Bi T T, Du J F, Pang X J. Tribological behavior of *in situ* fabricated graphene-nickel matrix composites. *RSC Adv* **8**(39): 22113–22121 (2018)
- [31] Fredriksson W, Malmgren S, Gustafsson T, Gorgoi M, Edström K. Full depth profile of passive films on 316L stainless steel based on high resolution HAXPES in combination with ARXPS. *Appl Surf Sci* **258**(15): 5790–5797 (2012)

- [32] Zavieh A H, Espallargas N. The effect of friction modifiers on tribocorrosion and tribocorrosion-fatigue of austenitic stainless steel. *Tribol Int* **111**: 138–147 (2017)
- [33] Yu B, Zhou F, Pang C J, Wang B, Liang Y M, Liu W M. Tribological evaluation of  $\alpha$ ,  $\omega$ -diimidazoliumalkylene hexafluorophosphate ionic liquid and benzotriazole as additive. *Tribol Int* **41**(8): 797–801 (2008)
- [34] Long Y, De Barros Bouchet M I, Lubrecht T, Onodera T, Martin J M. Superlubricity of glycerol by self-sustained chemical polishing. *Sci Rep* **9**(1): 6286 (2019)
- [35] Marcus P, Bussell M E. XPS study of the passive films formed on nitrogen-implanted austenitic stainless steels. *Appl Surf Sci* **59**(1): 7–21 (1992)
- [36] Ding Y F, Zhang F, Xu J C, Miao Y Q, Yang Y Z, Liu X G, Xu B S. Synthesis of short-chain passivated carbon quantum dots as the light emitting layer towards electroluminescence. *RSC Adv* **7**(46): 28754–28762 (2017)
- [37] Li H P, Zhu S W, Zhang M, Wu P W, Pang J Y, Zhu W S, Jiang W, Li H M. Tuning the chemical hardness of boron nitride nanosheets by doping carbon for enhanced adsorption capacity. *ACS Omega* **2**(9): 5385–5394 (2017)
- [38] Urtis L A, Arcifa A, Zhang P, Du J X, Fantauzzi M, Rauber D, Hempelmann R, Kraus T, Rossi A, Spencer N D. Influence of water on tribolayer growth when lubricating steel with a fluorinated phosphonium dicyanamide ionic liquid. *Lubricants* **7**(3): 27 (2019)
- [39] Rokosz K, Hryniewicz T, Simon F, Rzadkiewicz S. Usporedne XPS analize sastojaka pasivnih slojeva nastalih na Duplex 2205 SS poslije standardnog elektropoliranja i elektropoliranja strujom velike gustoće. *The Vjesn* **23**(3): 731–735 (2016)
- [40] Kirchheim R, Heine B, Fischmeister H, Hofmann S, Knot H, Stolz U. The passivity of iron-chromium alloys. *Corros Sci* **29**(7): 899–917 (1989)
- [41] Wang Z C, Di-Franco F, Seyeux A, Zanna S, Maurice V, Marcus P. Passivation-induced physicochemical alterations of the native surface oxide film on 316L austenitic stainless steel. *J Electrochem Soc* **166**(11): C3376–C3388 (2019)
- [42] Wang Z C, Paschalidou E M, Seyeux A, Zanna S, Maurice V, Marcus P. Mechanisms of Cr and Mo enrichments in the passive oxide film on 316L austenitic stainless steel. *Front Mater* **6**: 232 (2019)
- [43] Detriche S, Vivegnis S, Vanhumbecq J F, Felten A, Louette P, Renner F U, Delhalle J, Mekhalif Z. XPS fast depth profile of the native oxide layers on AISI 304, 316 and 430 commercial stainless steels and their evolution with time. *J Electron Spectrosc Relat Phenom* **243**: 146970 (2020)
- [44] Mischler S, Mathieu H J, Landolt D. The investigation of passive films on iron—Chromium alloys by AES and XPS. *Surf Interface Anal* **12**(7): 429 (1988)
- [45] Sahoo R R, Biswas S K. Frictional response of fatty acids on steel. *J Colloid Interf Sci* **333**: 707–718 (2009)
- [46] Lin M M, Kim D K. In situ thermolysis of magnetic nanoparticles using non-hydrated iron oleate complex. *J Nanopart Res* **14**(2): 688 (2012)
- [47] Simič R, Kalin M. Adsorption mechanisms for fatty acids on DLC and steel studied by AFM and tribological experiments. *Appl Surf Sci* **283**: 460–470 (2013)
- [48] Munoz A I, Espallargas N, Mischler S. *Tribocorrosion*. Cham (Switzerland): Springer International Publishing, 2020.
- [49] Hu E Z, Dearn K, Yang B X, Song R H, Xu Y F, Hu X G. Tribofilm formation and characterization of lubricating oils with biofuel soot and inorganic fluorides. *Tribol Int* **107**: 163–172 (2017)
- [50] Rice S L, Nowotny H, Wayne S F. Formation of subsurface zones in impact wear. *ASLE Trans* **24**(2): 264–268 (1981)
- [51] Büscher R, Fischer A. The pathways of dynamic recrystallization in all-metal hip joints. *Wear* **259**(7–12): 887–897 (2005)
- [52] Perret J, Boehm-Courjault E, Cantoni M, Mischler S, Beaudouin A, Chitty W, Vernot J P. EBSD, SEM and FIB characterisation of subsurface deformation during tribocorrosion of stainless steel in sulphuric acid. *Wear* **269**(5–6): 383–393 (2010)
- [53] Bruce R W. *Handbook of Lubrication and Tribology, Volume II: Theory and Design*. 2nd ed. New York (USA): CRC Press, 2012.
- [54] Bernat S, Armada S, Espallargas N. Effect of contamination on the friction and wear of carboxylic acids in aqueous lubricants. *Tribol Lett* **66**(4): 158 (2018)



**Wahyu WIJANARKO.** He received his bachelor degree in mechanical engineering in 2005 from Sepuluh Nopember Institute of Technology, Surabaya, Indonesia. Then, he received his master degree in

materials science in 2010 from University of Aveiro, Portugal. Currently he is a Ph.D. student in Norwegian Tribology Center, Department of Mechanical and Industrial Engineering, Norwegian University of Science and Technology, Trondheim, Norway. His research interests include tribology and lubrication.



**Hamid KHANMOHAMMADI.** He received his master degree in materials science and engineering in 2011 from University of Tehran, Iran. He received his Ph.D. degree in materials engineering from the same university in 2017, focused on

tribocorrosion behaviour of PEO coatings. Currently he is a postdoctoral researcher in Norwegian Tribology Center, Department of Mechanical and Industrial Engineering, Norwegian University of Science and Technology, Trondheim, Norway. His research areas are tribocorrosion, water-based lubricants, and surface interactions in tribology.



**Nuria ESPALLARGAS.** She is a professor at the Department of Mechanical and Industrial Engineering of the Norwegian University of Science and Technology (NTNU, Norway). She has a M.S. degree in chemistry and a Ph.D. degree in surface engineering from University of Barcelona

(Spain). Since 2011 she is the NTNU leader of the Gemini Centre Tribology. She has performed two international research stays at EPFL and ETH (Switzerland) in the fields of tribocorrosion and nano-tribology. Her scientific and research interests are within surface chemistry and engineering, tribology, lubricants, tribocorrosion, and nano-tribology.

*This page is intentionally left blank*

## **Paper II**

**Ionic Liquid Additives in Water-Based Lubricants for Bearing Steel – Effect of Electrical Conductivity and pH on Surface Chemistry, Friction and Wear**

Frontiers in Mechanical Engineering 2022, Vol. 7

DOI: [10.3389/fmech.2021.756929](https://doi.org/10.3389/fmech.2021.756929)

*This page is intentionally left blank*



# Ionic Liquid Additives in Water-Based Lubricants for Bearing Steel – Effect of Electrical Conductivity and pH on Surface Chemistry, Friction and Wear

W. Wijanarko<sup>1,2\*</sup>, H. Khanmohammadi<sup>1</sup> and N. Espallargas<sup>1\*</sup>

<sup>1</sup>Norwegian Tribology Center, Department of Mechanical and Industrial Engineering, Norwegian University of Science and Technology (NTNU), Trondheim, Norway, <sup>2</sup>Department of Mechanical Engineering, Sepuluh Nopember Institute of Technology (ITS), Surabaya, Indonesia

## OPEN ACCESS

### Edited by:

Jun Qu,  
Oak Ridge National Laboratory (DOE),  
United States

### Reviewed by:

Anthony Somers,  
Deakin University, Australia  
Xin He,  
Oak Ridge National Laboratory (DOE),  
United States

### \*Correspondence:

W. Wijanarko  
wahyu.wijanarko@ntnu.no  
wijanarko@me.its.ac.id  
N. Espallargas  
nuria.espallargas@ntnu.no

### Specialty section:

This article was submitted to  
Tribology,  
a section of the journal  
Frontiers in Mechanical Engineering

Received: 11 August 2021

Accepted: 02 December 2021

Published: 04 January 2022

### Citation:

Wijanarko W, Khanmohammadi H and  
Espallargas N (2022) Ionic Liquid  
Additives in Water-Based Lubricants  
for Bearing Steel – Effect of Electrical  
Conductivity and pH on Surface  
Chemistry, Friction and Wear.  
*Front. Mech. Eng* 7:756929.  
doi: 10.3389/fmech.2021.756929

Water-based lubricants have the potential to become the largest environmentally friendly lubricants in applications such as electric vehicles and the newly emerging green technologies of the future due to their inherent low viscosity and cooling properties. In order to be environmentally acceptable (EAL), both base lubricants and additives should comply with biodegradability, non-toxicity, and non-bioaccumulation requirements. Additives for water-based lubricants should ideally be polar and soluble in water and, at the same time, should not increase the electrical conductivity to critical levels for corrosion. However, most additives used in synthetic or mineral oils are non-polar. Ionic liquids have recently gained attention as lubricant additives due to their high polarity, making them highly surface-active (i.e. high tendency to adsorb on metal surfaces). However, they are seen as highly corrosive for many metal alloys. In this work, a water-glycol lubricant containing two different ionic liquids has been investigated as a potential green lubricant for a bearing steel AISI 52100 with accurate control on electrical conductivity and pH. The selected ionic liquids were tributylmethylphosphonium dimethylphosphate (PP) and 1-butyl-1-methylpyrrolidinium tris(pentafluoroethyl)trifluorophosphate (BMP). The tribological behaviour of the ionic liquids was compared with a well-known organic friction modifier, dodecanoic acid (C12). The ionic liquids showed lower friction and wear rate than the water-based lubricant alone. However, they showed higher friction than the lubricant formulated with C12, in which PP gave lower friction than BMP due to low pH. A detailed subsurface analysis of the wear track using scanning-transmission electron microscopy (STEM) showed that a thick oxide tribofilm was built on the wear track for both lubricants formulated with ionic liquids due to high electrical conductivity. This tribofilm gave beneficial effect on wear. Although PP and BMP gave thicker tribofilms than C12, it was not durable, resulting in cracking and detachment.

**Keywords:** water-based lubricant, ionic liquids, pH, electrical conductivity, tribofilm

## 1 INTRODUCTION

The production of electric vehicles (EVs) has grown in recent years. Ninety-eight EVs models were introduced to the market in 2019 compared to only two models available in 1997, and it is predicted to triple in 2025 (Transport and Environment, 2019; Chen et al., 2020). The EVs are considered as “green” vehicles compared to combustion engine vehicles (ICEVs) because they reduce the CO<sub>2</sub> emissions and other air pollutants (NO<sub>x</sub>, carbon monoxide, unburnt hydrocarbons), which can reduce the global warming effect. According to the European Environment Agency data, the CO<sub>2</sub> emission of ICEVs is around 210 gCO<sub>2</sub>/km, and it reduces to 70 gCO<sub>2</sub>/km for EVs (European Environment Agency, 2019). In addition, the EVs have higher energy efficiency compared to ICEVs, in which EVs use up to 77% of total electric energy to drive the vehicle, whereas ICEVs only use up to 21% of total fuel energy (Holmberg and Erdemir, 2019). Similar to ICEVs, the components of EVs also need lubrication to operate in a tribological environment effectively. The tribological components of EVs will work at a higher speed than those in ICEVs, which makes the lubricant in EVs to function more as a torque transfer rather than as a load-bearing (Van Rensselar, 2019). The higher the speed of the tribological component, the higher the temperature generated in the lubricant. Because of that, the development of lubricants for EVs nowadays is moving towards low viscosity lubricants, which have better cooling properties and higher temperature stability (Narita and Takekawa, 2019).

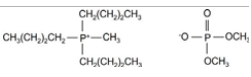
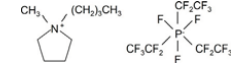
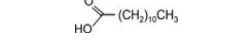
Water-based lubricants are promising candidates as low viscosity lubricants for EV applications and others in which load-carrying capacity is not the main requirement. They have desirable properties such as better cooling ability, low toxicity, and fire resistance. Therefore, water-based lubricants are nowadays already used as an alternative to petroleum-based lubricants in applications such as hydraulic fluids (Tomala et al., 2010), cooling fluids for metal cutting (Khan et al., 2021), and bearings of the stern tubes in propeller shafts of ships (Huang et al., 2019). Moreover, water-based lubricants are used to mimic the body fluids to perform *in vitro* studies of the corrosion and tribocorrosion behaviour of bearing implant materials such as CoCrMo (Espallargas et al., 2015). However, water-based lubricants in many current applications have several drawbacks, such as high pour point, poor corrosion protection, high polarity (competing with additives for surface sites), and low viscosity (in cases when load-carrying capacity is needed), leading to poor lubricating performance as compared with mineral or synthetic oils. Therefore, the uncertainty in the tribological performance of water-based lubricants might hinder their application in EVs. There are some strategies to overcome the main drawbacks of water, such as using glycols (or similar substances) to increase the viscosity and decrease its pour point. In addition to glycols, the use of other additives to enhance the tribological performance (e.g. friction and wear) of water is a must (Tomala et al., 2010). Short-chain friction modifiers such as organic friction modifiers (OFMs) are typically used in water-glycol hydraulic fluids (Spikes, 2015; Bernat et al., 2018a; Bernat et al., 2018b). Other additives such as antiwear

(AW) or extreme pressure additives can also be used for water-based lubricants in case the application requires it (Chang et al., 2011). AW additives usually contain active elements such as phosphorus (P), sulphur (S), or halogens. One commonly used antiwear additive in petroleum-based lubricants is zinc dialkyldithiophosphate (ZDDP). It was initially developed in the 1940s as an antioxidant, but soon it showed antiwear and corrosion inhibition properties for engine oils (Spikes, 2004; Nicholls et al., 2005). Even though ZDDP has several advantages as lubricant additive for engine oils however, in the recent years attempts to find alternatives to it have begun due to environmental issues. ZDDP is aquatically toxic, and it is an issue in environmentally sensitive applications like forestry, marine, etc. (Canter, 2019). Therefore, this additive is not suitable for environmentally friendly lubricant formulations. ZDDP contains zinc that generates ash upon combustion, resulting in degradation of the catalysts systems in cars. It is believed that the sulphur and phosphorus oxide together with the metallic ashes block the exhaust giving a rise in carbon monoxide and hydrocarbon emissions from the engine (Spikes, 2008). Therefore, in the case of oils for ICEVs the need to reduce the amount of sulphated ash, phosphorus, and sulphur (referred as SAPS) has become crucial. Indeed, the main metallic source for sulphated ash is zinc, which is present in ZDDP. And also, several governments have regulated the concentration limit of P and S in lubricants for ICEVs (THE EUROPEAN COMMISSION, 2014). Therefore, the need for more environmentally friendly additives has boosted the development and study of metallic-free or ashless additives with low or no P and S content as alternative to ZDDP. Worth noticing is that not all forms of phosphorous (P) and sulphur (S) are toxic to the environment, therefore the regulations limit the use of P and S in lubricant formulations, but not fully ban them (Candelaria, 2018).

Ionic liquids (ILs) are organic salts with a low melting point (below 100°C), consisting of anions and cations. ILs are attractive compounds due to their unique properties, such as low volatility, high thermal stability, and non-flammability (Seddon, 1997; Welton, 1999; Wasserscheid and Welton, 2002). They were used for the first time in the 1910s as a need to have salts at room temperatures. In the 1980s, they were “re-discovered” to be used as solvents in chemical reactions. Since then, they have been considered environmentally friendly substances for “green chemistry,” although there is some controversy around this topic (Welton, 2018). One of the many applications that boosted in the early 2000s for ILs was their use as high-performance lubricants (Ye et al., 2001; Liu et al., 2002). ILs are considered attractive lubricants because they tend to adsorb very effectively on surfaces (Somers et al., 2013). Therefore, ILs have been studied as neat lubricants but also as additives (Minami, 2009; Somers et al., 2013; Amiril et al., 2017; Xiao, 2017; Zhou and Qu, 2017). ILs as additives in water-based lubricants might be disadvantageous due to their ionic nature (i.e. corrosion attacks in metals). Therefore most studies of ILs as additives in water-based lubricants have focused on ceramic-on-ceramic contacts (Phillips and Zabinski, 2004; Xie et al., 2009) or non-halogenated ILs (Zheng et al., 2017; Wang et al., 2018; Dong et al., 2020). However, recent work in our group has shown that



**TABLE 1** | Chemical formula, density, and chemical structure of all additives.

Abbr	Chemical name	Chemical formula	Density (g/cm <sup>3</sup> )	Chemical structure
PP	Tributylmethylphosphonium dimethylphosphate	C <sub>15</sub> H <sub>36</sub> O <sub>4</sub> P <sub>2</sub>	1.004	
BMP	1-butyl-1-methylpyrrolidinium tris(pentafluoroethyl) trifluorophosphate	C <sub>15</sub> H <sub>20</sub> F <sub>18</sub> NP	1.647	
C12	Dodecanoic acid	CH <sub>3</sub> (CH <sub>2</sub> ) <sub>10</sub> COOH	1.007	

halogenated ILs as additives in water-glycol form an efficient tribofilm that reduces friction and wear in stainless steel sliding against alumina (Khanmohammadi et al., 2020).

This work aims to investigate the viability of ILs as lubricant additives for low corrosion-resistant alloys such as bearing steel. The focus will be on corrosion resistance (controlling electrical conductivity and pH) and friction and wear performance. Two ILs (tributylmethylphosphonium dimethylphosphate and 1-butyl-1-methylpyrrolidinium tris(pentafluoroethyl) trifluorophosphate) have been investigated in a water-glycol lubricant. No anticorrosion additives (or any other) were used with the aim of studying the effect of ILs alone. An OFM, dodecanoic acid, was used as a reference.

## 2 MATERIALS AND METHODS

### Materials

AISI 52100 bearing steel, purchased from Smith Stål (Trondheim, Norway), was chosen as the test material. Sample disks were prepared by cutting the 30 mm diameter steel rod with a thickness of 6 mm. The samples were ground using a resin-bonded diamond disk, subsequently polished using 9, 6, and 3 μm diamond suspensions. The polished samples were ultrasonically cleaned in distilled water-ethanol mixture (ca. 1:1) for 5 min, then rinsed with fresh ethanol and dried with pressurized air. The base lubricant was prepared by mixing water with glycol in a 1:1 proportion (abbreviated WG). Two ionic liquids (ILs) were used as additives in WG, i.e. tributylmethylphosphonium dimethylphosphate (abbreviated PP) and 1-butyl-1-methylpyrrolidinium tris(pentafluoroethyl) trifluorophosphate (abbreviated BMP). The tribological behaviour was compared with an organic friction modifier, i.e. dodecanoic acid (abbreviated C12). Glycol (≥99% purity) and PP (97%) were purchased from Acros Organics and Fluorochem, respectively. Meanwhile, both BMP (≥98%) and C12 (≥99%) were purchased from Sigma-Aldrich. All chemicals were used as received. The chemical formula, density, and chemical structure of all additives used in this work are shown in **Table 1**. In an independent study performed in our research group, ILs in the same base lubricant had been tested at different concentrations (0.25, 0.5, 1, 2, and 4 wt %). It was found that ILs were fully soluble at all concentrations, however the friction was stable only at concentrations equal and above 1 wt%, therefore 1 wt% was

selected as the concentration for ILs. In the case of C12, a previous study conducted in our research group showed that 0.1 wt% is the optimal concentration for C12 in water glycol lubricant, therefore 0.1 wt% of C12 was chosen as the reference lubricant for the present work (Bernat et al., 2018b). The base lubricant and additives were mixed using magnetic stirring for 4 h at 50°C. The lubricant was continuously stirred at room temperature for 20 h before being used.

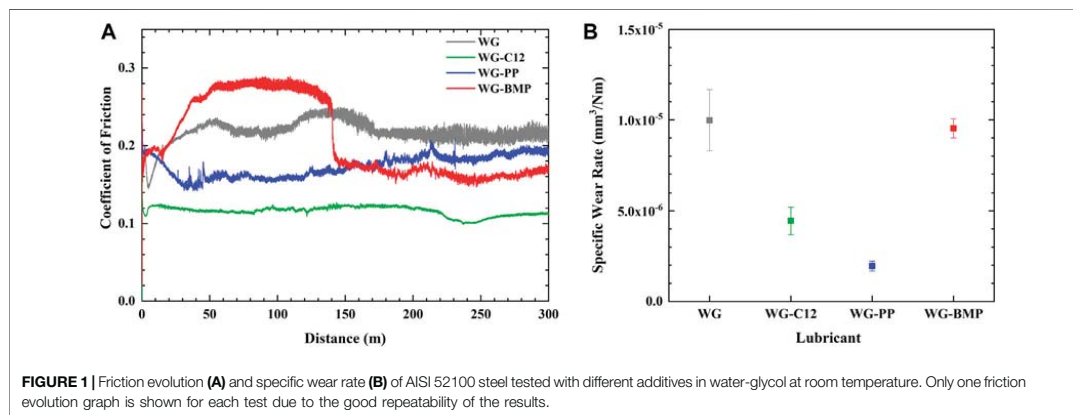
### Testing and Characterization Methods

The density of the lubricants was measured by the constant fluid volume weighing method. The dynamic viscosity at 23°C in humid air was measured using a rheometer (Haake Mars Rotational Rheometer with a CC27 cylinder measuring system, with the built-in Peltier element). The electrical conductivity of the lubricants was measured using a conductivity meter (Hanna Instruments HI-2300). The pH of the lubricant was measured using a pH meter (Hanna Instruments HI-2210). The open circuit potential (OCP) was measured for 4 h using a Gamry Interface 1000 Potentiostat with Ag/AgCl KCl saturated reference electrode. Friction and wear were measured using a rotating ball-on-disk tribometer (Phoenix tribology). In this test, a stationary alumina ball, purchased from Precision Ball and Gauge Co. Ltd., was in contact with the flat AISI 52100 disk using a dead weight in the presence of the lubricants at room temperature. The diameter of the alumina ball was 6 mm, and the normal load applied was 20 N, resulting in an initial maximum Hertzian contact pressure of 1.96 GPa. The disk's rotation speed and the track diameter were set to 40 rpm and 10 mm, respectively, which gave a sliding speed of 2.09 cm/s. The calculated EHL Hamrock-Dowson lambda (λ) value is 0.016, indicating boundary lubrication conditions. The additives have only a slight effect on the dynamic viscosity of the lubricant. As a result, the λ value still meets the boundary lubrication conditions. At least two tests were performed for each condition to verify the repeatability of the results.

Alicona Infinite Focus optical 3D microscope and MountainsMap software were used to quantify the wear volume from four different locations of the wear track. Archard's equation was used to calculate the average specific wear rate (SWR) from two samples for each condition (Archard, 1953). The average SWR value and the standard deviation were reported.

**TABLE 2** | Detailed curve-fitting parameters of compounds used for XPS characterization.

Signal	Binding energy (±0.1 eV)	FWHM (±0.1 eV)	Line shape	Assignment	References
Fe 2p	712.8	2.9	GL (30)	Fe <sup>3+</sup>	Fredriksson et al. (2012), Viesca et al. (2013), Zavieh and Espallargas (2017)
	712.6	2.9	GL (30)	FePO <sub>4</sub>	
	711.0	2.9	GL (30)	Fe <sub>3</sub> O <sub>4</sub>	
	709.5	2.9	GL (30)	FeO	
	706.8	0.9	LF (0.8,2,20,0)	Fe 2p <sub>3/2</sub>	
F 1s	684.9	1.6	GL (30)	F <sup>-</sup>	Yu et al. (2008), Viesca et al. (2013)
Cr 2p	578.7	1.5	GL (30)	CrO <sub>3</sub>	Fredriksson et al. (2012), Zavieh and Espallargas (2017)
	577.3	1.5	GL (30)	Cr(OH) <sub>3</sub>	
	576.1	1.5	GL (30)	Cr <sub>2</sub> O <sub>3</sub>	
	573.9	1.2	LF (0.8,2,8,0)	Cr 2p <sub>3/2</sub>	
O 1s	531.6	1.8	GL (30)	O-H	Zavieh and Espallargas (2017), Long et al. (2019)
	530.5	1.1	GL (30)	O-M	
P 2p	133.7	1.6	GL (30)	(PO <sub>4</sub> ) <sup>3-</sup>	Rokosz et al. (2016), Urtis et al. (2019)



FEI Helios Nanolab DualBeam focused ion beam and scanning electron microscopy (SEM-FIB) was used to study the surface and cross-section of the wear tracks. Platinum or carbon was deposited on the wear track surface to protect it from the milling and polishing processes. Deposition, milling, and polishing were carried out using a Gallium ion source. The secondary electron images of the wear track surface and cross-section were taken using the Everhart-Thornley detector (ETD) and through lens detector (TLD), respectively. The SEM-FIB was also used to prepare thin wear track lamellae with thickness less than 60 nm. The lamellae were examined by scanning-transmission electron microscopy (STEM, Hitachi SU9000) equipped with an x-ray energy dispersive spectroscopy (EDS) detector (Ultim Extreme, Oxford Instruments).

The elemental composition of the wear tracks was studied by x-ray photoelectron spectroscopy (XPS) (Kratos Axis Ultra DLD machine). A monochromatic Al K $\alpha$  was used as the x-ray source with accelerating voltage and current of 10 kV and 10 mA, respectively. Electrostatic lens mode was selected to collect the elemental data during acquisitions with a  $9 \times 10^{-9}$  Torr chamber pressure. The

elemental map was collected using survey acquisition with a pass energy of 160 eV and a step size of 1 eV. From the survey acquisition results, iron (Fe), chromium (Cr), oxygen (O), phosphorus (P), and fluorine (F) were selected for the high-resolution scan with a pass energy of 20 eV and a step size of 0.1 eV. Elemental data acquisition below the surface was performed by milling the surface using Argon ions at a pressure of  $4.4 \times 10^{-7}$  Torr, an energy of 4 kV, and a raster size of  $2.5 \times 2.5$  mm. The sputtering rate was calibrated using tantalum oxide (Ta<sub>2</sub>O<sub>5</sub>) of known thickness, resulting in a 2 nm/min sputtering rate. CasaXPS software was used to fit the curves with the curve-fitting parameters (Table 2) for evaluation and quantification.

### 3 RESULTS

#### Tribological Testing

The friction evolution and specific wear rate of the AISI 52100 steel sliding against alumina in the presence of all lubricants are presented in Figure 1. The coefficient of friction (COF) of WG

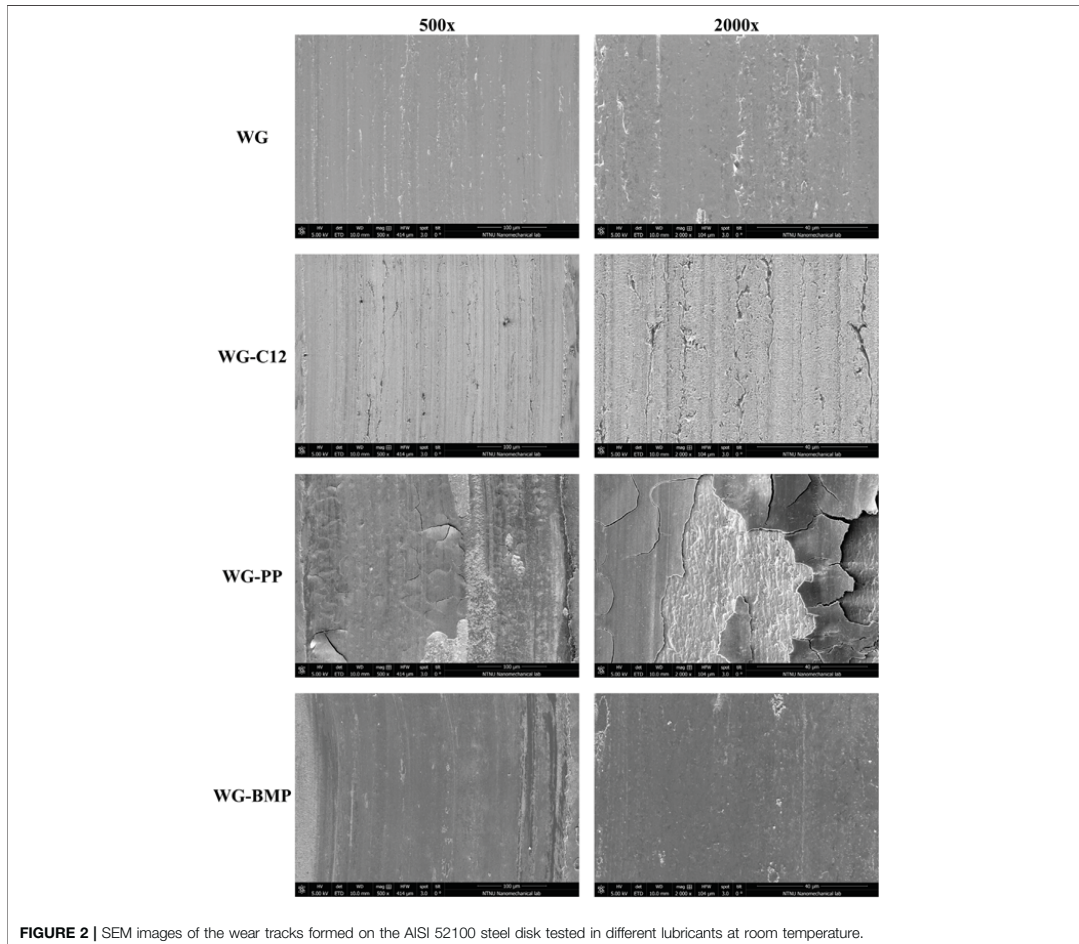


**FIGURE 2** | SEM images of the wear tracks formed on the AISI 52100 steel disk tested in different lubricants at room temperature.

alone shows a value of 0.21 after the running-in period and slightly fluctuates for the rest of the test. The base lubricant with dodecanoic acid (WG-C12) shows a short running-in period and stabilizes at values between 0.10 and 0.12. The addition of 1 wt% PP to the base lubricant (WG-PP) shows a COF of 0.16 during the running-in period, followed by a steady increase to 0.19 at the end of the test. The friction evolution of BMP-containing lubricant (WG-BMP) shows two distinct regions: a COF of 0.28 after the running-in period during 100 m of sliding, followed by an abrupt drop to 0.18 until the end of the test. For wear, the base lubricant generates the highest wear rate of  $9.98 \times 10^{-6} \text{ mm}^3/\text{Nm}$ , followed by BMP, C12, and PP with wear rates of  $9.53 \times 10^{-6}$ ,  $4.45 \times 10^{-6}$ , and  $1.95 \times 10^{-6} \text{ mm}^3/\text{Nm}$ , respectively.

### Wear Track Morphology

**Figure 2** shows the SEM images of the wear tracks' surface at two different magnifications. The wear track of the sample tested with

base lubricant only shows a smooth surface with little sign of plastic deformation. The wear track of the sample tested with WG-C12 is not as smooth as the base lubricant alone, and some surface cracks are observed. The wear track morphology is utterly different for WG-PP, in which many cracks are observed, resulting in detachments in some areas. The wear track of the sample tested with WG-BMP shows a smooth surface with no signs of plastic deformation.

SEM-FIB was used to investigate the wear track cross-section, as shown in **Figure 3**. The length of the cross-section was  $20 \mu\text{m}$  and was taken from the centre of the wear track and perpendicular to the sliding direction. Different degrees of recrystallization and plastic deformation are observed. Samples lubricated with base lubricant alone show a high degree of recrystallization and plastic deformation due to the high friction. The addition of C12 to the base lubricant (which reduced the coefficient of friction by 50%) results in a lower

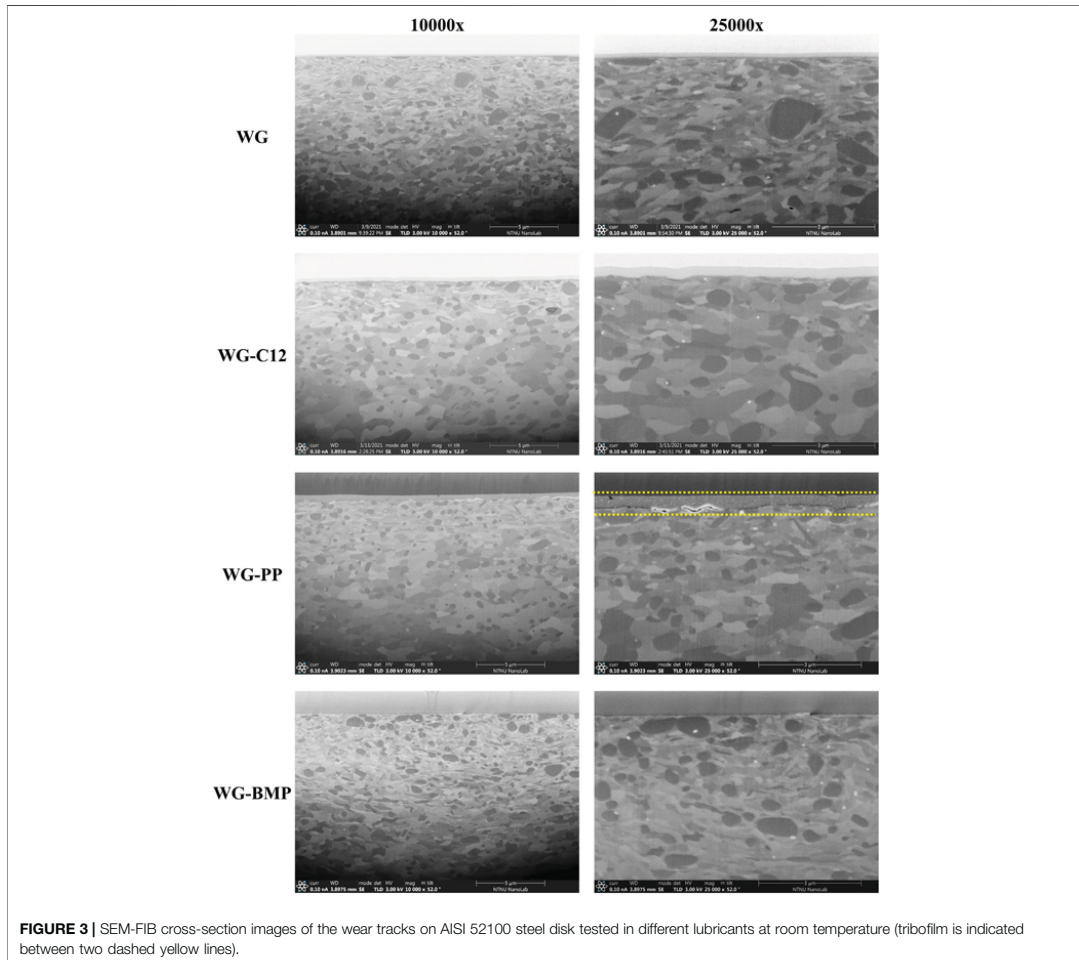


**FIGURE 3 |** SEM-FIB cross-section images of the wear tracks on AISI 52100 steel disk tested in different lubricants at room temperature (tribofilm is indicated between two dashed yellow lines).

degree of recrystallization and plastic deformation and in a rougher surface that is in agreement with the view of the wear track surface (Figure 2). In the WG-BMP sample, the degree of recrystallization and plastic deformation are in between WG and WG-C12. However, the WG-PP sample shows a lower degree of recrystallization and plastic deformation, despite the high coefficient of friction. Interestingly, the top surface of the WG-PP sample is clearly covered by a thick layer (tribofilm), which might be responsible for the lower recrystallization and plastic deformation.

For the WG-BMP sample, a new test was performed for 100 m before the drop in friction is observed (Figure 1A) to analyse this abrupt transition on friction evolution. The top view and cross-section images of the WG-BMP 100 m sample wear track are shown in Figure 4, along with the WG-BMP 300 m sample for comparison. The WG-BMP 100 m sample wear track shows wear

marks, surface cracks, and plastic deformation, whereas a smooth surface without wear marks is observed for the WG-BMP 300 m sample. These wear surface morphologies are in agreement with the friction evolution (Figure 1A), where rougher surfaces produced higher friction and vice versa. Despite having higher friction, the test performed at 100 m resulted in lower recrystallization and plastic deformation than the test at 300 m due to a thick tribofilm formed on the surface, as similarly observed for WG-PP (Figure 3).

### Tribofilm Characterization

In order to investigate the tribofilms, the cross-section of all samples was examined by STEM. A thin lamella of 60 nm from each sample was prepared using SEM-FIB. The STEM images and the EDS elemental mapping are presented in Figure 5. The chosen elements for mapping are oxygen, iron, chromium,

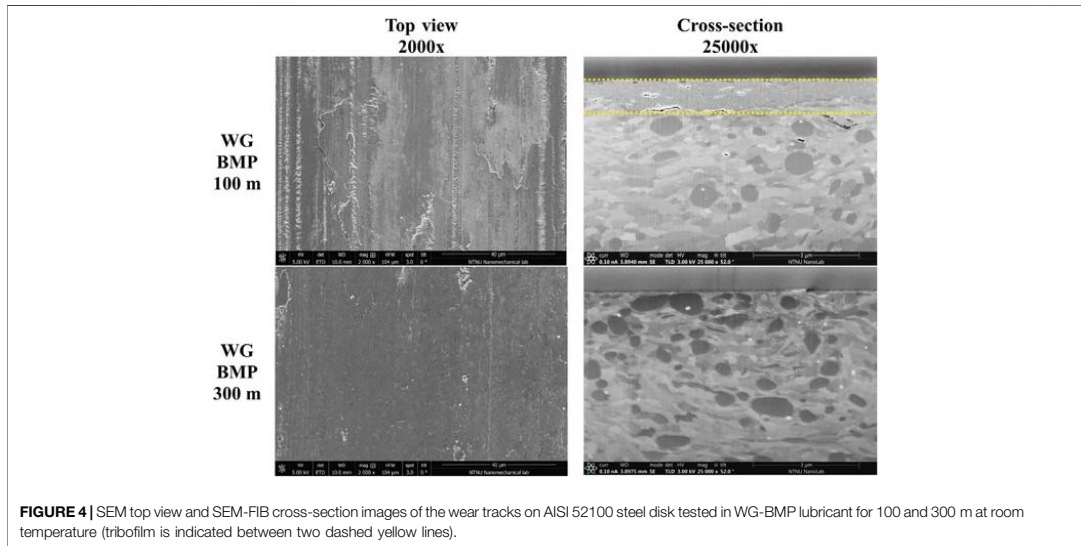


**FIGURE 4** | SEM top view and SEM-FIB cross-section images of the wear tracks on AISI 52100 steel disk tested in WG-BMP lubricant for 100 and 300 m at room temperature (tribofilm is indicated between two dashed yellow lines).

and phosphorous, which are present in the bulk material AISI 52100 steel and the ILs. The oxygen is an indicator of the presence of oxides. Although BMP contains fluorine, this element was not selected for EDS mapping due to the close F K $\alpha$  and Fe L $\alpha$  energy. A platinum protective layer was deposited before the FIB milling processes for WG and WG-C12 samples. For WG-PP and WG-BMP samples, carbon was used as a protective layer instead of platinum to provide better mapping contrast because Pt M $\alpha$  and P K $\alpha$  energies are close to each other.

As seen from the STEM images, the sample lubricated with WG alone shows a thin tribofilm on the surface with a thickness of less than 10 nm (measured from higher magnification images). The lack of additives could be the reason for this thin tribofilm. The WG-C12 sample shows a slightly thicker tribofilm detected on the surface with a ca. 20 nm thickness. A very thick tribofilm is observed for the WG-PP sample of 400–900 nm thickness. In addition, wear debris is observed in the tribofilm, as indicated from the STEM and Fe mapping images. The tribofilm is not fully adhered to the base material, as indicated by a crack at the interface with the base material. Similar characteristics, such as thick tribofilm, wear debris inside the tribofilm, and crack at the interface with the base material, are also observed for the WG-BMP 100 m sample. The thickness of the tribofilm is ca. 600–1,300 nm. For WG-BMP 300 m sample, there is only a tribofilm with a thickness of less than 20 nm observed. EDS mapping of the cross-sections shows high oxygen levels in the tribofilms of all samples, indicating they consist mainly of oxides. Only an additional element, phosphorous, is detected in the WG-PP sample.

Point EDS analysis was performed to get a detailed chemical composition of the tribofilm from each sample, and the results are shown in **Table 3** along with the tribofilm thickness after STEM. The point analysis shows mostly Fe and O, as already seen with the mapping (**Figure 5**). Chromium is not detected in the

tribofilms since it is mainly found as chromium carbide precipitate (**Figure 5**).

Surface chemical analysis inside the wear tracks was studied by x-ray photoelectron spectroscopy (XPS) for WG-PP 300 m, WG-BMP 300 m, and WG-BMP 100 m samples only. These three samples were selected to evaluate more in detail the chemical bonding states of phosphorous and fluorine because these elements were difficult to detect with EDS. The XPS analysis was done by sputtering the wear track with Argon for 300 s (ca. 10 nm depth), reaching half of the tribofilm in WG-BMP 300 m and the top surface of the WG-PP 300 m and WG-BMP 100 m tribofilms. The detailed XPS spectra are shown in **Figure 6**.

The results show the presence of Fe only, and no Cr was found. Deconvolution of the Fe spectra shows that they consist of Fe metal (Fe<sup>0</sup>), Fe oxides (FeO, Fe<sub>3</sub>O<sub>4</sub>, Fe<sub>2</sub>O<sub>3</sub>), FePO<sub>4</sub>, and Fe hydroxides (FeOOH, Fe(OH)<sub>3</sub>). The Fe<sup>0</sup> percentage in WG-PP is higher than in WG-BMP 300 m even though the depth of analysis is far from the bulk material (minimum ca 380 nm from the bulk). This can be due to wear debris spreading in the tribofilm (**Figure 5**) or due to the large tribofilm detachment areas (**Figure 4**). The O spectra show mostly metal hydroxide and metal oxide, in agreement with the Fe spectra. Phosphate (PO<sub>4</sub>)<sup>3-</sup> is detected from the Fe2p and P2p spectra in the case of WG-PP, which is in agreement with the EDS analysis (**Figure 5**). In the case of WG-BMP (both 100 and 300 m), no P and F are detected in the tribofilm, and only oxides and hydroxides are present.

## 4 DISCUSSION

### Chemical Effects on the Tribofilm Formation

The tribofilm formation is influenced by several factors, such as lubricant chemical composition, contact mechanics,



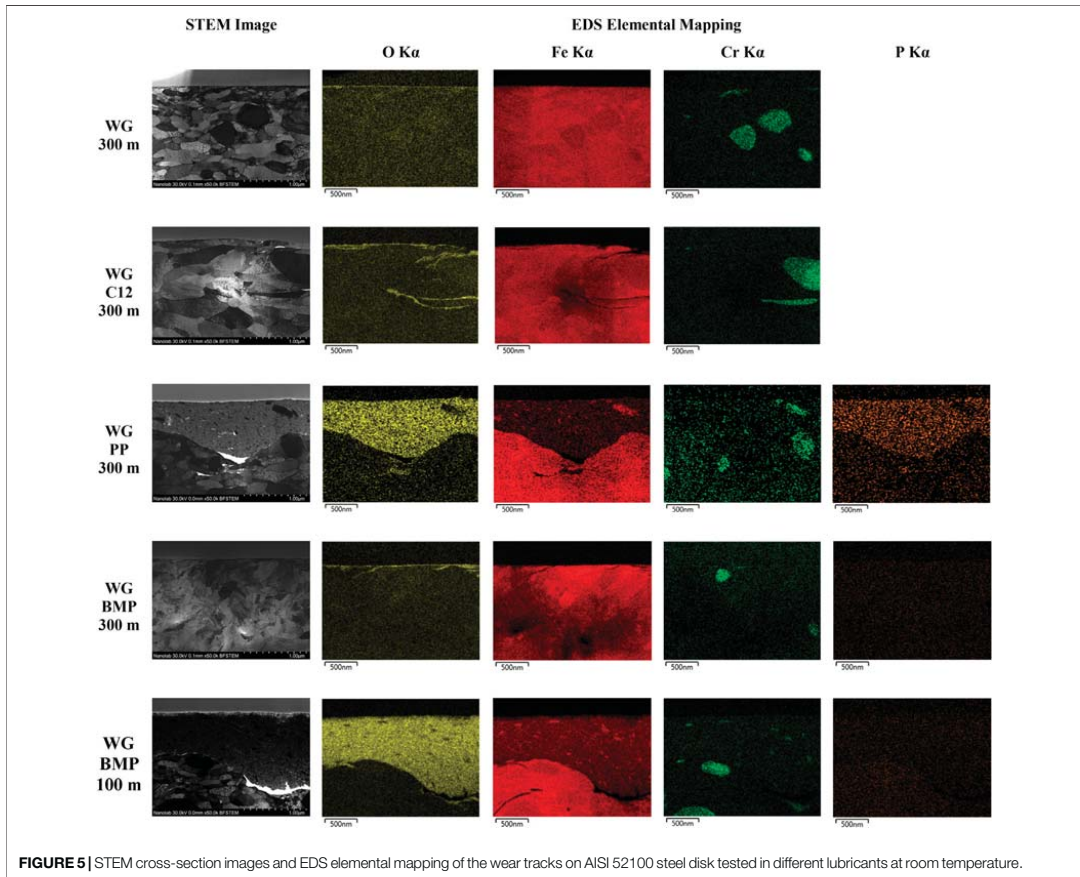


**FIGURE 5** | STEM cross-section images and EDS elemental mapping of the wear tracks on AISI 52100 steel disk tested in different lubricants at room temperature.

**TABLE 3** | Relative concentration inside the tribofilm (at%).

Sample	Tribofilm thickness (nm)	Elemental concentration in tribofilm (at%)			
		Fe	Cr	O	P
WG 300 m	<10	57.81	0.00	42.19	–
WG-C12 300 m	20	42.60	0.00	57.40	–
WG-PP 300 m	400 – 900	29.46	0.00	64.60	5.94
WG-BMP 300 m	20	49.67	0.00	50.33	0.00
WG-BMP 100 m	600 – 1,300	44.82	0.00	55.18	0.00

environment, and types of materials (Kapsa and Martin, 1982; Morina and Neville, 2007; Jacobson et al., 2010). In this work, the lubricant chemical composition was varied by adding different ionic liquids to the base lubricant to study the effect of electrical conductivity and pH on tribofilm formation, friction and wear. **Table 4** shows the different physical and chemical characteristics of all the lubricant-additive mixtures studied in this work.

The electrical conductivity of the lubricant slightly increases when adding C12. However, it increases by two orders of magnitude when adding the ionic liquids, but it is still below the electrical conductivity of tap water. Of the two ILs, PP results in the highest electrical conductivity (twice higher than BMP). PP and BMP increases the electrical conductivity of the based lubricant due to the nature of the ionic liquid which act as a charge carrier inside the lubricant. The higher molecular weight

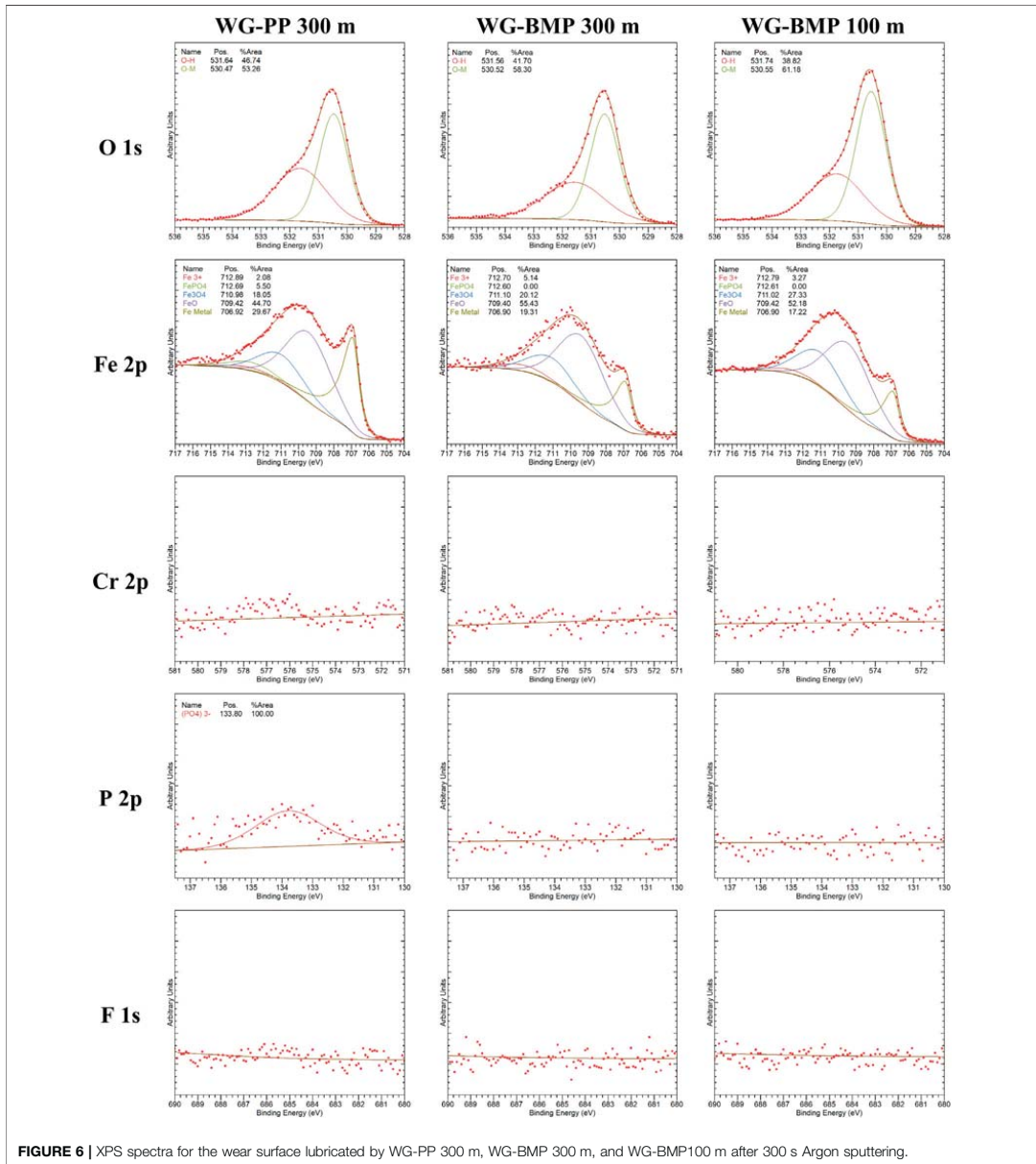


**FIGURE 6 |** XPS spectra for the wear surface lubricated by WG-PP 300 m, WG-BMP 300 m, and WG-BMP100 m after 300 s Argon sputtering.

of BMP can be the reason for its lower electrical conductivity compared to PP in water media. C12 and PP decrease the pH to acidic values. The deprotonation of the carboxylic group (COOH) is the main reason for the drop of pH in this case. In the case of PP, the possible formation of phosphoric acid is the

reason for dropping in pH due to the ionic interaction between the cation or the anion of PP with water. However, BMP keeps the pH value of the base lubricant possibly due to the low electrical conductivity and therefore the lower interaction of the anions and cations with water as compared to PP. The OCP of the metal,

**TABLE 4** | Physical and chemical properties of all lubricants.

Lubricant	Additive concentration (wt%)	Density (g/cm <sup>3</sup> )	Dynamic viscosity (mPa.s)	Electrical conductivity (μS/cm) <sup>a</sup>	pH	OCP vs Ag/AgCl (mV)
WG	—	1.040	13.99	2.5	7.3	−537
WG-C12	0.1	1.041	13.53	4.3	4.7	−396
WG-PP	1	1.039	13.76	211.2	3.4	−588
WG-BMP	1	1.045	14.02	109.3	7.0	−522

<sup>a</sup>For comparison, the electrical conductivity of tap water is ca 500 μS/cm and for seawater is ca 5,000 μS/cm.

**TABLE 5** | Wear track chemical composition after XPS analysis.

Sample	Tribofilm thickness (nm) (after STEM from Table 3)	XPS chemical analysis (at%)				Fe oxides/Fe <sup>0</sup> ratio
		Fe <sup>0</sup>	FeO	Fe <sub>3</sub> O <sub>4</sub>	FePO <sub>4</sub>	
WG 300 m	<10			Not measured		
WG-C12 300 m	20			Not measured		
WG-PP 300 m	400–900	29.67	44.70	18.05	5.50	2.11
WG-BMP 300 m	20	19.31	55.43	20.12	0	3.91
WG-BMP 100 m	600–1,300	17.22	52.18	27.33	0	4.62

in all cases, around −500 mV, whereas it was only 100 mV more positive (ca. −400 mV) for C12. These OCP values are well in agreement with carbon steel exposed to water media and represent an active dissolution corrosion process (Fontana, 1987).

The differences in pH and electrical conductivity have an effect on the chemistry of the metal surface and, therefore, on the tribofilm formation. In **Table 5**, the chemical composition of the tribofilms obtained from XPS analysis is shown, along with the Fe oxides to metal ratio and tribofilm thicknesses. The lowest electrical conductivity leads to thin tribofilm formation (WG and WG-C12). Likewise, the highest electrical conductivity results in thicker tribofilms (WG-PP and WG-BMP 100 m). The tribofilm thickness only increases significantly if the electrical conductivity is high enough (**Table 5**). The Fe oxides to metal ratio is an indicator of the relative number of oxides inside the tribofilm. The sample lubricated with WG-PP shows the lowest Fe oxides to metal ratio (2.11). In the case of WG-BMP 300 m and WG-BMP 100 m the ratio increases to 3.91 and 4.62, respectively, indicating BMP produced more oxide compared to PP.

Based on the pH values (**Table 4**), it can be expected that in an acidic medium such as WG-PP (pH of 3.4) carbon steel would undergo iron dissolution compared to the medium with neutral pH (WG-BMP, pH of 7.0). Indeed, it was found by XPS (**Table 5**) that the WG-BMP 100 m has more oxides to metal ratio compared to WG-PP, however WG-PP had FePO<sub>4</sub> in addition to oxides. These two additives yielded a very thick tribofilm with very different chemical compositions (**Table 5**). The different tribofilm chemical compositions resulted in different tribological responses: WG-PP showed lower friction and wear rate than WG-BMP (**Figure 1**). Therefore, iron oxides and FePO<sub>4</sub> together have a more beneficial effect than iron oxides alone in the tribofilm. This is clearly seen by the friction evolution of WG-BMP in the first 150 sliding meters of the test, which is twice higher than in the last sliding meters. Once the iron oxide

tribofilm has been removed, its build-up is very slowly decreasing friction. In the case of WG-PP, friction is low throughout the test due to the presence of phosphates. However, this is not enough to reach the lowest friction values of WG-C12, since in this case, the friction mechanism is controlled by surface adsorption and not by tribofilm formation.

Unlike ZDDP, which has a metal atom in its structure, PP and BMP require external metal supply to grow a tribofilm. The source of the metal should come from the nascent base metal surface or the wear debris. Tribofilm formation consists of three stages, i.e. tribofilm initiation, wear debris generation and breakdown, and tribofilm growth (Zhou et al., 2017). Tribofilm initiation occurs when the lubricant reacts with the nascent metal surface to form a thin oxide film. This oxide film acts as an interlayer, providing a good bonding between the metal surface and the tribofilm, or acting as a barrier hindering further tribofilm growth (Stachowiak and Batchelor, 2014; Zhou et al., 2017). In the second stage, the material is removed from the top metal surface, generating wear debris, which reacts with the lubricant (i.e. oxidizes). Some of the wear debris gets trapped in the contact area, where it grinds and breaks down in nanosized particles. In the third stage, the tribofilm growth can occur via three mechanisms, i.e. mechanical deposition, chemical deposition, and oxygen diffusion (Zhou et al., 2017). In this work, the thick tribofilms found in WG-PP and WG-BMP 100 m have grown up via mechanical deposition and compacting of the wear debris nanoparticles in the contact area. This is clearly seen in **Figure 5** and later confirmed from the XPS analysis (**Figure 6** and **Table 5**), where iron oxides, iron phosphate and metallic iron are found in the tribofilms (at 10 nm from the surface). In addition, chemical deposition and oxygen diffusion have occurred, resulting in the formation of iron oxide and/or iron phosphate compounds in the tribofilm, leading to further tribofilm growth.



In this work, the electrical conductivity has controlled the tribofilm growth after the first stage of tribofilm formation. This is clear when looking at WG and WG-C12, where the first stage thin oxide film builds on the surface (Table 5) however, due to the low electrical conductivity, the dissolution of this oxide film is slower and hinders further wear debris deposition. Moreover, in the case of WG-C12, not only the thin oxide film is present on the surface, but also dodecanoic acid is strongly adsorbed providing low shear and preventing further tribofilm growth. For WG-PP and WG-BMP, the dissolution of the first stage thin oxide film takes place due to the high electrical conductivity providing active metal surface sites for wear debris deposition, facilitating further tribofilm build up.

### The Effect of Tribofilm Formation on Friction Evolution

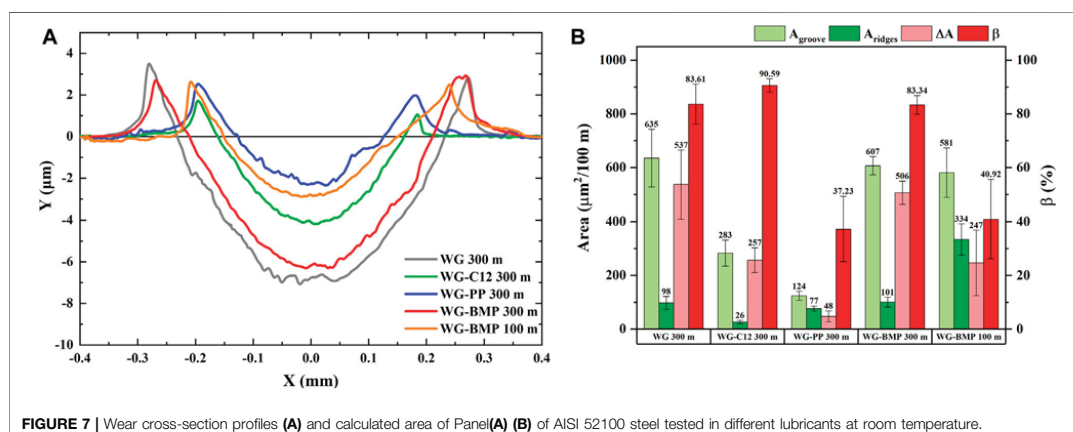
As shown in Figure 1, the friction evolution of WG alone was the highest, and by adding C12, the friction reduces drastically. According to the literature, the friction reduction of carboxylic acid in polar media is due to the thin oxide film formation and the adsorption of carboxylic acid onto the rubbing surface (Zavieh and Espallargas, 2017; Bernat et al., 2018b). Furthermore, a quartz crystal microbalance (QCM) study showed that carboxylic acid forms adsorbed layers with high rigidity and high modulus of elasticity, meaning that the carboxylic acid strongly bonds to the metal surface (Khanmohammadi et al., 2020). The thin oxide film and the strongly adsorbed layer act as a barrier hindering further tribofilm growth, resulting in low and steady friction throughout the test.

On the other hand, the friction mechanism of ILs is controlled by tribofilm formation, which depends on the electrical conductivity and the pH of the media. Both PP and BMP bring the same level of electrical conductivity to the base lubricant, but different pH having an effect on the tribofilm build up process. In the case of WG-BMP, due to the neutral pH, the presence of mainly iron oxides in the tribofilm was favoured,

in accordance with XPS results (Table 4). The tribofilm growth occurs via mechanical and chemical deposition, as shown in the STEM image for WG-BMP 100 m (Figure 5). The tribofilm growth influences the friction evolution (Figure 1), in which there is an increase of friction at the beginning of the test. The friction remains at high values for ca. 150 m when a thick tribofilm is present on the surface, and it reduces as the tribofilm is removed at the last 150 m of the test (Figure 1). In WG-PP, due to the high electrical conductivity, the tribofilm also grows. However, due to the low pH, more active dissolution ( $\text{Fe}^{2+}$ ) occurs, and competition between tribofilm growth and active dissolution takes place. At the first 40 m of the sliding test, active dissolution overcomes the tribofilm growth, resulting in decreased friction (Figure 1). However, phosphorus (in the form of iron phosphate) in the tribofilm (Figure 5) stabilizes the tribofilm growth for the rest of the test. This allows for keeping a steady friction evolution. However, the friction values are higher than for C12 since the tribofilm is more rigid than the adsorbed carboxylic acid layer.

### The Effect of Tribofilm on Wear

The additives resulted in a lower wear rate than the neat base lubricant (Figure 1), showing the additives' importance in the antiwear performance. As stated in Section 2.2, the wear rate was calculated based on the total volume loss occurring during the whole test. To further study the wear mechanism, a more detailed analysis of the volume loss was conducted. Wear profiles from each lubricant condition (Figure 7A) show the formation of ridges and a groove. Based on these 2-D wear profiles, the actual volume loss (area loss in this case) can be calculated from the difference between the groove and the ridges. The ridges area ( $A_{\text{ridges}}$ ), groove area ( $A_{\text{groove}}$ ), and area loss ( $\Delta A$ ) are presented in Figure 7B along with the degree of material loss ( $\beta$ ). The measured areas are normalized to 100 m for easier comparison. The degree of material loss is defined as the ratio between area loss and groove area as shown in the following equation (Bruce, 2012):



$$\beta = \frac{A_{\text{groove}} - A_{\text{ridges}}}{A_{\text{groove}}} \times 100 = \frac{\Delta A}{A_{\text{groove}}} \times 100$$

$\beta$  can be used as an indication of the type of wear, in which higher  $\beta$  indicates more abrasive wear whereas lower  $\beta$  indicates more plastic deformation.

**Figure 7B** shows that WG 300 m, WG-C12 300 m, and WG-BMP 300 m samples have comparable  $\beta$  values, indicating a similar wear mechanism, which corresponds to predominantly abrasive wear. However, the  $\beta$  values of WG-PP 300 m and WG-BMP 100 m are the lowest, indicating predominantly plastic deformation. This discrepancy in wear mechanisms is in agreement with the differences in tribofilm formation.

As shown from the STEM images and the EDS data (**Figure 5** and **Table 3**), WG-PP 300 m and WG-BMP 100 m produced a very thick tribofilms with the highest degree of oxidation. Indeed, the degree of oxidation is well correlated with the lower area loss ( $\Delta A$ ). This was also observed for the WG-BMP samples in which WG-BMP 100 m sample shows lower area loss ( $\Delta A$ ) than WG-BMP 300 m. The high electrical conductivity (i.e. oxidation degree) creates a thick tribofilm that reduces wear. Moreover, the WG-PP 300 m tribofilm also contains iron phosphate (**Figure 6** and **Table 5**), enhancing its antiwear properties. Therefore, the formation of a thick tribofilm has a beneficial effect on the wear reduction of the steel.

However, when looking at the wear track surface and the FIB cross-sections, the thickest tribofilms (WG-PP and WG-BMP 100 m) have poor adhesion to the metal (**Figure 2, 3, 4**) that can have a detrimental effect on the tribofilm integrity. The different mechanical properties of the tribofilm and the metal might be responsible for this behaviour, where under pressure, the ductile metal tends to plastically deform leading to cracking and detachment of the more brittle oxide tribofilm at the interface.

## 5 CONCLUSION

The effect of lubricant additive chemistry on friction and wear of AISI 52100 steel was investigated in a water-based lubricant. The following conclusions can be drawn:

- Dodecanoic acid showed a significant reduction in friction due to the adsorption on the metal surface. However, the oxide film growth was limited due to lower electrical conductivity, leading to higher wear rates.

## REFERENCES

- Amiril, S. A. S., Rahim, E. A., and Syahrullail, S. (2017). A Review on Ionic Liquids as Sustainable Lubricants in Manufacturing and Engineering: Recent Research, Performance, and Applications. *J. Clean. Prod.* 168, 1571–1589. doi:10.1016/j.jclepro.2017.03.197
- Archard, J. F. (1953). Contact and Rubbing of Flat Surfaces. *J. Appl. Phys.* 24, 981–988. doi:10.1063/1.1721448
- Bernat, S., Armada, S., and Espallargas, N. (2018). Effect of Contamination on the Friction and Wear of Carboxylic Acids in Aqueous Lubricants. *Tribology Lett.* 66, 1–12. doi:10.1007/s11249-018-1116-9

- The ionic liquids investigated in this work increase the lubricant's electrical conductivity affecting the oxidation degree of the metal and the tribofilm formation. The resulting very thick tribofilms (400–1,300 nm) decrease the wear rate of the steel. However, these thick tribofilms do not significantly decrease friction.
- Ionic liquids influence the pH of the lubricant and therefore affect the chemical composition of the tribofilm, yielding different tribological responses. Lower pH generates more iron dissolution resulting in friction reduction due to the formation of iron phosphate.
- Iron phosphate stabilizes the tribofilm growth and provides it with better mechanical properties, being the effect more positive for wear than for friction.
- Thick and rigid tribofilms on the ductile base metal are brittle and promote crack formation at the interface, resulting in detachment and debris formation.

## DATA AVAILABILITY STATEMENT

The original contributions presented in the study are included in the article/supplementary material, further inquiries can be directed to the corresponding authors.

## AUTHOR CONTRIBUTIONS

WW planned and carried out the experiments, analyzed the data and wrote the manuscript. HK contributed to the design and implementation of the research, to the analysis of the results and to the writing of the manuscript. NE conceived the original idea of the research, was in charge of overall direction and planning the study and was the project supervisor. All authors discussed the results and commented on the manuscript.

## ACKNOWLEDGMENTS

The authors would like to acknowledge the financial support from Indonesia Endowment Fund for Education (LPDP), M-ERA.NET GreenCOAT project with Project Number 4153, and the Norwegian Micro- and Nano-fabrication facility, NorFab, for providing the characterization facilities.

- Bernat, S., Armada, S., and Espallargas, N. (2018). Friction Mechanisms by Carboxylic Acids in Aqueous Lubricants. *Tribology Lett.* 66, 1–15. doi:10.1007/s11249-018-1035-9
- Bruce, R. W. (2012). *Handbook of Lubrication and Tribology, Volume II: Theory and Design*. Boca Raton: CRC Press.
- Candelaria, K. (2018). Finding Alternatives to ZDDP. Available at: [https://www.lubesngreases.com/magazine/24\\_11/finding-alternatives-to-zddp/](https://www.lubesngreases.com/magazine/24_11/finding-alternatives-to-zddp/) (Accessed December 12, 2021).
- Canter, N. (2019). Special Report: ZDDP's Uncertain Future. Available at: [https://www.stle.org/files/TLTArchives/2019/09\\_September/Tech\\_Beat.aspx](https://www.stle.org/files/TLTArchives/2019/09_September/Tech_Beat.aspx) (Accessed December 12, 2021).
- Chang, Z. Y., Breeden, D., and McDonald, M. (2011). The Use of Zinc Dialkyl Dithiophosphate as a Lubricant Enhancer for Drilling Fluids Particularly

- Silicate-Based Drilling Fluids. *Proc. - SPE Int. Symp. Oilfield Chem.* 2, 587–593. doi:10.12118/141327-ms
- Chen, Y., Jha, S., Raut, A., Zhang, W., and Liang, H. (2020). Performance Characteristics of Lubricants in Electric and Hybrid Vehicles: A Review of Current and Future Needs. *Front. Mech. Eng.* 6, 1–19. doi:10.3389/fmech.2020.571464
- Dong, R., Yu, Q., Bai, Y., Wu, Y., Ma, Z., Zhang, J., et al. (2020). Towards superior Lubricity and Anticorrosion Performances of Proton-Type Ionic Liquids Additives for Water-Based Lubricating Fluids. *Chem. Eng. J.* 383, 123201. doi:10.1016/j.cej.2019.123201
- Espallargas, N., Torres, C., and Muñoz, A. I. (2015). A Metal Ion Release Study of CoCrMo Exposed to Corrosion and Tribocorrosion Conditions in Simulated Body Fluids. *Wear* 332–333, 669–678. doi:10.1016/j.wear.2014.12.030
- European Environment Agency (2019). CO<sub>2</sub> Emissions from Cars: Facts and Figures. Available at: <https://www.europarl.europa.eu/news/en/headlines/society/20190313STO31218/co2-emissions-from-cars-facts-and-figures-infographics> (Accessed December 12, 2021).
- Fontana, M. G. (1987). *Corrosion Engineering*. New York (USA): McGraw-Hill.
- Fredriksson, W., Malmgren, S., Gustafsson, T., Gorgoi, M., and Edström, K. (2012). Full Depth Profile of Passive Films on 316L Stainless Steel Based on High Resolution HAXPES in Combination with ARXPS. *Appl. Surf. Sci.* 258, 5790–5797. doi:10.1016/j.apsusc.2012.02.099
- Holmberg, K., and Erdemir, A. (2019). The Impact of Tribology on Energy Use and CO<sub>2</sub> Emission Globally and in Combustion Engine and Electric Cars. *Tribology Int.* 135, 389–396. doi:10.1016/j.triboint.2019.03.024
- Huang, J., Zhou, X., Wang, J., Tang, X., and Kuang, F. (2019). Influence of Temperature on Friction of Polymeric Materials in Water. *Wear* 426–427, 868–876. doi:10.1016/j.wear.2019.01.115
- Jacobson, S., and Hogmark, S. (2010). “Tribofilms – On the Crucial Importance of Tribologically Induced Surface Modifications” in *Recent Developments in Wear Prevention, Friction and Lubrication*. Editor G K Nikas (Kerala, India: Research Signpost), 661, 197–225.
- Kapsa, P., and Martin, J. M. (1982). Boundary Lubricant Films: A Review. *Tribology Int.* 15, 37–42. doi:10.1016/0301-679x(82)90110-4
- Khan, T., Broderick, M., and Taylor, C. M. (2021). Investigating the Industrial Impact of Hydraulic Oil Contamination on Tool Wear during Machining and the Development of a Novel Quantification Methodology. *Int. J. Adv. Manuf. Technol.* 112, 589–600. doi:10.1007/s00170-020-06370-y
- Khanmohammadi, H., Wijanarko, W., and Espallargas, N. (2020). Ionic Liquids as Additives in Water-Based Lubricants: From Surface Adsorption to Tribofilm Formation. *Tribol Lett.* 68, 130. doi:10.1007/s11249-020-01377-8
- Liu, W., Ye, C., Gong, Q., Wang, H., and Wang, P. (2002). Tribological Performance of Room-Temperature Ionic Liquids as Lubricant. *Tribology Lett.* 13, 81–85. doi:10.1023/a:1020148514877
- Long, Y., Bouchet, M. B., Lubrecht, T., Onodera, T., and Martin, J. M. (2019). Superlubricity of Glycerol by Self-Sustained Chemical Polishing. *Sci. Rep.* 9, 1–13. doi:10.1038/s41598-019-42730-9
- Minami, I. (2009). Ionic Liquids in Tribology. *Molecules* 14, 2286–2305. doi:10.3390/molecules14062286
- Morina, A., and Neville, A. (2007). Tribofilms: Aspects of Formation, Stability and Removal. *J. Phys. D: Appl. Phys.* 40, 5476–5487. doi:10.1088/0022-3727/40/18/s08
- Narita, K., and Takekawa, D. (2019). Lubricants Technology Applied to Transmissions in Hybrid Electric Vehicles and Electric Vehicles. SAE Technical Papers.
- Nicholls, M. A., Do, T., Norton, P. R., Kasrai, M., and Bancroft, G. M. (2005). Review of the Lubrication of Metallic Surfaces by Zinc Dialkyl-Dithiophosphates. *Tribology Int.* 38, 15–39. doi:10.1016/j.triboint.2004.05.009
- Phillips, B. S., and Zabinski, J. S. (2004). Ionic Liquid Lubrication Effects on Ceramics in a Water Environment. *Tribology Lett.* 17, 533–541. doi:10.1023/b:tril.0000044501.64351.68
- Rokosz, K., Hryniewicz, T., Simon, F., and Rzdakiewicz, S. (2016). Comparative XPS analyses of passive layers composition formed on Duplex 2205 SS after standard and high-current-density electropolishing. *Tehnicki Vjesnik* 23, 731–735. doi:10.17559/TV-20141107094438
- Seddon, K. R. (1997). Ionic Liquids for Clean Technology. *J. Chem. Technol. Biotechnol.* 68, 351–356. doi:10.1002/(sici)1097-4660(199704)68:4<351:aid-jctb613>3.0.co;2-4
- Somers, A., Howlett, P., MacFarlane, D., and Forsyth, M. (2013). A Review of Ionic Liquid Lubricants. *Lubricants* 1, 3–21. doi:10.3390/lubricants1010003
- Spikes, H. (2004). The History and Mechanisms of ZDDP. *Tribology Lett.* 17, 469–489. doi:10.1023/b:tril.0000044495.26882.b5
- Spikes, H. (2008). Low- and Zero-Sulphated Ash, Phosphorus and sulphur Anti-wear Additives for Engine Oils. *Lubrication Sci.* 20, 103–136. doi:10.1002/l.s.57
- Spikes, H. (2015). Friction Modifier Additives. *Tribology Lett.* 60, 1–26. doi:10.1007/s11249-015-0589-z
- Stachowiak, G. W., and Batchelor, A. W. (2014). *Engineering Tribology*. Oxford (UK): Elsevier.
- THE EUROPEAN COMMISSION (2014). *Commission Regulation (EU) No 136/2014*. Brussel, Belgium: Official Journal of the European Union.
- Tomala, A., Karpinska, A., Werner, W. S. M., Olver, A., and Störi, H. (2010). Tribological Properties of Additives for Water-Based Lubricants. *Wear* 269, 804–810. doi:10.1016/j.wear.2010.08.008
- Transport and Environment (2019). *Electric Surge: Carmakers' Electric Car Plans across Europe 2019-2025*. Available at: <https://www.transportenvironment.org/discover/electric-surge-carmakers-electric-car-plans-across-europe-2019-2025/> (Accessed December 12, 2021).
- Urtis, L. A., Arcifa, A., Zhang, P., Du, J., Fantauzzi, M., Rauber, D., et al. (2019). Influence of Water on Tribolayer Growth when Lubricating Steel with a Fluorinated Phosphonium Dicyanamide Ionic Liquid. *Lubricants* 7, 27. doi:10.3390/lubricants7030027
- Van Rensselar, J. (2019). The Tribology of Electric Vehicles. *Tribology Lubrication Technol.* 75, 34–43.
- Viesca, J. L., García, A., Hernández Battez, A., González, R., Monge, R., Fernández-González, A., et al. (2013). FAP– Anion Ionic Liquids Used in the Lubrication of a Steel-Steel Contact. *Tribol Lett.* 52, 431–437. doi:10.1007/s11249-013-0226-7
- Wang, Y., Yu, Q., Cai, M., Zhou, F., and Liu, W. (2018). Halide-Free PN Ionic Liquids Surfactants as Additives for Enhancing Tribological Performance of Water-Based Liquid. *Tribology Int.* 128, 190–196. doi:10.1016/j.triboint.2018.07.018
- Wasserscheid, P., and Welton, T. (2002). *Ionic Liquids in Synthesis*. Weinheim (Germany): Wiley-VCH Verlag GmbH & Co. KGaA.
- Welton, T. (1999). Room-Temperature Ionic Liquids. Solvents for Synthesis and Catalysis. *Chem. Rev.* 99, 2071–2084. doi:10.1021/cr980032t
- Welton, T. (2018). Ionic Liquids: A Brief History. *Biophys. Rev.* 10, 691–706. doi:10.1007/s12551-018-0419-2
- Xiao, H. (2017). Ionic Liquid Lubricants: Basics and Applications. *Tribology Trans.* 60, 20–30. doi:10.1080/10402004.2016.1142629
- Xie, G., Liu, S., Guo, D., Wang, Q., and Luo, J. (2009). Investigation of the Running-In Process and Friction Coefficient under the Lubrication of Ionic Liquid/Water Mixture. *Appl. Surf. Sci.* 255, 6408–6414. doi:10.1016/j.apsusc.2009.02.029
- Ye, C., Liu, W., Chen, Y., and Yu, L. (2001). Room-Temperature Ionic Liquids: A Novel Versatile Lubricant. *Chem. Commun.* 21, 2244–2245. doi:10.1039/b106935g
- Yu, B., Zhou, F., Pang, C., Wang, B., Liang, Y., and Liu, W. (2008). Tribological Evaluation of  $\alpha$ -diimidazoliumalkylene Hexafluorophosphate Ionic Liquid and Benzotriazole as Additive. *Tribology Int.* 41, 797–801. doi:10.1016/j.triboint.2008.02.004
- Zavieh, A. H., and Espallargas, N. (2017). The Effect of Friction Modifiers on Tribocorrosion and Tribocorrosion-Fatigue of Austenitic Stainless Steel. *Tribology Int.* 111, 138–147. doi:10.1016/j.triboint.2017.03.008
- Zheng, G., Zhang, G., Ding, T., Xiang, X., Li, F., Ren, T., et al. (2017). Tribological Properties and Surface Interaction of Novel Water-Soluble Ionic Liquid in Water-Glycol. *Tribology Int.* 116, 440–448. doi:10.1016/j.triboint.2017.08.001
- Zhou, Y., and Qu, J. (2017). Ionic Liquids as Lubricant Additives: A Review. *ACS Appl. Mater. Inter.* 9, 3209–3222. doi:10.1021/acsmi.6b12489
- Zhou, Y., Leonard, D. N., Guo, W., and Qu, J. (2017). Understanding Tribofilm Formation Mechanisms in Ionic Liquid Lubrication. *Sci. Rep.* 7, 8426–8428. doi:10.1038/s41598-017-09029-z

**Conflict of Interest:** The authors declare that the research was conducted in the absence of any commercial or financial relationships that could be construed as a potential conflict of interest.

**Publisher's Note:** All claims expressed in this article are solely those of the authors and do not necessarily represent those of their affiliated organizations, or those of the publisher, the editors and the reviewers. Any product that may be evaluated in this article, or claim that may be made by its manufacturer, is not guaranteed or endorsed by the publisher.

Copyright © 2022 Wijanarko, Khanmohammadi and Espallargas. This is an open-access article distributed under the terms of the Creative Commons Attribution License (CC BY). The use, distribution or reproduction in other forums is permitted, provided the original author(s) and the copyright owner(s) are credited and that the original publication in this journal is cited, in accordance with accepted academic practice. No use, distribution or reproduction is permitted which does not comply with these terms.

*This page is intentionally left blank*

### **Paper III**

Effect of steel hardness and composition on the boundary lubricating behavior of low viscosity PAO formulated with dodecanoic acid and ionic liquid additives

Langmuir 2022, Vol. 38, 2777–2792

DOI: 10.1021/acs.langmuir.1c02848

*This page is intentionally left blank*

# Effect of Steel Hardness and Composition on the Boundary Lubricating Behavior of Low-Viscosity PAO Formulated with Dodecanoic Acid and Ionic Liquid Additives

Wahyu Wijanarko,\* Hamid Khanmohammadi, and Nuria Espallargas\*



Cite This: *Langmuir* 2022, 38, 2777–2792



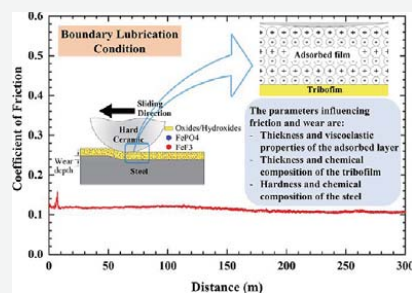
Read Online

ACCESS |

Metrics & More

Article Recommendations

**ABSTRACT:** Two ionic liquids, tributylmethylphosphonium dimethylphosphate (PP) and 1-butyl-1-methylpyrrolidinium tris(pentafluoroethyl)-trifluorophosphate (BMP), as lubricant additives in polyalphaolefin (PAO) were studied under boundary lubricating conditions on two types of steel (AISI 52100 bearing steel and AISI 316L stainless steel). The tribological behavior of these ILs was compared with dodecanoic acid, a well-known organic friction modifier. This study employs a ball-on-disk tribometer with an alumina ball as a counterpart. A range of advanced analytical tools are used to analyze the tribofilms, including scanning electron microscopy equipped with a focused ion beam, scanning transmission electron microscopy equipped with X-ray energy-dispersive spectroscopy, and X-ray photoelectron spectroscopy. A quartz crystal microbalance with dissipation was used to study the surface adsorption of the additives on iron- and stainless steel-coated sensors to reveal the adsorption kinetics, adsorbed layer mass, and bonding strength of the adsorbed layer on the metallic surfaces. The most important factors controlling friction and wear are the thickness and viscoelastic properties of the adsorbed layer, the thickness and chemical composition of the tribofilm, and the hardness and chemical composition of steel. Among all additives studied, BMP on stainless steel gives a strongly adsorbed layer and a durable tribofilm, resulting in low friction and excellent antiwear properties.



## INTRODUCTION

Friction between moving parts and their associated wear is estimated to be directly responsible for 23% of the world's energy consumption.<sup>1</sup> Road transport is responsible for 22% of Europe's CO<sub>2</sub> emissions. An electric car charging on the European electricity grid corresponds to about 20 g/km of CO<sub>2</sub> emissions. In electric cars, moving parts work at a higher speed than in internal combustion engine cars, making the lubricants function more as a torque transfer than as a load-bearing.<sup>2</sup> The higher the speed of the tribological component, the higher the temperature generated in the lubricant. Therefore, low-viscosity lubricants with better cooling properties and higher temperature stability are the trend for meeting the UN sustainable goals.<sup>3,4</sup> The performance of low-viscosity lubricants can be maintained by advancing the technology of additives with multiple functions, for example, simultaneous friction-reducing and antiwear properties. In recent years, researchers have attracted great interest in ionic liquids (ILs) since they are seen as potential high-performance lubricant additives due to their inherent polarity, which provides strong surface adsorption. Moreover, ILs can be easily tailored and tuned to meet different properties; therefore, they are potential candidates for multifunctional lubricant additives.

ILs are organic salts with a low melting point (below 100 °C).<sup>5,6</sup> ILs consist of cations and anions with an asymmetric structure and delocalized electrical charges, preventing them from forming solid crystals. As a result, ILs are liquid at room temperature. ILs were first studied as an alternative to space lubricants in the early 2000s due to their unique properties, such as nonflammability, low melting point, low volatility, high thermal stability, and high polarity.<sup>7–10</sup> Since then, the tribological performance of ionic liquids has been compared with conventional hydrocarbon-based lubricants, such as perfluoropolyether (PFPE),<sup>11–13</sup> polyalphaolefin (PAO),<sup>13,14</sup> and mineral oils.<sup>14–16</sup> However, due to their complex synthesis and price, recent works on ILs have focused on their performance as lubricant additives.<sup>17–22</sup>

Two lubrication mechanisms of ILs are proposed in the literature: (1) ILs adsorb to the worn surface to form adsorbed layers and (2) ILs react with the worn surface to form a

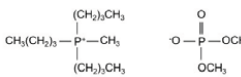
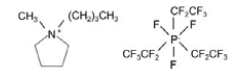
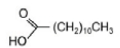
Received: October 25, 2021

Revised: February 10, 2022

Published: February 23, 2022



Table 1. Chemical Formula, Density, and Chemical Structure of All Additives

Abbr.	Chemical Name	Chemical Formula	Density (kg/m <sup>3</sup> )	Chemical Structure
PP	Tributylmethylphosphonium dimethylphosphate	C <sub>15</sub> H <sub>36</sub> O <sub>4</sub> P <sub>2</sub>	1004	
BMP	1-butyl-1-methylpyrrolidinium tris(pentafluoroethyl) trifluorophosphate	C <sub>15</sub> H <sub>20</sub> F <sub>18</sub> NP	1647	
C12	Dodecanoic acid	CH <sub>3</sub> (CH <sub>2</sub> ) <sub>10</sub> COOH	880	

protective tribofilm.<sup>19</sup> For the first mechanism, the rubbing action during the test removes the electrons from the metal surface, leaving a positively charged surface.<sup>23</sup> The anion moieties of ILs are attracted to the surface, while the cation moieties face the lubricant, forming the first adsorbed layer. Subsequently, the adjacent IL in the lubricant is attracted to the first adsorbed layer in the same manner, forming a multilayer structure at the surface.<sup>24–27</sup> For the second mechanism, localized high temperature and high pressure are generated at the contact area, decomposing the ILs. Consequently, the decomposition products of ILs reacts with the nascent worn surface to form a protective tribofilm.<sup>28–32</sup> Most research on ILs as lubricant additives focuses on the boundary lubricating condition and tribofilm formation.<sup>28–38</sup> Only a few study the adsorption mechanisms of ILs;<sup>22,35,39</sup> therefore, the lubricating mechanism of ILs is still far from being fully understood.

This paper studies ILs as potential additives in a low-viscosity nonpolar medium. Two ILs (tributylmethylphosphonium dimethylphosphate and 1-butyl-1-methylpyrrolidinium tris(pentafluoroethyl)trifluorophosphate) have been studied in a polyalphaolefin base lubricant with a viscosity of 8 cSt at 100 °C (PAO8). No additional additives were used to isolate the effect of the ILs alone. The lubricating mechanisms of ILs are compared with a well-known organic friction modifier (dodecanoic acid). The lubricating mechanisms have been investigated by studying their behavior on two steel materials (AISI 52100 bearing steel and AISI 316L austenitic stainless steel) due to their wide range of applications in tribological components. Therefore, the effect of surface chemistry and mechanical properties on the lubricating mechanisms could be investigated. For the surface adsorption study, a quartz crystal microbalance with dissipation mode (QCM-D) using iron- and stainless steel-coated sensors was employed. X-ray photoelectron spectroscopy (XPS) and scanning transmission electron microscopy equipped with X-ray energy-dispersive spectroscopy (STEM-EDS) were used to study the tribofilm formation.

## MATERIALS AND METHODS

**Materials.** Two ionic liquids (ILs) were used as additives in a nonpolar lubricant, i.e., tributylmethylphosphonium dimethylphosphate (abbreviated as PP) and 1-butyl-1-methylpyrrolidinium tris(pentafluoroethyl)trifluorophosphate (abbreviated as BMP). A well-known organic friction modifier is used as a reference, i.e., dodecanoic acid (abbreviated as C12). Polyalphaolefin with a viscosity of 8 cSt at 100 °C (abbreviated as PAO) was chosen as the base lubricant. PP (97% purity and a molar mass of 342.40 g/mol) was purchased from Fluorochem. Both BMP (≥98%, 587.27 g/mol) and C12 (≥99%,

200.32 g/mol) were purchased from Sigma-Aldrich. Meanwhile, PAO was obtained from Chevron Phillips Chemical. All chemicals were used as received without further purification. Table 1 shows the chemical formula, density, and chemical structure of all additives used in this study. The selected additive concentrations are 1 and 0.1 wt % for ILs and C12, respectively. The concentrations of ILs are chosen based on a two-way ANOVA analysis performed by us in an independent work. The optimum concentration for ILs in PAO was 1 wt % (different concentrations were tested: 0.25, 0.5, 1, and 2 wt %). In contrast, 0.1 wt % was the optimum concentration for C12.<sup>40</sup> A magnetic stirrer was used to blend the base lubricant and the additive for 4 h at 70 °C, followed by 20 h at room temperature.

The tribological performance of each lubricant was studied on AISI 52100 bearing steel and AISI 316L stainless steel. Both steels were purchased from Smith Stål (Trondheim, Norway) with hardness values of 60 HRC and 217 HB (equivalent to 18 HRC) for AISI 52100 bearing steel and AISI 316L stainless steel, respectively. The elastic modulus and Poisson's ratio of both steels are 210 GPa and 0.29, respectively. Disk samples with a thickness of 6 mm were prepared from a 30 mm diameter rod. Surface preparation was done by following the procedure in the metalog guide provided by Struers for each material until it reached a surface finish of Ra = 0.090 ± 0.003 μm.<sup>41</sup> After surface preparation, the sample disks were ultrasonically cleaned in a distilled water–ethanol mixture (ca. 1:1) for 5 min, then rinsed with fresh ethanol, and dried with pressurized air.

**Testing and Characterization Methods.** The stability of the lubricant mixture at room temperature was examined by a turbidity meter (Hanna Instruments HI-88713). The lubricants were put in an ultrasonicator for 1 h before the test. The turbidity number (FNU) was measured by calculating the average value of 12 measurements taken from 2 h tests. PAO, PAO-C12, and PAO-PP have stable turbidity for 2 h, transparent and without phase separation. On the other hand, PAO-BMP resulted in the highest turbidity numbers of all mixtures, indicating lower solubility. However, the turbidity numbers were stable throughout the test. The dynamic viscosity of the lubricants was measured using a rheometer (Haake Mars Rotational Rheometer, with a CC27 cylinder measuring system, with the built-in Peltier element). The measurements were conducted by applying a shear rate of 500 s<sup>-1</sup> for 30 s at 23 °C in humid air. The measured viscosity of the PAO base lubricant was 81 mPa·s. The addition of C12 did not change the viscosity of the base lubricant, and the ILs slightly increased the lubricant's viscosity to 87 and 85 mPa·s for PAO-PP and PAO-BMP, respectively. The density of the lubricants was measured by the weighing method at constant volume. The measured density of the PAO base lubricant was 831.8 kg/m<sup>3</sup>. The addition of the additives slightly increased the density of the lubricant to 840.9, 853.6, and 840.8 kg/m<sup>3</sup> for PAO-PP, PAO-BMP, and PAO-C12, respectively.

The tribological tests were performed using a unidirectional ball-on-disk tribometer (Anton Paar with Phoenix tribology software) to evaluate the tribological performance of each lubricant on AISI 5200 steel and AISI 316L stainless steel. The tests were conducted using a stationary alumina ball against a rotating disk sample of AISI 5200 or AISI 316L stainless steel under boundary lubricating conditions. The



alumina ball (fused ceramic) was purchased from Precision Ball and Gauge Co., Ltd with an elastic modulus of 300 GPa and a Poisson's ratio of 0.21. The roughness of the alumina ball was 0.025  $\mu\text{m}$ . The test parameters were as follows: a ball diameter of 6 mm, a free-weight load of 20 N (corresponding to a maximum initial contact pressure of 1.96 GPa), a disk rotation speed of 40 rpm, and a rotation track diameter of 10 mm. From these parameters, the calculated lambda ( $\lambda$ ) value according to the EHL Hamrock–Dowson equation is 0.039 for the PAO base lubricant (the pressure-viscosity coefficient of PAO is 13  $\text{GPa}^{-1}$  at 25  $^{\circ}\text{C}$ );<sup>42</sup> therefore, the boundary lubricating condition is met. The calculated  $\lambda$  value for PAO-PP, PAO-BMP, and PAO-C12 was 0.040 (assuming the same pressure-viscosity coefficient for additivated PAO as the PAO base lubricant), indicating that the lubricating regime was still in the boundary condition. All lubricants were tested for a distance of 300 m (4 h) at room temperature. For each lubricant–substrate combination, at least two tests were performed to verify the repeatability of the results.

The wear volume was quantified using an optical three-dimensional (3D) microscope (Alicona Infinite Focus Microscope, IFM), followed by surface image analysis using MountainsMap software. The wear volume was measured from four wind directions of the wear tracks, and the average value was then calculated. After that, the specific wear rate was calculated by the following equation<sup>43</sup>

$$\text{SWR} = \frac{V}{N \cdot s} \quad (1)$$

where SWR is the specific wear rate ( $\text{mm}^3/\text{Nm}$ ),  $V$  is the volume loss ( $\text{mm}^3$ ),  $N$  is the normal load ( $N$ ), and  $s$  is the sliding distance ( $m$ ). The average SWR value and the standard deviation of each lubricant–substrate combination were reported.

The wear track top surface was observed using a Quanta FEG 650 scanning electron microscope (SEM). The wear track secondary electron images were recorded using an Everhart–Thornley detector (ETD). The wear track cross section was prepared and studied using an FEI Helios Nanolab DualBeam scanning electron microscope with a focused ion beam (SEM-FIB). A gallium liquid metal ion source was used for preparing the cross section by deposition, milling, and polishing processes. To protect the wear track surface from damage, double layers of platinum were deposited in sequence before milling and polishing processes. The secondary electron images of the cross section were taken using a through lens detector (TLD). After the images were recorded, the process was continued to make a thin lamella sample with a thickness of less than 60 nm using the same SEM-FIB. The tribofilm characterization and chemical composition were studied by examining the lamella by scanning transmission electron microscopy (STEM, Hitachi SU9000) equipped with an X-ray energy-dispersive spectroscopy (EDS) detector (Ultim Extreme, Oxford Instruments).

The elemental composition inside the wear track was examined by X-ray photoelectron spectroscopy (XPS, Kratos Axis Ultra DLD) with monochromatic Al K $\alpha$  as the X-ray source with 10 kV accelerating voltage and 10 mA current. The sample analysis chamber was set to vacuum with a pressure of  $9 \times 10^{-9}$  Torr during the acquisition. Electrostatic and hybrid lenses were used for AISI 52100 steel and AISI 316L stainless steel samples. A high-resolution scan with 20 eV pass energy and 0.1 eV step size was selected to collect the elemental data of phosphorus (P) and fluorine (F). To study the tribofilm, depth profiling was done by sputtering the surface with Argon ions with the following parameters: a pressure of  $4.4 \times 10^{-7}$  Torr, an energy of 4 kV, and a raster size of  $2.5 \times 2.5$  mm. The selected sputtering times were 5 and 85 s. A sputtering time of 5 s was used to remove the contamination on the surface, and a sputtering time of 85 s was used to study the tribofilm chemical composition. The XPS elemental data were analyzed by CasaXPS software using the curve-fitting parameters shown in Table 2 for detailed quantification.

The adsorption studies were performed using a quartz crystal microbalance with dissipation (QCM-D, Biolin Scientific). Two sensors were used in this study, i.e., an iron (Fe)-coated sensor and a stainless steel (SS)-coated sensor from Biolin Scientific. Before the experiment, the sensors were cleaned based on the cleaning procedure provided by Biolin Scientific. The experiment was started by injecting

**Table 2. Detailed Curve-Fitting Parameters of Compounds Used for XPS Characterization**

signal	binding energy ( $\pm 0.1$ eV)	FWHM ( $\pm 0.1$ eV)	line shape	assignment
F 1s <sup>44,45</sup>	684.9	1.6	GL(30)	F <sup>-</sup>
P 2p <sup>46,47</sup>	133.7	1.6	GL(30)	(PO <sub>4</sub> ) <sup>3-</sup>

the base lubricant into the sensor and monitoring the frequency and dissipation shift for at least 30 min to obtain a steady baseline. After that, the solution was changed to the formulated lubricant (base lubricant and additive) for 2 h to measure the adsorption behavior of the additive. Then, the solution was changed back to the base lubricant for 1 h to remove the weakly bonded additive and measure the frequency and dissipation shift of the strongly adsorbed additive species. The experiment was performed with a flow rate of 50  $\mu\text{L}/\text{min}$  using a peristaltic pump. Only the frequency and dissipation change of the fundamental frequency (1st overtone) could be recorded because the viscosity of the tested lubricants was high enough to dampen the quartz crystal, resulting in a high noise-to-peak ratio at higher overtones. At least two experiments were conducted for each solution to check the repeatability of the results.

## RESULTS

**Tribological Testing.** The effectiveness of the additives in the nonpolymer lubricant was examined by sliding tribological tests. The friction evolution results on AISI 52100 steel and AISI 316L stainless steel are presented in Figure 1A,B, respectively. During the running-in period, the coefficient of friction (COF) of AISI 52100 steel lubricated by PAO alone starts from 0.13 and decreases to 0.11. Then, the COF begins to increase after 20 m reaching a value of 0.19 at 70 m before gradually declining to 0.14 at the end of the test. Similar trends are observed for PAO-PP and PAO-BMP, in which PP and BMP delayed the increase of the COF to 30 and 110 m, respectively. In the case of PAO-C12, the COF increases during the running-in from 0.10 to 0.12 for 20 m, followed by a slight decrease until the end of the test. By comparing PAO, PAO-PP, and PAO-BMP lubricants, it is worth noticing that the order of COF from low to high is PAO-BMP, PAO-PP, and PAO during the whole duration of the test. Compared to PAO, PAO-PP, and PAO-BMP, the COF of PAO-C12 is the highest at the beginning of the test and the lowest at the end of the test due to the abrupt COF change of PAO, PAO-PP, and PAO-BMP.

In the case of AISI 316L stainless steel, the friction evolution of PAO alone is characterized by a long running-in period with high friction (0.44) at the start and reaching a steady COF of 0.14 after ca. 50 m until the end of the test. PP in PAO reduces the running-in period drastically, keeping friction slightly lower than PAO alone after running-in. In the case of PAO-BMP, the running-in period decreases, and the friction evolution is steady from the start until the end of the test with a COF similar to PAO-PP. C12 in PAO increases friction to 0.15 and fluctuates during the whole test, indicating unstable friction.

Figure 1C,D shows the influence of the additives on the specific wear rate (SWR) of AISI 52100 steel and AISI 316L stainless steel, respectively. In the case of AISI 52100 steel, the SWR value is  $5.70 \times 10^{-6}$   $\text{mm}^3/\text{Nm}$  for the PAO base lubricant alone. PP and BMP in the base lubricant reduce the SWR by 7 and 36%, respectively. Meanwhile, C12 shows the lowest SWR with a 49% reduction.

In the case of AISI 316L stainless steel, the SWR value for PAO alone is  $1.68 \times 10^{-5}$   $\text{mm}^3/\text{Nm}$  (ca. 3 times higher than AISI 52100 steel). Both PP and BMP reduce the SWR of AISI 316L stainless steel, in which BMP gives the lowest reduction of

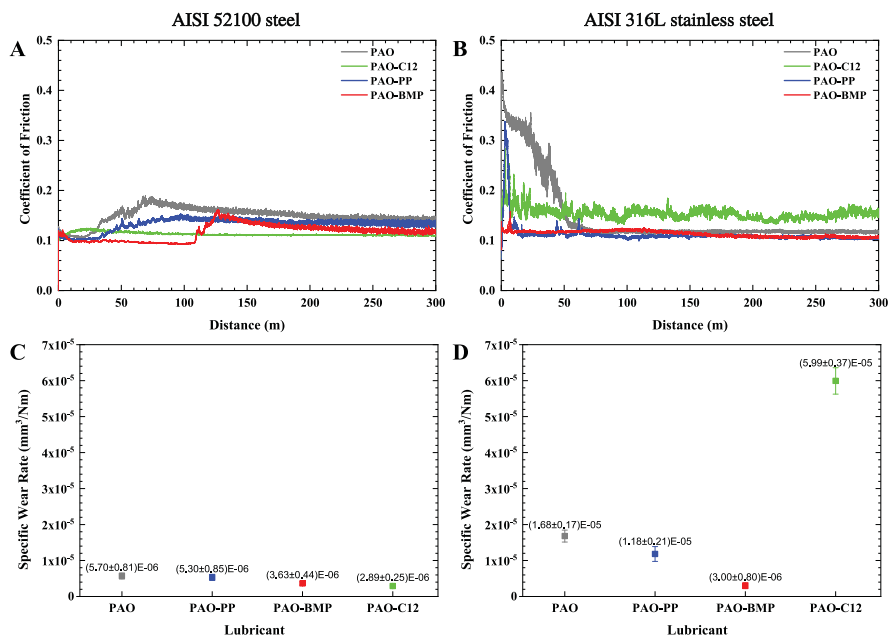


**Figure 1.** Friction evolution and specific wear rate of AISI 52100 steel (A, C) and AISI 316L stainless steel (B, D) lubricated by PAO with and without additives.

82% and PP gives a 30% reduction. C12 results in the highest SWR with a value of ca. 3.5 times higher than the PAO base lubricant alone.

Figure 2 shows the SEM images of the wear tracks after testing. The wear track morphology of AISI 52100 steel lubricated by PAO alone shows abrasive wear marks with minor plastic deformation. In the case of PAO-PP and PAO-BMP, the wear tracks of AISI 52100 steel have a similar morphology, in which abrasive wear with minor plastic deformation is observed. On the other hand, a smoother wear surface with no plastic deformation is observed on AISI 52100 steel lubricated by PAO-C12, which is in agreement with the friction evolution and wear results. The wear morphology of AISI 316L stainless steel lubricated by PAO shows a smooth wear surface with signs of abrasive wear and plastic deformation.

In the case of AISI 316L stainless steel lubricated by PAO-PP, the wear track shows plowing with signs of plastic deformation and delamination in some areas. On the other hand, PAO-BMP shows a smooth surface and abrasive grooves with no signs of plastic deformation. PAO-C12 shows delamination, wear flakes, and severe plastic deformation inside the wear track.

The cross-sectional images of the wear tracks prepared by FIB are shown in Figure 3. Double Pt protective layers are visible in the images. The cross-sectional images were recorded at the center of the wear track and perpendicular to the sliding direction. The microstructure of all AISI 52100 steel samples consists of deformed grains with chromium carbide (dark round particles). AISI 52100 steel lubricated by PAO, PAO-PP, and PAO-BMP shows a similar degree of recrystallization and plastic deformation. AISI 52100 steel lubricated by PAO-C12 shows a lower degree of recrystallization and plastic deformation.

AISI 316L stainless steel shows a higher degree of recrystallization and plastic deformation. AISI 316L stainless steel lubricated by PAO, PAO-PP, and PAO-C12 shows a very fine recrystallized area along the cross section. Moreover, the top microstructures underwent severe recrystallization for PAO, resulting in nanometer-size grains. AISI 316L stainless steel lubricated by PAO-BMP shows a lower degree of recrystallization with a thinner deformed region, indicating lower shear strain at the subsurface region.

**Tribofilm Characterization.** STEM was used to investigate the tribofilms formed on all samples. The STEM images and EDS elemental mapping are shown in Figure 4 for AISI 52100 steel and AISI 316L stainless steel samples. The chosen elements for mapping were oxygen and iron. The oxygen elemental mapping reveals the presence of oxides in the tribofilm. Phosphorous (P) and fluorine (F) are not shown in the elemental mapping because (1) the Pt  $M\alpha$  and P  $K\alpha$  peaks' energies are too close, resulting in poor contrast between the platinum protective layer and the phosphorous inside the tribofilm and (2) the overlapping of the F  $K\alpha$  and Fe  $L\alpha$  peaks' energies make it difficult to distinguish these peaks.

The AISI 52100 steel samples lubricated by PAO, PAO-PP, and PAO-BMP show a thick tribofilm on the surface with a thickness of ca. 50–250 nm (Figure 4). In addition, subsurface cracks are observed for PAO and PAO-PP samples; however, no visible subsurface cracks are observed for PAO-BMP. PAO-C12 shows a thin tribofilm (ca. 15 nm), and cracks are observed in the vicinity of the carbides and on the surface. In the case of AISI 316L stainless steel lubricated by PAO alone, a tribofilm is built on the surface (50–100 nm thickness, Figure 4). Thicker tribofilms are observed for PAO-PP (100–200 nm) and PAO-BMP (100–300 nm). No visible subsurface cracks are observed

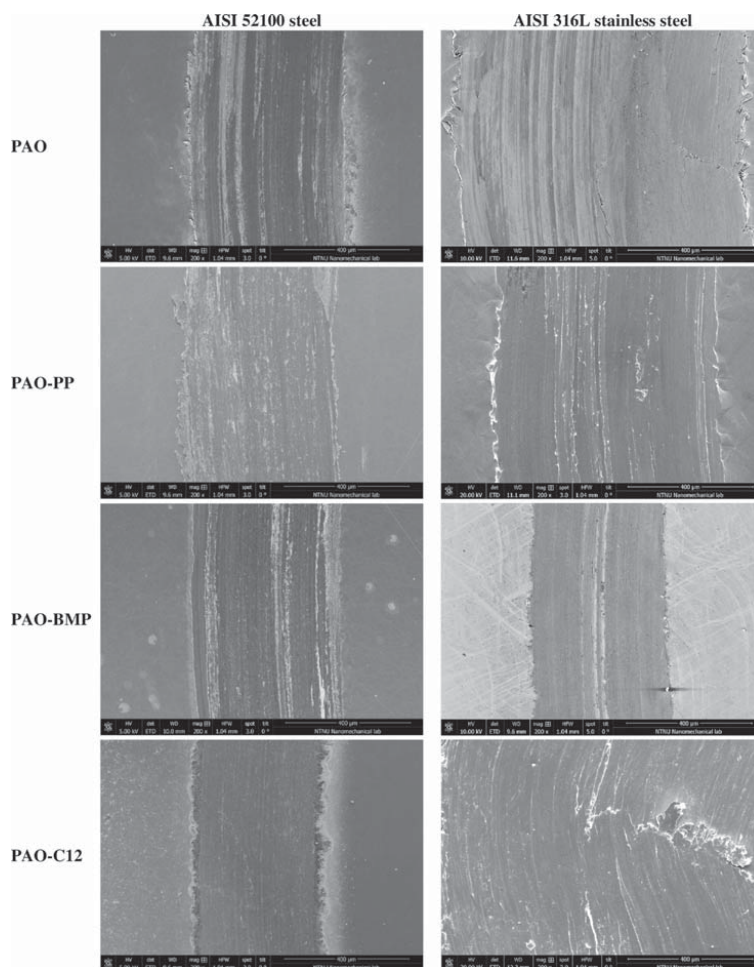


**Figure 2.** SEM images of the wear tracks of AISI 52100 steel and AISI 316L stainless steel disk tested in different lubricants at room temperature.

for AISI 316L stainless steel samples lubricated by PAO, PAO-PP, and PAO-BMP. PAO-C12 shows a thin tribofilm (ca. 15 nm) with signs of oxides trapped deeper into the subsurface region.

EDS point analysis was performed in each sample to obtain a detailed chemical tribofilm composition (Table 3). In the case of all AISI 52100 steel samples, the tribofilm consists of iron and oxygen. Chromium is not detected in the tribofilm because it forms stable chromium carbide. No phosphorous is detected for the PAO-PP sample, indicating that the ILs did not react with the worn surface. In the case of AISI 316L stainless steel samples, the tribofilm consists of iron, chromium, nickel, and oxygen for PAO-PP and PAO-BMP samples. Iron, chromium, and nickel originate from the stainless steel material, whereas phosphorous comes from the IL structure, indicating a reaction between the IL and the worn surface.

**Adsorption Study of Additives on Iron- and Stainless Steel-Coated Sensors.** QCM analysis was performed to study the adsorption of the lubricant additives on iron (Fe)- and stainless steel (SS)-coated sensors. Figure 5 shows the evolution of frequency and dissipation during 10 min of introduction of the base lubricant, followed by 1 h of injection of the formulated lubricant and 1 h of rinsing with the same base lubricant. Note that only the fundamental frequency could be obtained (see the Testing and Characterization Methods section). By comparing the frequency and dissipation evolution, three phenomena are found: (1) the adsorption kinetics, (2) the initially adsorbed layer, and (3) the strongly adsorbed layer after rinsing. The first 10 min act as a reference for further changes in frequency and dissipation. During the introduction of the formulated lubricant, the frequency slope shift represents the adsorption kinetics, and the frequency shift represents the initially adsorbed layer. The additive can be physically and chemically adsorbed to the QCM sensor's surface during this process. During rinsing the base

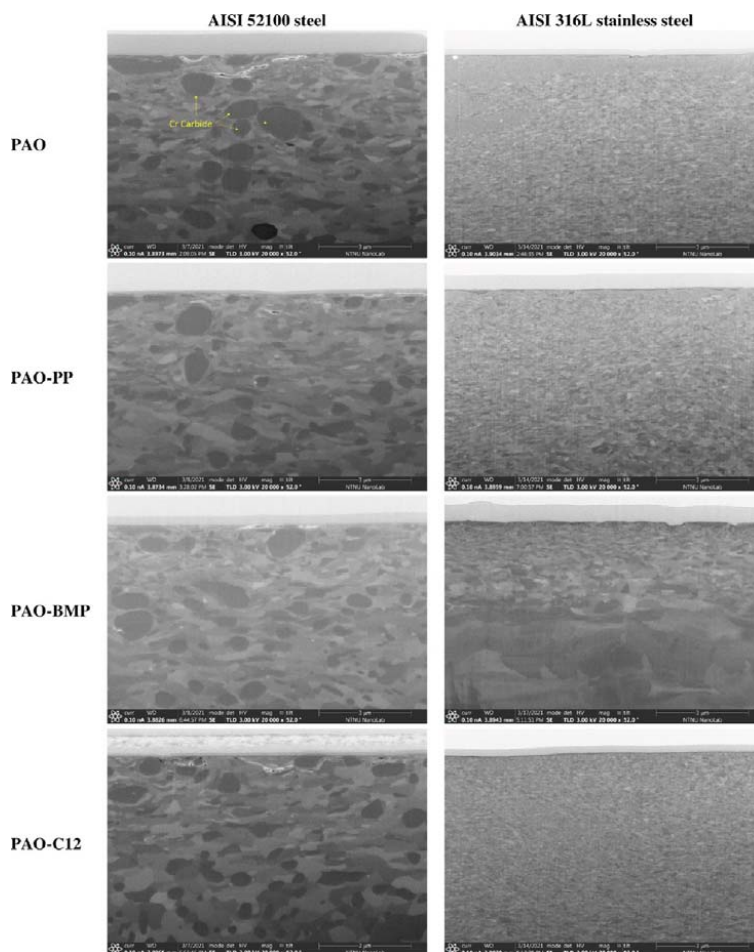


**Figure 3.** FIB cross-sectional images of the wear tracks of AISI 52100 steel and AISI 316L stainless steel disk tested in different lubricants at room temperature.

lubricant, the adsorbed additive can still stay on the surface or can be partially or completely removed from the surface depending on the bonding strength. The frequency shift during the rinsing defines the bonding strength of the adsorbed layer on the surface.

The frequency and dissipation shifts, shown in Figure 5, indicate utterly different adsorption behaviors for all additives. PP shows higher slope and frequency shift than BMP, indicating faster adsorption kinetics and a larger amount of the initially adsorbed layer on the surface; however, no strongly adsorbed layer is observed after rinsing. By comparing the adsorption on Fe- and SS-coated sensors, PP has slightly faster adsorption kinetics and a slightly higher initially adsorbed layer on the SS-coated sensor. BMP shows strong adsorption and remains on the surface after rinsing despite having slow adsorption kinetics and a low initially adsorbed layer. By comparing the adsorption on Fe- and SS-coated sensors, BMP has faster adsorption kinetics, a higher initially adsorbed layer, and a strongly adsorbed layer

after rinsing on the SS-coated sensor. On the other hand, the frequency and dissipation shifts of C12 show opposite behavior to PP or BMP, with a frequency shift toward positive values and a dissipation shift toward negative values. After rinsing, the frequency and dissipation return back to the reference values, indicating complete removal of the adsorbed layer. Similar adsorption behavior is observed for C12 on both Fe- and SS-coated sensors.

## DISCUSSION

**Additives' Adsorption on the Tribosurface.** The adsorption study performed with QCM showed different responses in the adsorption behavior of the additives. While the QCM measurements are conducted in static conditions, the tribological test conditions are dynamic where the adsorbed species are continuously removed from the contact surface due to the rubbing action. For the additives to have an effect on the tribological performance, the additive species need to replenish



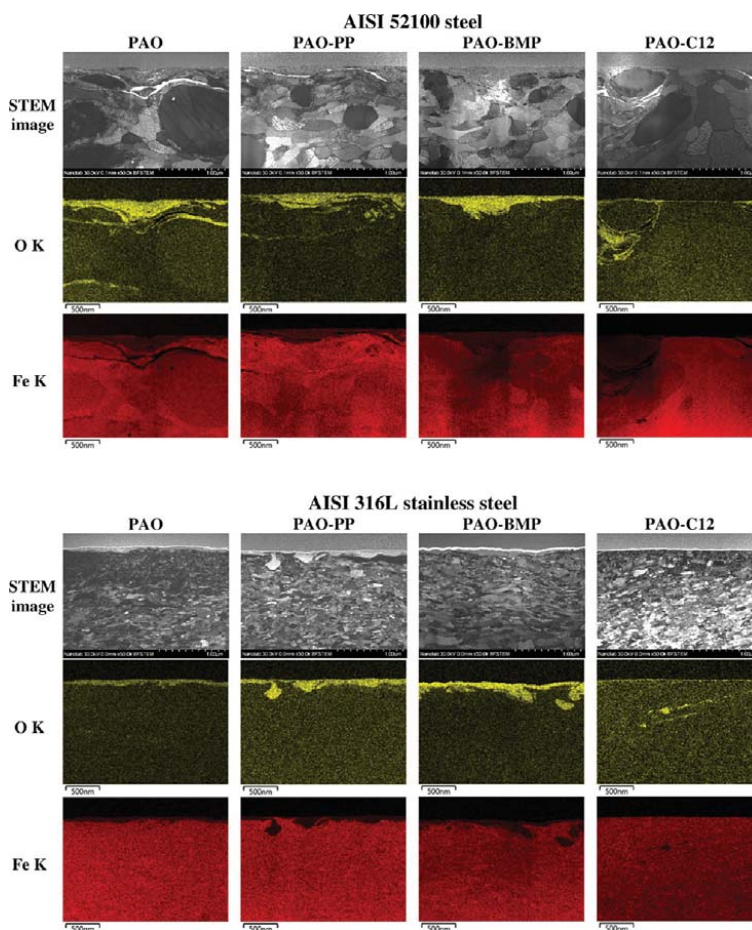


**Figure 4.** STEM cross-sectional images and EDS elemental mapping of the wear tracks on AISI 52100 steel and AISI 316L stainless steel tested in different lubricants at room temperature.

**Table 3.** EDS Chemical Composition Analysis of the Tribofilms (atom %)

sample	lubricant	tribofilm thickness (nm)	elemental concentration in the tribofilm (atom %)				
			Fe	Cr	Ni	O	P
AISI 52100 steel	PAO	50–250	46.49	0		53.51	
	PAO-PP	50–250	48.87	0		51.13	0
	PAO-BMP	50–250	44.60	0		55.40	0
	PAO-C12	15	40.31	0		59.69	
AISI 316L stainless steel	PAO	50–100	31.06	8.23	3.46	57.25	
	PAO-PP	100–200	25.59	5.79	3.02	60.36	5.24
	PAO-BMP	100–300	21.54	5.18	2.74	69.91	0.63
	PAO-C12	15	37.92	10.42	5.28	46.38	

the tribosurface, which is controlled by the adsorption behavior of the additives. During the rubbing action, the adsorbed species are continuously removed from the contact area of the tribosurface. At the same time, electrons are emitted from the worn area, leaving a positively charged surface that attracts the additives to replenish the contact surface again.<sup>23</sup> Thus, the

readsorption of the additive species plays an important role in the tribological behavior. A first-order Langmuir adsorption rate equation can be used to model the adsorption kinetics of the additives as follows<sup>48,49</sup>

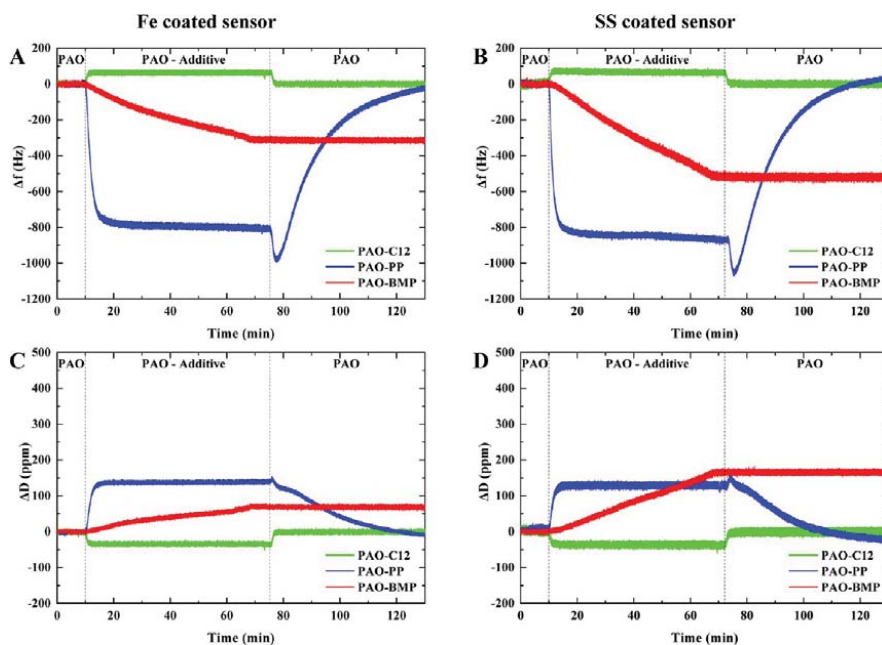


Figure 5. Frequency and dissipation evolution during QCM testing using (A, C) Fe- and (B, D) SS-coated sensors at room temperature.

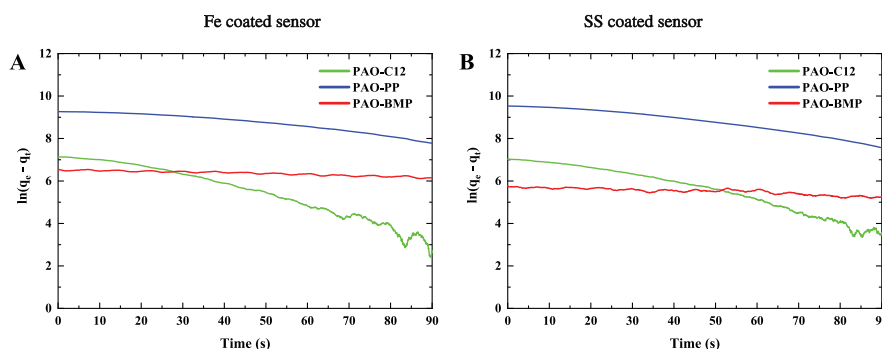


Figure 6. Adsorption kinetics of the additives on the surface of (A) Fe- and (B) SS-coated sensors.

$$\frac{dq_t}{dt} \approx k_1(\theta_e - \theta_t) \quad (2)$$

where  $k_1$  is the first order of the adsorption kinetic constant, and  $\theta_e$  and  $\theta_t$  are the occupied adsorption sites at equilibrium and time  $t$ . By integrating eq 2, the adsorption kinetic constant is obtained by plotting the dependency of the amount of adsorbed mass versus time as follows

$$\ln(q_e - q_t) = \ln(q_e) - k_1 t \quad (3)$$

where  $q_e$  and  $q_t$  are the masses adsorbed at equilibrium and time  $t$ . The logarithmic dependency of the amount of the adsorbed mass versus time is shown in Figure 6 for the first 90 s of adsorption. As shown in eq 3 and Figure 6, the slope of the graph represents the adsorption kinetic constant. By applying linear

regression, the adsorption kinetic constants are obtained. For the Fe-coated sensor, the adsorption kinetic constants are 0.0470, 0.0164, and 0.0041  $\text{s}^{-1}$  for C12, PP, and BMP, respectively. In the case of the SS-coated sensor, the adsorption kinetic constants are 0.0411, 0.0218, and 0.0052  $\text{s}^{-1}$  for C12, PP, and BMP, respectively. Thus, on both sensors, C12 holds the fastest adsorption kinetics followed by PP and BMP.

The relationship between the frequency shift and the mass change of the QCM sensor was first proposed by Sauerbrey in the following Sauerbrey equation<sup>50</sup>

$$\Delta f = -\frac{f_0}{\rho_Q \cdot d_Q} \left( \frac{\Delta m}{A_Q} \right) \quad (4)$$

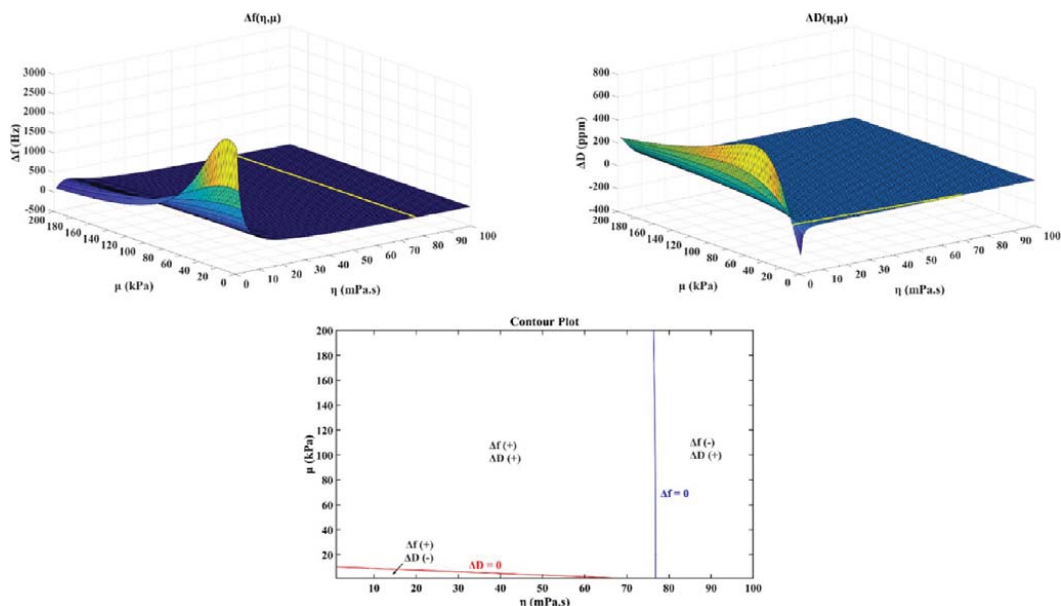


**Figure 7.** Numerical simulation of the frequency shift (A) and the dissipation shift responses (B) as a function of the shear elasticity modulus and the shear viscosity coefficient of the thin viscoelastic C12 layer. A contour plot is taken from (A) and (B), showing the different regions of  $\Delta f$  and  $\Delta D$  values (C).

where  $\Delta f$  and  $\Delta m/A_Q$  are frequency shift (Hz) and mass change per unit area ( $\text{kg}/\text{m}^2$ ).  $f_0$ ,  $\rho_Q$ , and  $d_Q$  are the natural frequency in vacuum (Hz), density ( $\text{kg}/\text{m}^3$ ), and thickness (m) of the quartz plate, respectively. Note that Sauerbrey performed his experiments under vacuum; therefore, the Sauerbrey equation is the basis for using QCM to measure adsorption in vacuum or gas phase regardless of the viscoelastic properties of the adsorbate.

Due to their ionic nature and their high dipole moment, ILS have a higher tendency to be adsorbed on the metallic surface to form a single- or multilayer structure.<sup>35</sup> Using the Sauerbrey equation, the adsorbed layer structure can be predicted. In the case of PP, one molecule of PP has a length of 2.03 nm (from the structure analysis using MarvinSketch software), which gives a frequency shift of  $-9.34$  Hz for one adsorbed layer. Using the same procedure for BMP (the length of one molecule is 2.11 nm), the calculated frequency shift is  $-15.93$  Hz for one adsorbed layer. As shown in Figure 5, the frequency shift of PP and BMP on the Fe-coated sensor are  $-820$  and  $-320$  Hz, and on the SS-coated sensor, they are  $-877$  and  $-525$  Hz, respectively. Thus, it is expected that PP and BMP will form multilayer structures on both Fe- and SS-coated sensors. PP will have a thicker adsorbed layer compared to BMP. Generally, ILS in nonpolar media, such as PAO, exhibit no ionic dissociation, maintaining the dipole moment of the molecule. As shown in Figure 5, BMP stays on the surface of the sensor after rinsing with PAO, indicating strong adsorption of BMP to the sensor surface. The strong adsorption of BMP indicates a chemisorption process, which promotes the formation of a tribofilm. The presence of high electronegative atoms (F) promotes strong adsorption to the metallic surface. Similar behavior was observed for BMP in water–glycol,<sup>39</sup> confirming that the high electronegative atoms play a role in the adsorption process and the

further tribofilm formation. On the other hand, PP weakly adsorbs to the surface, showing that it undergoes a physisorption process. The anion of PP has a smaller density of negative charge than BMP and its smaller size generates a weaker interaction with the metal surface. Figure 5 shows that the stainless steel surface tends to adsorb more ILS, probably due to the different surface chemistry (i.e., stainless steel creates a nanometric passive film of chromium oxide on the surface). In the case of C12, a positive but low frequency shift was observed, indicating a thinner adsorbed layer than the ILS. In addition, complete removal of the adsorbed layer after rinsing with PAO indicates a physisorption process (Figure 5).

A simulation approach has been used to understand the adsorption of C12 on Fe- and SS-coated sensors. In 1999, Voinova et al. proposed a continuum mechanics approach to describe the adsorption of a layered polymer film in a liquid environment.<sup>51</sup> There are several theoretical methods for quantitative interpretation of the viscoelastic response of QCM data, such as continuum mechanics, electrical circuit, and transmission line analysis methods.<sup>52,53</sup> However, only the continuum mechanics approach directly links the QCM data to the adsorbed layer's physical description, which correlates the measured frequency and dissipation with the adsorbed layer properties. Using Voinova's approach, the viscoelastic properties of an adsorbed layer with an arbitrary thickness covering the surface of a quartz sensor immersed in liquid can be analyzed. The Voigt element was used to model the viscoelastic material in this approach. Spring and dashpot in a parallel arrangement represent the shear elasticity modulus ( $\mu$ ) and the shear viscosity coefficient ( $\eta$ ) of the layered film, respectively. Assumptions for the adsorbed layer are rigidly attached (no slip), evenly

Table 4. Summary of the Adsorbed Layer Properties on Both Fe- and SS-Coated Sensors

additive	adsorption kinetics	initially adsorbed layer	strongly adsorbed layer	mass layer contribution	shear viscosity (compared to bulk liquid)	shear elasticity modulus
SS-PP	medium-high	very high	no	very high	high	high
Fe-PP	medium	high	no	high	high	high
SS-BMP	slow	medium-high	yes	medium-high	high	high
Fe-BMP	very slow	medium	yes	medium	high	high
SS-C12	very fast	very low	no	very low	low	low
Fe-C12	very fast	very low	no	very low	low	low

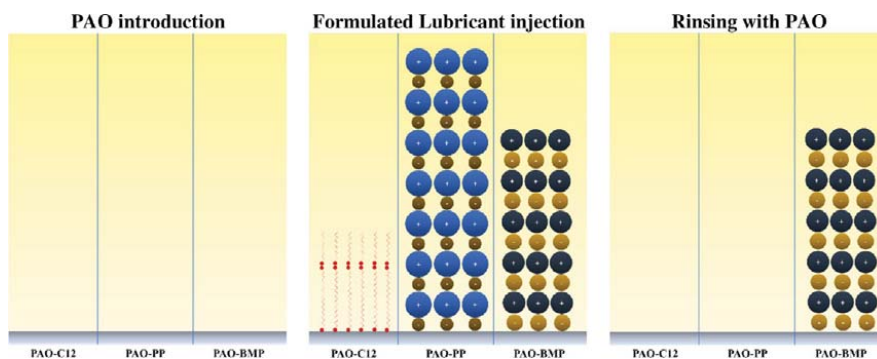


Figure 8. Molecular assemblies' illustration of the additives on both the Fe and SS surfaces during the QCM tests.

distributed, and homogeneous thickness, density, viscosity, and elasticity properties.

The acoustic response of the QCM was modeled with MATLAB varying the viscoelastic layer properties ( $\eta$  and  $\mu$ ) using the general solution of the wave equation for the thin viscoelastic layer immersed in a bulk liquid. Figure 7 shows the result of the numerical simulation of the model for the thin viscoelastic C12 layer of a thickness of 10 nm and a density of 880 kg/m<sup>3</sup> when the sensor oscillates with a frequency of 5 MHz in PAO ( $\rho = 840.8$  kg/m<sup>3</sup>,  $\eta = 83.13$  mPa·s). A C12 thickness of 10 nm for the analysis was selected based on the thickness measured using atomic force microscopy (AFM).<sup>40</sup> In Figure 7A,B, the zero value line (yellow line) is presented, forming the basis for constructing Figure 7C.

To explain the acoustic response in Figure 7, the following simplified equations are provided by considering one thin viscoelastic layer under bulk liquid and keeping only the first-order approximation<sup>51</sup>

$$\Delta f \approx -\frac{1}{2\pi\rho_Q d_Q} \left\{ \frac{\eta_B}{\delta_B} + d_A \rho_A \omega - 2d_A \left( \frac{\eta_B}{\delta_B} \right)^2 \frac{\eta_A \omega^2}{\mu_A^2 + \eta_A^2 \omega^2} \right\} \quad (5)$$

$$\Delta D \approx \frac{1}{2\pi f_0 \rho_Q d_Q} \left\{ \frac{\eta_B}{\delta_B} + 2d_A \left( \frac{\eta_B}{\delta_B} \right)^2 \frac{\mu_A \omega}{\mu_A^2 + \eta_A^2 \omega^2} \right\} \quad (6)$$

$$\delta_B = \sqrt{\frac{2\eta_B}{\rho_B \omega}} \quad (7)$$

$$\omega = 2\pi f_0 \quad (8)$$

where  $\rho_B$  and  $\eta_B$  are the density (kg/m<sup>3</sup>) and viscosity (Pa·s) of bulk liquid, whereas  $d_A$ ,  $\rho_A$ ,  $\mu_A$ , and  $\eta_A$  are the thickness (m),

density (kg/m<sup>3</sup>), shear elasticity modulus (Pa), and shear viscosity coefficient (Pa·s) of the adsorbed layer, respectively. In eq 5, the resonance frequency shift depends on the bulk liquid term ( $\eta_B$  and  $\delta_B$ ), and the difference between the layer mass contribution ( $d_A \rho_A \omega$  and  $\omega$ ) and layer viscoelastic contribution ( $\mu_A$  and  $\eta_A$ ), whereas in eq 6, the resonance dissipation shift depends on the bulk liquid term  $\eta_B/\delta_B$  and layer viscoelastic contribution ( $\mu_A$  and  $\eta_A$ ). Note that eqs 5 and 6 take the reference from vacuum, meaning the bulk liquid contribution is relative to vacuum. In a liquid medium, the contribution of the reference liquid should be included in the equations as follows

$$\Delta f \approx -\frac{1}{2\pi\rho_Q d_Q} \left\{ \left( \frac{\eta_B}{\delta_B} - \frac{\eta_R}{\delta_R} \right) + d_A \rho_A \omega - 2d_A \left( \frac{\eta_B}{\delta_B} \right)^2 \frac{\eta_A \omega^2}{\mu_A^2 + \eta_A^2 \omega^2} \right\} \quad (9)$$

$$\Delta D \approx \frac{1}{2\pi f_0 \rho_Q d_Q} \left\{ \left( \frac{\eta_B}{\delta_B} - \frac{\eta_R}{\delta_R} \right) + 2d_A \left( \frac{\eta_B}{\delta_B} \right)^2 \frac{\mu_A \omega}{\mu_A^2 + \eta_A^2 \omega^2} \right\} \quad (10)$$

$$\delta_R = \sqrt{\frac{2\eta_R}{\rho_B \omega}} \quad (11)$$

where  $\rho_R$  and  $\eta_R$  are the reference liquid's density (kg/m<sup>3</sup>) and viscosity (Pa·s), respectively. In the case of similar density and viscosity between reference and bulk liquids, the influence between these two can be canceled



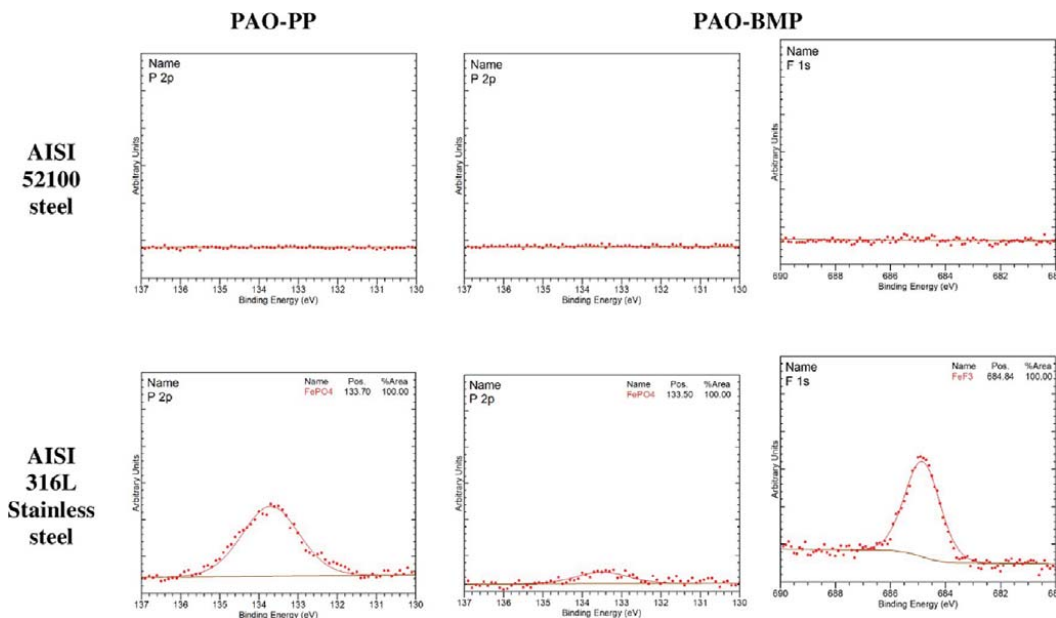


**Figure 9.** P and F XPS spectra inside the tribofilm of AISI 52100 steel and AISI 316L stainless steel lubricated by PAO-PP and PAO-BMP (taken after 85 s sputtering time).

$$\Delta f \approx -\frac{1}{2\pi\rho_Q d_Q} \left\{ d_A \rho_A \omega - 2d_A \left( \frac{\eta_B}{\delta_B} \right)^2 \frac{\eta_A \omega^2}{\mu_A^2 + \eta_A^2 \omega^2} \right\} \quad (12)$$

$$\Delta D \approx \frac{1}{2\pi f_0 \rho_Q d_Q} \left\{ 2d_A \left( \frac{\eta_B}{\delta_B} \right)^2 \frac{\mu_A \omega}{\mu_A^2 + \eta_A^2 \omega^2} \right\} \quad (13)$$

It is worth noticing that due to the approximation, the layer mass contribution is neglected in eq 13. However, from the simulation in Figure 7B (without approximation), there is a region with a negative dissipation value when the layer has a low shear elasticity modulus with the shear viscosity lower than the shear viscosity of the bulk.

From the simulation results and according to eq 12, the unexpected positive frequency shift (and negative dissipation shift) found experimentally for C12 in Fe- and SS-coated sensors (Figure 5) is a result of the layer viscoelastic contribution rather than the adsorption mass contribution. The C12 adsorbed layer has both low shear viscosity and a low shear elasticity modulus compared to the bulk liquid (PAO), thus resulting in a positive shift of the frequency and a negative shift of the dissipation (Figure 7C). Therefore, the negative frequency shift of PP and BMP additives is mostly influenced by the adsorption mass contribution. Thus, the adsorbed layer of PP and BMP must have high shear viscosity and a high shear elasticity modulus compared to the bulk liquid (PAO). All of the adsorption responses are summarized in Table 4, and the molecular assemblies expected on the surface of the sensors after QCM testing and simulation results are illustrated in Figure 8.

**Effect of Lubricant Formulation on the Tribofilm Chemical Composition.** PAO-PP and PAO-BMP promote

noticeable tribofilm formation on both surfaces, as shown in Figure 4. Interestingly, PAO alone creates a thick tribofilm, indicating that only the presence of oxygen in the lubricant is enough to contribute to a tribochemical reaction leading to tribofilm growth. In the case of PAO-C12, a thin tribofilm is formed, indicating that C12 hinders tribofilm growth by occupying the active sites for the tribochemical reaction. Tribofilm formation consists of three stages, i.e., tribofilm initiation, wear debris generation and breakdown, and tribofilm growth.<sup>54</sup> For tribofilm initiation, the reactive elements inside the lubricant, such as oxygen, ILS, and ILS' decomposition products, adsorb to and react with the nascent surface to form a thin interlayer film. This interlayer can act as a good bonding layer between the metallic substrate and the tribofilm or, on the other hand, it can act as a barrier layer hindering tribofilm growth. The mechanical action will generate wear debris at the contact zone. Some wear debris may get trapped and broke down to nanosize in the contact zone, and others may be wiped away. The nanosized wear debris will consequently react with reactive elements in the lubricant due to the thermomechanical process in the contact area. Both unreacted and reacted wear debris are deposited and smeared on the tribosurface (which is occupied by an interlayer film from tribofilm initiation), thus leading to further film growth.

XPS was used to study the tribofilm chemical composition of the tribofilms on both the surface and the subsurface. For surface analysis, the wear track was sputtered with argon for 5 s to remove the contamination before the XPS data acquisition. For subsurface analysis, the wear track was sputtered for 85 s (going deeper in the tribofilm thickness). Surface and subsurface analysis revealed the same chemical composition. The detailed XPS spectra for subsurface analysis are shown in Figure 9. No P or F was detected in the tribofilm of AISI 52100 in any of the

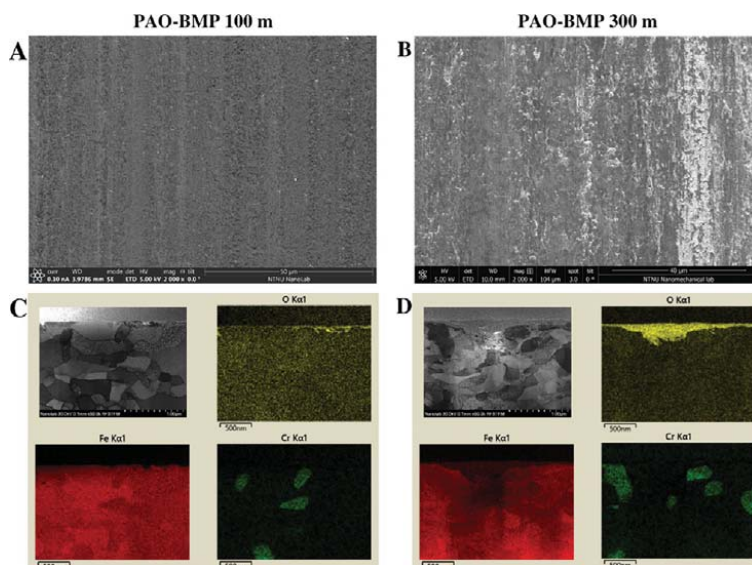


**Figure 10.** Top view and STEM image with elemental mapping of the AISI 52100 steel worn surface lubricated by PAO-BMP tested for 100 m (A, C) and 300 m (B, D).

lubricants formulated with ILs. In the case of AISI 316L stainless steel, P is detected in the tribofilms of both PP and BMP. XPS analysis further found that P created an iron phosphate phase. In addition, F in the form of iron fluoride was found for BMP. The XPS results have confirmed that the adsorption of the ILs did not result in any chemical reaction with AISI 52100 steel, but they did react with AISI 316L stainless steel. This confirms that the surface chemistry of the moving parts influences the tribofilm formation given the same lubricant composition. Interestingly, it was found by QCM that the adsorption kinetics and the initially adsorbed layer of the ILs were larger on SS than those on Fe-coated sensors (Table 4 and Figure 6).

**Tribofilm and Adsorbed Layer Effects on Friction.** As shown in Figure 1A, there is a transition in the friction evolution of AISI 52100 steel lubricated by PAO, PAO-PP, and PAO-BMP, which results in higher friction than PAO-C12. High friction, together with the high initial Hertzian contact pressure (1.96 GPa), results in a higher degree of recrystallization and plastic deformation (Figure 3). As shown in Table 3, thick tribofilms are formed for PAO, PAO-PP, and PAO-BMP, whereas a thin tribofilm is formed for PAO-C12. Therefore, the formation of thick tribofilms can increase friction. This phenomenon has also been observed when using ZDDP, a well-known antiwear additive. Dawczyk et al. showed that an increase in friction is a direct result of the increase in the effective roughness of the worn surfaces due to tribofilm formation.<sup>55</sup> As shown in Figure 2, PAO, PAO-PP, and PAO-BMP create rougher worn surfaces than PAO-C12 due to thicker tribofilm formation.

To further understand the influence of tribofilm and surface roughness on friction, a shorter test was performed for PAO-BMP on AISI 52100 (terminated after 100 m sliding, right before the friction transition seen in Figure 1A). The top view of the worn surface and the STEM image with elemental mapping of PAO-BMP 100 m are shown in Figure 10 along with PAO-

BMP 300 m sample for comparison. The PAO-BMP 300 m wear track shows a rougher surface, whereas a smoother surface is observed for PAO-BMP 100 m due to thin tribofilm formation. These wear surface morphologies are in agreement with the friction evolution of PAO-BMP on AISI 52100 steel in Figure 1A, in which a smoother surface results in lower friction and vice versa. Therefore, in the case of AISI 52100 steel, a thick oxide tribofilm is responsible for high friction.

However, a friction increase due to the thick tribofilm is not observed for AISI 316L stainless steel. As shown in Figure 1B, the friction evolution of AISI 316L stainless steel lubricated by PAO, PAO-PP, and PAO-BMP shows low values even though a thick tribofilm was formed, implying that a thick tribofilm might not be the factor playing the most important role in friction for stainless steel. As shown in Table 3 and Figure 9, the formed tribofilm on stainless steel contains oxides and hydroxides from different metals, P and F, whereas the tribofilm on AISI 52100 steel only contains Fe oxides and hydroxides. Therefore, the chemical composition of the tribofilm resulted in a different frictional response.

In addition, the friction behavior is influenced not only by the presence of a tribofilm but also by the adsorbed additives on the tribosurface.<sup>35</sup> The adsorbed layer properties, such as thickness or mass, viscoelastic properties, and bonding strength, define its friction-reducing ability. Comparing PAO, PAO-PP, and PAO-BMP friction in Figure 1A, the effect of the type of additive on friction is clear, where PAO-BMP gives the lowest friction evolution both before and after tribofilm formation. As shown in Table 4, PP has faster adsorption kinetics and adsorption mass and weak adsorption. BMP shows slower adsorption kinetics and lower adsorption mass but adsorbs strongly to the sensor surface, indicating that the bonding strength plays the most important role in the friction-reducing ability. A strongly adsorbed layer (BMP) maintains the layer's integrity during the sliding action. In addition, a stronger adsorbed layer

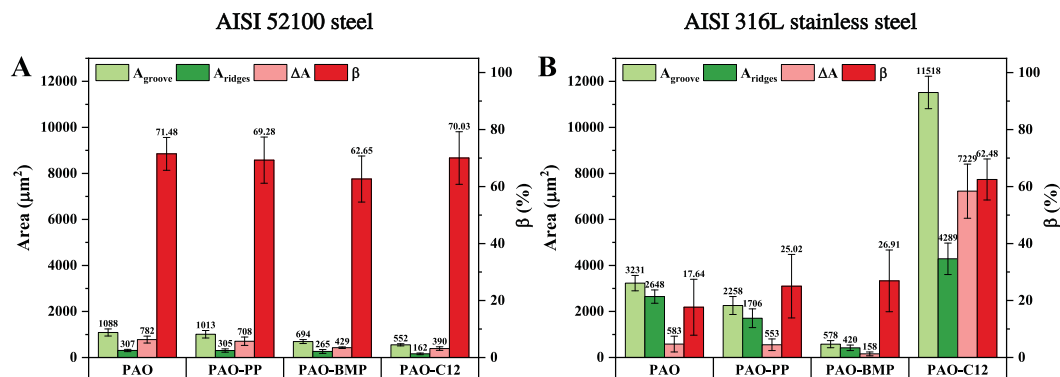


Figure 11. Calculated wear area of AISI 52100 steel (A) and AISI 316L stainless steel (B) lubricated by PAO with and without additives.

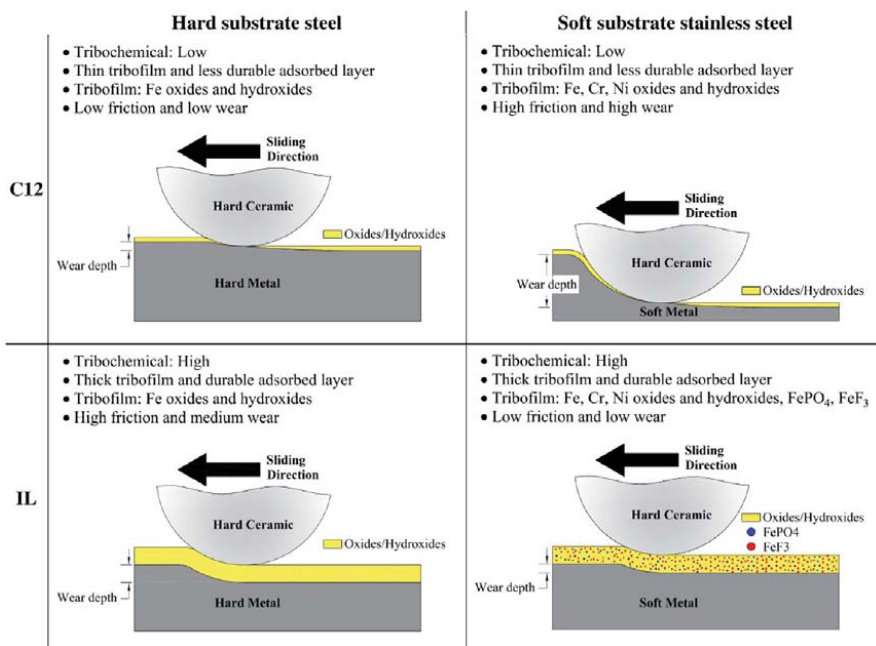


Figure 12. Schematic illustration of the boundary lubricating mechanisms of hard versus soft substrate lubricated by PAO-C12 and PAO-IL.

produces a more durable layer; thus, BMP maintains lower friction on longer distances than PP. In the case of AISI 316L stainless steel, the adsorbed layer influences the running-in period, in which a durable adsorbed layer (BMP) reduces the running-in period significantly (Figure 1B). This leads to the thinnest recrystallization region, i.e., less severe shear forces (Figure 3).

In the case of PAO-C12, a thin tribofilm and a less durable adsorbed layer were formed both on AISI 52100 steel and AISI 316L stainless steel, but different friction behaviors were still observed. PAO-C12 shows steady and low friction evolution on AISI 52100 steel (Figure 1A); in contrast, higher friction evolution with high fluctuation is observed for AISI 316L

stainless steel (Figure 1B). Both tribofilms on AISI 52100 steel and AISI 316L stainless steel are thin oxide layers (Table 3), and the QCM study indicates that C12 formed a less durable adsorbed layer both on Fe- and SS-coated sensors (Table 4). The main difference in this case is the mechanical properties of the substrates, in which AISI 52100 steel has a higher hardness than AISI 316L stainless steel. For the lower hardness material, a less durable adsorbed layer and thin tribofilm cannot withstand the boundary lubricating conditions, resulting in plastic deformation, as shown in Figure 2. On the other hand, the harder material, with a less durable adsorbed layer and a thin tribofilm, can withstand the applied boundary lubricating condition, thus maintaining low friction.

**Tribofilm and Adsorbed Layer Effects on Wear.** A detailed wear analysis was performed by investigating the wear profiles taken by IFM for each tested condition. From the wear profile analysis (not shown in this paper), ridges were formed along the wear track due to material displacement to the sides of the wear track during testing, indicating plastic deformation. From the wear profile, the difference between the area of the ridges ( $A_{\text{ridges}}$ ) and the area of the wear track groove ( $A_{\text{groove}}$ ) gives the actual area loss ( $\Delta A$ ). The ratio between the area loss and wear track groove is the material loss degree ( $\beta$ ) and it is calculated by the following equation<sup>56</sup>

$$\beta = \frac{A_{\text{groove}} - A_{\text{ridges}}}{A_{\text{groove}}} \times 100\% = \frac{\Delta A}{A_{\text{groove}}} \times 100\% \quad (14)$$

The  $\beta$  value indicates the wear mechanism, where lower  $\beta$  means more plastic deformation and higher  $\beta$  more abrasive wear. The wear profile analysis results are shown in Figure 11.

In the case of AISI 52100 steel, all additives reduce the area loss ( $\Delta A$ ). Interestingly, the  $\beta$  value between all lubricants is comparable (60–70%), indicating a similar abrasive wear mechanism. Similar to the friction behavior, wear is also highly influenced by the presence of a tribofilm and adsorbed layer. As the tribofilms have similar thickness and chemical composition for PAO-PP and PAO-BMP, the wear reduction is mainly affected by the adsorbed layer. A durable adsorbed layer (BMP) gives lower wear. The shorter test performed for PAO-C12 and PAO-BMP (terminated after 100 m sliding, right before the thick tribofilm formation) showed that the area loss  $\Delta A$  for PAO-BMP 100 m ( $133 \mu\text{m}^2$ ) was 50% lower than PAO-C12 100 m ( $56 \mu\text{m}^2$ ). In addition, the calculated  $\beta$  value for PAO-BMP 100 m (24%) was smaller than for PAO-C12 100 m (39%), indicating more plastic deformation. Therefore, in the absence of a thick tribofilm (100 m tests), a durable adsorbed layer provides better wear resistance.

In the case of AISI 316L stainless steel lubricated by PAO, PAO-PP, and PAO-BMP, a thick tribofilm also forms on the tribosurface, as shown in Table 3. These tribofilms contain metallic oxides and hydroxides of iron, chromium, nickel, and iron phosphates and fluorides, yielding durable tribofilms. Figure 11A shows that PAO, PAO-PP, and PAO-BMP have similar low  $\beta$  values, indicating a similar plastic deformation wear mechanism mostly due to the lower hardness of the substrate. Interestingly the wear of PAO-BMP is the lowest among all tested lubricant–substrate combinations, suggesting that the combination of a durable tribofilm with a durable adsorbed layer significantly reduces wear regardless of the hardness of the substrate. For PAO-C12, abrasive wear was the main mechanism (Figure 11B). Similar to AISI 52100 steel, C12 creates a thin tribofilm and a less durable adsorbed layer. C12 produces higher wear on AISI 316L stainless steel than on AISI 52100 steel, indicating that substrate hardness plays an important role in this case.

**Effect of Steel Hardness and Composition on the Lubricating Mechanisms.** In this study, it was found that to control friction and wear of the lubricated tribosystems, the mechanical properties and chemical composition of the tribomaterial are as important as the surface adsorption behavior of the additives on the tribosurfaces. Figure 12 illustrates the lubrication mechanisms of C12 and ILs in PAO as a function of tribomaterial hardness and composition. In the case of C12, thin tribofilms and a less durable adsorbed layer were formed on the tribosurfaces; thus, the hardness of the substrate has been the

predominant factor affecting the tribological behavior of the system. A thin tribofilm and a less durable adsorbed layer formed on the soft metal substrate (AISI 316L stainless steel) were not strong enough to withstand the boundary lubricating conditions, resulting in severe plastic deformation (Figure 2), which in turn increased the surface roughness leading to high friction and subsequent wear.

In the case of ILs, thick tribofilms and durable adsorbed layers were formed on the tribosurfaces. The tribofilm chemical composition was the predominant factor influencing frictional and wear behavior for the ILs. The tribofilms' composition was different depending on the steel composition. The tribofilm formed on AISI 316L stainless steel consisted of Fe oxides and hydroxides and the chemical elements associated with the ILs (P and F). The tribofilm formed on AISI 52100 steel consisted of Fe oxides and hydroxides only. These different tribofilms resulted in different friction and wear behaviors. In both cases, the wear rates were at the same order of magnitude; however, the presence of  $\text{FePO}_4$  and  $\text{FeF}_3$  in the tribofilms significantly increased the wear resistance of AISI 316L stainless steel (Figure 11). The main differences between the two steels were found for friction. In the case of AISI 52100 steel, despite forming a durable adsorbed layer, the presence of hard Fe oxides and hydroxides and the lack of F and P in the tribofilm created rougher tribosurfaces leading to high friction. For the AISI 316L stainless steel, the durable adsorbed layer and the presence of  $\text{FePO}_4$  and  $\text{FeF}_3$  in the tribofilm provided low and steady friction.

## CONCLUSIONS

The lubricating mechanisms of two ionic liquids as lubricant additives in PAO on AISI 52100 steel and AISI 316L stainless steel have been investigated and compared with dodecanoic acid (C12) as a reference additive. The following conclusions can be drawn from this work

- The adsorption study by QCM-D reveals that C12 formed thin and less durable adsorbed layers on both Fe- and SS-coated sensors. In the case of ILs, two different surface adsorption behaviors were observed: (1) a thick but not strongly adsorbed layer in the case of PP and (2) a thick and strongly adsorbed layer in the case of BMP. The sensor's chemical composition does not influence the adsorption behavior of C12; however, it influences the adsorption behavior of ILs in which the SS-coated sensor tends to adsorb more ILs than the Fe-coated sensor.
- The tribofilm analysis shows that C12 hinders the tribofilm growth, resulting in thin tribofilm formation; on the other hand, ILs promote noticeable tribofilm formation on both AISI 52100 steel and AISI 316L stainless steel. The chemical composition of the substrate determines the chemical composition of the tribofilm in which the tribofilm formed on AISI 52100 steel consists of Fe oxides and hydroxides. In contrast, the tribofilm formed on AISI 316L consists of Fe, Cr, and Ni oxides and hydroxides and the chemical elements associated with the ILs (P and F). The differences in the chemical composition influence the mechanical properties and durability of the tribofilms.
- C12 showed better tribological performance on AISI 52100 steel than on AISI 316L stainless steel despite it created less durable adsorbed layers and thin tribofilms. The tribomaterial hardness played the most important



role in the tribological performance of this additive, where a higher hardness could withstand the boundary lubricating conditions.

- For the ILs, the tribological performance was controlled by tribofilm formation for a high hardness substrate (AISI 52100 steel), where the presence of oxide tribofilms increased friction and wear. In the case of a low hardness substrate (AISI 316L stainless steel), the tribological performance was controlled by both the adsorbed layer properties and the tribofilm durability, where a strongly adsorbed layer led to a durable tribofilm with excellent friction-reducing and antiwear performance.
- BMP on AISI 316L stainless steel showed the best tribological performance of all tests due to the formation of a durable adsorbed layer and a strong tribofilm. The durability of the BMP adsorbed layer was a result of the high electronegativity of fluorine atoms, whereas the durability of the tribofilm was a result of the tribochemical reaction of BMP with the tribosurface, resulting in the formation of  $\text{FePO}_4$  and  $\text{FeF}_3$  precipitates in the tribofilm.

## AUTHOR INFORMATION

### Corresponding Authors

**Wahyu Wijanarko** – Norwegian Tribology Center, Department of Mechanical and Industrial Engineering, Norwegian University of Science and Technology (NTNU), Trondheim 7491, Norway; Department of Mechanical Engineering, Sepuluh Nopember Institute of Technology (ITS), Surabaya 60111, Indonesia; [orcid.org/0000-0001-8534-4301](https://orcid.org/0000-0001-8534-4301); Email: [wahyu.wijanarko@ntnu.no](mailto:wahyu.wijanarko@ntnu.no), [wijanarko@me.its.ac.id](mailto:wijanarko@me.its.ac.id)

**Nuria Espallargas** – Norwegian Tribology Center, Department of Mechanical and Industrial Engineering, Norwegian University of Science and Technology (NTNU), Trondheim 7491, Norway; Email: [nuria.espallargas@ntnu.no](mailto:nuria.espallargas@ntnu.no)

### Author

**Hamid Khanmohammadi** – Norwegian Tribology Center, Department of Mechanical and Industrial Engineering, Norwegian University of Science and Technology (NTNU), Trondheim 7491, Norway

Complete contact information is available at:  
<https://pubs.acs.org/10.1021/acs.langmuir.1c02848>

### Notes

The authors declare no competing financial interest.

## ACKNOWLEDGMENTS

The authors would like to acknowledge financial support from Indonesia Endowment Fund for Education (LPDP), M-ERANET GreenCOAT project with Project Number 4153, and the Norwegian Micro- and Nanofabrication Facility, NorFab, for providing the characterization facilities.

## REFERENCES

- (1) Holmberg, K.; Erdemir, A. Influence of Tribology on Global Energy Consumption, Costs and Emissions. *Friction* **2017**, *5*, 263–284.
- (2) Van Rensselaar, J. The Tribology of Electric Vehicles. *Tribol. Lubr. Technol.* **2019**, *75*, 34–43.
- (3) Holmberg, K.; Erdemir, A. The Impact of Tribology on Energy Use and CO<sub>2</sub> Emission Globally and in Combustion Engine and Electric Cars. *Tribol. Int.* **2019**, *135*, 389–396.
- (4) Narita, K.; Takekawa, D. Lubricants Technology Applied to Transmissions in Hybrid Electric Vehicles and Electric Vehicles. *SAE Tech. Pap.* **2019**, *1*, No. 7.
- (5) Earle, M. J.; Seddon, K. R. Ionic Liquids. Green Solvents for the Future. *Pure Appl. Chem.* **2000**, *72*, 1391–1398.
- (6) Comelles, F.; Ribosa, I.; González, J. J.; García, M. T. Interaction of Nonionic Surfactants and Hydrophilic Ionic Liquids in Aqueous Solutions: Can Short Ionic Liquids Be More than a Solvent? *Langmuir* **2012**, *28*, 14522–14530.
- (7) Ye, C.; Liu, W.; Chen, Y.; Yu, L. Room-Temperature Ionic Liquids: A Novel Versatile Lubricant. *Chem. Commun.* **2001**, *21*, 2244–2245.
- (8) Liu, W.; Ye, C.; Gong, Q.; Wang, H.; Wang, P. Tribological Performance of Room-Temperature Ionic Liquids as Lubricant. *Tribol. Lett.* **2002**, *13*, 81–85.
- (9) Wasserscheid, P.; Welton, T. *Ionic Liquids in Synthesis*; Wiley-VCH Verlag GmbH & Co. KGaA: Weinheim (Germany), 2002.
- (10) Kamijo, T.; Arafune, H.; Morinaga, T.; Honma, S.; Sato, T.; Hino, M.; Mizukami, M.; Kurihara, K. Lubrication Properties of Ammonium-Based Ionic Liquids Confined between Silica Surfaces Using Resonance Shear Measurements. *Langmuir* **2015**, *31*, 13265–13270.
- (11) Lu, Q.; Wang, H.; Ye, C.; Liu, W.; Xue, Q. Room Temperature Ionic Liquid 1-Ethyl-3-Hexylimidazolium-Bis-(Trifluoromethylsulfanyl)-Imide as Lubricant for Steel-Steel Contact. *Tribol. Int.* **2004**, *37*, 547–552.
- (12) Wang, H.; Lu, Q.; Ye, C.; Liu, W.; Cui, Z. Friction and Wear Behaviors of Ionic Liquid of Alkylimidazolium Hexafluorophosphates as Lubricants for Steel/Steel Contact. *Wear* **2004**, *256*, 44–48.
- (13) Kamimura, H.; Kubo, T.; Minami, I.; Mori, S. Effect and Mechanism of Additives for Ionic Liquids as New Lubricants. *Tribol. Int.* **2007**, *40*, 620–625.
- (14) Somers, A. E.; Khemchandani, B.; Howlett, P. C.; Sun, J.; Macfarlane, D. R.; Forsyth, M. Ionic Liquids as Antiwear Additives in Base Oils: Influence of Structure on Miscibility and Antiwear Performance for Steel on Aluminum. *ACS Appl. Mater. Interfaces* **2013**, *5*, 11544–11553.
- (15) Qu, J.; Truhan, J. J.; Dai, S.; Luo, H.; Blau, P. J. Ionic Liquids with Ammonium Cations as Lubricants or Additives. *Tribol. Lett.* **2006**, *22*, 207–214.
- (16) Jiménez, A.; Bermúdez, M. D. Ionic Liquids as Lubricants for Steel-Aluminum Contacts at Low and Elevated Temperatures. *Tribol. Lett.* **2007**, *26*, 53–60.
- (17) Somers, A. E.; Howlett, P. C.; MacFarlane, D. R.; Forsyth, M. A Review of Ionic Liquid Lubricants. *Lubricants* **2013**, *1*, 3–21.
- (18) Minami, I. Ionic Liquids in Tribology. *Molecules* **2009**, *14*, 2286–2305.
- (19) Xiao, H. Ionic Liquid Lubricants: Basics and Applications. *Tribol. Trans.* **2017**, *60*, 20–30.
- (20) Zhou, Y.; Qu, J. Ionic Liquids as Lubricant Additives: A Review. *ACS Appl. Mater. Interfaces* **2017**, *9*, 3209–3222.
- (21) Amiril, S. A. S.; Rahim, E. A.; Syahrullail, S. A Review on Ionic Liquids as Sustainable Lubricants in Manufacturing and Engineering: Recent Research, Performance, and Applications. *J. Clean. Prod.* **2017**, *168*, 1571–1589.
- (22) Ngo, D.; He, X.; Luo, H.; Qu, J.; Kim, S. H. Competitive Adsorption of Lubricant Base Oil and Ionic Liquid Additives at Air/Liquid and Solid/Liquid Interfaces. *Langmuir* **2020**, *36*, 7582–7592.
- (23) Ferrante, J. Exoelectron Emission from a Clean, Annealed Magnesium Single Crystal during Oxygen Adsorption. *ASLE Trans.* **1977**, *20*, 328–332.
- (24) Atkin, R.; El Abedin, S. Z.; Hayes, R.; Gasparotto, L. H. S.; Borisenko, N.; Endres, F. AFM and STM Studies on the Surface Interaction of [BMP]TFSA and [EMIm]TFSA Ionic Liquids with Au(111). *J. Phys. Chem. C* **2009**, *113*, 13266–13272.
- (25) Perkin, S.; Albrecht, T.; Klein, J. Layering and Shear Properties of an Ionic Liquid, 1-Ethyl-3-Methylimidazolium Ethylsulfate, Confined to Nano-Films between Mica Surfaces. *Phys. Chem. Chem. Phys.* **2010**, *12*, 1243–1247.

- (26) Foulston, R.; Gangopadhyay, S.; Chiutu, C.; Moriarty, P.; Jones, R. G. Mono- and Multi-Layer Adsorption of an Ionic Liquid on Au(110). *Phys. Chem. Chem. Phys.* **2012**, *14*, 6054–6066.
- (27) Perez-Martinez, C. S.; Perkin, S. Interfacial Structure and Boundary Lubrication of a Dicationic Ionic Liquid. *Langmuir* **2019**, *35*, 15444–15450.
- (28) Qu, J.; Bansal, D. G.; Yu, B.; Howe, J. Y.; Luo, H.; Dai, S.; Li, H.; Blau, P. J.; Bunting, B. G.; Mordukhovich, G.; Smolenski, D. J. Antiwear Performance and Mechanism of an Oil-Miscible Ionic Liquid as a Lubricant Additive. *ACS Appl. Mater. Interfaces* **2012**, *4*, 997–1002.
- (29) Zhou, Y.; Dyck, J.; Graham, T. W.; Luo, H.; Leonard, D. N.; Qu, J. Ionic Liquids Composed of Phosphonium Cations and Organophosphate, Carboxylate, and Sulfonate Anions as Lubricant Antiwear Additives. *Langmuir* **2014**, *30*, 13301–13311.
- (30) Barnhill, W. C.; Qu, J.; Luo, H.; Meyer, H. M.; Ma, C.; Chi, M.; Papke, B. L. Phosphonium-Organophosphate Ionic Liquids as Lubricant Additives: Effects of Cation Structure on Physicochemical and Tribological Characteristics. *ACS Appl. Mater. Interfaces* **2014**, *6*, 22585–22593.
- (31) González, R.; Bartolomé, M.; Blanco, D.; Viesca, J. L.; Fernández-González, A.; Battez, A. H. Effectiveness of Phosphonium Cation-Based Ionic Liquids as Lubricant Additive. *Tribol. Int.* **2016**, *98*, 82–93.
- (32) Wijnarko, W.; Khanmohammadi, H.; Espallargas, N. Ionic Liquid Additives in Water-Based Lubricants for Bearing Steel-Effect of Electrical Conductivity and pH on Surface Chemistry, Friction and Wear. *Front. Mech. Eng.* **2022**, *7*, No. 756929.
- (33) Ge, X.; Li, J.; Zhang, C.; Wang, Z.; Luo, J. Superlubricity of 1-Ethyl-3-Methylimidazolium Trifluoromethanesulfonate Ionic Liquid Induced by Tribochemical Reactions. *Langmuir* **2018**, *34*, S245–S252.
- (34) Yu, B.; Bansal, D. G.; Qu, J.; Sun, X.; Luo, H.; Dai, S.; Blau, P. J.; Bunting, B. G.; Mordukhovich, G.; Smolenski, D. J. Oil-Miscible and Non-Corrosive Phosphonium-Based Ionic Liquids as Candidate Lubricant Additives. *Wear* **2012**, *289*, 58–64.
- (35) Huang, G.; Yu, Q.; Ma, Z.; Cai, M.; Liu, W. Probing the Lubricating Mechanism of Oil-Soluble Ionic Liquids Additives. *Tribol. Int.* **2017**, *107*, 152–162.
- (36) Yu, Q.; Wang, Y.; Huang, G.; Ma, Z.; Shi, Y.; Cai, M.; Zhou, F.; Liu, W. Task-Specific Oil-Miscible Ionic Liquids Lubricate Steel/Light Metal Alloy: A Tribochemistry Study. *Adv. Mater. Interfaces* **2018**, *5*, No. 1800791.
- (37) Qu, J.; Luo, H.; Chi, M.; Ma, C.; Blau, P. J.; Dai, S.; Viola, M. B. Comparison of an Oil-Miscible Ionic Liquid and ZDDP as a Lubricant Anti-Wear Additive. *Tribol. Int.* **2014**, *71*, 88–97.
- (38) Qiao, D.; Wang, H.; Feng, D. Tribological Performance and Mechanism of Phosphate Ionic Liquids as Additives in Three Base Oils for Steel-on-Aluminum Contact. *Tribol. Lett.* **2014**, *55*, 517–531.
- (39) Khanmohammadi, H.; Wijnarko, W.; Espallargas, N. Ionic Liquids as Additives in Water-Based Lubricants: From Surface Adsorption to Tribofilm Formation. *Tribol. Lett.* **2020**, *68*, No. 130.
- (40) Bernat, S.; Armada, S.; Espallargas, N. Friction Mechanisms by Carboxylic Acids in Aqueous Lubricants. *Tribol. Lett.* **2018**, *66*, No. 83.
- (41) Bjerregaard, L.; Geels, K.; Ottesen, B.; Rückert, M. *Metalog Guide: Your Guide to the Perfect Materialographic Structure*; Struers A/S: Rødovre (Denmark), 2020.
- (42) Rudnick, L. R. *Synthetics, Mineral Oils, and Bio-Based Lubricants*; Rudnick, L. R., Ed.; CRC Press: Boca Raton, Florida (USA), 2020.
- (43) Stachowiak, G. W.; Batchelor, A. W. *Engineering Tribology*; Elsevier: Oxford (UK), 2014.
- (44) Viesca, J. L.; García, A.; Hernández Battez, A.; González, R.; Monge, R.; Fernández-González, A.; Hadfield, M. FAP- Anion Ionic Liquids Used in the Lubrication of a Steel-Steel Contact. *Tribol. Lett.* **2013**, *52*, 431–437.
- (45) Yu, B.; Zhou, F.; Pang, C.; Wang, B.; Liang, Y.; Liu, W. Tribological Evaluation of  $\alpha$ ,  $\omega$ -Diimidazoliumalkylene Hexafluorophosphate Ionic Liquid and Benzotriazole as Additive. *Tribol. Int.* **2008**, *41*, 797–801.
- (46) Urtis, L. A.; Arcifa, A.; Zhang, P.; Du, J.; Fantauzzi, M.; Rauber, D.; Hempelmann, R.; Kraus, T.; Rossi, A.; Spencer, N. D. Influence of Water on Tribolayer Growth When Lubricating Steel with a Fluorinated Phosphonium Dicyanamide Ionic Liquid. *Lubricants* **2019**, *7*, No. 27.
- (47) Rokosz, K.; Hryniewicz, T.; Simon, F.; Rzadkiewicz, S. Comparative XPS Analyses of Passive Layers Composition Formed on Duplex 2205 SS after Standard and High-Current-Density Electropolishing. *Teh. Vjesn. - Tech. Gaz.* **2016**, *23*, 731–735.
- (48) Liu, Y.; Shen, L. From Langmuir Kinetics to First- and Second-Order Rate Equations for Adsorption. *Langmuir* **2008**, *24*, 11625–11630.
- (49) Nalam, P. C.; Pham, A.; Castillo, R. V.; Espinosa-Marzal, R. M. Adsorption Behavior and Nanotribology of Amine-Based Friction Modifiers on Steel Surfaces. *J. Phys. Chem. C* **2019**, *123*, 13672–13680.
- (50) Sauerbrey, G. Verwendung von Schwingquarzen Zur Wägung Dünner Schichten Und Zur Mikrowägung. *Z. Phys.* **1959**, *155*, 206–222.
- (51) Voinova, M. V.; Rodahl, M.; Jonson, M.; Kasemo, B. Viscoelastic Acoustic Response of Layered Polymer Films at Fluid-Solid Interfaces: Continuum Mechanics Approach. *Phys. Scr.* **1999**, *59*, 391–396.
- (52) Kanazawa, K. K.; Gordon, J. G. Frequency of a Quartz Microbalance in Contact with Liquid. *Anal. Chem.* **1985**, *57*, 1770–1771.
- (53) Rodahl, M.; Kasemo, B. On the Measurement of Thin Liquid Overlayers with the Quartz-Crystal Microbalance. *Sens. Actuators, A* **1996**, *54*, 448–456.
- (54) Zhou, Y.; Leonard, D. N.; Guo, W.; Qu, J. Understanding Tribofilm Formation Mechanisms in Ionic Liquid Lubrication. *Sci. Rep.* **2017**, *7*, No. 8426.
- (55) Dawczyk, J.; Morgan, N.; Russo, J.; Spikes, H. Film Thickness and Friction of ZDDP Tribofilms. *Tribol. Lett.* **2019**, *67*, No. 34.
- (56) Bruce, R. W. *Handbook of Lubrication and Tribology, Volume II: Theory and Design*, 2nd ed.; CRC Press: Boca Raton, Florida (USA), 2012.

*This page is intentionally left blank*

*This page is intentionally left blank*



ISBN 978-82-326-5366-9 (printed ver.)  
ISBN 978-82-326-5264-8 (electronic ver.)  
ISSN 1503-8181 (printed ver.)  
ISSN 2703-8084 (online ver.)



**NTNU**

Norwegian University of  
Science and Technology